A Fine Resolution Atmosphere-Ocean Model of the Bay of Bengal: Impact on the Storm Surge Forecast

Thesis submitted in accordance with the requirements of the
University of Liverpool for the degree of Master in Philosophy
by Jennifer Mari Kirwan-Evans

February 17, 2018

Abstract

A Fine Resolution Atmosphere-Ocean Model of the Bay of Bengal: Impact on the Storm Surge Forecast, by Jennifer Mari Kirwan-Evans

Storm surges and extreme waves associated with tropical cyclones are a major cause of coastal flooding in the Bay of Bengal and can be devastating both in terms of loss of resources as well as loss of life.

Previous work has found that increasing the grid resolution of atmospheric models can result in a more accurate representation of tropical cyclone intensity and structure. Here, a modelling system for the Bay of Bengal is set up using the Weather, Research and Forecasting Model (WRF) for the atmospheric component, the Proudman Oceanographic Laboratory Coastal Ocean Modelling System (POLCOMS) for the ocean component, and the WAve Model (WAM) as the wave component. The high resolution atmospheric simulation used moving, storm centred nests of 4 km and 1.3 km grid spacing. The coarse resolution simulation used a single 12 km domain, which is identical to the outer domain in the simulation with nests. The ocean and wave models were two-way coupled to incorporate wave-current interactions, and the ocean domain matched the largest WRF domain at 1° resolution.

The modelling system was tested using a hindcast of Cyclone Phailin, a tropical cyclone which occurred in the Bay of Bengal during October 2013. The Phailin simulation was checked against the available atmospheric and oceanic observational data, and the modelled cyclone, surge and waves were found to be similar to reality in location and magnitude. Maximum wind, rate of intensification and radius of maximum winds, as well as the surge and wave heights, were sensitive to the atmospheric model resolution. The coarse resolution model simulated lower maximum wind values, over a larger extent of ocean, and generated larger magnitude surge and waves. The cyclone track, surge location and maximum waves position were found to be insensitive to the changes in atmospheric model grid resolution.

Different atmospheric initial conditions were tested, and cyclone simulation accuracy increased with increased resolution of the initial conditions dataset. A full high-resolution simulation of a later model start time for Cyclone Phailin was used to further assess the sensitivity of the model to small changes in the initial fields. The maximum intensity, rate of cyclogenesis, and the cyclone track were all sensitive to the initial conditions used. The storm surge and and waves, which were generated, changed with the differing atmospheric forcing. The relationship between cyclone simulation and initial conditions used is complex

and further work is needed to better understand this link.

Acknowledgements

The path towards finishing this thesis has not been straightforward. I would like to thank all the people who have helped me arrive where I am now, whether that's by supporting me initially back when this project was a PhD, advising me through difficult decisions such as converting to an MPhil degree, and patiently assisting me while I completed the work part-time.

I would specifically like to thank the UK Natural Environment Research Council (NERC) studentship, which as part of the Earth, Atmosphere, Ocean Doctoral Training Program, allowed me to spend the last 3 years studying a fascinating subject. My supervisors Judith Wolf, Kevin Horsburgh, David Schultz and Chris Hughes have been instrumental to my success, by supporting and advising with research decisions, providing encouragement and guidance when I needed it, and allowing my attendance to both national and international conferences. Thank you.

I would like to dedicate this MPhil to my husband, Thomas Kirwan-Evans. He was my shoulder to cry on when times were hard, he was my technical advisor with all things MatLab, and he gave me the drive to finish writing up - so I will be more qualified than him. I would not be where I am today without Thom.

Contents

List of Figures

List of Tables

List of Terms

A_i Wave amplitude.
C_d Drag transfer coefficient.
C_k Enthalpy transfer coefficient.
D Unperturbed depth of ocean.
$E(f)$ Variance density spectrum.
H_s Significant wave height.
K_N Nikuradse legth scale.
K_b Enthalpy of the atmosphere at sea level.
K_x^* Enthalpy of the ocean surface.
$M = (M_x, M_y)$ Mass transport terms in the east-west and north-south directions.
R_d Gas constant for dry air.
S_{Total} Resultant action density.
S_{in} Wave input source term.
T_s Temperature of the atmosphere at sea level.
$U = (u, v)$ Components of the depth averaged current.
$W = (w_x, w_y, w_z)$ Wind velocities and their components.
W_m Maximum wind velocity.
α_i Wave phase.
β Rossby parameter.
ϵ Thermodynamic efficiency.
η Sea surface elevation.
γ Ratio of heat capacities of dry air.
$\hat{\alpha}$ Charnock parameter.
κ Von Karman's constant.
λ_p Wavelength at the peak of the wave spectrum.
μ Mas per unit area.
ω Intrinsic angular frequencies.
ϕ Geopotential.
ψ Wave direction.
ρ_a Atmospheric density at sea level.
ρ_w Sea water density.
σ Terrain following vertical coordinate.
τ_b Ocean bottom stress due to friction.
τ_s Wind stress.
θ_* Scaling temperature.
θ Potential temperature.
ζ Covariant vertical velocity.
c_σ, c_θ Wave propagation velocities in spectral space.
c_p Wave phase speed.
c_x, c_y Wave propagation velocities.
c Phase celerity of waves.
f_i Wave frequency.
f Coriolis parameter.
g Gravitational acceleration.
h Total water depth.
k Apparent roughness felt by current due to waves.
l Wave number.
m_x, m_y Map factors.
p_a Atmospheric pressure at sea level.
p_h Hydrostatic pressure.
q_* Scaling moisture.
t Time.
w_* Friction velocities.
w_{10} Wind velocity measured 10 m above ground level.
z_0 Roughness length.

List of Abbreviations

ADCIRC ADvanced CIRCulation numerical model, developed by the University of North Carolina
All Resolution Bay of Bengal model scenario using the 12 km, 4 km, and 1.3 km WRF model output as meteorological boundary forcing to the ocean domain
ARW Advanced Research WRF - dynamic solver used by WRF numerical model
BoB Bay of Bengal
BODC British Oceanographic Data Centre
CAPE Convective Available Potential Energy
CAWOMS Coupled Atmosphere Wave Ocean Modelling System, developed by University of North Carolina
CFL Criterion Courant-Friedrich-Lewy criterion
CICE Los Alamos Climate Ocean and Sea Ice model - a component of POLCOMS
D26 Depth of the 26 °C isotherm from the ocean surface
ECMWF European Centre for Medium-Range Weather Forecasts
ERA-Interim Atmospheric reanalysis dataset published by ECMWF
ERSEM European Regional Sea Ecosystem Model - a component of POLCOMS
GFS Global Forecast System - global atmospheric modelling system developed by NCEP
GFDL Geophysical Fluid Dynamics Laboratory
GOTM General Ocean Turbulence Model - a component of POLCOMS
HiRAM High-Resolution Atmospheric Model - developed by GFDL
HWRF Hurricane WRF - WRF set-up developed by NOAA
IBTrACS International Best Track Archive for Climate Stewardship
IIT-D Indian Institute of Technology - Delhi
IMD Indian Meteorological Department
INCOIS Indian National Centre for Ocean Information Services
INSAT Indian National satellite system
ITCZ Intertropical Convergence Zone
JTWC Joint Typhoon Warning Centre
LSM Land Surface Model - a component of WRF
NCAR National Centre for Atmospheric Research, USA
NCEP National Centres for Environmental Protection, USA
NMM Non-hydrostatic Mesoscale Model - dynamic solver of WRF
NOAA National Oceanic and Atmospheric Administration, USA
NWP Numerical Weather Prediction
PBL Scheme Planetary Boundary Layer scheme - component of WRF

POLCOMS Proudman Oceanographic Laboratory Coastal Ocean Modelling System
POM Princeton Ocean Model
RMW Radius of maximum winds - the distance between the centre of a tropical cyclone and the band of strongest winds
SWH Significant Wave Height
SST Sea Surface Temperature
ST1 Bay of Bengal model scenario initialised at 0000 UTC 9 October
ST2 Bay of Bengal model scenario initialised at 1200 UTC 9 October
SWAN Simulating WAves Nearshore - wave model developed by Delft University of Technology
TC Tropical cyclone, also known as hurricane and typhoon
TPXO Global ocean modelling ocean tides
WPS WRF Preprocessing Sysmte - component of WRF
WRF Weather Research and Forecasting atmospheric model, developed collaboratively by NCAR and NCEP

Chapter 1

Introduction

The injury and loss of life, and damage to property and infrastructure caused by tropical cyclone (TCs) in coastal areas can be catastrophic. TCs in the North Indian Ocean can have a profound impact on the surrounding countries of the Bay of Bengal (BoB) and the Arabian Sea, and the area is known for its potential to generate devastating high storm tides - a major killer associated with TCs. The coastal flood risk from TC storm surges is high in this location due to the favourable geomorphic and bathymetric effects of the BoB, coupled with the densely populated, low lying coastal plain (Ali, 1979; Dube et al., 1997). Out of the world's 10 most damaging TCs on record in terms of the most fatalities (from about 40,000 to over 200,000 deaths), 8 were located in the BoB and Arabian Sea with 5 in Bangladesh and 3 in India (World Meteorological Organisation, 2016). Furthermore, the highest ever recorded storm tide of 13.7 m occurred in 1876 near the Megna Estuary, Bangladesh (World Meteorological Organisation, 2016). These natural disasters highlight the need to provide regional governments and their coastal populations with as much advance warning as possible.

Fortunately, TC fatalities in Bangadesh and India have decreased in recent decades (Dube et al., 2009a). In 1991, TC Gorky caused approximately 140,000 fatalities (Dube et al., 1997), while for TC Sidr, a storm with similar intensity in terms of wind speed and atmospheric pressure, the death toll was 3,406 (Paul, 2009). Part of the reason for the difference in loss of life may be due to TC Gorky causing a storm surge of 7.6 m (Dube et al., 1997), compared with Sidr's 5.75 m (Paul, 2009). Nevertheless, the IIT-D (Indian Institute of Technology - Delhi) storm surge mathematical model, which is operationally used by the Indian Meteorological Department (IMD) as part of their early warning system, successfully forecasted the maximum water level of TC Sidr with relatively good accuracy (Paul, 2009). This allowed the nearly 4000 TC shelters, built across several districts of Bangladesh prior to the cyclone, be used and reduced the number of fatalities (Paul, 2009).

In 2013, the massive evacuation of 800,000 people in a 48 hour period and improved emergency management processes, such as mobile phone alerts, reduced the number of fatalities to only 23 for TC Phailin with a storm surge of 3 m (Murty et al., 2014b; IMD Report, 2013). This increased warning time was made possible by using computer based numerical models, which can predict the location and intensity of TC and their associated ocean hazards.

These examples of recent BoB TCs demonstrate the value of accurate forecasts in terms of number of lives saved. Accurate, dependable forecasts are crucial in the socio-economic context as well - false alarms reduce the general public's belief and faith in the forecasting network, and unnecessary evacuations carry an extremely high economic cost.

Tropical cyclones and their interaction with the ocean are complex and the combination of atmospheric and oceanic components make an analytical solution of TC, storm surge and wave prediction difficult. Therefore, both statistical and physics-based TC and storm tide numerical models are very important in a number of early flood warning systems and can provide accurate simulations of TC and sea level (Rappaport et al., 2009b; Horsburgh et al., 2008). These numerical modelling techniques are continuously being developed and updated to improve simulation accuracy and increase the amount of warning time and forecast detail.

Numerical models are not exact replicas of reality, and so, they have various inherent inaccuracies within them. These uncertainties can be a result of the numerical methods and simplification used to impose continuous numerical equations onto a grid, with discrete time steps. They may also be the propagation of errors contained within the boundary and initial conditions into the model domain. For storm surge numerical models, the meteorological input data at the atmospheric boundary can be one large source of uncertainty. Therefore, inaccuracies within TC numerical forcing data can transfer to the ocean simulation and cause inaccuracies in the storm surge forecast. This is one of the most significant causes of storm surge forecast uncertainty, especially in the BoB, as meteorological observations are limited in this area.

As stated above, it is extremely important for storm surge and wave prediction to accurately forecast the meteorological input. Increasing the grid resolution of atmospheric models has been shown to improve the TC simulation by refining the representation of storms, capturing mesoscale features, as well as complex convective events (Lakshmi et al., 2017). In particular, it has been shown that decreasing the grid spacing lower than 4 km can produce a measurable improvement in TC intensity and structure prediction (Davis et al., 2010a).

The majority of research in fine resolution TC atmospheric models has focussed on the impact to the cyclone's intensity and track forecast simulations. In this study, the high resolution atmospheric modelling will be applied to storm surge and wave prediction models to investigate whether the forecast improvements seen in atmospheric studies propagates into the ocean domain.

Of specific interest in the present work is the impact for the BoB. This region is extremely vulnerable to TCs and storm tides and would greatly benefit from any improvements to the operational flood warning system. To this end, the study focusses on a particular historical TC event in the BoB - very severe cyclone Phailin which occurred during October 2013. TC Phailin, meaning 'sapphire' in Thai, was one of the strongest TCs ever recorded in the northern BoB (IMD Report, 2013). Making landfall on the Odisha coast, India, in October 2013, very severe cyclone Phailin is next only to the 1999 Orissa super cyclone, in terms of

maximum wind speed and central atmospheric pressure (Murty et al., 2014a). This cyclone was chosen for the current study as an example of a recent, intense TC in the northern BoB.

To assess the impact of fine resolution atmospheric forcing on the storm surge forecast for TC Phailin, a high resolution, one-way coupled ocean-atmosphere modelling system is established. The performance of the modelling system for the TC Phailin hindcast is summarised, the impact of increased atmospheric resolution is assessed, and in addition, the effect of initial conditions on the storm surge and wave forecast are examined. There are three objectives of the work which are described below.

1.1 Objectives of the Study

The main objective of this study is to investigate the sensitivity of storm surge and wave forecast simulations to changes in the atmospheric forcing data, in the Bay of Bengal.

In order to achieve this aim, there are three technical objectives: the first involves setting up a numerical modelling system to simulate a tropical cyclone in the Bay of Bengal; the second and third use this system to investigate how sensitive the modelled processes are to certain model variables, and whether or not this adversely impacts the results obtained.

These objectives provide the focus of this manuscript with the rest of this section introducing background information and context, Section 2 providing a review of the background literature; Section 3 describing the method for approaching answers to the objectives; Section 4 presenting the results of the numerical experiments; and Section 5 providing a discussion of how the results relate to the objectives and whether the they have been answered satisfactorily.

1.1.1 Objective One - Set up a numerical modelling system for a tropical cyclone in the Bay of Bengal

In this study, one of the aims is to set up and run a mathematical model of the atmosphere and ocean to numerically simulate Cyclone Phailin. Phailin is a tropical cyclone which occurred in the Bay of Bengal in October 2013. The full details of this storm are given in Section 1.6. This model will incorporate the storm's impact on the ocean, both in terms of sea surface elevation and waves generated.

The model domain will be large enough to cover the whole of the Bay of Bengal to avoid any propagation of boundary condition errors into the area of interest. Appropriate boundary and initial conditions will be identified or calculated for both the atmospheric and oceanic domains, which incorporate as many physical processes as possible. The Cyclone Phailin simulation will last for several days from the storm's generation to landfall and dissipation.

The modelled simulation will be evaluated against the available observational data. This includes both atmospheric information about the tropical cyclone, sea surface elevation data and wave height and direction. The data is very limited and will generally be used to check the model is in the correct range of values for each variable.

This modelling system will be the basis for the next two objectives.

1.1.2 Objective Two - How sensitive is the modelling system to atmospheric horizontal resolution?

All numerical models are limited by their spatial and temporal resolution. This is the length scale of the grid over which the model calculates the discretised dynamic equations. In Section 2.1.1, the impact of higher resolution numerical models is described and explained. This section also explains the motivation for including this particular objective. If higher resolution models give more accurate or more conservative results for storm surge and wave forecasting, then this may advance forecast modelling of these hazards.

Here, the study focusses on increasing the horizontal resolution of the atmospheric model, and the impact on the meteorological output is described and explained. The propagation of the changes in atmospheric fields into the ocean domain is also investigated using the modelling system. This set of experiments will highlight any trends in model accuracy, however, due to the limited availability of the observational data, they will generally focus on differences between high and low resolution modelling results.

1.1.3 Objective Three - Does atmospheric start time make a difference for the modelled Cyclone Phailin simulation?

Numerical models of the atmosphere and ocean are very sensitive to the initial conditions they are given. Initialisation of tropical cyclone models is a large field of research, summarised in Section 2.1.2.

One way of changing atmospheric initial conditions of the modelling system is to alter the start time of the tropical cyclone simulation. This will result in a slightly different starting storm circulation, and the differences in location, wind speed, pressure and other meteorological variables will propagate through both the atmospheric and oceanic simulations.

Similarly with Objective Two, due to the limited atmosphere and ocean observed data, the study will focus on changes between different start time simulations.

1.2 Tropical Cyclones

In this section, tropical cyclones are described in detail. This includes the processes of formation, translation and dissipation, along with where these storm occur, the naming conventions used and how the atmospheric processes interact with the ocean.

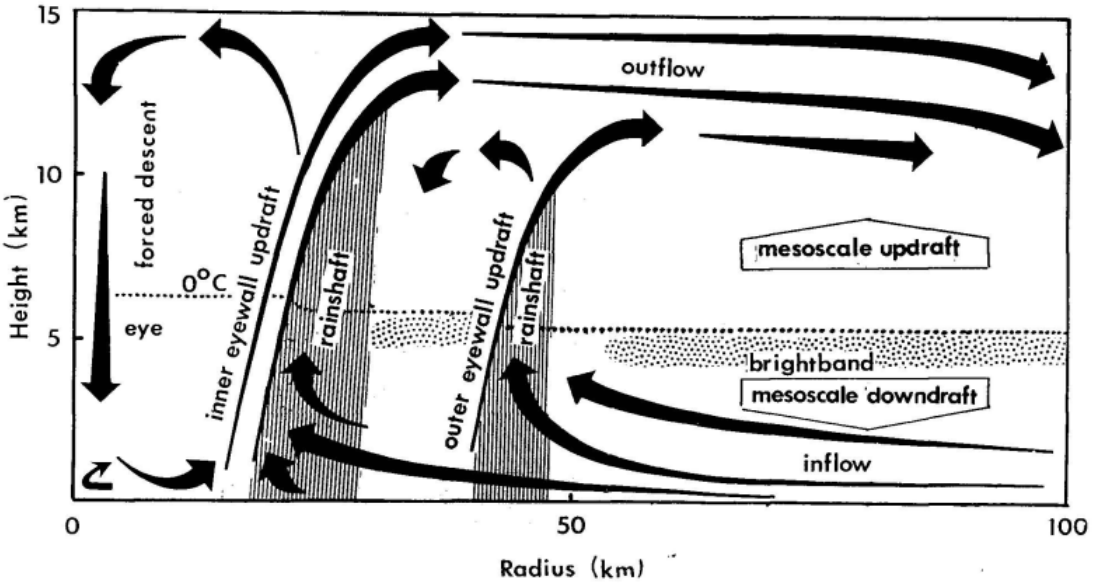

Figure 1.1: TC Structure Schematic, including the eye and eyewall, secondary structure and circulation (Willoughby, 1988)

1.2.1 Tropical Cyclone Structure and Formation

Tropical cyclones (TCs) are intense atmospheric vortices generated over the Earth's warm tropical oceans. They are some of the most spectacular, yet devastating natural features and have been a topic of much scientific interest and research for many centuries.

TCs are systems of relatively low pressure in the troposphere with a warmer environment at their centre ('warm core') and rapidly cyclonically rotating air around the eye (centre of circulation) - anticlockwise in the northern hemisphere, clockwise in the southern hemisphere. They are generally between 400 km and 700 km wide. The air flows radially inward from the outer edge to the centre, and the rotation is caused by conservation of angular momentum. Near the centre the air rapidly ascends to the top of the troposphere and, once aloft, flows outwards producing vast areas of high cloud. The area of rising air is usually located at the eyewall, where the strongest surface winds and heaviest rain occur, known as the radius of maximum winds (RMW).

The circular cyclone eye is cloud free with calm winds due to descending air suppressing cloud formation. Eye diameters range from under 10 km to over 100 km, but are typically around 40 km. The dynamics within the eye, eyewall and radius of maximum wind are complex and may involve processes such as eyewall replacement cycles and flow instabilities. Figure 1.1, taken from Willoughby (1988), shows the structure of a TC.

Although there is uncertainty regarding the exact formation process of tropical cyclones, some key factors have been found to be essential (Gray, 1979):

- A warm ocean to fuel the cyclone. Studies have found that the sea surface temperature must be at least approximately 26.5 °C. In fact, water of this temperature is actually

required to a depth of roughly 50 m (Gray, 1979). This is the reason that tropical cyclones do not form outside of the tropics, where the waters are cooler.

- The atmosphere must cool fast enough with height to be 'potentially unstable' to moist convection. This means that warming at the bottom of the boundary layer will cause severe convection through the troposphere, with deep, moist convection allowing the heat energy stored in the ocean to be released via latent heat processes. This is the main mechanism for tropical cyclone development.

- The mid-troposphere must also be relatively high humidity, again to support sustained moist convection.

- The development location must be more than 500 km (roughly 5° latitude) away from the equator. This is to ensure that the Coriolis effect is large enough for near gradient wind balance to occur. Without the Coriolis force, the low pressure, cyclonic circulation would not be maintained.

- There must be a pre-existing low pressure disturbance, with sufficient surface convergence and vorticity. TCs cannot form 'spontaneously' and need a trigger mechanism, often a weakly organised system.

- There must also be low values of vertical wind shear between the upper troposphere and the surface. Large differences in wind with height can cause disruption to the storm's circulation, preventing genesis, or weakening and destroying previously formed TCs.

Having these factors met is important, however they are not always sufficient for TC formation as many systems do not develop even when appearing to have these favourable conditions. Previous work (Zehr, 1992) suggests that mesoscale convective systems (large thunderstorm systems, for example) may play an important role in impacting the inertial instability of the atmosphere, allowing tropical cyclogenesis to occur. More recently, McTaggart-Cowan et al. (2015) revisited the sea surface temperature threshold stated by many, and found that the presence of a baroclinc precursor disturbance can alter the formation process sufficiently to promote development over cooler waters. The importance of the ocean, including air-sea heat, moisture and momentum fluxes may also play a more important role in the potential TC genesis than previously explored; this is discussed in detail in Section 1.2.5.

The factors mentioned above, limit the extent of tropical cyclones across the global oceans. Most TCs form between 10° and 30° latitude, where the Coriolis force is strong enough to maintain the low pressure circulation and the ocean water is warm enough to provide the necessary latent heat energy.

TCs can be formed in the equatorial band of convection known as the Intertropical Convergence Zone (ITCZ), or the Monsoon Trough (Gray, 1979). The ITCZ extends semi-continuously around the globe, and occurs as a convergence line between easterly Trade Winds from the Northern and Southern Hemispheres, or as a convergence zone where there

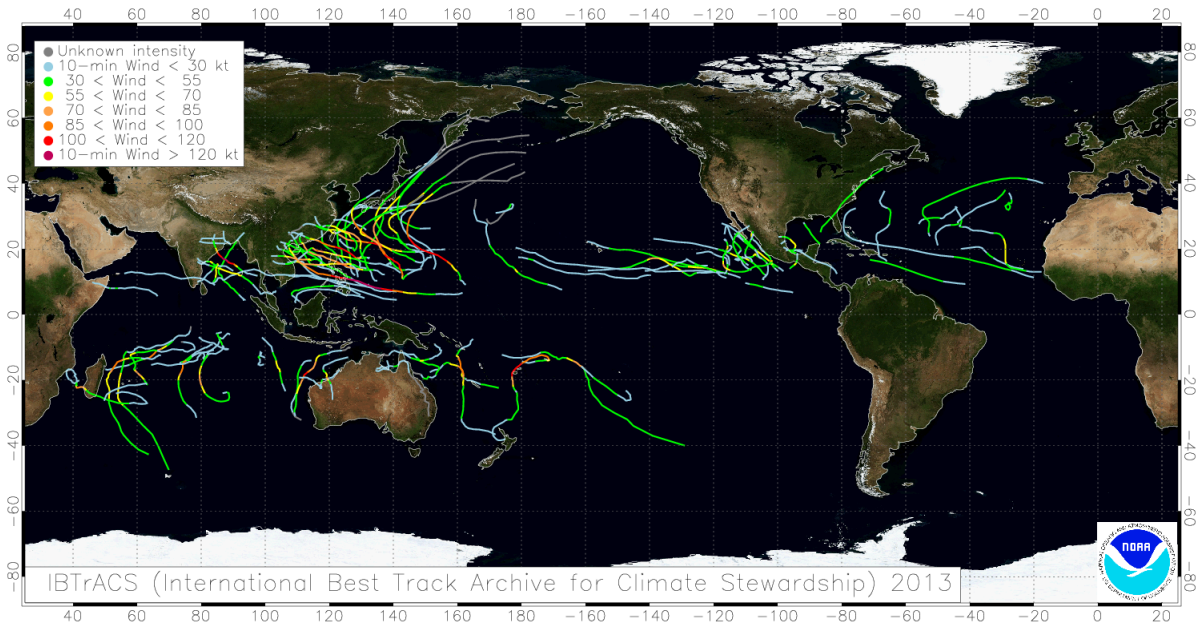

Figure 1.2: An International Best Track Archive for Climate Stewardship (IBTrACS) image of the global tropical cyclones in 2013. Note that there are several events in the North Indian Ocean and the Bay of Bengal

westerly monsoon flow meets easterly Trade Winds on its poleward side. The ITCZ provides both the necessary severely unstable and moist atmosphere, as well as the initial low pressure disturbance. This formation trigger occurs in all basins at different times in the year, with the exception of the North Atlantic. Another source of large scale atmospheric instability are tropical waves (or easterly waves), a type of trough (area of low pressure) which move across the tropics from east to west causing areas of deep, moist convection.

1.2.2 Locations of Cyclogenesis and Naming Conventions

There are seven main tropical cyclone basins, as can be seen in Figure 1.2. These are the North Atlantic, the Eastern and Western Pacific, the Northern Indian Ocean (Bay of Bengal and the Arabian Sea), the South West Indian Ocean, the Australian region and the Southern Pacific. Each area is active for different seasons, generally coinciding with the area's late summer months, when the difference in temperature between the sea surface and the atmosphere aloft is the largest. There generally are not TCs in the Southern Atlantic, however in March 2004 Cyclone Catarina became the first ever recorded in this basin.

In all locations TC intensity is measured as the maximum sustained wind speed. However, in the different TC locations there are varying methods of classification as well as different ways of calculating the wind speed.

In the North Atlantic and North East Pacific the 1-minute mean wind speed is used as well as the Saffir-Simpson Scale classification. In other areas, 3-minute or 10-minute mean

Table 1.1: The Saffir Simpson hurricane intensity scale (Western Pacific Weather, 2015).

Strength	Wind Speed (kt)	Wind Speed (ms^{-1})	Pressure (hPa)
Category 1	64-82	33-42	>980
Category 2	83-95	43-49	965-979
Category 3	96-113	50-58	945-964
Category 4	114-135	58-70	920-944
Category 5	>135	>70	<920

wind speed are used.

The Saffir-Simpson hurricane wind scale (see Table 1.1) is probably the most well known scale of TC intensity. A TC is classed as a hurricane (in the locations mentioned above) if the maximum sustained wind speed (1 minute mean) is at least 74 mph (33 ms^{-1}; 64 kt; 119 kmh^{-1}). The most severe classification in this scale is category 5 where maximum sustained wind speeds exceed 156 mph (70 ms^{-1}; 136 kt; 25 kmh^{-1}).

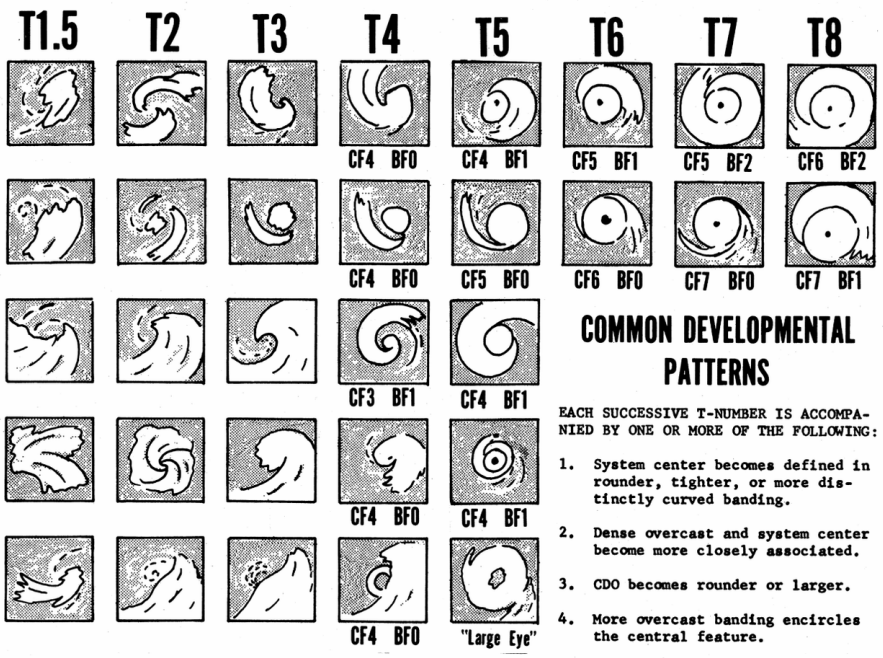

Figure 1.3: The Dvorak TC intensity estimation technique - a diagram of the TC patterns and their estimated intensities (Dvorak, 1973).

In the North West Pacific, the same threshold for hurricane-strength winds is used, however the term 'typhoon' instead of the Saffir Simpson hurricane categories is adopted. In the southern hemisphere and Indian Ocean, neither 'hurricane' or 'typhoon' is used. Instead tropical storms are referred to as tropical cyclones, severe tropical cyclones or very intense tropical cyclones.

In the North Indian Ocean the TC intensity classification called the Dvorak technique (Dvorak, 1975) is used. This method estimates a TC intensity from visible and infra-red satellite images using knowledge of the different developmental cloud patterns that TCs may take. The TC's cloud formation is used to attribute a T number which defines the upper and lower limits on its intensity. The main patterns identified and their associated T number are shown in Figure 1.3 with Table 1.2 giving the intensity ranges in terms of the 1 minute wind speed and pressure deficit. The cloud formations include a curved band pattern (T1.0-4.5), a shear pattern (T1.5-3.5), central dense overcast pattern (T2.5-5.0), central cold cover pattern and banding eye pattern (T4.0-4.5) and eye pattern (T4.5-8.0). This method may seem basic, however it is regularly used by several TC forecast organisations including the US Joint Typhoon Warning Centre (JTWC), the Indian Meteorology Department (IMD), NOAA Satellite Analysis Branch, and the National Hurricane Centre's Tropical Analysis and Forecast Branch. This highlights the lack of quantitative meteorological measurements available for TCs (see Section 3.4.1).

Along with T-number, the IMD also classifies low pressure systems in the Bay of Bengal with certain definitions. These can be found in Table 1.2.

Table 1.2: IMD Classification of low pressure systems with corresponding T number, pressure deficit and wind speed (India Meteorological Department, 2009).

System	**T Number**	**Pressure Deficit (hPa)**	**Wind Speed (ms^{-1})**
Well Marked Low	1	1.0	<9
Depression	1.5	1 to 3	10 to 14
Deep Depression	2	3 to 4.5	15 to 17
Cyclonic Storm	3	4.5 to 8.5	18 to 24
Severe Cyclone Storm	3.5	8.5 to 15.5	25 to 32
Very Severe Cyclonic Storm	4 to 6	15.5 to 65.6	33 to 61
Super Cyclonic Storm	6.5 to 8	>65.6	>62

1.2.3 Tropical Cyclone Movement

Along with intensity, the movement or track of a tropical cyclone is a feature of much research and interest. The dynamics can be broken into two attributes: the 'steering' by the background environment, and the impact of a varying Coriolis parameter known as the 'beta drift'.

The background steering flow in its most simple form is the advection of the storm by the local ambient flow, often termed the 'steering' flow. This is the dominant effect in most cases.

TCs move from east to west in both the southern and northern hemispheres. At the band of latitudes where tropical cyclones are generated and develop, the dominant circulation pattern is dominated by the easterly Trade Winds on the equatorial side of the subtropical high. These Trade Winds are from the southeast in the northern hemisphere, and from the

northeast in the southern hemisphere, hence the westward and poleward movement of most cyclones.

In certain locations, other synoptic flow patterns impact the track. For example, in the North Atlantic and North-east Pacific, a type of atmospheric trough called tropical easterly waves move east to west across the tropics (mentioned above). They are elongated areas of low pressure which are carried westward by the prevailing easterly Trade Winds. They can lead to the formation of tropical cyclones and their subsequent advection westward.

Of note in the Indian Ocean is the monsoon trough, which can similarly affect tropical cyclogenesis and advection. The monsoon trough is part of the ITCZ, which moves northwards and southwards bringing changing seasons. TCs commonly form in the vicinity of this low pressure zone, as mentioned above, and may be advected along with it.

The beta drift is the impact of the Coriolis force field, changing from zero at the equator to a maximum at the poles. In most cases in dynamical meteorology the impact of the varying Coriolis parameter is small, as very few low pressure systems span a distance in the scale of several degrees of latitude. However, tropical cyclones can span hundreds of kilometres and can impact the surface of the globe for thousands of kilometres, therefore they are subject to the beta drift. The effect is named after the Rossby parameter β which is defined as:

$$\beta = \frac{\partial f}{\partial y} \tag{1.1}$$

where f is the Coriolis parameter and y is in the direction of increasing latitude.

This effect is induced indirectly by the storm itself as a result of the advection of the background potential vorticity by the cyclone's circulation. In the most simple cases, the background potential vorticity gradient is equal to the Rossby parameter. This effect causes cyclones to move poleward and westward relative to the motion they would have if the background vorticity field were unperturbed by the storms, irrespective of the direction of environmental flow. The associated drift speed is generally small, just 1-2 ms^{-1}.

1.2.4 Landfall and Dissipation

When the centre of a tropical cyclone crosses the coast, landfall has occurred. When this happens, extreme winds, torrential rainfall, a storm surge, wave overtopping and flooding may be experienced at the coast. These storm conditions actually occur before TC landfall, due to the size of the storm system. In fact, the strongest winds may occur prior to landfall, as the radius of maximum winds crosses a coastal location.

Once landfall has occurred, and the tropical cyclone moves overland, the system no longer has the input of energy from the warm ocean and quickly loses strength. This typically occurs very quickly, and generally a TC becomes an extratropical cyclone or disorganised area

of low pressure within a couple of days. This process is accelerated if high ground or mountains are close by, due to increased friction and topographically forced rainfall. However a cyclone may regenerate after landfall if it is advected back over an area of open warm water.

TCs can also dissipate when they move over seas which are cooler, generally below 26 °C. The warm core will erode and cease to exist, and the TC will lose its extreme characteristics and become a remnant area of low pressure.

Weakening or dissipation may also occur with changes of vertical wind shear, where the main convection moves away from the centre of the cyclone. Other dissipation mechanisms include: merging with nearby frontal zones which can cause TCs to transition into extra-tropical storms; merging with another depression, becoming a larger area of low pressure, but perhaps no longer a TC; and large amounts of dust which may also reduce the strength of tropical cyclones.

1.2.5 Interaction with the Ocean

As mentioned in Section 1.2.1, TCs are strongly coupled to the ocean surface and mixed layer via exchanges of heat, momentum and moisture at the air-sea interface. The primary energy source for a TC to develop and intensify comes from the ocean via the evaporation of warm sea water and the subsequent atmospheric convection. The warm, moist air cools as it is lifted through the troposphere, allowing condensation to occur and clouds to form (rainbands and eyewall). During this condensation, large amounts of latent heat are released, fuelling the TC circulation.

Intense convection, and the associated up-draughts and down-draughts, cause the surface winds to strengthen during cyclogenesis. The strong winds drive surface waves and ocean currents through momentum transfer, enhancing turbulent mixing in the upper-ocean. This mixing results in entrainment of cooler thermocline water into the upper mixed layer of the ocean, reducing the sea surface temperatures and allowing a cold wake to develop behind the TC (Price, 1981; Ginis, 2002).

As a cyclone intensifies, the winds strengthen and enhance the evaporation rate, increasing the amount of latent heat available. However the stronger winds also act to deepen the ocean mixed layer and cool sea surface temperatures hence causing a reduction in heat and moisture fluxes and a negative feedback on intensity. As well as the large surface waves generated inducing sea surface cooling, they also affect the sea surface roughness and therefore the air-sea momentum and enthalpy fluxes (see Section 1.4).

Emanuel (1986) presents a method for estimating the maximum potential TC intensity, which uses the energy cycle of the storm (using an analogy between the TC and a heat engine) to estimate the largest possible surface wind speed W_m. The expression for this maximum wind speed is:

$$W_m^2 = \frac{C_k}{C_d} \epsilon T_s (k_s^* - k_b)_m \tag{1.2}$$

where C_k is the enthalpy transfer coefficient, C_d is the drag transfer coefficient (see Section 1.4), T_s is the temperature of the atmosphere near to the ocean surface, ϵ is the thermodynamic efficiency, roughly 1/3 in a typical TC, k_s^* and k_b are the enthalpies of the ocean surface and atmosphere near the surface respectively.

k_s^* is closely linked to the sea surface temperature (SST), therefore so is the potential intensity of a TC. This is described in Section 1.2.1, with TCs only developing over warm oceans with SST of 26 °C or more (Palmen, 1948). However, it has also been shown that the integrated thermal content of the upper ocean (from the sea surface to a depth of the 26 °C isotherm - D26) called the tropical cyclone heat potential (TCHP), plays a more important role in TC intensity changes (Shay et al., 2000). Although SST and TCHP are strongly linked, there is evidence of observed changes in the subsurface thermal structure (via sea surface height anomalies) which are not reflected by changes in the SST (Gopalan et al., 2000).

TC intensification has been linked to high values of TCHP contained in areas of deep mixed layers or certain mesoscale features, e.g. warm ocean eddies, provided the atmospheric conditions are favourable. Considering the atmosphere-ocean interaction described, it is known that strong winds and currents induced as the TC intensifies enhance entrainment of cooler water from beneath the thermocline upwards into the mixed layer. This results in the mixed layer depth increasing and surface waters cooling. In a warm ocean eddy the mixed layer depth is large and D26 may be more than a hundred metres deep, therefore a higher degree of upwelling is needed before the surface water cooling negatively feeds back to the TC. Essentially, deeper mixed layers and higher values of TCHP provide larger heat (energy) sources for intensification of TCs.

A classic example of the effect of a warm core ocean eddy is the sudden unexpected intensification of Hurricane Opal in the Gulf of Mexico which decreased in central pressure from 965 hPa to 916 hPa over a 14 hour period (Shay et al., 2000).

The background climatological ocean heat structure is an important factor determining how great an impact ocean eddies can have on TC intensification. Lin et al. (2008) found that in the North West Pacific, two different conditions exist. The first is in the western North Pacific south eddy zone and in the Kuroshio region, where the climatological warm layer is relatively shallow (D26 around 60 m). This means that ocean features become crucial to TC intensification because they effectively deepen the mixed layer (D26 can be over 100 m) restraining TC sea surface cooling.

The second condition is in the central region of the subtropical gyre. Here, the background climatological mixed layer is deeper (typically D26 105-120 m). TCs can intensify to category 5 (on the Saffir-Simpson scale) when travelling over both anticyclonic and even cyclonic mesoscale features.

Translation speed is also an important factor on the required subsurface thermal structure. To generate a category 5 TC in relatively shallow mixed layers is still possible with a fast moving storm. This was observed in the North-West Pacific in Lin et al. (2009b). For deeper subsurface layers, a much slower TC is ncessary.

For recent category 5 TCs in the North West Pacific, TCHP input into statistical models has improved the forecast by 5% with larger improvements for individual storms (Mainelli et al., 2008).

1.3 Storm Surge

The dynamics of storm surges are described here. This includes how they are generated, observation and measuring techniques, storm surge forecasting systems and how they interact with the tide.

1.3.1 Introduction and Storm Surge Dynamics

Storm surges are natural hazards directly caused by extreme winds in coastal regions. Almost all of the loss of life and damage by TCs is attributed to the storm surge, both directly and indirectly. Storm surges are the rise in ocean water level generated by the strong winds and low pressure of atmospheric cyclones (both tropical and extra-tropical), over and above the predicted tide. The storm surge which is generated by a TC arguably causes the largest impact in both economic and social terms, bringing extreme flooding to exposed coastlines of many of the globe's oceans.

Storm surges are shallow water waves caused by the force of the winds moving cyclonically around the storm, effectively pushing water towards the shoreline. Differences in atmospheric pressure also act to generate the storm surge, however the impact of this pressure forcing is minimal in comparison with the wind stress in shallow water - the shear stress exerted by the wind force on the ocean surface. As the atmospheric disturbance moves towards land and the water depth decreases, the surge grows. Storm surges can propagate along the coast as trapped Kelvin waves (Fandry et al., 1984) causing extreme sea levels not just at the point at which the cyclone makes landfall but further along the coastline as well.

If air pressure alone is considered, and if the ocean adjusted instantaneously to changes in air pressure, then it is said to have an isostatic response where sea level and air pressure changes are related by the local inverse barometer equation:

$$\Delta\eta = -\frac{\Delta p_a}{\rho_w g} \tag{1.3}$$

Here ρ is sea water density, g is the acceleration due to gravity, Δp_a is the air pressure change and $\Delta\eta$ is the change in sea level elevation.

It is worth noting that the equilibrium state described by these assumptions can only exist if the change in pressure is not too rapid and there is no restriction to the flow of water into the low pressure region. Therefore, it is only expected to be valid in the open ocean or in regions along the coast where the water is not too shallow, i.e. not where large storm surges occur.

In this isostatic model 1 hPa of air pressure increase/decrease results in 1 cm of sea level rise/fall. Extreme tropical cyclone surge heights can be as high as between 5-10 m (Pugh and Woodworth, 2014) above the astronomical tides, so compared with this, the impact of this forcing is fairly small and, as mentioned previously, for storm surges from TCs the wind forcing is much more significant.

The wind stress is calculated in terms of the wind speed at a certain height above the surface, usually 10 m, by the following equations:

$$\tau_{sx} = \rho_{air} C_d w_x \sqrt{w_x^2 + w_y^2} \text{ and}$$

$$\tau_{sy} = \rho_{air} C_d w_y \sqrt{w_x^2 + w_y^2} \tag{1.4}$$

where τ_{sx} and τ_{sy} are the x and y components of the wind stress, $W = (w_x, w_y)$ are the components of the wind velocity, ρ_{air} is the density of air and C_d is the drag coefficient, a dimensionless quantity used to quantify the drag of the surface. A common assumption is that C_d increases linearly with the 10 m wind speed, implying that the sea surface roughness increases with increasing wind speed. For most purposes this is a sufficient assumption, however after a certain threshold of wind speed, the drag coefficient becomes constant and even decreases which is crucial for cyclone surges (see Section 2.1.4).

The depth-averaged, non-linear, shallow water equations which describe the dynamics of storm surges are shown below. This version of the equations given is two dimensional, in Cartesian coordinates, and includes the air pressure and wind forcing, omitting tide generation, and horizontal eddy viscosity.

$$\frac{\partial u}{\partial t} + u\frac{\partial u}{\partial x} + v\frac{\partial u}{\partial y} - fv = -g\frac{\partial \eta}{\partial x} - \frac{1}{\rho}\frac{\partial p_a}{\partial x} + \frac{1}{\rho_w h}(\tau_{sx} - \tau_{bx}), \tag{1.5}$$

$$\frac{\partial v}{\partial t} + u\frac{\partial v}{\partial x} + v\frac{\partial v}{\partial y} + fu = -g\frac{\partial \eta}{\partial y} - \frac{1}{\rho}\frac{\partial p_a}{\partial y} + \frac{1}{\rho_w h}(\tau_{sy} - \tau_{by}), \tag{1.6}$$

$$\frac{\partial \eta}{\partial t} + \frac{\partial}{\partial x}(hu) + \frac{\partial}{\partial y}(hv) = 0, \tag{1.7}$$

where:

$t = time$

η = sea surface elevation

u, v = horizontal components of the depth averaged current

τ_{bx}, τ_{by} = components of the bottom stress due to friction

p_a = atmospheric pressure on sea surface

$h = D + \eta$ = total water depth, where D is unperturbed depth

g = acceleration due to gravity

f = the Coriolis parameter

Notice that the inverse barometer relationship can be derived from these first two terms on the right hand side of equations 1.5 and 1.6, by assuming the wind and currents are weak and negligible.

From these equations, it can be seen that near the coast, where the water is shallow, the wind stress term becomes more significant. Neglecting the other terms, including the bottom stress which is reasonable except in very shallow water, gives:

$$\frac{\partial \eta}{\partial x} = \frac{\tau_s}{\rho_w g D} \tag{1.8}$$

and combining with equation 1.4 above gives:

$$\frac{\partial \eta}{\partial x} = \frac{\rho_a C_d W^2}{\rho_w g D} \tag{1.9}$$

This equation provides a simple means of estimating the storm surge height from the maximum wind.

The wind effect arises from both the onshore and alongshore wind stress components, with their relative importance depending on the water depth and the duration over which the wind blows. In deep water, due to the Earth's rotation, the alongshore component of the wind stress induces Ekman transport toward (or away from) the coast. This flow of water toward the coast piles up water within a distance of the Rossby radius from the coastline and produces extreme high water levels (Gill, 1982; Pugh and Woodworth, 2014). This describes a positive storm surge, however negative storms surges also occur; where the water is forced away from the coast causing extreme low water levels.

From the shallow water equations, mechanics of this Ekman transport can be derived as a balance between the Coriolis force and wind stress. Ekman theory is based on several assumptions including no boundary dynamics, infinitely deep water, a constant eddy viscosity, a steady wind that has been blowing for a long time, no geostrophic flow and a constant Coriolis parameter. This simplifies equations 1.5 and 1.6 into:

$$\frac{1}{\rho}\frac{\partial \tau_{sx}}{\partial z} = -fv \tag{1.10}$$

$$\frac{1}{\rho}\frac{\partial \tau_{sy}}{\partial z} = fu \tag{1.11}$$

Integrating each equation over the Ekman layer gives:

$$\tau_{sx} = -M_y f \text{ and } \tau_{sy} = M_x f \tag{1.12}$$

where

$$M_x = \int_z^0 \rho_w u dz \text{ and } M_y = \int_z^0 \rho_w v dz \tag{1.13}$$

Here M_x and M_y represent the mass transport terms in the east-west and north-south directions. These equations show that contrary to the non-rotating case, north-south winds cause mass transport in the east-west direction. If this transport impinges on a coast, water will pile up along the coast, and therefore an alongshore component of wind stress will cause a positive or negative storm surge if the coast is at right angles to the wind.

From equation 1.13, it can be seen that the mass transport and, therefore, the amount by which the sea level will rise, depends on the magnitude of the alongshore current produced by the alongshore winds. Even under strong winds it is rare for the current to exceed about 100 cms^{-1} due to bottom friction (Weisberg and Zheng, 2006).

So while the alongshore component of wind stress accounts for the sea level surges of a metre or so, as synoptic weather fronts go by, it can only account for a portion of the surge by TCs. Here, the onshore component of wind stress is the main cause.

1.3.2 Measurement and Observation

Surge heights can be measured directly at the coastal, tidal stations using tide gauges. The storm surge is the difference between the expected tide and the observed rise in water level. This observation is generally the most reliable, however as there are only a limited number of tidal stations along the global coastlines, observing a storm surge relies on the high water level occurring at a particular station. Tide gauges are usually designed to measure the still level of water, so any waves will not be observed using this equipment.

After a surge has occurred and receded, the height of inundation can be measured by surveyors mapping the high water marks on land. This is a detailed, rigorous process often involving teams of deployed surveyors producing photos and written descriptions of the wrack marks, often marks created by foam, seeds or other debris. The marks may also use GPS methods to determine their location, and are mapped relative to a vertical reference datum. This measurement of the high-water marks is the observed storm tide (see Figure 1.4), however with further analysis, the portion attributed to the storm surge may be identified. This observation method is useful for finding the highest surge recorded, however the marks are perishable so surveys need to be undertaken as quickly as possible after the event,

and records are often subjective and include the impact of waves.

It is becoming more common for sensors to be deployed ahead of forecasted surge events. This may involve pressure sensors temporarily placed in locations that will be submerged, to measure the water level producing information such as storm surge duration, times of surge arrival and retreat, and the maximum water depth.

1.3.3 Factors for Forecasting Storm Surges

None of the tropical cyclone scales described in Section 1.2 include a description of the storm surge expected, even though this hazard usually causes the most damage. Storm surges depend on too many different factors for simple scales such as these to be used. The impacting factors include the atmospheric pressure difference and storm intensity or wind speed as well as the cyclone translation speed, the track and landfall location of the storm, the radius of maximum winds and the size of the cyclone, the shape of the coastline and other coastal features such as bays and estuaries, and the width and bathymetry of the continental shelf.

Hurricane Katrina is an example of a cyclone where the intensity was relatively low at landfall, category 3 on the Saffir-Simpson scale, but produced a very high storm surge of over 8 m on the Mississippi coast. Hurricane Camille, on the other hand, was a category 5 storm which produced a lower than expected surge of 6.5 m for this storm intensity. This is thought to be because of the sizes, or radius of maximum winds, of each of these storms (Irish et al., 2008).

In general, the following result in a high surge:

- lower pressure, as described.
- stronger winds, as described.
- a larger storm. Irish et al. (2008) show, by undertaking idealised model experiments varying the radius of maximum winds, that storm size plays a very important part in surge generation, particularly for very intense storms on a gently sloping continental shelf. They also found that storm surge varies by as much as 30% over a reasonable range of storm sizes. This is intuitive as a larger storm forces a larger area of the ocean for a longer time and therefore a larger volume of water is forced towards the coast.
- a slower storm translation speed. It takes finite time to transport water from one point to another. Fast moving storms often cause a smaller surge since there may not be sufficient time to fully set up the sea surface slope that comprises the surge (Weisberg and Zheng, 2006)
- a cyclone which moves onshore perpendicular to the coast. The angle of approach is important in the affect on sea level set-up in advance of the eye. If the direction means that the wind is blowing offshore ahead of landfall, when the surge occurs, it is happening from an already depressed sea level and is, therefore, smaller in magnitude.

- a concave coastline landfall location, as this introduces a funnelling effect.
- a wide, gently sloping continental shelf or a long estuary, due to the across shore sea surface slope being inversely proportional to the water depth. The shallower the water, the larger the sea surface slope, the larger the surge (Weisberg and Zheng, 2006).

1.3.4 Interaction with Other Forcing

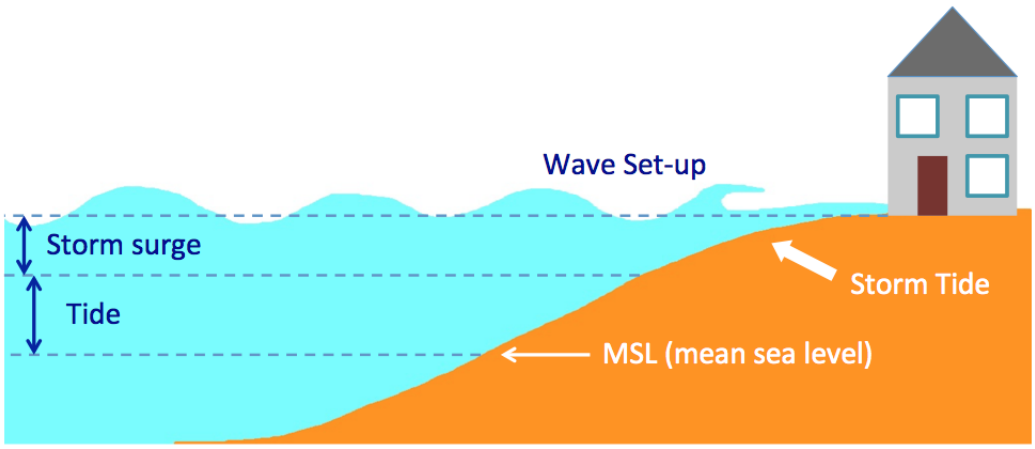

Figure 1.4: Schematic of the storm tide and its components.

The total extreme sea level during a storm surge event is called a storm tide (see Wolf 2009 and Figure 1.4) and is made up of mean sea level, the tide, the storm surge itself, and contributions from waves and currents. Each of these components is strongly linked to the others, making it difficult to study one separately from the others.

Interaction between the tide and surge is mainly a result of the changing water depth (Wolf, 1981; Pugh and Woodworth, 2014). In the shallow water equations (1.5 and 1.6), the last term contains the reciprocal of depth. Therefore, wind stress will be more effective at storm surge generation at low, rather than high, tide due to the water depth reduction. The change in water level a storm surge brings impacts both the shallow water wave speed (equal to $\sqrt{gh}$) and bottom friction (equal to $\tau_b/\rho_w h$), meaning that the tidal propagation will be, in turn, influenced by storm surge sea surface elevations.

The tide-surge interaction is seen when examining observed records of sea surface elevation. The residual is the difference between the recorded sea surface elevation and the expected sea surface height due to the tide, shown in Figure 1.5. If a surge could occur at any time during a tidal cycle, then the residual would be independent of the tidal cycle, with large residuals expected at any time. This is not the case. In fact, large residuals are suppressed when the water depth is largest, i.e. at the astronomical tide high water.

Following from work completed by Wolf (1981), Horsburgh and Wilson (2007) studied the distribution of residuals in the Thames Estuary for surge events in the record and found

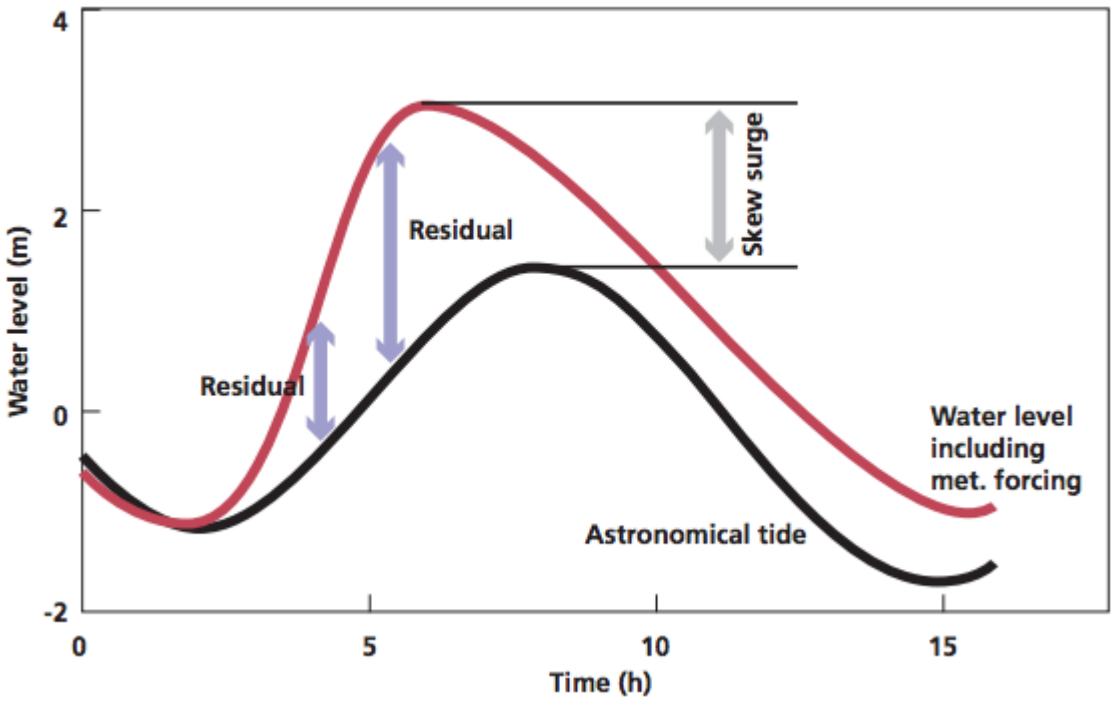

Figure 1.5: A graphical illustration of the skew surge parameter of the storm surge component within a storm tide, taken from Lowe et al. (2009).

that most of the maximum positive residuals occurred about 4 hours before the tidal high water. Two-thirds of the events showed a clear phase shift in the high water turning point of the observations with respect to the predicted tide. This phase shift is most easily explained as an artefact of the small advances in the timing of the tidal high water due to the increased water depth provided by the surge (Horsburgh and Wilson, 2007; Antony and Unnikrishnan, 2013), since the phase speed of a shallow water wave, like the tide, is proportional to $\sqrt{gh}$.

For this reason, a more significant and practical measure of the surge height than the peak residual is the skew surge (see Figure 1.5), which is the difference between the elevation of the predicted high water and the nearest observed high water, irrespective of difference in timing (as in Batstone et al. (2013) and Lowe et al. (2009)). Skew surge is independent from the predicted high water and therefore is a more useful measure of the meteorological effects on water levels.

1.4 Wave Dynamics

This section gives an introduction into oceanic waves, including their formation, propagation and the interaction waves have with both the atmosphere and storm surges.

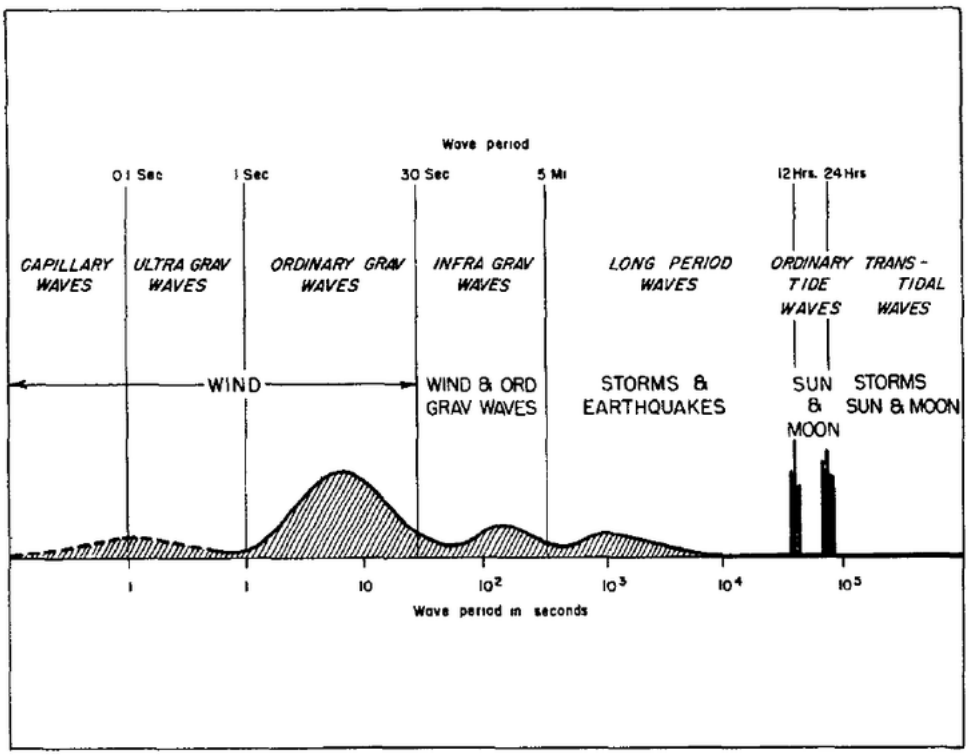

Figure 1.6: Frequencies and periods of vertical motions of the ocean surfaces from Munk (1951). This demonstrates the various types of ocean waves, their associated wave period, and where storm surges and wind waves fall within this spectrum.

1.4.1 Introduction to Ocean Waves

The wave contribution to a storm tide is made of several components: wave set-up, the increase in sea level near to the coast due to the transfer of wave momentum to the water column on wave breaking; wave run up, the vertical extent of the wave rushing up the shore; and the more direct impact of waves overtopping at the coast, releasing a large amount of energy onto the shoreline.

The wind generated waves described above are only one type of ocean waves. The other waves which occur are often described in terms of their period or wavelength. Figure 1.6 from Munk (1951) shows the different waves, the different wave periods, and the forcing which creates them. The longest waves are 'trans-tidal' waves, which are generated by low-frequency fluctuations in the Earth's crust and atmosphere. Tides are waves with slightly shorter wavelengths, with periods that range from a few hours to more than a day and wavelengths which vary between a few hundred and a few thousand kilometres.

Storm surges have wavelengths which are generally shorter than the tides. The space and time scales of a storm surge are roughly equal to those of the generating storm or cyclone; typically a few hundred kilometres and one or two days.

Tsunamis and seiches are waves with smaller wavelengths and periods than surges, along with infra-gravity waves, which are commonly made up of groups of wind-generated waves.

Finally on the wave spectrum we come to wind generated waves. These sets of waves are also known as gravity waves due to their restoring force, and they generally have a period of less than 30 seconds. When they are generated by the local wind they are generally irregular and short-crested, referred to as a 'wind sea'. When they leave the location where they are generated, they take on a regular and long-crested appearance and are called swell.

Five factors influence the formation of wind waves (Holthuijsen, 2007):

- The wind speed relative to wave speed, with the wind moving faster than the waves for energy transfer.
- The uninterrupted distance of open water over which the wind is acting without significant changes in direction - called the fetch.
- The width of area affected by fetch.
- The duration the wind acts upon the water, i.e. the time the wind is blowing over the water without significant changes in direction.
- The water depth.

All these factors combine to determine the size of wind waves and the structure of flow.

In TC conditions, the wind speed is very high by definition, depending on the particular cyclone's intensity. In coastal areas, where the waves have the largest impact, the depth reduces to zero. Therefore, the height of the waves generated may depend more upon the length and width of the fetch, and the duration of the wind. This can lead to two situations, where the waves are fetch-limited and duration-limited. The height of TC waves are sensitive to these quantities and this is seen in the results of this study, described in Section 4.

Many of the different waves described occur at the same time, and in reality observations of the ocean surface are composed of waves of various lengths and periods. In order to describe this, ocean waves are described as a wave spectrum where an observed sea surface height record can be reproduced as the sum of a large number of harmonic wave components (i.e. a Fourier Series).

$$\eta(t) = \sum_{i=1}^{N} A_i cos(2\pi f_i t + \alpha_i) \tag{1.14}$$

where A_i and α_i are the amplitude and phase, respectively, of each frequency $f_i = i/D$ with D equal to the duration between successive wave peaks.

From equation 1.14, the variance density spectrum $E(f)$ can be defined which describes how the variance of the sea-surface elevation is distributed over all frequencies. If the variance density spectrum is multiplied by $\rho_w g$ the energy density spectrum is obtained. This

is easier to explain and the spectrum shows how the wave energy is distributed over the frequencies.

The combined appearance of the ocean waves can be inferred from the shape of the spectrum. The narrower the spectrum, the more regular the waves are. Therefore, a wider spectrum describes an irregular, more chaotic wave field. In practice, the combination of wind waves and swell on the ocean surface is called the sea state. For the wind sea, this is closely linked to the Beaufort Scale describing wind speed in meteorology (Holthuijsen, 2007).

1.4.2 Measurement and Observation of Ocean Waves

Waves have been observed for many years, by sailors, meteorologists, surfers, and passers-by. Historically, visual observations of the height of the waves are taken by crew members on-board ships. These visual observations can be fairly reliable if carried out by experienced observers, but otherwise can contain large errors (Holthuijsen, 2007).

Instrumental observations are becoming increasingly common, as they are objective and seem to have little/no bias, although may also have their own limitations. For example, a buoy on the sea surface may move around or capsize in very steep waves. Remote sensing techniques generally rely on instruments that are positioned above the water, which may be sensitive to atmospheric conditions.

In-situ observation techniques involve an instrument located at or below the sea surface including floating surface buoys, and pressure transducers at the sea bed. Most of these instruments measure the up-and-down motion of the surface at one (horizontal) location. The most common technique is to measure the vertical acceleration with an on-board accelerometer. By integrating the vertical acceleration twice, the vertical motion of the buoy and thus of the sea-surface elevation over time is obtained. They may also measure the directional information about the waves.

Remote-sensing techniques involve instruments which are above the water surface on a fixed or moving platform. The platform may be a tower at sea, a ship, an aeroplane, or a satellite. The instruments receive reflections from the sea surface of visible or infra-red light, or radar energy. They can cover a large area in a short period of time, particularly if the platform is a satellite. However, this method is generally more expensive than in-situ measurements.

The observational records are generally described with average wave parameters including significant wave height and significant wave period. Wave height is defined as the vertical distance between the highest and lowest surface elevation in a wave. The $significant$ wave height is defined as the mean of the highest one-third of waves in the wave record. This may seem an odd description of a characteristics wave height, however experiments have shown that the value of this wave height is close to the value of the visually estimated wave height. Similarly to the significant wave height, the significant wave period is the mean period of

the highest one-third of waves.

The techniques described above are also useful for measuring waves during storm surge and tropical cyclone events. This relies on in-situ observation locations being in the 'right place', where the storm surge is occurring. Remote sensing can often be interrupted by the extreme atmospheric conditions. The techniques often measure the storm tide, with the waves as well as the storm surge included in the measurements. It can be very difficult to separate the observational records into their component parts, which makes validating wave models separately from the sea surface elevation challenging.

1.4.3 Surface Drag Dynamics

As with all wind-driven waves, surface waves are initially caused by friction between the atmosphere and ocean, and small pressure fluctuations. They then grow as momentum transfers from the wind to the surface water. With extreme winds, the amount of momentum available for wind-wave generation is large, and therefore the waves carry great amounts of energy.

In this section, the mechanics of this momentum transfer are introduced. There are several different available ways of parametrising the surface drag and momentum transfer associated for use in a numerical model. The options are discussed here.

Above the earth's surface, the air in immediate contact with the boundary has zero velocity, thus there is a velocity shear near to the ground. This shear flow is unstable and turbulent eddies form when small disturbances grow, which modify the shear. Over a sufficiently long time, however, a well-defined mean velocity, u, can be determined for each discrete value of height above the ground, z. When the shear is large, these eddies transfer fast moving flow downward and slow moving flow upward, i.e. transferring momentum. The mean value of this vertical flux of momentum over a sufficiently large area or time is equal to the mean tangential stress τ_s, seen in equation 1.4.

As the surface is approached, the velocity shear increases and is, in fact, inversely proportional to the height above the ground. In general a logarithmic mean velocity profile occurs close to the ground for steady winds where the shear is strong (and where other atmospheric effects, for example convection, are sufficiently small). This can be stated mathematically as:

$$u = \left(\frac{w_*}{\kappa}\right) ln \left(\frac{z}{z_0}\right) \tag{1.15}$$

where κ is Von Karman's constant, w_* is the friction velocity and z_0 is a property of the surface called the roughness length. The friction velocity is defined by:

$$\tau_s = \rho_a w_*^2 \tag{1.16}$$

In order to relate the wind stress τ_s to the observed wind speed (often measured at 10 m w_{10}), dimensional analysis can be used to define:

$$\tau_s = C_d \rho_w w_{10}^2 \tag{1.17}$$

where C_d is a dimensionless coefficient called the drag coefficient (as seen above). Its value depends on the roughness of the surface and can also be affected by changes of temperature and air density with altitude.

All the wind driven theory above is valid for the earth's solid surface. The ocean is not a solid surface, but even so surface wind velocities are still very much lower than those in the free atmosphere. The main difference is that as the wind blows, waves form on the ocean surface thus increasing the roughness. Up to a point, the drag coefficient C_d for the sea surface increases with wind speed. To first-order, a linear relationship can be fitted to this increase (observed to be true up to a certain threshold wind speed). Alternatively, a commonly used relation can be obtained on dimensional grounds (Charnock, 1955).

$$z_0 = \hat{\alpha} \frac{w_*^2}{g} \tag{1.18}$$

where
$hat\alpha$ is the dimensionless Charnock parameter.

Hence the total stress τ_s can be related to the wind velocity and this Charnock parameter:

$$\tau_s = w_*^2 = C_d w_{10}^2 = C_d \left(\frac{w_*}{\kappa} ln \left(\frac{z}{z_0} \right) \right)^2 = C_d \left(\frac{w_*}{\kappa} ln \left(\frac{z}{\hat{\alpha} \frac{w_*^2}{g}} \right) \right)^2 \tag{1.19}$$

And we have a formulation for the drag coefficient in terms of the friction velocity and the Charnock parameter:

$$C_d = \frac{w_*^2}{\left(\frac{w_*}{\kappa} ln \left(\frac{z}{z_0} \right) \right)^2} \tag{1.20}$$

This formulation is very useful for many numerical models, as if the Charnock parameter value is set, the wind stress can be derived and the effect of the wind on the ocean's surface can be estimated. This formulation is trying to fit one simple relationship to a wide range of potential sea states and atmospheric circulations, without looking at the real momentum fluxes. It is, therefore, limited, particularly for tropical cyclones where the wind speed and direction change rapidly, and the wind sea remains young and never fully develops.

There have been several authors who, instead of using a constant value for the Charnock parameter, have proposed empirical relationships for the Charnock coefficient.

Donelan (1990) proposed a wave-age dependency for the roughness with:

$$\hat{\alpha} = \frac{z_0}{H_s} = A_1 \left(\frac{w_*}{c_p} \right)^{B_1} \tag{1.21}$$

where H_s is the significant wave height, c_p is the wave phase speed, and A_1 and B_1 are calibration constants. Although wave-age scaling have been around for many decades, its usefulness is not universally accepted. Part of the problem relates to the the fact that both the Charnock parameter defined in equation 1.21 and the wave age depend on the friction velocity w_* giving potentially spurious correlation among the variables.

Taylor and Yelland (2001) instead suggested that the roughness length can be parametrised as a function of the significant wave height, H_s, and the wavelength at the peak of the wave spectrum, λ_p. H_s/λ_p is the wave steepness, and the formulation for the drag relation is given by:

$$\hat{\alpha} = \frac{z_0}{H_s} = A_2 \left(\frac{H_s}{\lambda_p} \right)^{B_2} \tag{1.22}$$

Again, A_2 and B_2 are constants to be honed during calibration. The formula was found to describe a variety of datasets, both in the field and laboratory, with the notable exception of very young wave age field data. This scaling does not suffer from spurious correlation in w_*.

Drennan et al. (2005) compared the above formulations with bulk parametrisations to determine the roughness length for a wide set of wave conditions. A summary of the conclusions from these studies is that:

1. dominant wind-sea: both formulations outperform bulk formula
2. young wind-sea: wave-age formulation is best (equation 1.21 with $A_1 = 3.35$ and $B_1 = 3.4$)
3. mixed seas: steepness formulation better (equation 1.22 with $A_2 = 1200$ and $B_1 = 4.5$)
4. swell: none of them performed well

The fact that both mechanisms are poor on swell indicates that the scaling based on swell does not work and that the smaller wind driven waves are more important for transferring momentum. There are differences in the drag coefficient for different directions of swell relative to the wind direction, so potentially the scaling may work if extended to take into account the relative direction of the wind and swell.

1.4.4 Wave Set-Up

Cline (1920) described several cases of increased coastal water levels linked with waves propagating from distant TCs entering the Gulf of Mexico. These waves generated a shoreward flux of momentum known as radiation stress (Longuet-Higgins and Stewart, 1964), which contributes to wave set-up and elevated water levels several days before landfall. This process can add significantly to the ultimate high water levels during landfall. For example,

during Hurricane Georges (1998), it is estimated that wave set-up contributed 25% to 33% of the total rise in water levels (Weaver, 2004).

Radiation stress will be formulated in the modelling system of this study in order to simulate the contribution to the overall water level in the BoB. This is achieved as part of the ocean-wave interaction, described in Section 3.2. As a minimum depth of 10 m is used, the impact of wave set-up will not be included.

As stated above, wave set-up is linked to radiation stress which is defined as the excess flow of momentum due to the waves (Longuet-Higgins and Stewart, 1964). On a long sloping beach with waves flowing at right angles to the coast the radiation stress results in a set-down of sea level sea-ward of the breaking waves by an amount:

$$\Delta = -\frac{1}{2}\frac{A^2 l}{sinh2kD} \tag{1.23}$$

for monochromatic waves, where A is the wave amplitude, l is the wave number, and D is the water depth. In shallow depths, this reduces to:

$$\Delta = -\frac{1}{4}\frac{A^2}{D}$$

From these equations we see that as depth decreases, set-down becomes greater, reaching a maximum just before the waves break.

Wave set-up becomes particularly significant during storm events due to the large wave heights and rapid wave breaking, therefore it cannot be neglected as it contributes significantly to the total water level at the coast. This process can add 10-20% of the incident wave height to the sea level simulated using tide and surge models. Brown (2010) found that, in Liverpool Bay, increases of 0.5-1.5 m for particular simulated storm surge events were estimated. In reality, wave set-up can be difficult to measure separately from the overall influence of wave-tide-surge interactions.

Numerical models which include wave set-up show improved storm surge maximum elevation forecasts, however this is very computationally costly (Brown, 2010; Brown et al., 2011; Murty et al., 2014b). There are currently no operational flood warning schemes which forecasts wave set-up as well as surge and tide levels. Along with the large computational costs, this is also due to the sensitivity of the processes involved to beach slope, harbour and bay orientation, location and shape.

1.5 Bay of Bengal

The Bay of Bengal (BoB) in the Northern Indian Ocean is the largest bay in the world, lying roughly between 5°N and 22°N; and 79°E and 95°E. It is one of the regions where TCs frequently form (see Figure 1.2). Although the TC and storm surge frequency and severity here is lower than other areas (e.g. western North Pacific), the societal impacts caused by

the TC, storm surge, and waves can be extreme. This is due to many reasons; the high coastal population density of low lying deltas perhaps being the most obvious.

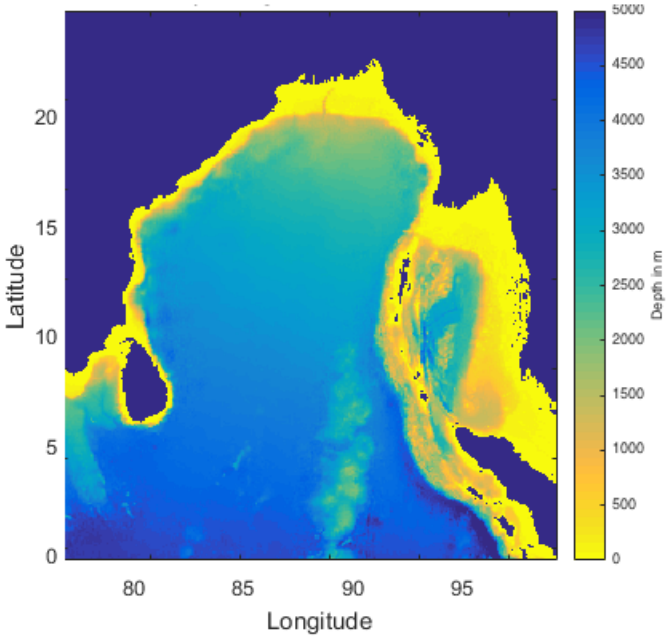

Figure 1.7: Bathymetry of the Bay of Bengal, from GEBCO 08 (GEneral Bathyemtric Chart of the Oceans) global dataset.

The world's most deadly cyclone on record occurred in the BoB in 1970, and is estimated to have caused between 300,000 and 500,000 fatalities in Bangladesh, primarily because of the 13 m storm surge that flooded much of the Ganges delta. In fact, seven of the top ten deadliest TCs on record formed in the BoB (Li et al., 2013). The most recent example from this list is TC Nargis at the end of April 2008. The cyclone suddenly intensified while travelling over a positive upper-ocean thermal anomaly (see Section 1.2) and made landfall in Myanmar claiming more than 130,000 lives (Dube et al., 2009b; Lin et al., 2009a, 2013). The estimated size of severely affected population reached 1.5 million and caused an estimated 10 million US dollars worth of destruction (Tasnim et al., 2015; Lin et al., 2009a).

Coastal flood risk is highest for the Bay's rim countries: India, Bangladesh, and Myanmar, due to the bathymetry of the bay enhancing the storm surge height, along with other effects including shallow coastal waters, high tides, low lying land and vast deltas including the world's largest river system, the Ganga-Brahmaputra-Meghna (Murty et al., 1986; Dube et al., 1997, 2009b).

The Bay covers an area of 2,172,000 km^2 and is bordered by Sri Lanka and India to the west, Bangladesh in the north, Myanmar and the northern part of Malay Peninsula in the east. It has a wide and shallow continental shelf with relatively flat and smooth bathymetry; the sea floor gradient decreases gradually from north to south. Figure 1.7 shows the bathymetry of the Bay of Bengal.

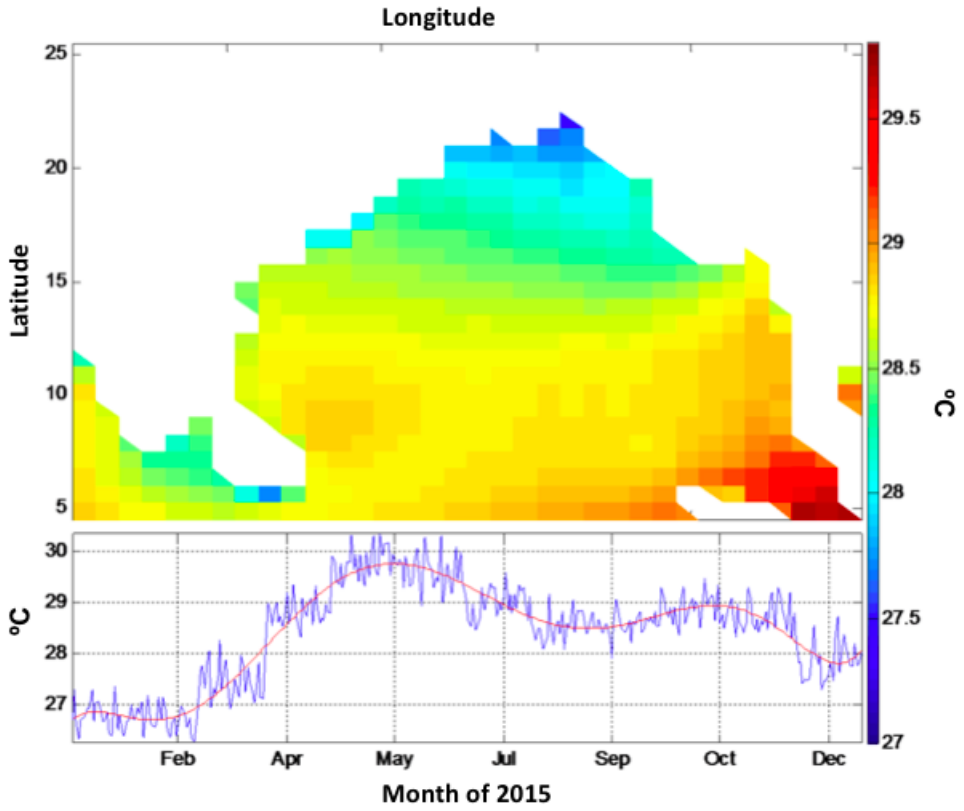

Figure 1.8: Top: Mean sea surface temperature across the BoB. Bottom: Annual bimodal fluctuation in sea surface temperature with 2015 values shown (Baisya et al., 2014).

This smooth bathymetry is caused by the large volumes of sediments deposited by the Ganges and the Brahmaputra rivers every year, the sediment travelling as far south as 7°S. The sediment cover is responsible for the ocean floor bathymetry, which is virtually featureless, and sediment thickness varies from about 20 km near Bangladesh (and the river delta) to 8 km in the central bay and <2 km in the south of the bay. There are many rivers which flow into the Bay of Bengal including the Ganges, the Meghna, the Brahmaputra, the Hooghly, the Mahanadi, Godavari, Krishna, Kaveri, and the Irrawaddy. Each of these rivers brings an influx of sediment and freshwater, making the world's largest river delta.

The Bay is characterised by semi-annually reversing monsoon winds which are north-easterly during December to February, and south-westerly during June to September. The inter-monsoon periods are weak and variable winds, with elevated heating during the summer months (May to September).

The SST climatological mean and bimodal annual are shown in Figure 1.8. Sea surface temperature also shows a prominent double peaked distribution, one peak in the pre-monsoon season and one in the post-monsoon.

The frequency of tropical cyclones is highly linked to the monsoon synoptic weather pattern and the distribution of SST. TCs occur during the transition of the monsoon winds, when the winds are lighter (as mentioned above). This creates a bimodal TC season echoing the annual distribution of SST, a feature which is unique to the North Indian Ocean and the Arabian Sea. In all of the other tropical cyclogenesis regions there is a single peaked distribution, coinciding with the area's summer. In the BoB TCs develop in March to May (pre-monsoon) and October to December (post-monsoon) even though from March to December the convective available potential energy (CAPE) and relative humidity close to the surface is large (due to SSTs being larger and therefore increasing evaporation). This unusual distribution is shown in Figure 1.9 and the cause is the topic of much research.

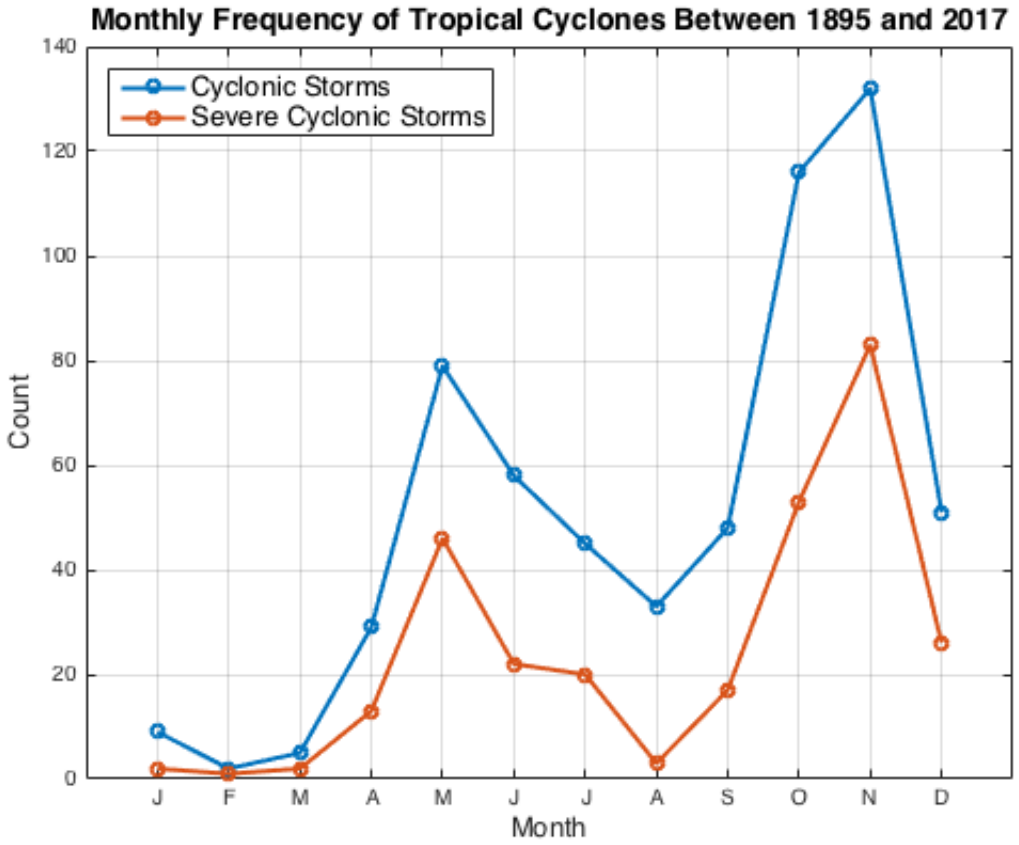

Figure 1.9: Frequency of tropical cyclones in the Bay of Bengal and Arabian Sea between 1895 and 2017. This figure includes data from Dube et al. (1997) and collated IMD and JTWC cyclone reports.

Li et al. 2013 examine the contributing tropical cyclogenesis factors in the BoB, including the absolute vorticity, vertical wind shear, relative humidity and potential intensity (Emanuel, 1986). They use statistical analysis of the NCEP Reanalysis Dataset I (Kalnay et al., 1996) including the genesis potential index (GPI) diagnosis to quantitatively evaluate each factor. They find that the dominant factor from March to May is the increase in relative humidity, and in October to December the decrease in vertical shear is found to be most important to TC development. The minimum in the summer, where the relative humidity is highest, is due to contributions from the other three factors examined - low absolute vor-

ticity, increased vertical wind shear and low potential intensity. In the winter, TCs do not occur due to the low relative humidity.

The frequency of TCs peaks in November, with a secondary peak in May. This may seem strange as the sea has a higher heat content (and SST - Figure 1.8) in May than in November. This, along with suppressed tropical cyclone activity during the mature monsoon season, shows that SST alone cannot explain cyclogenesis. Li et al. (2013) found that the mean relative humidity in the post-monsoon period is higher that the pre-monsoon, which corresponds to the higher frequency. Vissa et al. (2013) attribute the difference in TC frequency to changes in enthalpy flux and TCHP (see Section 1.2). During the monsoon, there is a large influx of freshwater from the many rivers into the bay causing a thick barrier layer to form. This layer inhibits wind stress induced vertical mixing of SST, therefore a lower accumulated TCHP is required for post-monsoon cyclones as the energy available for cyclogenesis is most persistent. The prolonged SSTs also cause an increase in enthalpy fluxes, again supporting TC formation and development.

Along with the unusual frequency distribution of TCs in the BoB, there is a confusing relationship between SST and TC intensity. Evans (1993) found that SST alone could not predict TC intensity, using monthly averaged SST and observational TC intensity data collected by reconnaissance flights in both the North Atlantic and North Pacific, and satellite data across all five ocean basins. They found that above a threshold value SST is not the dominant factor determining overall storm intensity. This work is echoed for the BoB using more accurate data by Ali et al. (2013), where the authors found that of the 75 TCs studied, more than 50% have no significant correlation between maximum intensity reached and SST.

As mentioned in Section 1.2.5, potential TC intensity is more commonly thought to be controlled by TCHP, the heat content of the ocean to a depth of the 26 °C isotherm. In the BoB areas of high TCHP are commonly caused by warm ocean anomalies (Ali et al., 2013).

Lin et al. (2009a) investigated Cyclone Nargis which devastated Myanmar in 2008. They found that Nargis rapidly intensified from a weak category 1 storm to category 4 in just 24 hours over a warm ocean anomaly. The anomaly was much warmer in the subsurface than climatology, resulting in a near 300% increase in air-sea enthalpy flux which supported the TC intensification. They also found, using a numerical model, that without the warm anomaly the enthalpy flux would not have supported the rapid intensification.

Ali et al. (2007) investigated the impact of sea surface height anomalies on two examples of tropical storms in the Bay of Bengal. One example showed the storm intensifying over a warm ocean anomaly and the other dissipating over a negative sea surface height anomaly. By definition, ccean eddies in the Bay of Bengal are variable in space and time but clearly can result in unexpected intensification (Ali et al., 2007), therefore observations of warm anomalies are crucial for a full picture of TC prediction.

1.6 Tropical Storm Phailin

As mentioned in the introduction to this study, Very Severe Cyclone Phailin was one of the strongest TCs ever recorded in the northern BoB (IMD Report, 2013). Phailin was the strongest tropical cyclone of 2013 in BoB, killing around 39 people and causing roughly 1.3 million people to be evacuated and 12 million people to be otherwise affected. Phailin was the strongest cyclone to make landfall in India for some 15 years, since the 1999 Odisha cyclone. Cyclone Phailin was chosen for simulation and analysis in this study as an example of a recent, extreme event which impacted the Indian coast of BoB.

The severe cyclonic storm left a wide area of damaged infrastructure, flooding of farmland with widespread death of livestock and a few instances of human fatalities along coastal Odisha and part of north-eastern Andhra Pradesh. Human loss was minimised as compared to the 1999 Odisha super cyclone, thanks to timely warnings and alertness by the national disaster management authorities, and mass evacuation efforts.

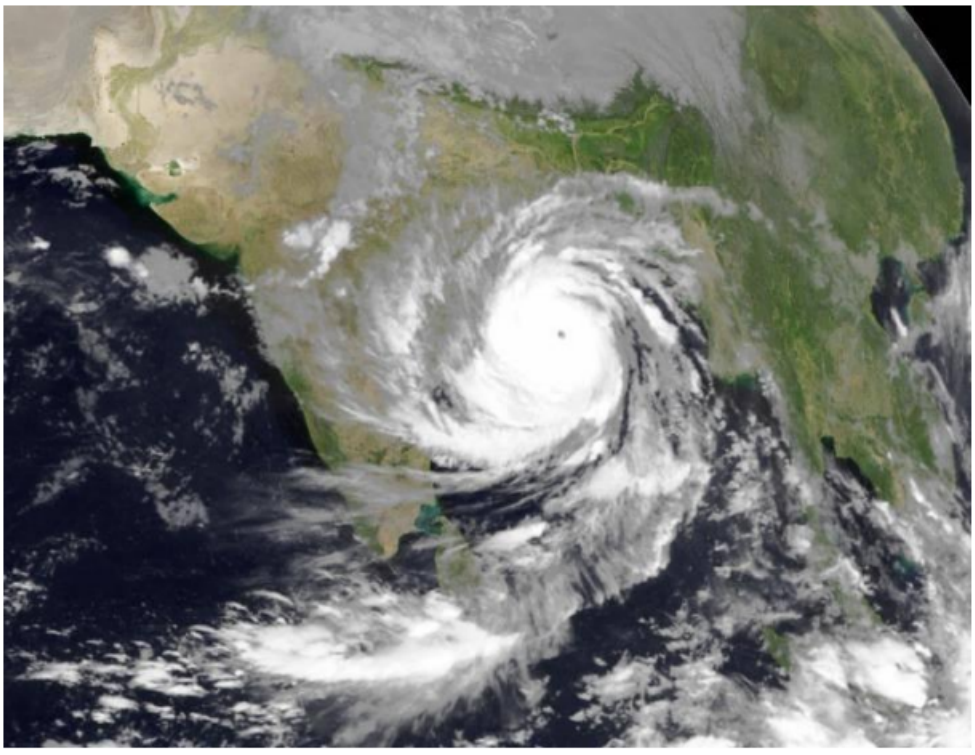

Satellite image with Super cyclone *Phailin* over the Bay of Bengal, October 11, 2013, 21 UTC
Image credit: fvalk.com / Eumetsat

Figure 1.10: Satellite image of Cyclone Phailin (Muhr et al., 2013).

Phailin originated as a tropical depression in the Gulf of Thailand on 4 October 2013. The cyclone passed over the Malay Peninsula, into the Andaman Sea (Eastern Indian Ocean) on 6 October, continuing to move north-westwards. Very intense convection was observed over the Andaman Sea and adjoining area, gradually increasing in height and organisation

over 24 hours, eventually merging on 8 October. Maximum sustained surface wind speed was estimated to be roughly 12 ms^{-1} around the centre, with gusts up to 18 ms^{-1}.

The sea surface temperature was 28-29 °C and the ocean thermal energy was about 60-80 MJm^{-2} was observed by various buoys and ships in the bay (IMD Report, 2013). An upper tropospheric ridge at 200 hPa height located along 21°N provided the required poleward outflow for intensification of the system. As a result, there was low level convergence and low relative vorticity, along with low to moderate vertical wind shear around the low pressure area. Due to all the above mentioned features, conditions were favourable for intensification and the low pressure developed into a deep depression at 0530 IST (0000 UTC) 9 October. The system gradually moved over west Bay of Bengal and became Cyclonic Storm Phailin at 1730 IST (1200 UTC) 9 October.

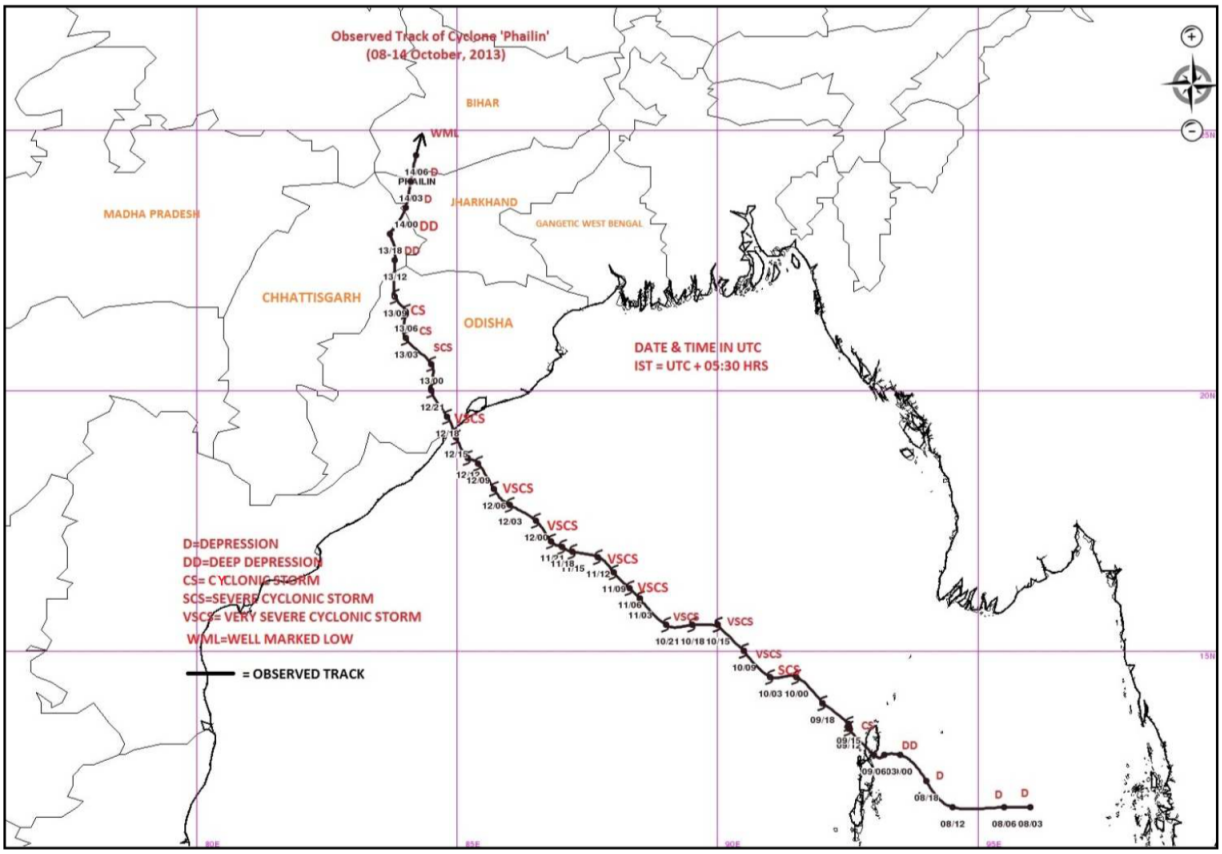

Figure 1.11: IMD observed track of Cyclone Phailin along with the cyclone classification (IMD Report, 2013).

Rapid intensification occurred during 10 October due to the high SSTs, high ocean thermal energy and especially low vertical wind shear. Very Severe Cyclonic Storm Phailin intensified, reaching a maximum intensity of 59 ms^{-1} in the morning of 11 October. Continuing to move north-westwards with translation speed 15 $kmhkmh^{-1}$, Phailin made landfall at Andhra Pradesh and Odisha coast near Gopalpur around 2230 IST (1700 UTC) 12 October

2013 with an estimated wind speed of 56-62 ms^{-1} and estimated central pressure of 940 hPa. After landfall, the system gradually weakened over 13 and 14 October into a depression over south-west Bihar.

According to the Indian Times and the BBC, Cyclone Phailin created a storm surge of 3 m (Muhr et al., 2013). This figure may be misleading, as it is at odds with both the forecasts given by the IMD for a storm surge of 1 m and the sea surface elevation data. The observed tidal series is available for the Paradip tide gauge, located at 20.267°N, 84.97°E, and shows a maximum residual of 0.6 m.

The wave rider buoy moored near to Gopalpur (19.28°N, 84.97°E) recorded the wave parameters, with a maximum significant wave height of 7.3 m at 1200 UTC 12 October. It is worth noting that the buoy lost its mooring and drifted during the storm's passage.

For more details on these observational datasets, see Section 3.4.

Chapter 2

Literature Review

Tropical cyclones, and the storm surges and large waves which they cause, are very complex in their generation, development and dissipation. Therefore, in order to accurately forecast these hazards such that appropriate emergency response and measures can be taken, complex numerical models can be used to simulate them.

No numerical model is a perfect representation of reality, especially where processes of widely varying length-scales are involved. There are well known problems specific to tropical cyclone modelling which are actively researched and improved. In this section, some of the most recent techniques are described and reviewed, which are used within this study. The review has informed and justifies the modelling choices made. See Section 3 for a description of the modelling system used for this work.

2.1 State-of-the-Art Modelling Techniques

Over the past decades tropical cyclone track forecasting ability has significantly improved, however forecasts using statistical models of tropical cyclone intensity are still providing better guidance than any dynamical model (Rappaport et al., 2009a; DeMaria et al., 2005). Statistical models use multiple regression techniques of climatology, persistence and storm environmental conditions to predict a TC's development. Because of this they can miss the very extreme (outlier) events which are most crucial to forecast and also the models do not give any insight into dynamical processes.

Operational, dynamical hurricane models, based on the mathematical formulation of atmospheric dynamics and physical processes, include those used in the National Hurricane Centre; the Geophysical Fluid Dynamics Laboratory hurricane model (GFDL) and NOAA's Hurricane Weather, Research and Forecasting model (HWRF) (see Rappaport et al. (2009a)). Numerical weather prediction (NWP) models alone can provide the needed quantitative meteorological information needed by decision makers to provide support and mitigation systems.

The difficulties in forecasting TC intensity occur because of the complexity and scale

of the processes involved. These include inner-core dynamics, upper-ocean interaction and atmospheric circulation processes (Emanuel, 1986, 1999; Emanuel et al., 2004; Schade and Emanuel, 1999; Zhang and Sippel, 2009) that are often poorly understood and represented by global and even regional atmospheric models (Gopalakrishnan et al., 2012).

The main uncertainty in storm surge prediction comes from the uncertainty in meteorological forecasts. Sea surface height can exhibit large variability even with small changes in the TC track, wind strengths, central pressure, translation speed, radius of maximum winds, angle of approach to the coast and the shape of the wind profile (Lin et al., 2013). For example, according to Rappaport et al. (2009a), a 55 km error in forecast landfall location can make a difference of more than 6 m between the level of surge expected from the erroneous forecast track and the storm surge that actually happens. The more intense a TC is, the stronger the winds are and the larger the radius of maximum winds is, therefore the more extreme a storm surge may be (Irish et al., 2008). This means that fully understanding processes involved in TC development and the air-sea interactions associated is of the utmost importance for storm surge forecasting.

Improvement of intensity forecasting is a top priority in the TC and storm surge research community and there is a focus on improving the understanding of the role the ocean plays (Emanuel, 1986; Schade and Emanuel, 1999; Liu et al., 2011; Green and Zhang, 2013), not only in terms of the sea surface temperature, but also of the upper-ocean thermal structure (Goni and Trinanes, 2003; Sadhuram et al., 2010). This is important not only for real-time forecasting, but also for climate scientists to understand the impact global warming has on frequency and intensity of such events.

There are various different approaches to tackle this complex problem. In this section, 5 main areas of research are described; improving initialisation of both meteorological and oceanographic fields, improving the parametrisation schemes used, ensemble modelling, increasing the resolution of the models and finally, using coupled atmosphere-ocean-wave models. Fine resolution modelling is described in Section 2.1.1 because this directly links to Objective Two of the study. Numerical model initialisation is detailed in Section 2.1.2, as this relates to Objective Three. A brief overview of other modelling methods is given in Section **??**, including coupled modelling and model parametrisations. Although these elements are not the focus of the current study, and are not varied in the main experiments, these elements are important aspects of the modelling system. The Objectives are stated in full in Section 1.1.

2.1.1 Fine Resolution Modelling

One of the foci of this study is the impact of increasing horizontal and vertical spatial resolution of the atmospheric model on the storm surge and wave field output.

The fundamental problem with numerically modelling the atmosphere and ocean is that the equations which describe their evolution are continuous. In order to solve them for a certain region, the domain must be discretised to create a regular grid of points on which

the governing equations will be numerically solved using finite difference methods. Finite element and volume (unstructured) grids also exist and can provide different insight into the physical processes and dynamical equations. Here, only finite difference models are described and used, as this allows the finer resolution grids to be concentrated on the moving TC vortex (see more in Section 4.2.1).

The spatial resolution of a numerical model describes the physical distance between these model points where variables are calculated every time step. This is commonly referred to as the cell size, or grid spacing, because the points are evenly spaced horizontally and vertically in space, altogether making a grid of cells with computed values of the particular model's variables.

Along with spatial resolution, there is temporal resolution, or the length of the model's time step. This refers to how frequently in simulated or 'model' time calculations of the various properties being modelled are calculated. For an explicit numerical scheme to be computationally stable, the time step must be small enough. The Courant-Friedrich-Lewy (CFL) criterion is one stability condition which states that the speed of propagation, c, times the time step, $\triangle t$, must be less than the grid spacing, $\triangle x$. In other words, the advective process must not move properties further than one grid space per time step.

Figure 2.1 demonstrates the value of increasing image resolution, and is used here as an analogue for numerical model resolution. As the resolution increases, the image becomes clearer and holds more information. However, for numerical modelling the increase in resolution also comes with a much increased computational cost. As a general rule, doubling the grid spacing of a model can lead to an increase in computational time by ten times, or ten times more computing power is required.

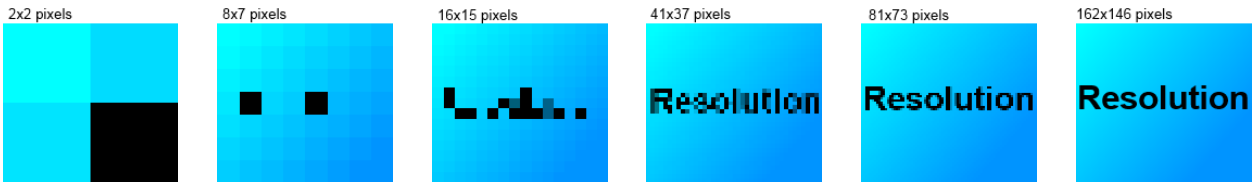

Figure 2.1: Demonstration of image resolution as a parallel for model resolution.

Increasing resolution can also lead to certain model parametrisations no longer being necessary, where the physical process may be resolved explicitly. In other words, the length scales associated with a particular physical process may be larger than the resolution, therefore discretisation of the governing equations can lead to accurate representation of the physical process. Therefore, a higher resolution removes some of the uncertainty related to the parametrisation scheme.

There has been considerable debate in recent decades about whether decreasing the horizontal grid spacing in models improves forecast quality. Many studies have shown that higher resolution atmospheric models have improved skill in TC intensity forecasting (e.g.

Davis et al. 2008a, 2010a). This is mostly due to the removal of cumulus parametrisation as the grid spacing decreases from around 10 km to 4 km or less, allowing the models to better resolve inner-core structures such as eyewalls and rainbands. The impact on track forecasting has been limited in these studies, as the track is principally dependent on large-scale processes.

One of the drawbacks of this approach is that it is very difficult to test whether the improvement of forecast results is due to the smaller grid size, or the different parametrisation schemes used. It is complicated to separate these two factors, especially the cumulus parametrisation schemes used, and this will not be the focus of this study.

Typically, as in Davis et al. (2010a), this enhanced atmospheric resolution is achieved through moveable, nested grids of higher resolution which follow the location of the vortex centre. Moving nests are critical to obtaining significantly enhanced horizontal resolutions within the TC inner core for a manageable increase in computational cost. This study looks to replicate these results, and then investigate the impact of increased atmospheric resolution on the storm surge and wave field.

The increased resolution in atmospheric models has also been applied to global climate models, in order to echo the improvements seen at the regional level, with regional TC forecasting models. Gall et al. (2011) describe the GFDL (Geophysical Fluid Dynamics Laboratory) High-resolution Atmospheric Model (HiRAM) as a TC forecasting tool both at the near-term and intraseasonal time scales. Their initial results are promising, however several improvements similar to those mentioned in this section are necessary before the system is operational.

Although resolution of 1-4 km begins to capture fine-scale asymmetries in the inner core of TCs, they are still too coarse to directly compute three-dimensional turbulence. The effects of turbulence have to be parametrised and the important features of simulations depends on poorly known empirical constants. For example, Bryan and Rotunno (2009) find a strong dependence of the maximum TC intensity on the assumed value for horizontal mixing length. Chen et al. (2008) conduct a series of model experiments of an idealised TC at grid spacing sizes from 1.3 km to 62 m to investigate the role of turbulence on TC intensity. When the resolution was increased from 185 m to 62 m there was a dramatic increase in the instantaneous wind speed, from 80 ms^{-1} to 120 ms^{-1} . The horizontal distribution of wind speed also showed smooth ring structures for the finest resolutions associated with energetic eddies. When the large-amplitude, high-frequency turbulence was filtered out, the vortex intensity reached was lower. For grid spacing greater than 185 m, the simulated turbulence was weaker, and the TC became stronger and stronger with increased grid size due to insufficient friction produced by the sub grid-scale turbulence parametrisation scheme.

Resolutions with grid spacing of less than 1 km are not a focus of the current study, although there is much ongoing research in this area.

Ocean model resolution has also been increased to assess impact on the storm surge and

wave forecast. Moon et al. (2009) investigated the impact of grid resolution and physical parametrisation of the drag coefficient on the simulated storm surge for Super Typhoon Maemi (2003). They compared grid resolutions of 1/12°, 1/60° and 1/360° and found that the finer resolution domains produced the higher peak surges. The largest difference was between the 1/360° and 1/12° at Busan, South Korea, with a change of 0.24 m in peak surge. The authors attribute this change to how the surge is calculated. In coarser resolutions, the surge height is averaged over a larger area and therefore will be lower. They also found that the effect of different drag parametrisations changed for different resolutions, which shows that increased resolution alone is not enough to improve a modelled storm surge simulation. Although larger storm surges were produced with higher resolution numerical modelling, there was no one grid size was consistently more accurate. The optimal grid size for storm surge forecasting would depend on the complexity of the coastline, with smaller grid allowing better representation of detailed topography and coastline changes.

It is expected that an increase in accuracy of fine resolution atmospheric models will translate to an increase in accuracy of the storm surge forecast. Bricheno et al. (2013b) used the WRF atmospheric model (Weather Research Forecasting - see Section 3.1) to force the coupled ocean and wave model system POLCOMS (Proudman Oceanographic Laboratory Coastal Ocean Model System) and WAM (3rd generation wave model), see Section 3.2, to investigate the effect of higher resolution meteorology on the storm surge and waves generated in the Irish Sea. They found that wind speed errors decreased more than 10% on average when moving from 12 km to 4 km resolution, but no further significant improvement was identified moving from 4 km to 1.3 km. The increased resolution forcing generally increased wave height by above 40 cm in places in the case study area, however the modelled surge showed little response to the improved resolution wind and pressure fields. Large improvements were seen near to the coast, attributed to the better representation of the coastline and atmospheric boundary layer. This study confirms that for extra tropical depressions, an increase in accuracy of atmospheric parameters leads to an increase in accuracy of storm surge and waves, but also that this improvement has diminishing returns below 4 km grid spacing.

In the above study, the authors focussed on extra-tropical storms. Here, this work will be expanded to look at TCs. It will be of interest to see whether a similar result is found, as the difference in storm formation and the interaction with the ocean will have an impact. The investigation of this hypothesis is the topic of the rest of this manuscript, as well as sensitivity testing the model initialisation.

2.1.2 Improving Initialisation

Initialisation is the process of defining the starting conditions within a numerical model domain. Initial conditions describe the initial value for every model variable, from which the governing equations develop the model simulation. For environmental numerical prediction, this is where observations are entered and where previous model simulation results can be used.

As the precise initial state of the atmosphere or ocean is impossible to know exactly, initialisation is a source of uncertainty in mathematical modelling. The atmosphere and oceans are chaotic systems, so small difference in the initial fields can give rise to large differences in model results. There is, therefore, much interest in improving observational systems, methodology and equipment, and in incorporating all relevant and useful data into the initialisation process.

Many regional meteorological models take their initial conditions from global analysis or model output. Because of the coarse resolution, this can lead to large errors in tropical cyclone forecasting, as initial errors tend to grow in time. In order to solve this problem, one technique used is vortex seeding or bogussing. This involves removing the low resolution vortex from the global analysis fields, and inserting a more realistic and detailed vortex based on theoretical relationships to calculate the size and intensity. This may be a basic mass-consistent vortex (as used in the GFDL model - see Bender et al. (2007)) or a model-consistent vortex using the previous model cycle vortex, relocated and adjusted to the most recent observations (as in HWRF - see Liu et al. (2006)). A number of studies have shown that improved initialisation of a vortex can significantly improve the forecast of TC track and intensity (Gopalakrishnan et al., 2012).

Another similar approach is the use of data assimilation. This involves incorporating all the available information to provide the best possible analysis, including previous model runs, observations and information about the current model error or bias. The errors can be assessed by the use of model ensemble runs, and ensemble Kalman filtering is one method of this process Whitaker and Hamill (2002).

Data assimilation techniques are also used in hydrodynamic models. For storm surge application, they can optimise the wind drag coefficients so as to minimise the difference between observed and modelled water levels (Peng et al., 2013), or optimise the water levels themselves (Peng and Xie, 2006). This is an active area of research especially thanks to the increasing amount of remote-sensing and satellite altimeter derived data becoming available.

Both vortex bogussing and data assimilation are reliant on the observations of the particular tropical cyclone that are available, which can be sparse due to the episodic nature and scale of TCs. Reconnaissance data are collected from dropsondes and aircraft flight measurements through the inner core, however this may not always be available. There have also been several programmes to improve the quality and amount of tropical cyclone observations, including CBLAST (Coupled Boundary Layers Air-Sea Transfer) during the 2003 hurricane season. The data recorded has been used for detailed analysis of the air-sea interface in particular (Bell et al., 2012). However, due to the extreme values of wind and pressure, amongst other meteorological variables, the data assimilation of these observations can increase the model error and/or bias particularly for smaller, newly developed storms (Gopalakrishnan et al., 2012).

Storm surge numerical models also benefit from accurate initial fields. For the majority of operational surge models, the model is run for a hindcast period using observed meteo-

rological and the modelled outputs are assimilated with the latest ocean observational data. This process may improve the initial state of the surge model (WMO, 2011). In this study, however, the available observational data is limited and data assimilation is not possible. A spin-up period of the ocean domain is undertaken, in order to better represent the initial conditions (described in Section 3.3.4.

2.1.3 Coupled Atmosphere-Ocean-Wave Modelling

As described in Section 1, TCs and storm surges involve highly interlinked processes including complex tide-surge, wave-surge and wave-wind interactions. In order to successfully numerically model tropical cyclones and their storm surges, coupled models are required to account for feedbacks between the ocean circulation, wave field and atmospheric dynamics.

When describing numerical models, 'coupling' refers to communication and interchange of information between different models. In a 'coupled' atmosphere-ocean model, the system evolves as a whole with exchanges of model data throughout the simulation. For example, instead of the atmosphere model seeing a static SST, the modelled SST from the ocean model is used. The allows for feedbacks between the different systems to be modelled.

Currently this approach is too computationally expensive to use routinely for operational TC surge forecasting, however there are various examples where coupled models have advanced knowledge of fluxes at the air-sea interface, improved hindcast results for TC and surges and also helped refine the parametrisations used in atmospheric and ocean numerical modelling (Bender and Ginis, 2000; Liu et al., 2011; Brown and Wolf, 2009; Murty et al., 2014b).

These examples focus on 2 main areas: atmosphere-ocean-wave coupling to improve TC intensity forecasting, and ocean-wave coupling for storm surge forecasting improvements and to better understand wave-current interaction effects.

The effect of tropical cyclone-ocean interactions on the intensity of observed TCs was investigated in Bender and Ginis (2000). Following on from work on idealized hurricane modelling using the same model system, the authors used the Geophysical Fluid Dynamics Laboratory (GFDL - see Kurihara et al. (1995)) TC model with Princeton Ocean Model (POM - see Blumberg and Mellor (1987); Mellor (2004)) to simulate various case studies, two from the western Atlantic: Hurricanes Felix (1995) and Fran (1996); and two from the Gulf of Mexico: Hurricanes Opal (1995) and Gilbert (1988). They showed that coupling interactions produced a significant cold wake, particularly when the storms were moving slowly, which had a large effect on the storm intensity. In each of the simulations, the inclusion of ocean coupling generally made substantial improvements to the storm intensity forecast, as measured by the storm's minimum sea level pressure.

In the study undertaken by Liu et al. (2011), the WRF atmospheric model (see Section 3.1) is coupled with the wave model SWAN (Simulating WAves Nearshore - for model details see Booij et al. (1999)) and POM (see above). This coupled atmosphere-wave-ocean

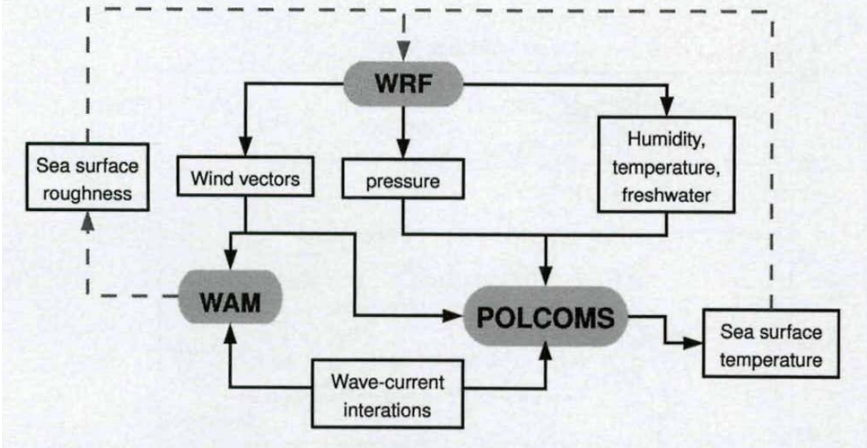

Figure 2.2: The ocean-wave-atmosphere model interactions in Bricheno et al. (2013b), with arrows showing the variables passed between the models and potential pathways for future work shown by the dashed lines. A very similar set-up is used in the current study, excluding the humidity, temperature and freshwater atmospheric forcing.

modelling system (CAWOMS) is based on integrating atmosphere, wave and ocean/current interactions processes including, but not limited to, sea-spray affected surface roughness, heat fluxes dependent on sea spray, wave state, sea surface temperature cooling and atmospheric feedbacks, and the impacts of sea surface currents on wind stress. They used this system to simulate an idealised TC to investigate the effects of coupling on TC intensity. They found that overall atmosphere-wave processes generally strengthen the TC, while thermodynamic ocean-atmosphere coupling weakens the TC (via sea surface temperature cooling). The overall effects are determined by the balance between these positive and negative feedbacks.

Brown and Wolf (2009) use a coupled wave and surge model system (POLCOMS-WAM, see above) in the Irish Sea to investigate whether a wave-dependent surface drag is needed for accurate storm surge prediction, or if an optimised Charnock parameter can represent this drag. Their results show that a constant Charnock parameter value can be tuned to give an accurate surge at a given location, however to be optimal everywhere a wave-dependent Charnock parameter may be used. The authors introduce metrics (trend error function and peak error function) which are useful to assess the accuracy of surge prediction across a region and can potentially be used in further work.

In Murty et al. (2014b) the authors also use a coupled wave and hydrodynamic modelling system, this time ADCIRC (ADvanced CIRCulation model - Luettich et al. (1992)) and SWAN (see above) in the Bay of Bengal. Using the case study of Cyclone Phailin, they studied the effect of wave-induced set up on the net water level elevation by comparing the output from the coupled model and an uncoupled run of the same event. Although there is very little observational data to verify their results, they found that wave-induced set-up contributes a significant amount (between 23% and 36%) of the peak storm surge.

In the current study, the coupled ocean-wave model system described by Brown and

Wolf (2009) is used, along with one way coupling with WRF as in Bricheno et al. (2013b) (shown in Figure 2.2). With this system, the impact of fine resolution of TC forcing on the ocean-wave models will be analysed, along with ocean-wave interaction processes.

2.1.4 Model Parametrisation Schemes

As described in Section 2.1.1, atmospheric and oceanic numerical models are often calculated on grids of equally spaced calculation points. When a physical process occurs at a scale less than that of the model grid resolution or it is too complex, then the phenomenon cannot be explicitly calculated on the domain. In order to include as many physical processes as possible, parametrisation schemes can be used to approximate this dynamic relationship which may otherwise be considered.

Parametrisation schemes aim to represent complex or sub-grid-scale processes by relating them to the variables which are on the scales which the model does resolve. They may be based on theoretical relationships between different variables, or on an observed (empirical) relationship.

Examples of processes which are frequently parametrised include atmospheric convection and cumulus cloud creation; cloud microphysics; turbulence and eddies; solar radiation; turbulence processes; surface and bottom friction; Reynolds' averaging e.g. eddy viscosity; and importantly for high wind simulation, surface drag and fluxes.

Historically, observations in the complex, dynamic TC core have been impossible and continue to be very difficult, therefore the physical parametrisations that initially existed as these may not have been reliable or realistic. They were based on the information available, and as there were no direct flux measurements over the open ocean for wind speeds above 22 ms^{-1} until the early 2000s (Black et al., 2007), scientists had to extrapolate data from low wind speeds.

Once observations near the sea surface in high wind speeds were taken, it became clear that these extrapolations were inaccurate, especially for the drag coefficient. Powell et al. (2003) calculated the drag coefficient using hundreds of dropsondes launch from aircraft into tropical cyclones. Powell found that after reaching a threshold wind speed (roughly 35 ms^{-1}), the drag coefficient actually levelled off and even decreased slightly as wind speeds increased further. This result was contrary to the drag coefficient formulations at the time, which assumed a linear relationship between wind speed and drag. This result was clarified by Donelan et al. (2004) using laboratory experiments to calculate drag coefficients at different wind speeds, where lower drag coefficient values were found for low winds, with a linear increase up to a maximum value of 0.0024 at approximately 35 ms^{-1}. Sea spray is one likely cause of the occurrence of this limiting value, as well as airflow separation induced by continuous wave breaking. Many studies, for example Moon et al. (2009); Green and Zhang (2013); Liu et al. (2011), have found that this improved parametrisation allows for more accurate tropical cyclone simulations.

The friction velocity, introduced in Section 1.4, is dependent on the drag coefficient parametrisation chosen in a model. It is also dependent on surface heat and moisture flux calculations and requires a scaling temperature θ_* or moisture q_*, both defined by similarity theory profiles. The different parametrisations of drag affect these quantities and several theories exist describing how the enthalpy exchange coefficient changes with drag, or friction velocity.

C_k can increase slowly with wind speed (Carlson and Boland, 1978), stay steady with wind speed (Large and Pond, 1981), or decrease with wind speed (Garratt, 1992). The proper wind speed dependence of C_k remains a topic of active research, but each of these formulations is available in WRF (see Section 3.1.2).

Sea spray produced by breaking surface waves and the wind tearing of wave crests also have significant impacts on the air-sea momentum flux (dependent on drag) and the air-sea heat and moisture fluxes. Since the main generation process is surface wave breaking, the amount of sea spray (and therefore changes in sea spray heat flux) is dependent upon wave state. One way of including this process is to use a parametrisation of the sea spray heat fluxes. Liu et al. (2011) used a more explicit sea spray parametrisation in a coupled model system. The module uses sea surface temperature, friction velocity, atmospheric temperature, specific humidity, and pressure, and wave state to calculate the sea spray fluxes. For a full description of the model interactions, see Xie et al. (2010). The study found that sea spray, under high winds, reduces the drag coefficient and favours TC intensification, and that the sea spray heat fluxes and dissipative heating of the ocean surface also strengthens the intensity of a cyclone.

The surface interactions are complex and there are many inter-dependencies as shown in the exchange coefficient examples above. This is of particular interest in this study, as generally atmosphere, ocean and wave models treat calculation of surface fluxes differently, depending on the model use and research focus. Coupling models together is one-way around the inconsistencies, or using the same parametrisation scheme in each type of model is crucial. In this study, the same parametrisation schemes have been chosen.

2.1.5 Ensemble Modelling

Ensemble techniques allow for the creation of probabilistic forecasts of track and intensity. Ensemble modelling involves repeating a simulation with slightly perturbed initial conditions, boundary forcing, or parametrisation variables to produce many different possible forecasts. The different outcomes can then be compared and used to produce a probabilistic overview: the most likely prediction and an idea of the uncertainty associated with it. For TC forecasting ensemble systems are generally based on model runs with slightly perturbed initial conditions, instead of climatology parameters. In Section 2.1.2, the importance and uncertainty of initialisation was described. Ensemble methods are one way to tackle this uncertainty. The ECMWF Variable Ensemble Prediction System (EPS) has shown skill in this area see Dupont et al. (2011) and Belanger et al. (2012).

The uncertainty in storm surge forecasting associated with meteorological forcing has also been addressed by ensemble forecasting (Flowerdew et al., 2010), where small perturbations to the initialisation of a mesoscale model are used to simulate different storm surge results. This has shown skill in developing probabilistic storm surge forecasts, although much of this work focused on mid-latitude storms rather than tropical cyclones. Davis et al. (2010b) created a probabilistic storm surge prediction framework which centred around using ensemble simulations of TCs track and intensity to create an ensemble of storm surge states. The framework showed potential, even in a time and data limited situation, hence the possibility for operational use.

Ensemble modelling will not be a focus of the current study, however it is useful to describe it as this method highlights the importance of initial conditions for TC and storm surge modelling.

Chapter 3

Methods

For this study, both high resolution atmospheric modelling, and coupled atmosphere-ocean-wave numerical modelling has been undertaken. This section describes the models used, how the model domains have been designed and created, and the runtime options used.

3.1 The WRF Model

3.1.1 Model Description

For the meteorological portion of the modelling investigation, the Weather Research and Forecasting model (WRF) atmospheric model has been utilised. WRF has been used for undertaking the high resolution Cyclone Phailin simulation, as well as being coupled with the ocean and wave models described in Section 3.2.

WRF is a numerical weather prediction model with many applications that span from regional weather forecasting to advanced meteorological research. The open source model gives flexibility to the user allowing for both very fine and coarse resolution models to be created, from grids of less than a metre, to grids of thousands of kilometres. This adaptability feature supports the wide range of uses WRF has. For example, many climate models need coarser grids running simulations hundreds of model years in length. Alternatively, microscopic resolutions may be used in cloud microphysics and aerosol research. Bespoke WRF models can be built for both of these scales, and many in between.

The WRF numerical equations are formulated for a terrain-following sigma (σ) vertical coordinate system defined by:

$$\sigma = \frac{(p_h - p_{ht})}{\mu} \text{ where } \mu = p_{hs} - p_{ht} \tag{3.1}$$

P_h denotes the hydrostatic component of pressure, and p_{hs} and p_{ht} refer to pressure at the surface and top boundaries respectively. As can be seen in Figure 3.1, this allows for vertical model surfaces to be distributed evenly throughout the atmosphere, without being dependent on the topography. It allows for the smooth representation of variables, especially near

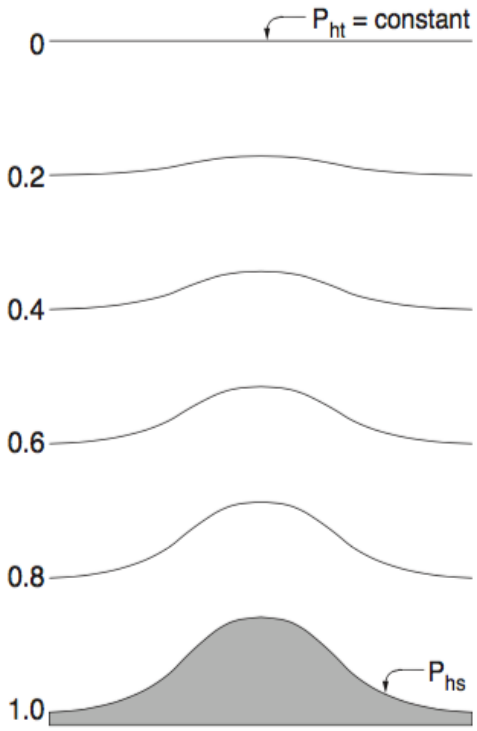

Figure 3.1: WRF Sigma Coordinates (Skamarock et al., 2008)

the surface in the lowest vertical layers of the model. Also, as atmospheric density decreases exponentially with height above the surface, the sigma coordinate system allows for greater vertical resolution near to the surface. The boundary layer is defined as the portion of the lower troposphere that is directly affected by the earth's surface, and is important as this is where humans live and are affected by the atmosphere. Therefore, higher vertical spatial resolution in this area is crucial for successfully modelling and forecasting the impact of meteorological hazards.

The sigma coordinate is used commonly in atmospheric models and may be referred to as a mass vertical coordinate. Sigma varies from 1 at the surface, to 0 at the domains upper boundary (see Figure 3.1). $\mu(x, y)$ denotes the mass per unit area in column (x, y) and thus we have:

$$\boldsymbol{W} = \mu\boldsymbol{w} = (W_x, W_y, W_z),\ \Omega = \mu\dot{\zeta},\ \Theta = \mu\theta \tag{3.2}$$

where $\boldsymbol{w} = (w_x, w_y, w_z)$ are the covariant velocities in the two horizontal and vertical directions, $\omega = \dot{\zeta}$ is the contravariant vertical velocity, and θ is the potential temperature.

WRF's governing equations are the fully compressible, non-hydrostatic Euler equations given below in their flux-form, using the definitions of the vertical coordinate sigma and the related covariant velocity matrices. They also include the non-conserved variables of the geopotential, $\phi = gz$, pressure, p, and the inverse density, $\alpha = \rho^{-1}$.

The Euler equations are a form of the Cauchy equations governing adiabatic and inviscid fluid flow, with conservation of mass, and balances of momentum and energy. They are a particular version of the Navier-Stokes equations, which describe both compressible and incompressible fluid, with zero viscosity and zero thermal conductivity. They are as follows:

$$\begin{aligned}
\frac{\partial}{\partial t}W_x + (\nabla \cdot \boldsymbol{W}w_x) - \frac{\partial}{\partial x}(p\phi_\sigma) + \frac{\partial}{\partial \sigma}(p\sigma_x) &= F_{W_x} \\
\frac{\partial}{\partial t}W_y + (\nabla \cdot \boldsymbol{W}w_y) - \frac{\partial}{\partial y}(p\phi_\sigma) + \frac{\partial}{\partial \sigma}(p\sigma_y) &= F_{W_y} \\
\frac{\partial}{\partial t}W_z + (\nabla \cdot \boldsymbol{W}w_z) - g(\frac{\partial}{\partial \sigma}p - \mu) &= F_{W_z} \\
\frac{\partial}{\partial t}\Theta + (\nabla \cdot \boldsymbol{W}\theta) &= F_\theta \\
\frac{\partial}{\partial t}\mu + (\nabla \cdot \boldsymbol{w}) &= 0 \\
\frac{\partial}{\partial t}\phi + \mu^{-1}[(\boldsymbol{W} \cdot \nabla\phi) - gW_z &= 0
\end{aligned} \tag{3.3}$$

These equations include Bernoulli's principle in the equation for the non-conserved property, the geopotential, which states that as a fluid accelerates, there must be a decrease in the fluid's pressure or potential energy.

Along with the above equations, WRF uses the diagnostic relation for the inverse density:

$$\frac{\partial}{\partial \sigma}\phi = -\alpha\mu, \tag{3.4}$$

and the equation of state

$$p = p_0(R_d\theta/p_0\alpha)^\gamma. \tag{3.5}$$

The equation of state includes the variables $\gamma = c_p/c_v = 1.4$, the ratio of heat capacities of dry air, R_d, the gas constant for dry air, and p_0, a reference pressure.

WRF also includes these equations formulated to include moist air and a description of these can be found in Skamarock et al. (2008), along with the equations' derivation.

WRF incorporates many complex physical processes, along with the governing dynamical equations, including long-wave and short-wave radiation and the effects of cloud and aerosols, cloud microphysics, cumulus convection, planetary boundary layer and surface. These processes are incorporated in the WRF model via parametrisation schemes. There are several different parametrisation scheme choices for each process and those relevant to this study are described in detail in Section 3.1.2.

ARW (Advanced Research WRF) refers to the dynamic solver used by WRF to numerically solve the governing equations. The ARW core is developed and maintained by the

Mesoscale and Microscale Meteorology Division of NCAR. The alternative dynamic core is the NMM (Non-hydrostatic Mesoscale Model), which is developed by NCEP. The main differences include that the governing equations in NMM are in an advective rather than flux form, ARW includes many more prognostic variables related to the differing form of the governing equations, NMM uses a different spatial discretisation, the sigma coordinate in NMM relaxes to a pressure coordinate near to the model's vertical top, and there are numerical subtleties in the time integration and splitting methods. In this study, the ARW core is used as this is the core used in AHW (see Section 3.1.3).

The ARW numeric solver supports four map projections - the Lambert conformal, polar stereographic, Mercator, and latitude-longitude projections. In order to solve the governing equations for different map projections, map factors are used to transform them. The map factors m_x and m_y are defined as the ratio of the distance in computational space, to the distance on the Earth's surface:

$$(m_x, m_y) = \frac{(\Delta x, \Delta y)}{\text{distance on earth}} \tag{3.6}$$

Using these map factors, equations 3.3 can be rewritten using transformed and redefined momentum variables. This allows for solutions that incorporate both Coriolis and curvature terms for the map projections listed above. In this study, the default Lambert conformal map projection is used.

The WRF numeric solver uses a time-split integration scheme. This means that slow or low-frequency meteorologically significant modes are integrated using a third-order Runge-Kutta time integration scheme, whereas the high-frequency acoustic modes are integrated over smaller time steps. This ensures numerical stability by treating the linear and non-linear steps separately, allowing a numerical solution to be found even when linear and non-linear interactions mean a general analytic solution is not possible. Previously high frequency modes such as gravity waves and buoyancy oscillations significantly constrained the time steps possible to maintain numerical stability. For more information, this process is described in detail in Skamarock et al. (2008).

The spatial discretisation of the solver uses an Akawara C-grid as shown in Figure 3.2. In this figure, (u, v, w) represent the components of the wind vector $\boldsymbol{W}$. This is a staggered grid where the normal velocities are half a grid length from the thermodynamic variables, as can be seen in the figure. The grid lengths Δx and Δy are constants in the model formulation, and although $\Delta\eta$ is not constant, it is specified in the model initialisation process. The main advantages of using a staggered C-grid is that the pressure and convergence terms are calculated over the distance Δx, which improves the resolution compared with a non-staggered A grid (Collins et al., 2013). The C-grid also allows for relatively straight forward computation of nested gridded domains. Similarly to the horizontal domain, the vertical grid is staggered such that the prognostic variables are at the centre of the vertical layers and the vertical velocity is at the boundary between layers.

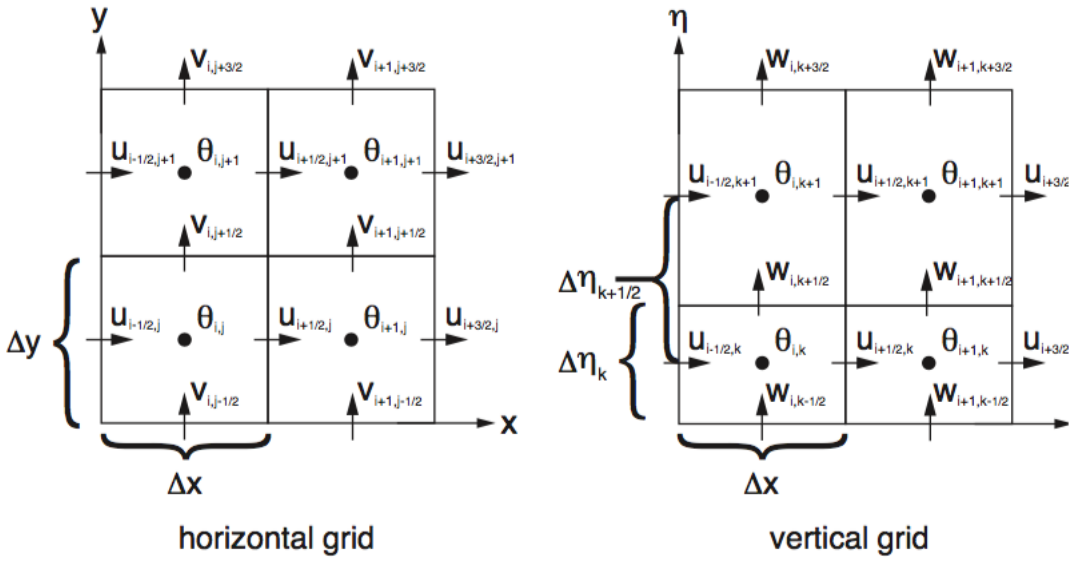

Figure 3.2: WRF's Arawaka C-Grid (Skamarock et al., 2008)

3.1.2 Parametrisation Schemes Available

The governing equations described in the previous section do not include all the necessary complex interactions and processes that occur in reality in the atmosphere. For example, very small-scale processes such as cloud microphysics (which has lengthscales ¡¡1 m) cannot be explicitly resolved at the model resolution generally used (grid sizes of ¿1 km), but are nevertheless highly important to include in a meteorological dynamical model. In this situation, parametrisation schemes are utilised to approximate the small-scale cloud microphysics. The available WRF model parametrisation schemes are described in this section, as well as any benefits associated with particular choices.

Convective clouds play an extremely important role in the meteorological and climate system. Clouds and their associated physical processes couple the dynamic and hydrological processes in the atmosphere via condensation, evaporation and redistribution of sensible and latent heat and momentum; they effect solar radiation in the atmosphere through reflection, absorption and emission; and they create precipitation and modify boundary layer processes (e.g. convective gusts). Due to the spatial scale on which individual convective clouds occur, explicit representation of convection in models is not always possible. Thus, the effects of convection must be estimated from the model variables, in other words using a parametrisation scheme.

Early models included a very basic convection parametrisation, which involved determining if a vertical column of air was unstable (i.e. the bottom is warmer than the top) then it would be overturned and the column would become mixed. More sophisticated schemes included other processes such as entrainment or further convection. One such parametrisation scheme which is available for use in the WRF model is the Kain-Fritsch scheme (Kain, 2004) which utilises a simple cloud model with moist updraughts and downdraughts, including the

effects of detrainment, entrainment, and relatively simple microphysics. The scheme has a minimum entrainment rate to suppress widespread convection in marginally unstable, relatively dry environments, and includes shallow non-precipitating convection. Other schemes are available in WRF including ensemble methods, such as Grell-Devenyi scheme (Grell and Devenyi, 2002), where multiple cumulus schemes run within each grid box and then the results are averaged to give the feedback to the model.

Below roughly 4 km grid resolution, convective processes can be explicitly resolved by WRF's governing equations of motion, meaning that the convective parametrisation schemes described are only necessary for coarser grid sizes (see Section 2.1.1 for further details).

Cloud microphysics is the example, given above, of a complex process which need to be incorporated in the numerical model. These processes lead to the formation, growth and precipitation of clouds. They are important to include as they provide atmospheric heat and moisture dependencies via latent heating and cooling; the amount of precipitation simulated depends on cloud microphysics; they are associated with moist downdraughts and therefore surface-wind gustiness; and they are linked to radiative transfer via the absorption and emission of long wave solar radiation.

Parametrisation schemes for cloud microphysics tend to fall into two different categories: bulk parametrisation, where the cloud particle distribution is assumed to be continuous and follow a functional form, and detailed or bin parametrisation, where the particle size distribution is discretised into bins. Bulk formulations predict bulk quantities, such as the mixing ratio, as a function of this particle size distribution. For WRF, bulk formulations are available including Kessler (Kessler, 1969), which separates liquid cloud water and rain, but does not include ice particles in clouds; WSM 3 class scheme (Hong et al., 2004), which has three different classes and includes ice processes below 0 °C; WSM 5 class scheme (Hong et al., 2004), with a five class system including supercooled water and snow melt along with ice, rainwater and liquid cloud water; the Ferrier scheme, which includes the 5 phases but is also designed for efficiency and so advects only the total condensate and vapour assuming the fractions of water and ice within the column are fixed during this advection; and WSM 6 class scheme (Hong et al., 2004), which also includes graupel.

Only a limited number of the available parametrisation schemes are listed here, as there are many more specific ones for different model uses. The microphysics will not be the focus of this study and WRF's default option (WSM 5 described above) is chosen for use. For details on the sensitivities of the inner-core structure of tropical cyclones to microphysics schemes see Zhu and D.-L.Zhang (2006).

The representation of the lower-tropospheric thermodynamics and kinematic structures are provided by planetary boundary layer (PBL) parametrisation schemes. The PBL procedures account for vertical mixing and surface exchanges of moisture, heat and momentum within the boundary layer. Turbulent eddies play a large role in this mixing and the associated exchanges, which cannot be explicitly calculated on grid scales and time steps used in most mesoscale atmospheric models. Therefore, their effects are expressed in the model

via PBL parametrisations. There are generally two major components of representing turbulence mathematically; the order of turbulence closure and whether a local or non-local mixing approach is used.

PBL parametrisation scheme development required the variables of the equations of motion to be decomposed into mean and perturbation components representing the time-averaged, background conditions and the deviations of turbulent fluctuations from this background state. The order of turbulence closure refers to the number of moments needed to empirically relate the unknown turbulence terms to lower-moment terms. Local closure schemes allow the known variables at a given point to affect those vertical levels that are directly adjacent to it. Non-local schemes can be used to determine variables at a given point across multiple vertical levels. Local schemes have a substantial disadvantage by not representing deep PBL circulations accurately (Skamarock et al., 2008).

WRF PBL schemes include one developed by Yonsei University (YSU) (Hong et al., 2006) which is non-local and has first-order closure and represents entrainment at the top of the PBL explicitly, and the Mellor-Yamada-Janjic (MYJ) (Janjic, 1994) which is local and has a 1.5-order closure scheme with an equation for prognosis of turbulent kinetic energy, along with many others to choose from depending on the study aims. In this study, the default PBL parametrisation of YSU is used.

Land surface models (LSMs) use atmospheric information from various of the other parametrisation schemes, including precipitation forcing from the cloud microphysics and convection, radiative forcing from the radiation scheme, and forcing from the surface layer scheme, to calculate heat and moisture fluxes over land and sea-ice points. These fluxes provide the lower boundary condition for the PBL schemes and therefore, are closely linked. The schemes output the land's state variables including the ground (skin) temperature, soil temperature profile, soil moisture profile, snow cover, and canopy properties.

The different LSMs in WRF have varying degrees of complexity. They can have multiple layers of soil, and include vegetation, root and canopy effects as well as snow-cover prediction. All the schemes are one-dimensional, so there is no horizontal interaction between neighbouring points and they can be regarded as a one-point column model for every WRF surface point. One of the most commonly used models is the NOAH LSM. The scheme was developed jointly by NCAR and NCEP and is used operationally in NCEP's North American Mesoscale Model. This has a 4-layer soil temperature and moisture model, including processes such as evapotranspiration, soil drainage, and runoff. Although other LSMs are available, the NOAH LSM is utilised in this study.

Along with LSM models, WRF also includes a basic ocean mixed-layer model. This is based on that of Pollard (1973). The model is one-dimensional, with 5 layers, and each column is independently coupled to the local atmosphere column. In the ocean mixed layer the variables included are mixed layer depth, vector horizontal current, mean temperature (taken as SST). This was primarily developed for use in TC modelling to simulate the cooling of the ocean beneath cyclones and the subsequent negative feedback on TC intensity. In this

study, a much more sophisticated ocean model will be used, therefore the 1D model that WRF provides is not utilised.

Closely linked to LSMs and PBL schemes are the surface layer parametrisations. These schemes calculate friction velocities and exchange coefficients that enable the calculation of fluxes in LSM and the surface stress used in PBL schemes. These schemes are often formed from the surface drag theory described in Section1.4.3, and are based on similarity theory to compute surface exchange coefficients for heat, moisture and momentum.

The different surface layer parametrisations available in WRF which are tied to the particular boundary-layer options chosen. The options include the MM5 similarity theory scheme uses various stability functions to compute surface exchanges coefficients (see Skamarock et al. (2008) for full details), and a convective velocity following Beljaars (1994) is used to enhance the heat and moisture surface fluxes. The Charnock relation for roughness length and friction velocity over water is used(see Section 1.4.3), with an option to instead use the Donelan relation, which has lower drag at hurricane force wind speeds, along with the Garrett formulation for enthalpy (see Section 2.1.4). This scheme must be used in conjunction with the YSU PBL scheme. There is an Eta surface later scheme which must be run in conjunction with the MYJ PBL scheme. This option includes parametrisation of a viscous sub-layer, following Janjic (1994). The MM5 option is used in this study.

The amount of solar radiation reaching the ground on changing terrain, or due to variable cloud cover, is parametrised in atmospheric models because this process occurs on the molecular scale, generally smaller than the grid resolution. The parametrisation schemes provide atmospheric heating due to the expected radiative flux divergence and downward long-wave and short-wave radiation impacting the ground heat budget. These budgets depend upon on both the amount of infra-red radiation which is absorbed or emitted by gases and surfaces, and the amount of upward long-wave radiative flux from the ground. This is determined by the surface emissivity processes including the absorption, reflection and scattering of short-wave radiation in the atmosphere which is highly sensitive to model predicted cloud and water vapour distributions.

All WRF radiation schemes are one dimensional, where each column is treated independently and the fluxes correspond to those in infinite horizontally uniform planes. This assumption is valid where the vertical thickness is much less than the horizontal grid length, but becomes less accurate for high horizontal resolution. The different schemes include either long-wave or short-wave radiation in differing number of spectral bands and the effects of different gases within the atmosphere. The default options for WRF for long-wave and short-wave radiation, respectively, are the rapid radiative transfer model (Mlawer et al. (1997)) and the Dudhia short-wave scheme (Dudhia, 1989). The RRTM is a spectral-band scheme using the correlated-k method, and accounts for water vapour, ozone, CO_2, trace gases and cloud optical depth. The Dudhia short-wave scheme has a simple integration of solar flux and accounts for clear-air scattering, water vapour absorption, and cloud albedo and absorption. In the newest version, this scheme also has an option for terrain slope and shadowing effects on the surface solar flux. Other radiation parametrisation schemes are available. The defaults

will be used in this study as the impact of radiation is not the focus of the model experiments.

Whilst the model parametrisations are defined in a modular way, there are many interactions between them via the model variables and their tendencies, and via the surface fluxes. All the physical schemes interact in some way with the surface physics (land-surface models or coupled ocean model), in some situations certain schemes have to be used with certain other ones due to the interactions which take place. New parametrisation schemes and the interactions between the existing formulations are active areas of research, see Section 2.1.4, but not the focus of the current study.

3.1.3 Advanced Hurricane WRF

The TC configuration of WRF is referred to as Advanced Hurricane WRF (AHW) (see Davis et al. 2008a) and is widely used by the TC research community. AHW is essentially a set-up of WRF (ARW core) which is defined by certain run-time options. Otherwise, this model uses the same dynamics, numerics and physics as WRF ARW. The following options are necessary for WRF ARW to be defined as AHW:

- Specific high wind parametrisation schemes. This includes the formulation of Donelan et al. 2004 for the air-sea drag coefficient, as well as several choices for the enthalpy flux (Carlson and Boland, 1978; Large and Pond, 1981; Garratt, 1992).
- Two-way interactive moving nests, which may be vortex following. These nested domains can be very high resolution to explicitly resolve convection and better represent TC inner structure (see Section 2.1.1).
- Optional use of one-dimensional ocean mixed layer model based on Pollard (1973). This optional ocean module aims to capture the negative feedback of SST on TC in a very basic way.
- Various initialisation techniques including directly from other models, using a TC relocation and bogussing utility program, TC bogussing using objective analysis, and data assimilation approaches including 3DVAR, 4DVAR and ensemble Kalman filters.

Parametrisation schemes which take into account the differences that occur at high wind speed are important when simulating TCs accurately. The amount of energy that is being lost from the atmosphere via drag on the ocean surface, and the way in which thermodynamic fluxes change with increased wind and wave speeds, are crucial processes that are not fully understood. Further parametrisation schemes that may be included in AHW in the future are always under development as new observational data and research experiments advise the numerical formulation of such processes. Currently different enthalpy flux and drag parametrisation schemes are available (see Section 3.1.2) and these can be tested easily in order to deduce which formulation is most representative for a given situation.

Moving nests are critical to obtaining significantly enhanced horizontal resolution within the TC vortex without being too computationally costly. The moving nest will be finer resolution than the larger (parent) domain, initially covering a well-defined vortex. The timing

and extent of a nest move is entirely defined by the user, however there is an option for automatic nest moves. The nest automatically moves to maintain the vortex in a central position of the fine grid, using the minimum of the 700 hPa geopotential height field as a reference to where the TC eye is located. The 700 hPa geopotential height is used as default in WRF as at this elevation the circulation and minimum value are generally stronger for less well defined vortices.

There is one-way interaction between the moving nest and the parent domain, so there is no feedback of higher resolution detail to the coarser grid of the larger domains. Even when the nested domain has moved a parent grid-cell distance, the majority of the domain data is still valid away from the nested domain location. Once this occurs, for the outer rows and columns of the nest the data is either discarded on the trailing edge, or horizontally interpolated from the parent domain on the leading edge.

As described in Section 2.1.1, high resolution atmospheric modelling can significantly improve TC simulations. AHW's moving nested domain is one way of achieving a higher resolution without the computing time becoming unmanageable. The domains can be used when the vortex is developing, however the vortex following domain is most reliable for a well-defined TC eye (Skamarock et al., 2008). Therefore, this mechanism should not be used during initialisation.

AHW also provides several options for improving the initialisation of TCs. These include a module for a simple tropical cyclone bogussing scheme (mentioned in Section 3.3.3). This module allows for detection and removal of an existing vortex in the initial fields, and insertion of an idealised vortex based on observational data. Although the scheme is currently set up to only process isobaric data, this technique may provide an improved cyclone initialisation. There is also the option for bogussing a TC using data assimilation techniques; including objective analysis to use extra observational datasets, 3DVAR and 4DVAR of different potential datasets, and ensemble Kalman filters as described in Sections 2.1.2 and 2.1.5.

In this study, the bogus initialisation option was not used. Instead, the circulation included in the initial condition was utilised as the initial vortex. Large TC track and intensity errors can result from poor initial conditions, and different initial conditions dataset were tested. As per Objective three, different start times were also run through the model, to see the impact of slightly different initial conditions on the resultant model outputs.

3.2 The POLCOMS-WAM Model System

3.2.1 Model Description

For the ocean component of this study, the 3D hydrodynamic, baroclinic model POLCOMS (Proudman Oceanographic Laboratory Coastal Ocean Modelling System, Holt and James (2001)) is used, coupled with the third-generation spectral wave model ProWAM (Komen

et al., 1994), known as WAM, modified for shallow water (Monbaliu et al., 2000). This model includes tide and surge modelling capability.

The coupled POLCOMS-WAM system has been developed at the National Oceanography Centre in Liverpool (formally the Proudman Oceanographic Laboratory) and has been used extensively for studies including Bricheno et al. (2013b), Brown (2010), Bolanos et al. (2011). The two-way coupling between these models takes into account wave-tide-surge interaction and the way this is achieved is described in Section 3.2.3.

POLCOMS was originally constructed to study frontal dynamics in the North Sea, and since then has been extensively developed as a hydrodynamic model, with multi-disciplinary applications due to its use of a sediment transport module, incorporation of an ecosystem model (ERSEM - European Regional Sea Ecosystem model), and a sea-ice model (CICE - the Los Alamos Climate Ocean and Sea Ice model). As well as ERSEM, CICE and WAM, POLCOMS has also been coupled to the General Ocean Turbulence Model (GOTM) to allow for the implementation of a range of turbulence models.

WAM was the first third-generation wave model, where the two-dimensional wave spectrum is allowed to freely evolve (up to a certain cut-off frequency) with no constraints on the spectral shape, by calculating the non-linear energy transfers explicitly. ECMWF uses and develops WAM, incorporating the model as the wave component of its ensemble forecasting system. Although other wave models such as WAVEWATCH III and SWAN have become increasingly popular, WAM has been chosen for this study as the model is very similar in approach to the two models mentioned, and has already been coupled to create the POL-WAM system, by local expert scientists and modellers, using a version of WAM optimized for shallow water applications in the EU PROMISE project, called PRO-WAM or ProWAM (Monbaliu et al., 2000).

POLCOMS is a three-dimensional, baroclinic model which may be used both for the deep ocean and continental shelf. Similarly to the WRF model, it solves the Boussinesq equation of motion. However, here the equations are incompressible and hydrostatic. Although this means that the ocean model is simpler than WRF, the level of complexity of the ocean model in this study is appropriate.

In POLCOMS the equations are divided into depth varying and depth independent parts. This is a method for including the vertical structure of the ocean, which is important for determining density variations and their impact on both horizontal and vertical exchange processes (for example, at the air-sea interface), whilst also reducing computational costs. Storm surge forecasting models often use the depth-averaged equations of motion to reduce model run times, however including vertical structure is important to provide a more accurate description of the surface current and current profile and is therefore relevant to include in this study. Also, ultimately it is important to to include 3D baroclinic for temperature and salinity variables in the ocean domain, which fully represent the thermodynamic processes which occur in TCs.

POLCOMS can be set up with a number of vertical levels allowing for accurate representation of depth varying current profile before the depth mean current is calculated. The 3D velocity profile is calculated in the baroclinic mode (with constant density). In the barotropic mode, the depth-averaged shallow water equations are solved, and the sea surface elevation is calculated via:

$$\begin{aligned}
&\frac{\partial \eta}{\partial t} + \frac{\partial}{\partial x}(D+\eta)u + \frac{\partial}{\partial y}(D+\eta)v = 0 \\
&\frac{\partial u}{\partial t} + g\frac{\partial \eta}{\partial x} = fv - \frac{1}{\rho_w}\frac{\partial p_a}{\partial x} + \frac{\tau_{sx} - \tau_{bx}}{(D+\eta)_x} \\
&\frac{\partial v}{\partial t} + g\frac{\partial \eta}{\partial y} = -fu - \frac{1}{\rho_w}\frac{\partial p_a}{\partial y} + \frac{\tau_{sy} - \tau_{by}}{(D+\eta)_y}
\end{aligned} \tag{3.7}$$

where t is time, u and v are the depth-mean velocity components in x and y directions respectively, η is the sea surface elevation, D is the water depth, τ is the surface or bottom stress denoted by the subscript s, or b respectively in the x and y directions, ρ_w is the water density and p_a is atmospheric pressure at sea level.

These governing equations are formulated in spherical polar, terrain-following vertical coordinates and solved on a staggered B-grid. The vertical coordinate is discretised onto levels which vary in the horizontal in sigma-space in a similar way to WRF's terrain-following sigma coordinate (see Section 3.1). The B-grid solution varies from WRF's C-grid formulation. Here, both components of velocity are defined (at so called u-points) half a grid space away from where the scalar variables are defined (b-points). This formulation means that land boundaries (and open boundaries) lie along b-points removing the need for a horizontal boundary condition at the land boundaries. A detailed description of the model physics and dynamics can be found in Holt and James (2001).

ProWAM is a third generation wave model which can be used for both deep and shallow water. The model has flexible spectral and spatial resolution and can either be run globally or regionally with open and closed boundaries.

WAM solves the wave action transport equation (3.8) explicitly without any assumptions on the shape of the energy wave spectrum. The equation is solved in terms of energy to describe the spatial evolution of the energy density spectrum $\mathrm{F}(t, x, y, \omega, \psi)$; where ω is a discrete number of intrinsic angular frequencies, and ψ is the wave direction (measured clockwise from true north).

$$\frac{\partial F}{\partial t} + \frac{\partial}{\partial x}(c_x F) + \frac{\partial}{\partial y}(c_y F) + \omega\frac{\partial}{\partial \omega}(c_\omega \frac{F}{\omega}) + \frac{\partial}{\partial \psi}(c_\psi F) = S_{total} \tag{3.8}$$

Here c_x and c_y are the propagation velocities in geographical space, c_ω and c_ψ are the propagation velocities in spectral space and S_{total} is the resultant action density. The first term on the left-hand-side of equation 3.8 represents the local rate of change of wave energy density, the second and third its propagation in geographical space, the fourth and fifth the shifting in frequency and refraction due to the spatial variation of the depth and current. S_{total}

represents all effects of generation and dissipation of the waves, including energy input from the wind, energy dissipation due to white-capping, non-linear wave-wave interactions, and energy dissipation due to bottom friction. This action density equation is equivalent to the action density conservation equation. This is important as in the presence of currents, wave action and not wave energy is conserved (see Monbaliu et al. (2000)).

Computationally, equation 3.8 is solved in two-parts. First, the left hand side is discretised and solved by setting the right hand side (energy input) to zero and using a first-order explicit upwind scheme. Here, the time step is limited by grid resolution. The source term contribution is then added using a semi-implicit forward time scheme.

The WAM grid may be either spherical polar (latitude-longitude) or Cartesian. The model allows for nested domain with different resolutions, interpolating results as necessary at the grid boundaries. The same interpolation process is used at any open boundaries where boundary conditions, often from coarser models, are provided.

A detailed description of the WAM model can be found in Komen et al. (1994).

3.2.2 Air-Sea Exchange Parametrisation Schemes Available

As described in the introduction, TCs, storm surges and waves are highly interlinked. In the numerical models at the air-sea interface, parametrisation schemes are needed to formulate the theory describing these complex interactions.

POLCOMS can use surface forcing including the air temperature, wind speed and direction, relative humidity, cloud cover, atmospheric pressure, and precipitation. Each of these variables requires a related transfer coefficient to calculate the fluxes of heat, momentum, and evaporation into or out of the ocean domain.

Although the model also includes North Sea specific equations for heat and moisture loss formulated from the North Sea Project (Lane, 1989), the Coupled Ocean-Atmosphere Response Experiment (COARE) bulk formulae Fairall et al. (2003) are generally used to parametrise these atmospheric drivers. The COARE2.5 bulk formulations bring together model results, theory, and observations, to provide transfer coefficient equations. The equations are commonly used in ocean models for heat and moisture fluxes, and give good results in a wide range of situations, except the most extreme (e.g. tropical cyclones).

For the air-sea momentum flux there are three parametrisation options which POLCOMS provides. These are the COARE bulk formulae as mentioned above, the Smith and Banke method (Smith and Banke, 1975), and the Charnock relation (Charnock, 1955).

The Smith and Banke formulation uses a wind-dependent drag coefficient:

$$C_d = (0.63 + 0.066W_{10}) * 10^{-3} \tag{3.9}$$

As the equation shows, this is a linear relationship with the drag coefficient increasing with wind speed. This parametrisation formula was calculated from observations of the surface wind stress using eddy correlation and dissipation method from the turbulent velocity fluctuations. In storm surge models, this formula has been found to under-predict the surge conditions (Flather and Williams, 2000; Mastenbroek et al., 1993). This formulation is not used in this study, as it does not take into account the wave field modelled using WAM.

The Charnock relationship is a parametrisation which relates the drag coefficient to the Charnock parameter $\hat{\alpha}$, as described in equation 1.20 in Section 1.4. In POLCOMS, this option requires a constant Charnock parameter value which is one of the model input fields. This allows for the Charnock value to be tuned to obtain the desired results at a certain location. However, the optimal value may vary with location (see Wolf and Flather (2005) and Brown and Wolf (2009)).

The WAM model uses a wave-related surface roughness to calculate the Charnock parameter (Brown and Wolf, 2009). This 'wave-age' dependent Charnock parameter varies in time and space dependent on the age of the sea with young seas have smaller values than older seas (Drennan et al., 2005; Janssen et al., 2004). In WAM, the Janssen (1991) method for predicting the effective roughness length z_e of the sea surface is used:

$$W(z) = \frac{w_*}{\kappa} ln \frac{z + z_1}{z_0 + z_1} \tag{3.10}$$

where κ is the von Karman's constant. It assumes the wind profile has a logarithmic shape for all sea states.

The $W(z)$ profile depends on a background roughness z_0, which accounts for processes such as flow separation that are not considered explicitly. This roughness length is parametrised by a Charnock equation:

$$z_0 = \frac{\hat{\alpha} w_*^2}{g} \tag{3.11}$$

where $\hat{\alpha}$ is constant related to the Charnock parameter. z_1 is the roughness length due to (short) gravity waves, and the effective roughness length is $z_e = z_0 + z_1$. This is calculated in WAM by the Charnock like relation:

$$z_e = \frac{\alpha w_*^2}{g}, \text{ where } \alpha = \hat{\alpha} / \sqrt{1 - \frac{\tau_w}{\tau_s}} \tag{3.12}$$

where τ_w is the wave stress and τ_s is the total wind stress given by:

$$\tau_s = \rho_a w_*^2 = \rho_a C_d W_{10}^2 \tag{3.13}$$

as detailed in Section 1.4.

This wave-age dependent Charnock parameter has been validated for the Irish Sea in Brown and Wolf (2009) and in the Mediterranean by Bolanos et al. (2011). In both of these studies, the formulation was tested with extra-tropical storms rather than TCs. All of the

available options suffer from the limitation described in Section refsec:param, where a linear equation for the drag coefficient is not appropriate for very high winds speeds. However, the WRF model will take into account this relationship and therefore, the impact on the wind velocity used at the atmospheric boundary is included in the study. The wave-age dependent Charnock parameter formulation is used in this study, as the most appropriate available parametrisation scheme.

As yet, a parametrisation scheme of sea spray processes is not available in the coupled ocean modelling system and, therefore, will not be included in this study.

3.2.3 Wave-Ocean Coupling

POLCOMS and WAM were first coupled (Wolf et al., 2002) in order to investigate the interaction between the wave and ocean dynamics in enclosed seas and on the continental shelf. They are two-way coupled to consider several processes: wave refraction by time-varying water depth and currents, bottom friction due to both currents and waves, and enhanced wind drag due to waves (Osuna and Wolf, 1994). These mechanisms have important impacts on a number of processes such as sediment transport, dynamics of nutrients and pollutants, and the movement of larvae, for example.

Bolanos et al. (2011) further improved the coupled system by including Stokes' drift and radiation stress, therefore wave induced currents and wave set-up are included as well as the Doppler velocity effect of the vertical current profile on the wave spectrum.

When the coupled model link module is activated by the user, different levels of interaction between POLCOMS and WAM are available at runtime. These include one way coupling, where the effects of currents on the waves is taken into account, but not the reverse; two way coupling, where the currents affect waves as in one-way coupling, and the waves affect the currents via wave-dependent sea-surface drag coefficient and bottom drag coefficient; and 3D two-way coupling, where as well as the interactions described in two-way coupling, the effect of Stoke's drift due to waves and the radiation stress are included in POLCOMS.

POLCOMS and WAM are coupled in a three-dimensional (two-dimensions for the radiation stress is recommended), two-way mode via a wave current interaction module. This module allows for the synchronous exchange of information between the models: the wave model is embedded within the baroclinic step of POLCOMS. This is implemented by POLCOMS including a WAM module, so the wave model can use the same bathymetry and wind information supplied to the hydrodynamic model. The model time steps are independent of each other, but as the wave model is included in the baroclinic step of POLCOMS, WAM time stepping must be an integer ratio of the POLCOMS baroclinic time step.

Data sent from POLCOMS to WAM include the barotropic and bottom current components, water depth, and time-interpolated wind components within a moving framework according to the barotropic current components.

The amount of inhomogeneity and unsteadiness in the current field affects the propagation of wave energy and refraction. To account for this impact of currents on waves, the barotropic and bottom layer current components (u, v) and total depth (h) are passed from POLCOMS to WAM, and updated every baroclinic time step. The grid of current values at nodes (i, j) in POLCOMS are imposed on the corresponding (i, j) nodes of the wave model. Once the values are transferred, they are used to compute kinematic wave parameters (i.e. the group velocity and wave number), which again are updated for every new value passed from POLCOMS. The wave energy refraction in spectral space is evaluated internally by the wave model.

Time interpolated 10 m wind components, (W_{10}^x, W_{10}^y), are also transferred from POLCOMS to WAM. Once passed to WAM these values are transformed to a moving frame of reference according to:

$$U_{10}^x = W_{10}^x - u \quad ; \quad U_{10}^y = W_{10}^y - v \tag{3.14}$$

where (u, v) are the barotropic current components. The bottom layer current components are also transferred in order to compute bottom friction in a combined wave-current flow using the Madsen formulation (Madsen, 1994).

As described in the previous section, the wave-dependent drag coefficient can be calculated as part of the ocean-wave coupling. In the coupled system, the drag coefficient is calculated as:

$$C_d = \Big(\frac{\kappa}{ln(10/z_0)}\Big)^2 \tag{3.15}$$

using equation 3.12 to define the roughness length dependent on the wave field. The use of the wave induced roughness length allows the affect of waves on the total water level to be included. The wave induced stress τ_w needed for equation 3.12 is computed in WAM by integrating the wave input source term, S_{in}:

$$\tau_w = \rho_w \int_0^{\infty} \int_0^{2\pi} c^{-1} S_{in}(\omega, \psi) d\omega d\psi \tag{3.16}$$

where c is the phase celerity of the waves and ρ_w is the water density. The implementation of this theory in WAM is described in Mastenbroek et al. (1993).

A similar approach to Souza et al. (2001) is used for the effect of wave-current interaction at the bottom. The current induced bed shear stress is computed as:

$$\tau_c = \frac{1}{2}\rho_w f_c u_b^2 \quad ; \quad f_c = \Big[\frac{\kappa}{ln(30 z_r/k_{bc})}\Big]^2 \tag{3.17}$$

In this equation z_r is a reference height, and k_{bc} is the apparent roughness felt by the current due to the presence of wind waves. When the effect of wind waves is small, this equation becomes the expression implemented in POLCOMS (Holt and James, 2001) as $k_{bc} = K_N = 30 z_0$

(where K_N is the Nikuradse length scale and $z_0 = 0.003$m is the roughness length at the bottom). When the effect of the wind waves on the bottom is larger, an apparent roughness length, z_{0a}, is used for the definition of k_{bc}. This is computed using the formulation of Madsen (1994) for the solution of a combined wave-current bottom boundary layer flow.

Osuna and Wolf (1994) implemented the POLCOMS-WAM modelling system for the Irish Sea, and found that wave-current coupling produced differences of up to 15% in significant wave height, associated with currents and wave travelling in opposite directions. They showed that changes in mean wave period due to Doppler shifting reached 20%. The impact of waves on the currents was less evident, with a validation point at 23 m depth showing little effect.

Brown and Wolf (2009) used the POLCOMS-WAM system for storm surge modelling, again in the Irish Sea. They showed an improvement of the prediction when implementing the wave-dependent Charnock parameter and using Janssen (1991).

3.3 Modelling System Set-up

The models used in this study have been described in the previous sections. The variables which are passed between the different models are shown in Figure 3.3.

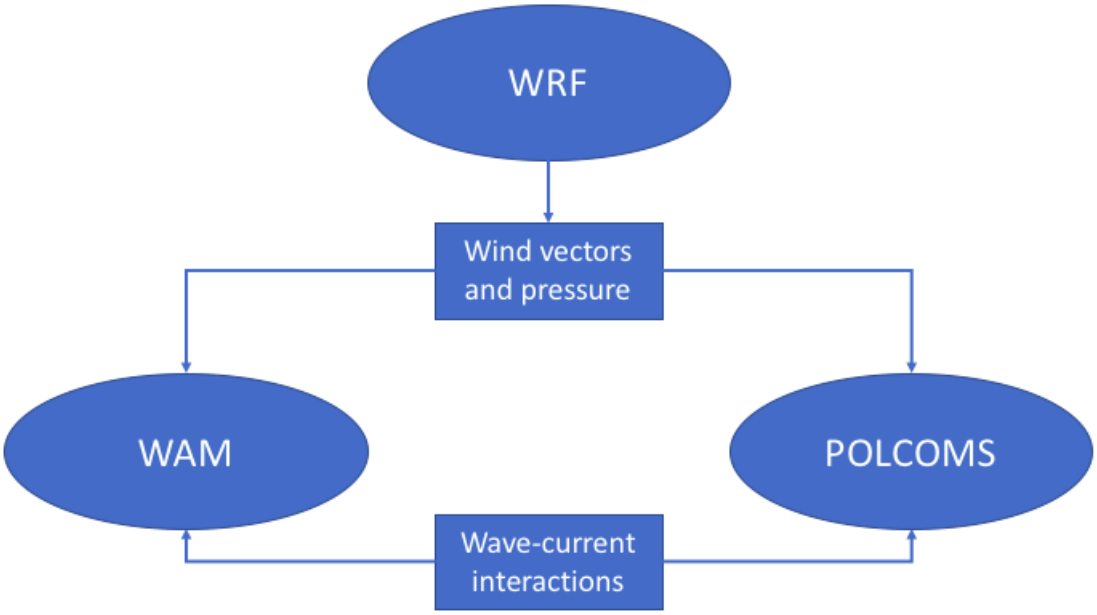

Figure 3.3: The ocean-wave-atmosphere interactions of this study. Arrows represent the variables passed between the models.

Here, the model system set-up for the BoB with a case study of cyclone Phailin is presented, with details about the domains, parametrisation schemes, initialisation, and boundary conditions which have been chosen.

3.3.1 The WRF Domains

For the WRF model of the Bay of Bengal, a large, 12 km resolution domain covering the northern Indian Ocean and surrounding countries was created, from latitude 0.4763°S to 29.4373°N and longitude 76.4287°E to 105.5713°E (see Figure 3.4). For higher resolution simulations of tropical cyclone Phailin, the moving nest capability of WRF was used.

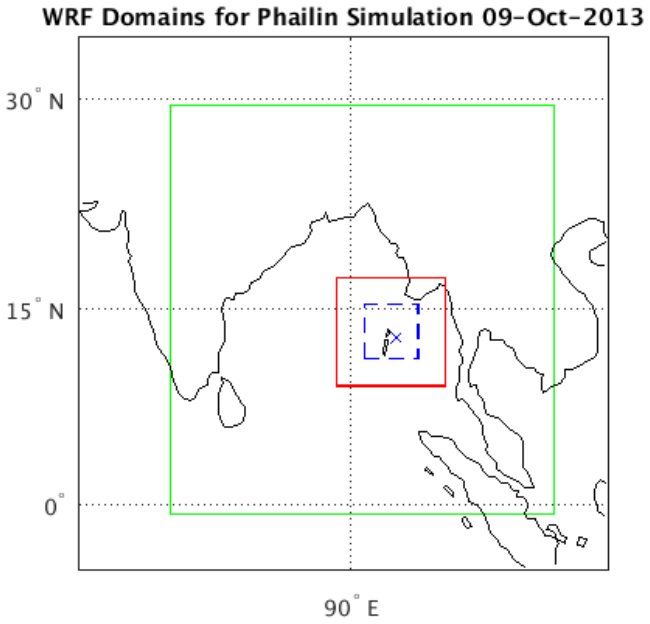

Figure 3.4: The initial locations of the 4 km (red) and 1.3 km (blue) nested domains within the parent domain (green) for the WRF simulation of TC Phailin. The x marks the observed centre of Phailin from the IMD IBTrACS data at 0000 UTC 9 October.

A triple nesting approach was taken with the large domain described above as the stationary parent domain, and two moving nests, one with resolution 4 km and one with resolution 1.3 km. This agrees with NCEPs advice that the ratio between a nested domain and its parent should be around 3:1 and is also the same resolution set up as Davis et al. (2008a) and Davis et al. (2010a). The 1.3 km grid was centred within the 4 km grid. The initial locations and sizes of the nested domains are shown in Figure 3.4.

The size of the domains is likely to have a non-negligible effect on the simulated TC. Goswami and Mohapatra (2014) investigated the impact of domain size on TC simulations in BoB. The parent domain used here is larger than any of those previously tested in order to limit the impact from the boundary data.

At 0000 UTC 9 October, the observational data shows that the circulation centre is at 13.0°N and 93.5°E, as shown by the x in Figure 3.4. The initial nest locations were chosen to cover this location.

The location of the circulation centre in the initial conditions (see Section 3.3.3) is in-

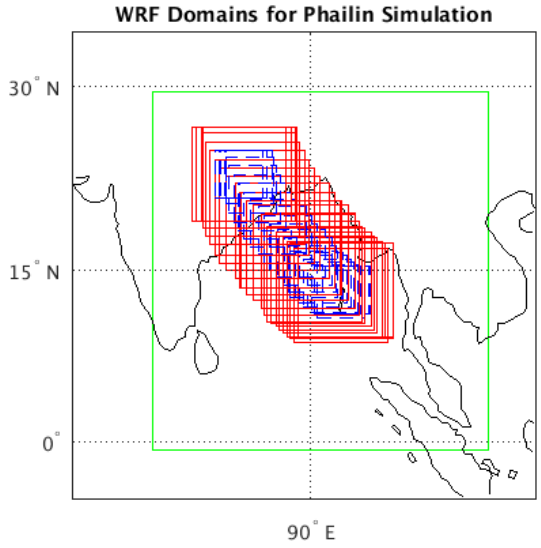

Figure 3.5: The locations every fifth movement of the 4 km and 1.3 km nested domain for the WRF simulation of TC Phailin.

terpolated by the WRF model to slightly different locations depending on where the nested domains are. For the start location described above, the initial centre is at 13.06°N and 92.99°E, which is well within the nested domains. This needed to be checked in order to make sure that all nest movement is related to the movement of the vortex (and not another low pressure point).

Figure 3.5 shows the movement direction of the telescoped nested domains during the WRF run. It shows that they followed the simulated cyclone track, thus fulfilling the high resolution requirements in this area.

Each domain has 35 vertical layers and a time step of 36 seconds is used for all simulations.

3.3.2 The POL-WAM Domain

A domain covering the Bay of Bengal was also required for POL-WAM, which matches the size and resolution of the largest WRF domain as closely as possible. This was not exactly possible, as WRF's resolution and domain size are defined in kilometres, whereas in POL-COMS they are defined in degrees latitude and longitude. Because of this and in order to use WRF as forcing for the entire domain, the POLCOMS domain was slightly smaller than the WRF parent domain. The domain chosen is shown in Figure 3.6.

As this is a new grid which had not been used before it was important to thoroughly test the domain for any singularities or problems that may arise when running the model. In order to do this, different elements were introduced one by one, in order to make sure they were working correctly and the outputs produced were as expected.

The POL-WAM domain requires input for bathymetry in the form of gridded depths.

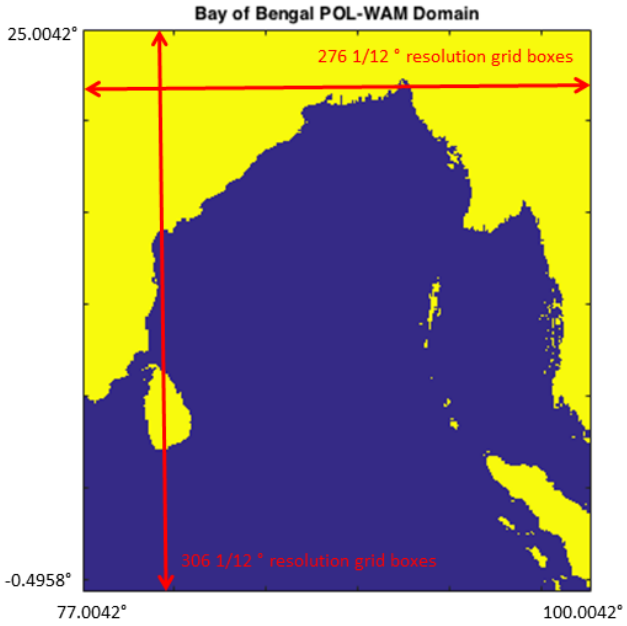

Figure 3.6: The POLCOMS-WAM domain (in dark blue).

This data was obtained from the publicly available GEBCO 08 (GEneral Bathymetric Chart of the Oceans) global dataset which is held by the British Oceanographic Data Centre (BODC). This data has a grid spacing of 30 arc-seconds and was generated using ship-track soundings and satellite-derived gravity data, amongst other methods, interpolating between observations.

As running a model domain the size of the Bay of Bengal at 1 km resolution would be very computationally expensive, this fine resolution bathymetry data was subsampled every 12 km (shown in Figure 3.7). Ideally, the 1 km resolution would be used throughout, or a fine resolution nest would be used. However this would be more computationally expensive and was not included at this stage of the project.

The number of vertical layers chosen for this study is 12. This is the same number of vertical levels as the Irish Sea POL-WAM modelled used in Bricheno

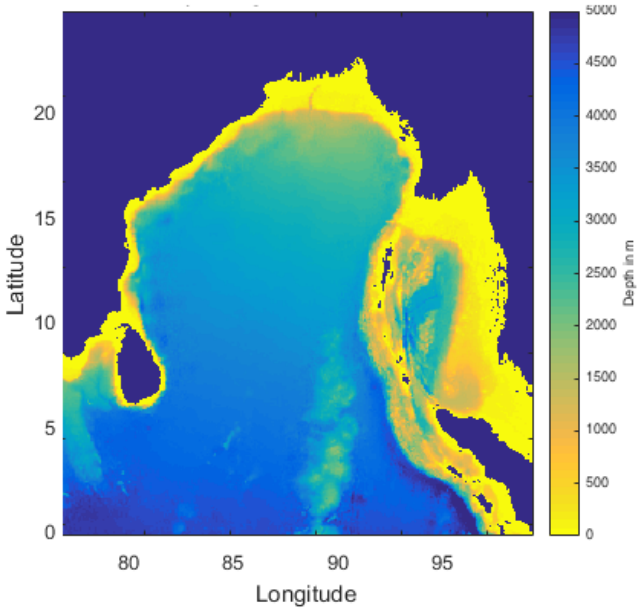

Figure 3.7: The POLCOMS-WAM domain bathymetry in metres.

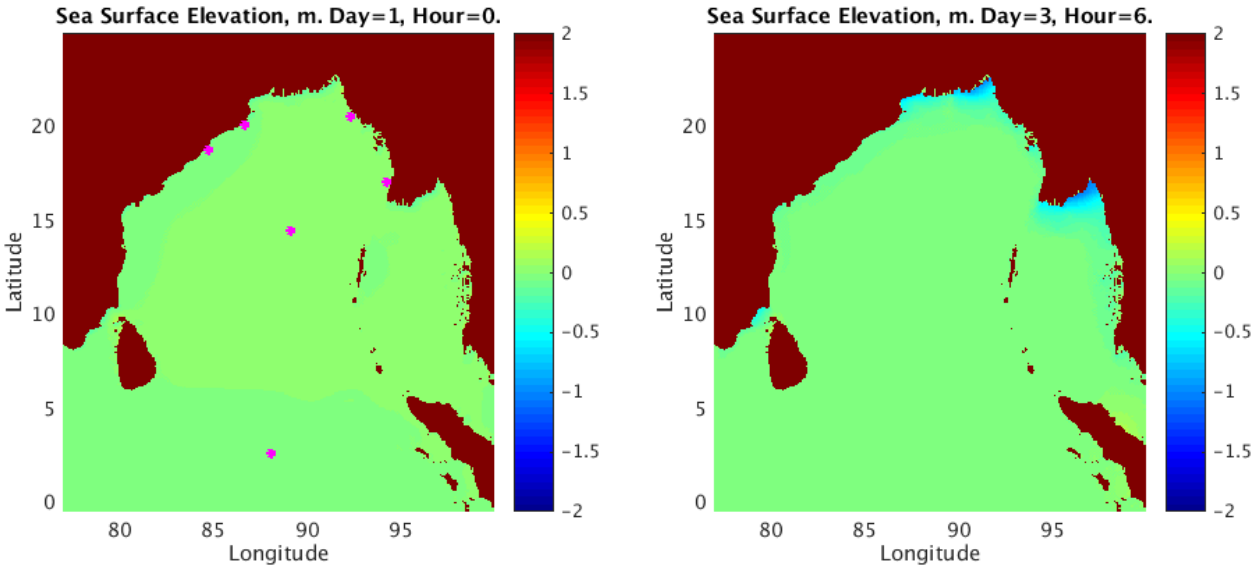

Timestep 1 Timestep 55

Figure 3.8: Snapshots of sea surface elevation from the POLCOMS sensitivity test without tide or wave dynamics, with Timestep 1 and Timestep 55 showing the first and last model frames, respectively. The magenta stars in Timestep 1 show the locations of the time series points for Figure 3.19.

et al. (2013a); Brown (2010), and allows for a fully three-dimensional simulation to be run without overly complicated the vertical dynamics and causing increased computation run times.

A minimum depth of 10 m was applied to the domain shown in Figure 3.7. This allows for representation of coastal bathymetric features, but prevents numerical instability due to drying areas occurring in the model domain as a consequence of tidal variation. Use of the 'wetting and drying' scheme described in Section 3.2.2 would eliminate the need for a minimum depth, however this was beyond the scope of the study.

To test the domain created, initial runs were completed using simplified versions of POLCOMS. Firstly, temperature and salinity were turned off, so the model is purely a dynamical one. All boundary forcing was removed, the WAM coupling was switched off, and the model ran from stationary initial fields with constant meteorological forcing. This tests that the meteorological boundary forcing files were formulated and input correctly, and that the domain's response was in line with the output expected.

As expected, the sea surface elevation changes very slowly using a steady north-west wind, chosen as one of the predominant monsoon wind directions. This can be seen in Figure 3.8 Timestep 55 with the majority of the domain's sea surface height remaining the same, only decreasing in sheltered locations (negative surge).

The WAM coupling was added next, testing both one-way and two-way wave-ocean coupling. Here, the two way coupling output is presented (one-way not shown). Significant

wave height, wave speed and wave direction at different time steps from the simulation are shown in Figure 3.9.

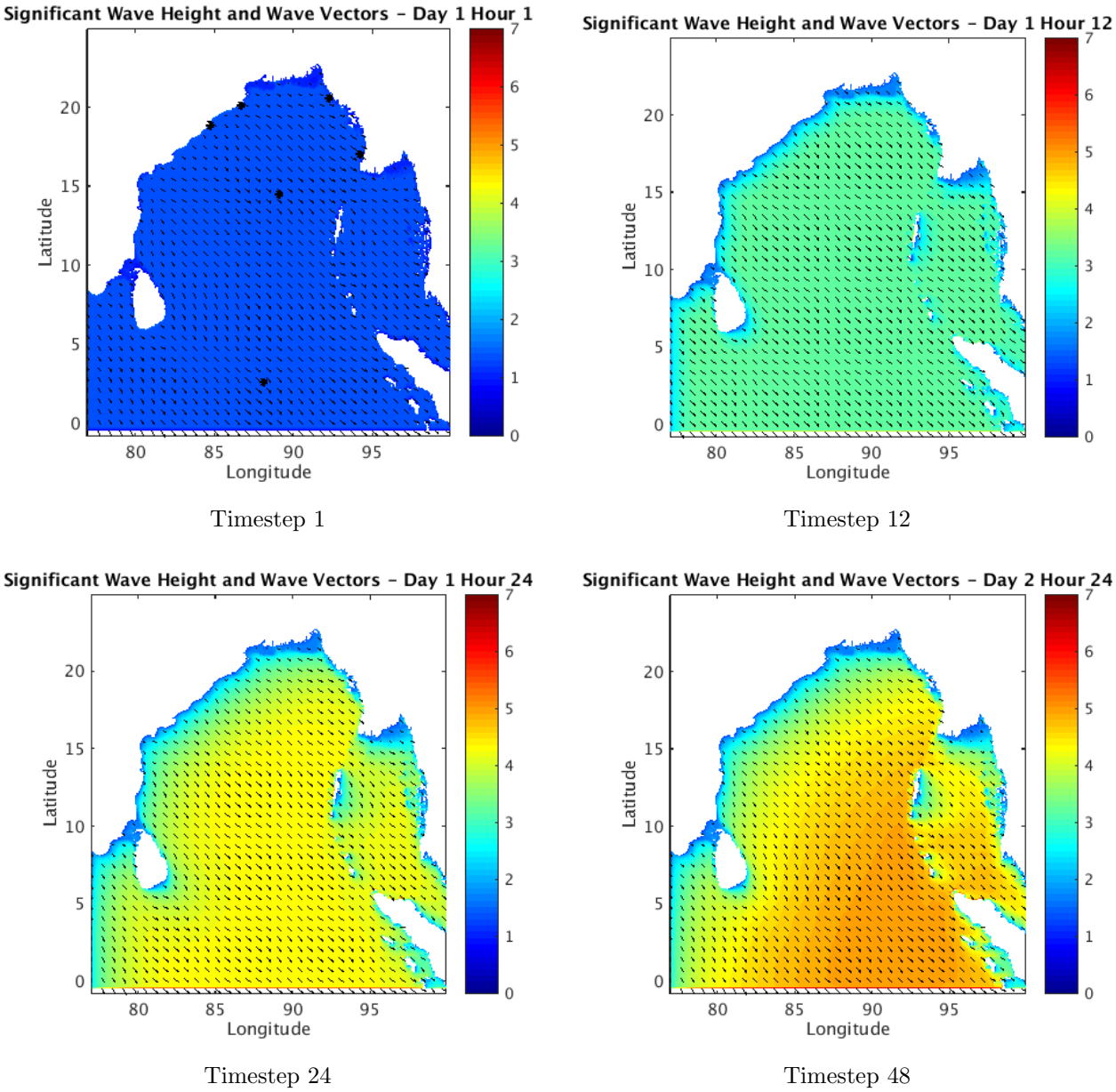

Timestep 1 Timestep 12

Timestep 24 Timestep 48

Figure 3.9: Snapshots of significant wave height from the POLCOMS-WAM sensitivity test, without tide dynamics, at four different output times throughout the simulation. The black stars in Timestep 1 show the locations of the time series points for Figure 3.19.

As the meteorological forcing includes a constant north-westerly wind, the expected result is that the significant wave height will increase towards the southeast. This highlights the fetch effect of wave generation. This is confirmed by the model run, with higher significant wave heights in the southeast of the domain at the end of the simulation. The figure also shows sheltering behind islands including Sri Lanka, the Myanmar peninsula and the

Andaman and Nicobar Islands, as well as slight wave refraction around land features. This is result expected, suggesting that the waves are being formulated with the correct dynamics.

Additional domain tests (not shown) were completed including varying each of the meteorological parameters, testing different boundary types, and testing the dynamical calculations. These initial tests allowed the created model domain to be tested for functionality and realistic simulation outputs. Therefore, the domain described was taken forward and used in the main numerical experiments.

3.3.3 WRF Initial and Boundary Conditions

In order to establish the most suitable atmospheric initial and boundary conditions available for the WRF numerical experiments simulating Cyclone Phailin, two different datasets were tested. ECMWFs ERA-Interim reanalysis dataset and the NCEP's GFS (Global Forecast System) global model analysis fields were chosen to this end, as both datasets are open-source, easily accessible, and included in WRF preprocessing module WPS (WRF Preprocessing System).

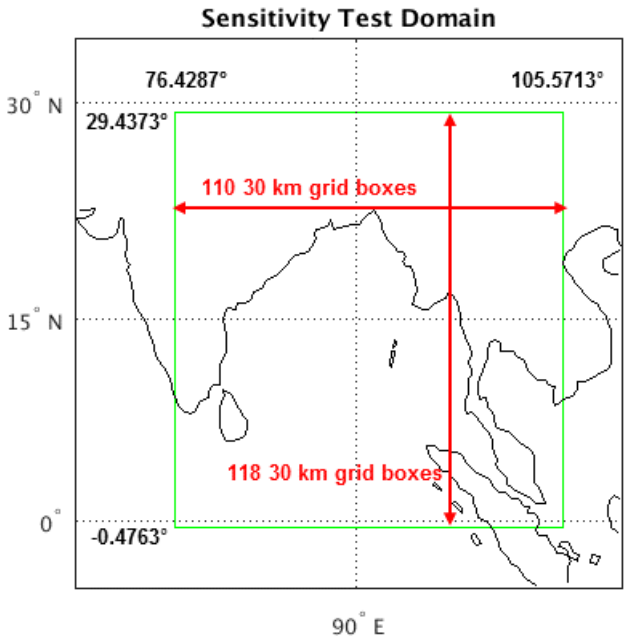

Figure 3.10: WRF domain used for initial testing.

The ERA-Interim data used has spatial resolution T255 (triangular truncation at 255), which is grid spacing of roughly 1.5° latitude in the Bay of Bengal domain, and 37 vertical levels. The temporal grid spacing is 3 hours. The reanalysis data is produced by combining model information and many different types of observations to make a consistent, global best estimate of the meteorological parameters. Dee et al. (2011) gives a complete description of

the ERA-Interim reanalysis dataset.

NCEP's GFS model has a spatial resolution of 0.5° with 64 vertical levels. GFS is a spectral numerical model run by the United States' National Weather Service, which produces forecasts for up to 16 days in advance. Here, for this study, just the analysis fields are needed. These are created by the Global Data Assimilation System (GDAS), which uses satellite and other conventional global observations to generate the initial conditions for the global forecasts. The global model is run 4 times a day and so analysis fields are available every 6 hours.

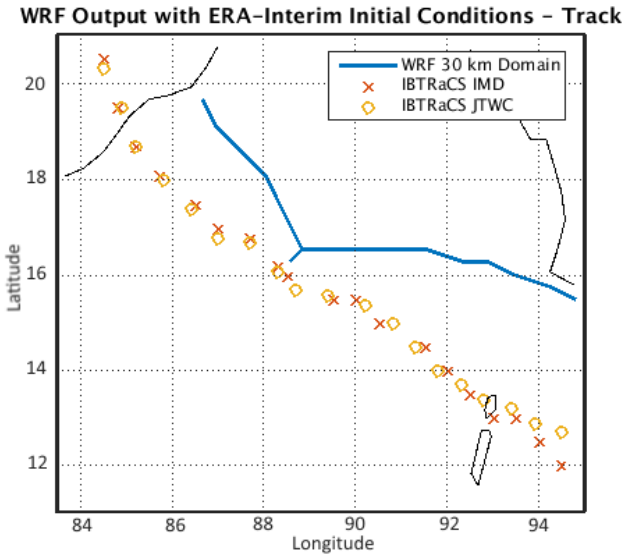

Figure 3.11: The track of the WRF simulation using ERA-Interim as initial conditions. The yellow circles represent the JTWC observed data, and the orange crosses show the IMD observations.

For both datasets, the model was run from 1200 UTC 8 October 2013 to 1200 UTC 14 October 2013. According to the IBTrACS, at the initial time the cyclone is categorized as a depression with wind speed of 12 ms^{-1} and minimum pressure of 1000 hPa. This time was chosen provisionally, as the most rapid intensification occurs on the 10 October, and so could be captured in the model simulation thus indicating the potential skill of the simulation. For each initial condition dataset the model was run using the parent domain described in Section 3.3.1 with a resolution of 30 km instead of 12 km, to enable shorter model run times. This domain is shown in Figure 3.10.

The parametrisation schemes chosen were the same as those used in the parent domain in Davis et al. (2008a), as these have been shown to be the most applicable to tropical cyclones. These include the Kain-Fritsch cumulus parametrisation (Kain, 2004), the WRF single-moment 3-class microphysics scheme (Hong et al., 2004) which uses one cloud phase variable and one precipitation variable (water/rain for T >0 °C and ice/snow for T <0 °C), and the Yonsei University scheme for the planetary boundary layer (Noh et al., 2003) which uses a first-order closure scheme. The drag formulation followed the theory in Charnock (1955), the heat flux used a similarity relationship (Skamarock et al., 2008), and the surface exchange coefficients for water vapour followed Carlson and Boland (1978).

The first run was completed with initial meteorological fields from the ERA-Interim data. The maximum wind, minimum pressure and storm track output from this first experiment can be seen in Figures 3.12 and 3.11.

The output values were compared with the IBTrACS data from both the IMD and JTWC. It is obvious from the figures that the tropical cyclone simulation is very weak. In fact, the

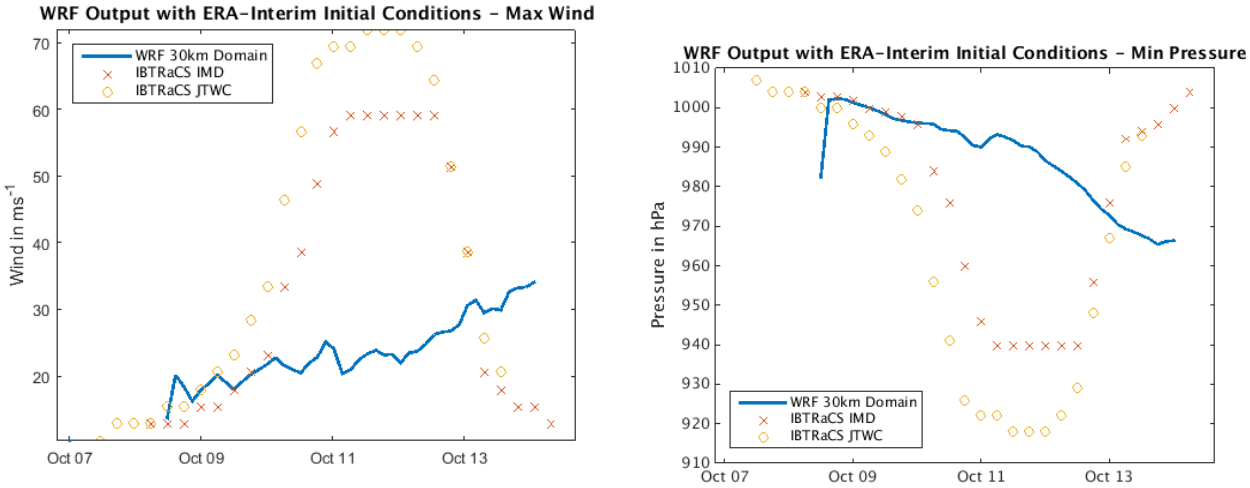

Figure 3.12: The maximum wind (left) and minimum pressure (right) WRF output using ERA-Interim as initial conditions. The yellow circles represent the JTWC observed data, and the orange crosses show the IMD observations.

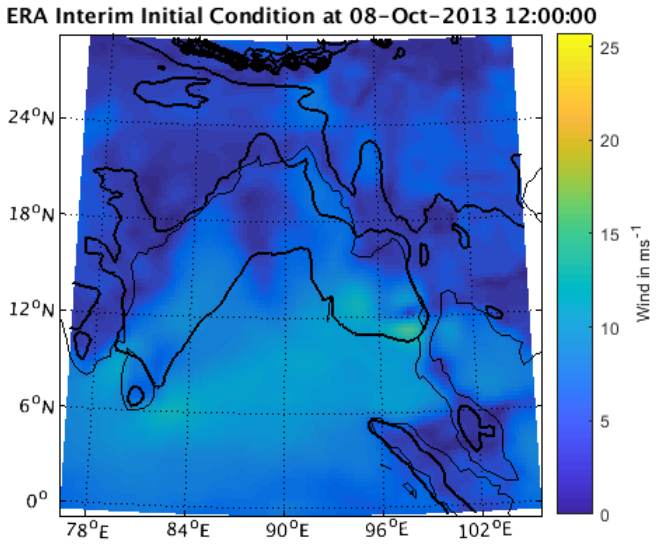

Figure 3.13: Initial conditions using the ERA-Interim fields. The colours show the wind speed in ms^{-1}, and the lines show the mean sea level pressure.

plots suggest that tropical cyclogenesis does not occur at all. The maximum wind throughout the run is 30 ms^{-1}, which is less than half the 59 ms^{-1} and 72 ms^{-1} maximum wind recorded in IBTRaCS. Similarly, the minimum pressure during the run is 973 hPa, much higher than 940 hPa and 918 hPa from IMD and JTWC respectively. Likewise, the track (based on the location of the lowest pressure in the domain at each time step) has large errors, never reaching land even after several days, shown in Figure 3.11.

The poor results obtained from using ERA-Interim initial conditions are most likely due to the coarse resolution of the reanalysis data. Due to the coarse resolution, the eye of the cyclone and eyewall structure is not well resolved in the ERA data, thus impacting the WRF simulation. Numerical convergence tests using mesoscale models suggest that a resolution less than 1 km may be required to simulate the complex inner core (see Section 2.1.1 and Emanuel et al. (2008)). Typically, reanalysis datasets do not have the fine resolution required (Murakami, 2014). In the initial field (see Figure 3.13) of the ERA-Interim data, only a very weak cyclone is represented in the data. This demonstrates the difficulties with initialisation of modelled tropical cyclones, as discussed in Section 2.1.2. Different start times were tested with very similar results (not shown).

A new approach had to be trialled: using the finer resolution GFS model analysis data. As the resolution is higher, the use of GFS for initial conditions were expected to improve the simulated cyclone.

The results from this second experiment can be seen in Figures 3.15 and 3.14. Intensification occurs much more rapidly and deeply than with the ERA-Interim initialisation, with pressure decreasing from 1000 hPa at the beginning of the simulation down to 940 hPa at 0000 UTC 12 October in line with the IMD lowest observed pressure of Phailin. Although the rate at which the deepening occurs is not exactly in line with the observations, the increase of pressure once the cyclone has made landfall is in line, showing very promising results. The maximum wind values have larger errors, although better than the ERA-Interim initialisation, with a maximum wind of 42 ms^{-1} during the run. Similarly, the track from WRF initialised with the GFS data, shown in Figure 3.14, has smaller errors than ERA-Interim, and actually make landfall (although in the wrong location).

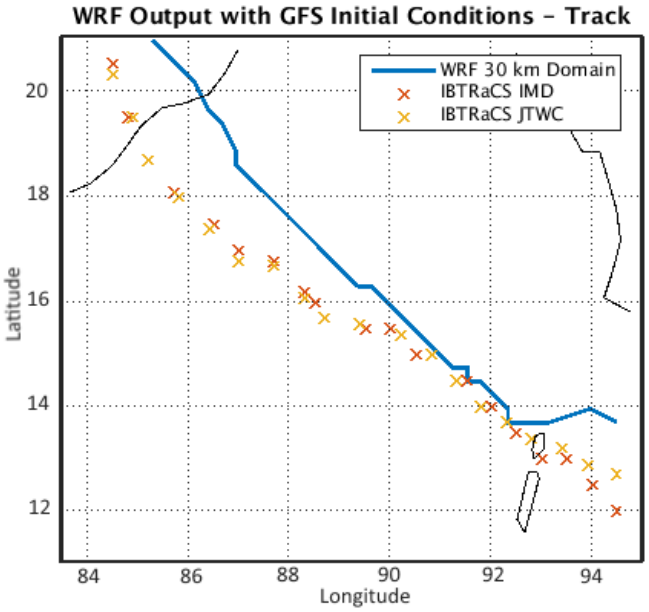

Figure 3.14: The track of WRF simulation using GFS Analysis as initial conditions. The yellow circles represent the JTWC observed data, and the orange crosses show the IMD observations.

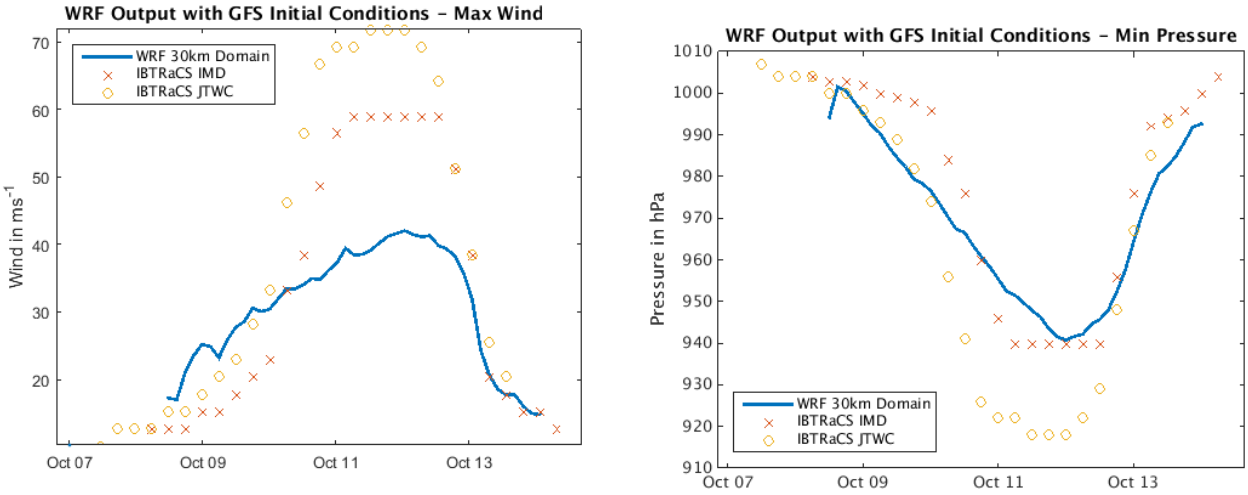

Figure 3.15: The maximum wind (left) and minimum pressure (right) WRF output using GFS Analysis as initial conditions. The yellow circles represent the JTWC observed data, and the orange crosses show the IMD observations.

The improved results obtained using GFS initial and boundary conditions is due to the finer resolution of the initial field. The initial field shows stronger winds and a more well defined low pressure circulation (see Figure 3.16), therefore it is unsurprising that the simulation is much more realistic. The larger errors in wind may be related to the resolution of the WRF simulation itself. A grid spacing of under 4 km is needed to explicitly resolve convection and the dynamics of the stronger winds of Phailin are associated with this.

Although not perfect, this simulation showed that using GFS data both as initial conditions and at the boundary is most suitable for the main numerical experiments.

As a result of the sensitivity tests, the data used for both the initial and boundary conditions are the GFS analysis fields. As mentioned previously, the data have a spatial resolution of 0.5° with 64 vertical levels and temporal resolution of 6 hours. Their use as boundary conditions should only impact the simulation near to the edges of the parent domain, which was made large enough so that these potential effects were not near the location of interest - the tropical cyclone and its centre.

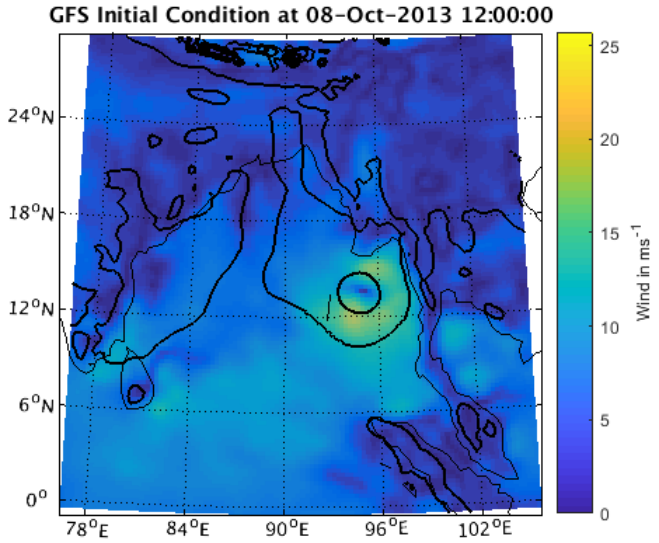

Figure 3.16: The initial conditions using the GFS Analysis fields. The colours show the wind speed in ms^{-1}, and the lines show the mean sea level pressure.

3.3.4 POL-WAM Initial and Boundary Conditions

As with the WRF model domain described in the previous section, the POL-WAM Bay of Bengal model needed an initial state and input at the boundaries. This section will describe the boundary and initial conditions used in this study.

Generally, POLCOMS simulations start with a level sea surface ($u = v = \eta = 0$). When the model has been run through once, a restart file can be created, which is then used to initialise the model currents and sea surface elevations. This is a robust way of spinning up the ocean domain, then outputting the steady state reached for future model runs.

In the set-up used for this study, temperature and salinity parts of the POLCOMS model were not used, therefore, initial and boundary values of these variables were not required. The open boundary forcing which can be input into POLCOMS consists of elevation and barotropic currents (tidal and residual, or combined together). For the present study, only the tidal currents and elevations are used. The tidal boundary condition is important to be included in the main experiments for two reasons. The first is in order to validate the model against observational data. As mentioned in Section 3.4.2.2, tide gauge data is available for one of the coastal areas affected by Phailin. To have a model simulation that is comparable to this data, the tides must also be included, otherwise errors may occur. The second reason is that tide-surge interaction plays an important role in surge dynamics and their prediction. As described in Section 1.3, tide surge interaction occurs due to changing the water depth, and therefore impacting the wind stress term in the shallow water equations. Also the total water level is composed of both the tide and the surge.

Figure 3.18: Locations of the time series shown. Paradip is at A, and Gopalpur is labelled B.

The TPXO 7.2 inverse tidal model was used to create the tidal boundary forcing. TPXO is a global model of tides which best fits, in a least squares estimate, the Laplace tidal equations and along-track averaged data from TOPEX/Poseidon and Jason satellites. The methods used in the model can be seen in more detail in Egbert et al. (1994).

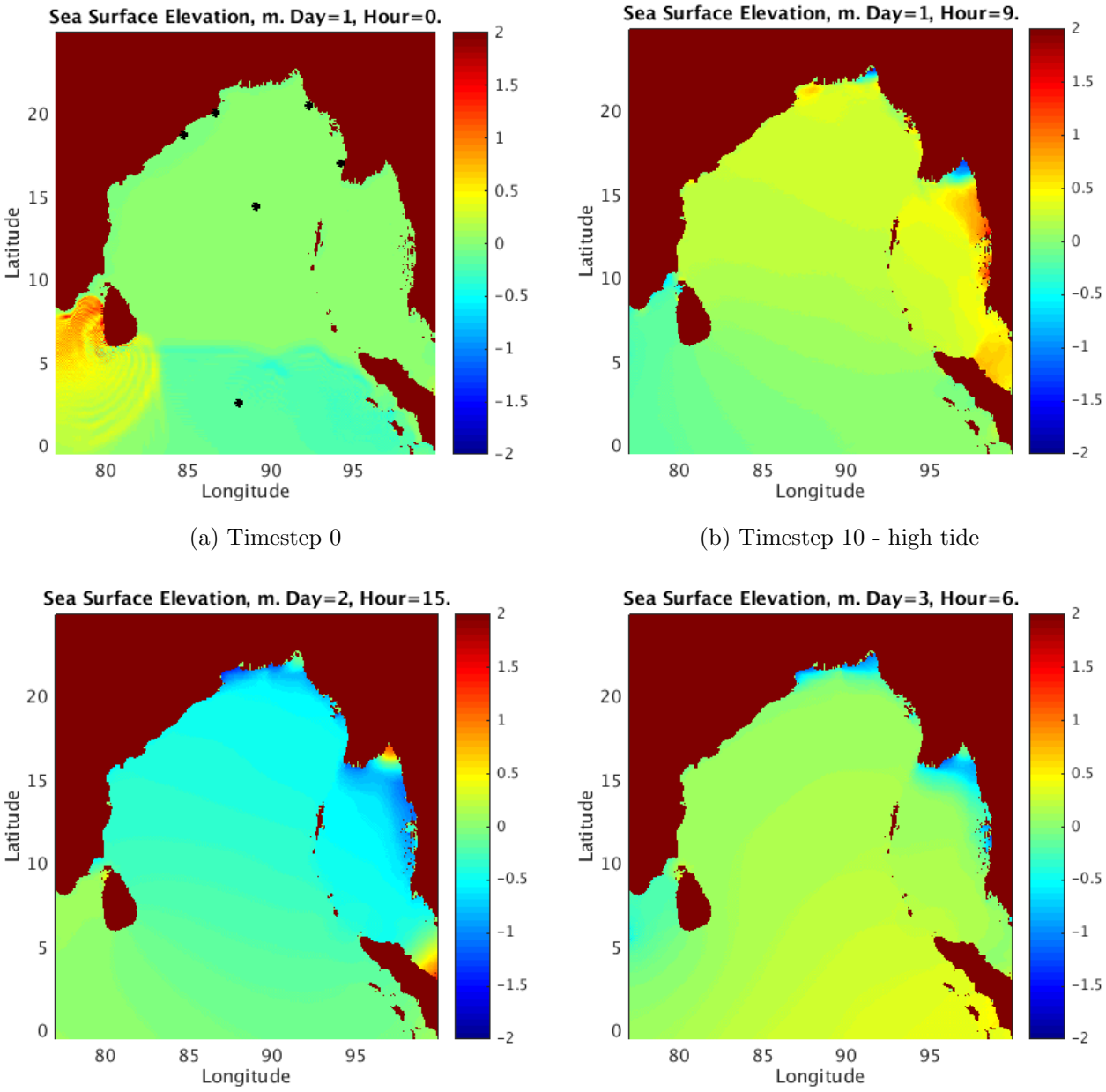

(a) Timestep 0

(b) Timestep 10 - high tide

(c) Timestep 40 - low tide

(d) Timestep 55 - midway through the tidal cycle

Figure 3.17: Snapshots of sea surface elevation from the tide only POLCOMS test at various different model times showing different parts of the BoB tidal cycle. The black stars in Timestep 0 show the locations of the time series points for Figure 3.19.

The model output includes 8 harmonic constituents of the tide, and is provided as complex amplitudes of earth-relative sea-surface, which are then converted to a time series of sea surface height and tidal velocity along the domain's open boundary.

In order to check the tidal processes within the model, an initial POLCOMS run was undertaken with just the tidal forcing as an input. Figure 3.17 shows snapshots of sea surface elevation at different time steps through the tidal simulation. The initial timestep in Figure

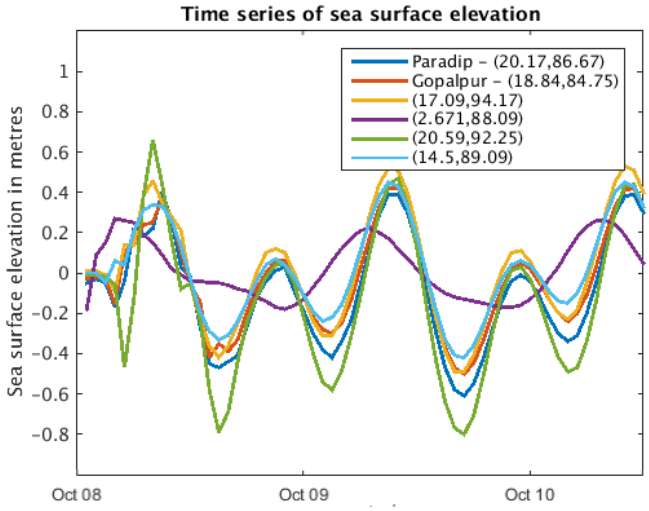

Figure 3.19: Time series of sea surface elevation for different locations within the BoB Domain (see Figure 3.18 for the point locations).

3.17 (Timestep 0) shows oscillations in the output fields near to the south coast of India and Sri Lanka. After several model timesteps, the output fields do not show this divergence in sea surface elevation values.

In Figure 3.19, time series of sea surface elevation at various location in the domain are shown. The locations of the output points for the time series shown can be seen by the black stars in Figure 3.17 - Timestep 0, and more clearly, by the markers in Figure 3.18. The time series show the initial instability in the model outputs, but after several model hours of spin up time a steady state solution is reached. Here, the spin up period is roughly 24 hours. Therefore, a restart file of this steady state was created to initialise future simulations by outputting the ocean variables at timestep 24. The restart initial condition variables include the sea surface elevation and barotropic tidal currents.

Figure 3.19 also show the different tidal regimes from across the BoB. At the northern coast there is a semi-diurnal tidal regimes, however to the south of the bay this is a diurnal tide. The different tidal regimes will have different impacts on the tide-surge interactions. This concept is not included as part of the current study, but may be of interest for further work.

The restart file created was tested to make sure the spin-up time is long enough and the main experiment simulations begin with steady state conditions. Figure 3.20 shows the output from this restart test. Here, the sea surface elevation time series shown is much smoother, confirming that a steady state tide has been achieved. This confirms that the restart file is appropriate and working as expected, and the file will be used in the main experiments.

Initialisation of the WAM module is also important. The standard WAM model has

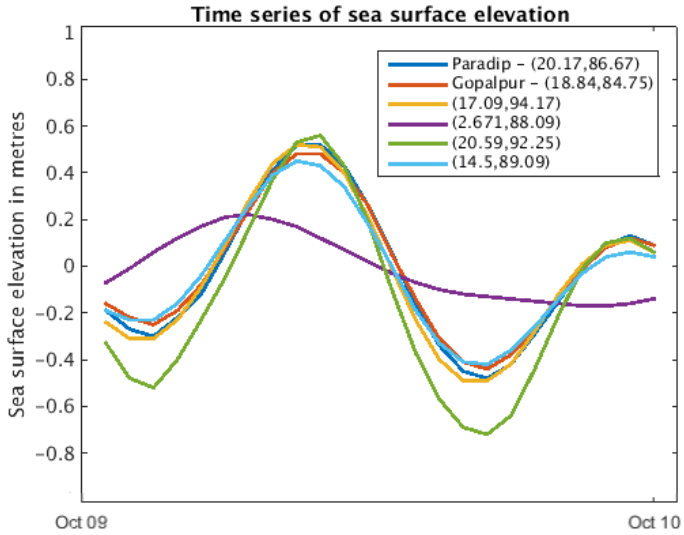

Figure 3.20: Time series of sea surface elevation for different points within the BoB domain, where a restart has been used to spin up the ocean domain.

the capability to generate the initial conditions according to the local wind read during the preprocessing stage. In POL-WAM, the wind information necessary for the computation of the initial wave conditions have to be in accordance with the preprocessing of winds by POLCOMS.

When POL-WAM is "cold started", the initial winds in POLCOMS are zero and they increase linearly up to the real value. If this zero wind was used in WAM, a zero energy field would be produced, which would remain throughout the WAM simulation as WAM lacks a mechanism for energy growth from flat calm. Therefore, in this situation the initial conditions were defined according to various parameters supplied by the user. In this study the following wave parameters were used for 'cold-starts': $\alpha = 0.018$, $FM = 0.2$, $\gamma = 3$, $\sigma_a = 0.07$, $\sigma_b = 0.09$ and a fetch of 30000m. See Komen et al. (1994) for more information on these parameters and the initial wave field they create.

Boundary wave information, although possible to include in POL-WAM simulations, was not used for the current study. Wave energy from the southern oceans may be significant, however, here the main interest is locally generated waves from the TC.

3.3.5 Model Runtime Options

This section summarises the different model runtime options used and the parametrisation scheme choices made in the present study, both for the WRF and POL-WAM models.

For the WRF model, the domains were as described in Section 3.3.1. Many of the features of AHW have been incorporated, along with other appropriate parametrisation schemes. The runtime options chosen included:

- two-way interactive moving nested domains as described in Section 3.3.1. The parent domain had 12 km grid resolution, with 4 km and 1.3 km grid resolution nested domains, moving with the centre of the cyclone.
- each domain had 35 vertical layers, which corresponds to the initial condition dataset used (see Section 3.3.3).
- a time step of 36 seconds was used for the parent domain, 12 seconds for the 4 km domain, and 4 seconds for the 1.3 km domain, in order to satisfy the CFL condition (see Section 2.1.1).
- the Donelan formulation of the air-sea drag coefficient for high winds was used in all domains.
- the Garrett formulation of the enthalpy flux was used.
- the Kain-Fritsch cumulus scheme was used in the parent domain (Kain, 2004). No cumulus scheme was used in the higher resolution domains, as convection is explicitly resolved.
- the WRF single-moment, 5-class cloud microphysics scheme was used for all domains, as per Liu et al. (2011).
- the Yonsei University planetary boundary layer scheme was chosen, as per Liu et al. (2011).
- the Dudhia short-wave and Rapid Radiative Transfer Model long-wave radiation schemes were used, again as per Liu et al. (2011).
- the Noah land surface model was used, as per NCEP North American Mesoscale Model (NAM). As most of the WRF domain is over the ocean, this will have very limited impact.

As mentioned, these choices are the same as the Liu et al. (2011) study, which investigates the impact of atmosphere-ocean-wave model coupling on TC intensity. Therefore, the parametrisation scheme choices were also deemed appropriate for the work presented here. For more details and references on the parametrisation schemes, see Section 3.1.2.

The POL-WAM domain is described in Section 3.3.2. The runtime options for POL-WAM were:

- 12 vertical layers and a barotropic time step of 3 seconds.
- A minimum depth of 10 m was applied to the coastal region of the domain in order to represent the coastal bathymetric features without inducing numerical instability. Wetting and drying was not implemented for this study. This will have an impact on the surge and wave heights and in the future wetting and drying should be included.

- As mentioned in Section 3.3.4, a version of POL-WAM was used which does not include temperature and salinity. The version of the model used was compiled without any temperature and salinity integration, in order to assess the impact of the meteorological forcing on the dynamics of the system only.
- Three meteorological variables were used as inputs. These were the two components of the wind, and mean sea level pressure, and cloud cover. The frequency of the forcing was hourly.
- TXPO tidal time series are calculated and applied at POLWAM's open boundary. No other ocean variables are implemented at the boundary.
- The main simulation used the full 3D two-way current-wave coupling, as described in Section 3.2.3.
- The WAM runtime options controlling the particular physics used here were the same as were used in Brown (2010) and Bricheno et al. (2013b). These included spherical polar coordinate propagation of waves, quadrant coordinate propagation, 21 frequency bins, as well as the shallow water version of WAM. Although part of the BoB are deep, with respect to waves, the areas of most interest are the shallower parts.

For further information on the details of these options, see Osuna and Wolf (1994), Holt and James (2001), and Komen et al. (1994), along with the particular references mentioned for each option.

3.4 Available Data

This section describes the available data which was used in this study for comparison with the modelling system. This allowed some model validation, although this was limited due to availability of reliable and accurate datasets.

3.4.1 Atmospheric Validation Data

The Bay of Bengal is a data poor region, especially in comparison with other basins where tropical cyclogenesis occurs. Observation strategies are expensive, especially when they involve state of the art observational equipment, and the countries which surround the Bay of Bengal do not have the available resources to provide such sophisticated programmes. Even in those locations where more data is available, tropical cyclone observations are highly uncertain and often involve a team of meteorologists measuring the radius of maximum winds from satellite imagery and using simple relationships between wind speed and air pressure, often at low temporal resolution.

The official dataset is described below and provides the only available record of Cyclone Phailin. Therefore, this was the dataset used in this study.

The observed tropical cyclone Best Track data used are obtained from the International Best Track Archive for Climate Stewardship (IBTrACS) (Knapp et al., 2010). IBTrACS

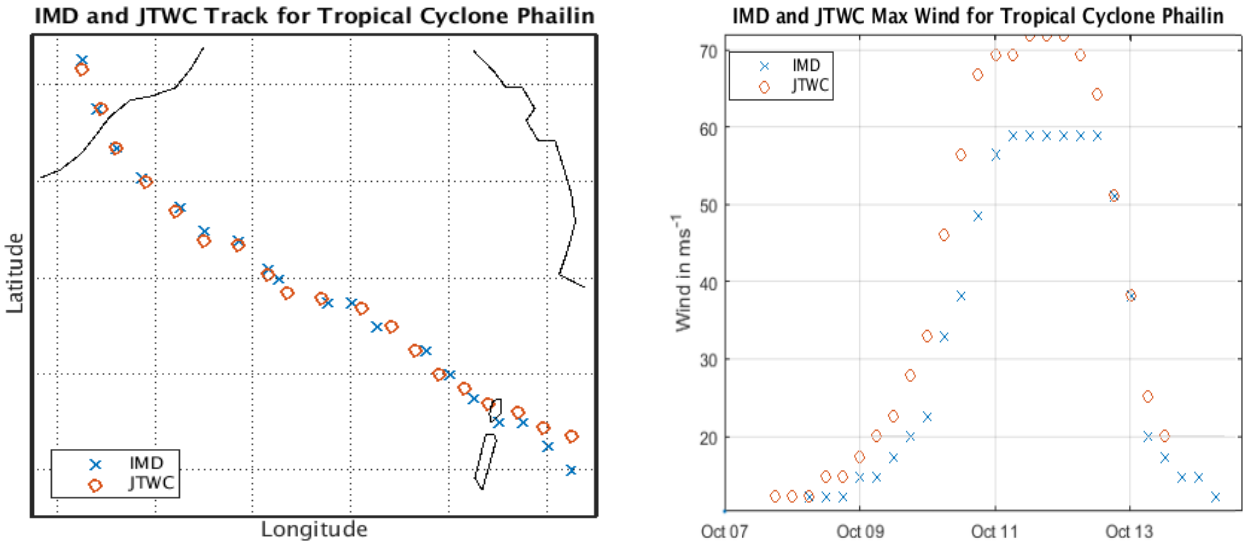

Figure 3.21: Comparison between the IMD and JTWC observations for TC Phailin, using blue crosses and red circles respectively. The left figure shows the cyclone track, and maximum wind speed is shown on the right.

provides details on each specific storm using information from different World Meteorological Organisation (WMO) approved, regional forecast agencies. For TC Phailin the database includes information from the Indian Meteorological Department (IMD) in New Delhi, and the Joint Typhoon Warning Centre (JTWC) in Hawaii, USA. The data includes 3-hourly values of WMO official maximum sustained wind, minimum pressure, latitude and longitude of central position, along with centre specific measurements, at different frequencies. The data provided by IMD and JTWC are every 6 hours, and the official 3-hourly data are interpolated from this raw data. The original dataset measures the maximum wind speed in knots, to the nearest 5 kt. Here, the data presented has been converted to ms^{-1}, to the neatest significant figure.

The IMD uses visible and infra-red satellite images along with the Dvorak technique to determine the track of the cyclone (see Section 1.2). The cyclone T-number from this technique, minimum pressure and maximum sustained wind speed corresponds to a classification used by the IMD (e.g. Cyclonic Storm). This classification is used throughout the IMD report (IMD Report, 2013). The radius of maximum winds is published only by the JTWC and is originally measured in nautical miles, but converted to kilometres here.

Each centre uses slightly different methods and definitions. For example, the average sustained wind speed is calculated differently between IMD and JTWC. The IMD uses a 3-minute averaged wind speed (WMO Panel on Tropical Cyclones, 2015) and the JTWC uses a 1-minute averaged wind speed (JTWC Frequently Asked Questions). This accounts for their varying values in the IBTrACS database (see Table 3.1, and Figure 3.21).

The IMD data maximum wind time observations flat line at 59 ms^{-1}. This recorded value does not change for over 24 hours, which implies this may be the maximum wind speed

which can be recorded by the equipment and that these observations do not have full details of the wind speed during Cyclone Phailin.

The difference between the two datasets, provided by different organisations, highlights the uncertainty of tropical cyclone data. Therefore, instead of comparing the model simulations directly against one of the datasets for validation, both sets of values will be used as a guide for model verification and will show whether or not the simulated tropical cyclone is of the correct magnitude and general location.

Table 3.1: IBTrACS Data for Phailin Including both IMD and JTWC Data.

ISO Time	**Latitude**		**Longitude**		**Wind (ms^{-1})**		**Pressure (hPa)**		**RMW (km)**
	IMD	**JTWC**	**IMD**	**JTWC**	**IMD**	**JTWC**	**IMD**	**JTWC**	**JTWC**
07/10/2013 12:00	-	11.8	-	97.6	-	10	-	1007	-
07/10/2013 18:00	-	12.1	-	96.4	-	13	-	1004	83
08/10/2013 00:00	-	12.3	-	95.6	-	13	-	1004	83
08/10/2013 06:00	12	12.6	95.5	95.1	13	13	1004	1004	83
08/10/2013 12:00	12	12.7	94.5	94.5	13	15	1003	1000	83
08/10/2013 18:00	12.5	12.9	94	93.9	13	15	1003	1000	83
09/10/2013 00:00	13	13.2	93.5	93.4	15	18	1002	996	83
09/10/2013 06:00	13	13.4	93	92.8	15	21	1000	993	83
09/10/2013 12:00	13.5	13.7	92.5	92.3	18	23	999	989	83
09/10/2013 18:00	14	14	92	91.8	21	28	998	982	83
10/10/2013 00:00	14.5	14.5	91.5	91.3	23	33	996	974	37
10/10/2013 06:00	15	15	90.5	90.8	33	46	984	956	28
10/10/2013 12:00	15.5	15.4	90	90.2	39	57	976	941	22
10/10/2013 18:00	15.5	15.6	89.5	89.4	49	67	960	926	22
11/10/2013 00:00	16	15.7	88.5	88.7	57	69	946	922	22
11/10/2013 06:00	16.2	16.1	88.3	88.3	59	69	940	922	22
11/10/2013 12:00	16.8	16.7	87.7	87.7	59	72	940	918	19
11/10/2013 18:00	17	16.8	87	87	59	72	940	918	19
12/10/2013 00:00	17.5	17.4	86.5	86.4	59	72	940	918	19
12/10/2013 06:00	18.1	18	85.7	85.8	59	69	940	922	28
12/10/2013 12:00	18.7	18.7	85.2	85.2	59	64	940	929	19
12/10/2013 18:00	19.5	19.5	84.8	84.9	51	51	956	948	19
13/10/2013 00:00	20.5	20.3	84.5	84.5	39	39	976	967	19
13/10/2013 06:00	21.5	21.5	84	84.1	21	26	992	985	19
13/10/2013 12:00	22.5	23.1	83.8	84.1	18	21	994	993	19
13/10/2013 18:00	23	-	83.5	-	15	-	996	-	-
14/10/2013 00:00	23.5	-	84	-	15	-	1000	-	-
14/10/2013 06:00	24.5	-	84.2	-	13	-	1004	-	-

3.4.2 Oceanographic Validation Data

As with atmospheric data across the BoB, there are very limited oceanic data sources. This is especially true for oceanic data during TC events, as often remote-sensing techniques are affected by the amount of cloud and precipitation, and other stationary data sources can be damaged by strong winds and flooding.

For TC Phailin, there are two oceanic data sources. These are the Gopalpur wave rider buoy and the Paradip tide gauge. Their data are described in this section.

3.4.2.1 Wave Rider Buoy Data

Wave data for tropical cyclone Phailin has been accessed from the Indian National Centre for Ocean Information Services (INCOIS). INCOIS maintains a wave buoy network comprising of eight locations along the Indian coast. The Golpalpur buoy data are used in this study as the buoy remained within 100 km of the cyclone track, even though it drifted from its usual moored location due to the cyclone event. The buoy is a Datawell Directional Wave rider buoy which is moored in 15 m water depth off Gopalpur ((19°16.870 N, 84°57.760 E), until at 0000 UTC 12 October the buoy drifted from this location (see Figure 3.22). Luckily, the GPS data show that the buoy remained reasonably close to the track (within 100 km).

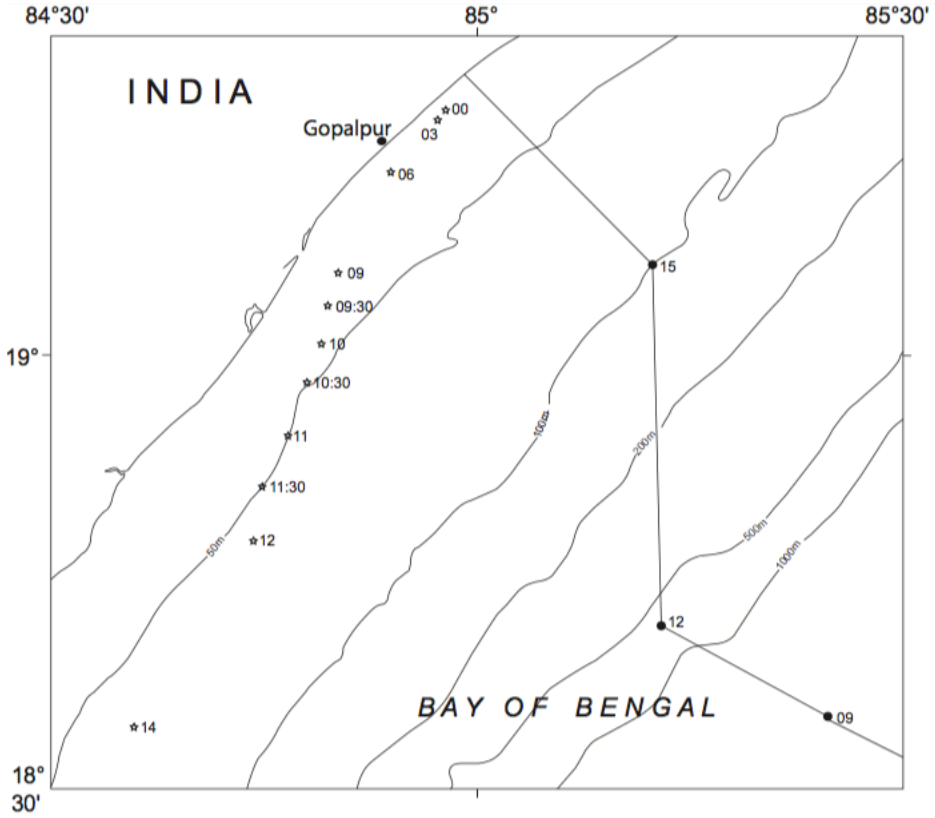

Figure 3.22: Waverider buoy location (star) compared with Phailin track (solid circle) on 12 October 2013 (Amrutha et al., 2014). The lines indicate the coastline and bathymetry of the coastal area.

The directional buoy measures surge and sway (horizontal acceleration) and heave (vertical acceleration) using an on board compass and accelerometers, giving displacements from two horizontal axes with a resolution of 1 cm and an accuracy of 3% (Barstow and Kollstad, 1991). This is then transferred to north-south and east-west displacement, and from these wave parameters, such as significant wave height, mean wave period and maximum wave height, can be calculated using fast Fourier Transforms and zero-crossing analysis of the surface elevation time series (see Section 1.4). These data are shown in Table 3.2 and Figure 3.23 below.

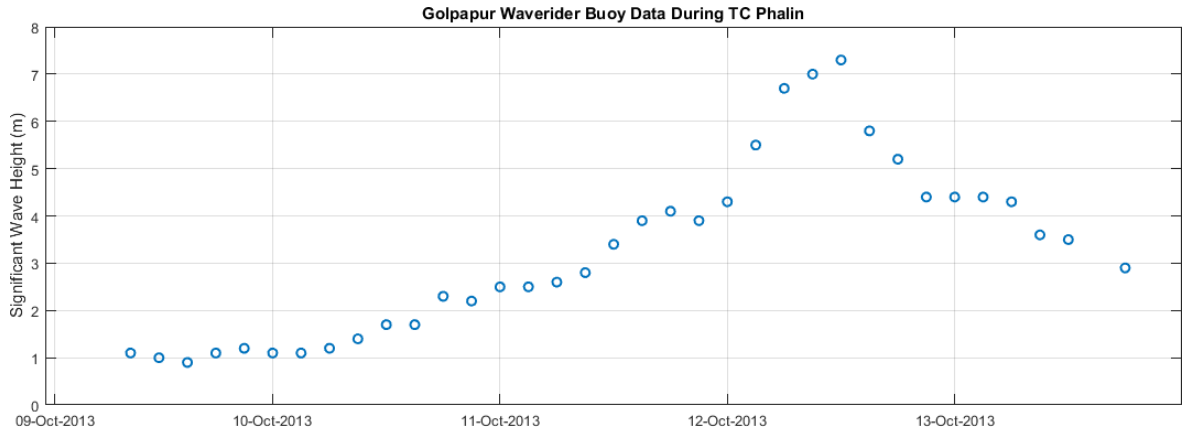

Figure 3.23: Waverider buoy observational data of significant wave height (m) during TC Phailin.

3.4.2.2 Tide Gauge Data

Observed sea surface elevation observations during cyclone Phailin were taken by a tide gauge in Paradip, India. The Indian National Centre for Ocean Information Services gave access to this data for inclusion in this work.

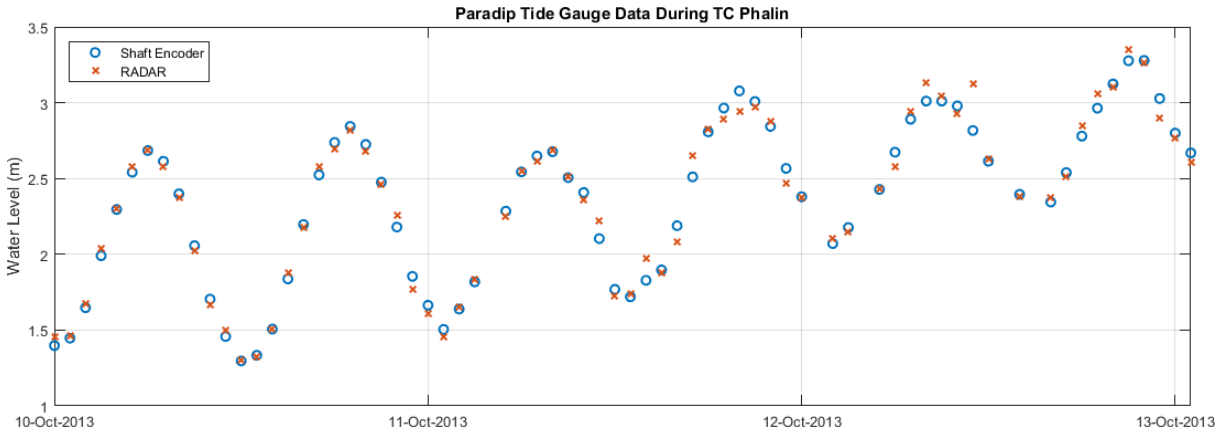

Figure 3.24: Tide gauge observational data of water level (m) during TC Phailin.

As well as a numerous wave buoys, INCOIS also maintains a tide gauge network along the Bay of Bengal coastline. The tide gauge station used in this study is located at 20.267°N,

86.7°E in Paradip, a major seaport town of the Odisha district. The tide gauge continuously measures the sea surface elevation hourly, using three sensors - a pressure sensor, shaft encoder and radar gauge. These allow extreme water levels to be recorded through a data logger and communicated to the INSAT (Indian National Satellite) system.

The gauge has been measuring sea surface maxima since 1966, and recorded during the Cyclone Phailin storm surge event. The gauge data is used in this study to compare against the modelled sea surface height at Paradip. The data is shown in Table 3.3 and Figure **??**, along with the storm surge residual published as part of Lakshmi et al. (2017).

Table 3.2: Waverider buoy location, distance from cyclone and wave parameters during 9-13 October 2013 (Amrutha et al., 2014)

ISO Time	**Buoy Location**		**Distance from cyclone** (km)	**Hs** (m)	**Tp** (s)	**Dp** (deg)
	Lat	**Lon**				
09/10/2013 09:00	19.2812	84.9635	1055.5	1.1	13.3	165
09/10/2013 12:00	19.2812	84.9635	1055.5	1.0	20.0	152
09/10/2013 15:00	19.2812	84.9635	1048.7	0.9	20.0	162
09/10/2013 18:00	19.2812	84.9635	977.6	1.1	20.0	146
09/10/2013 21:00	19.2812	84.9635	977.6	1.2	13.3	172
10/10/2013 00:00	19.2812	84.9635	899.9	1.1	20.0	153
10/10/2013 03:00	19.2812	84.9635	855.7	1.1	18.2	160
10/10/2013 06:00	19.2812	84.9635	777.7	1.2	18.2	153
10/10/2013 09:00	19.2812	84.9635	777.7	1.4	18.2	155
10/10/2013 12:00	19.2812	84.9635	699.8	1.7	18.2	155
10/10/2013 15:00	19.2812	84.9635	699.8	1.7	18.2	158
10/10/2013 18:00	19.2812	84.9635	656.2	2.3	18.2	158
10/10/2013 21:00	19.2812	84.9635	614.6	2.2	18.2	155
11/10/2013 00:00	19.2812	84.9635	536.1	2.5	16.7	162
11/10/2013 03:00	19.2812	84.9635	536.1	2.5	16.7	156
11/10/2013 06:00	19.2812	84.9635	504.7	2.6	20.0	155
11/10/2013 09:00	19.2812	84.9635	457.6	2.8	10.5	131
11/10/2013 12:00	19.2812	84.9635	410.5	3.4	11.1	132
11/10/2013 15:00	19.2812	84.9635	363.0	3.9	11.8	132
11/10/2013 18:00	19.2812	84.9635	339.8	4.1	11.8	134
11/10/2013 21:00	19.2812	84.9635	316.8	3.9	12.5	142
12/10/2013 00:00	19.2812	84.9635	261.4	4.3	11.8	135
12/10/2013 03:00	19.2687	84.9494	200.7	5.5	12.5	141
12/10/2013 06:00	19.2096	84.8967	152.2	6.7	11.8	118
12/10/2013 09:00	19.0906	84.8352	83.1	7.0	11.1	98
12/10/2013 12:00	18.7963	84.7293	53.4	7.3	11.1	103
12/10/2013 15:00	18.5021	84.5786	95.8	5.8	11.8	56
12/10/2013 18:00	18.2863	84.5187	138.4	5.2	9.1	212
12/10/2013 21:00	18.1281	84.4606	208.1	4.4	9.1	208
13/10/2013 00:00	17.9914	84.4150	278.9	4.4	9.1	214
13/10/2013 03:00	17.8768	84.3647	349.4	4.4	9.1	196
13/10/2013 06:00	17.7795	84.3228	415.0	4.3	9.1	191
13/10/2013 09:00	17.7119	84.2892	457.5	3.6	8.3	204
13/10/2013 12:00	17.6460	84.2574	541.8	3.5	7.1	207
13/10/2013 18:00	17.4855	84.1614	617.2	2.9	7.7	172

Table 3.3: IMD Paradip tide gauge data during Cyclone Phailin (Lakshmi et al., 2017)

ISO Time	**Water Level (m) - Shaft Encoder**	**Water Level (m) - RADAR**	**Sea Surface Residual (m)**
11/10/2013 00:00	1.664	1.608	0.338
11/10/2013 01:00	1.505	1.457	0.324
11/10/2013 02:00	1.639	1.649	0.313
11/10/2013 03:00	1.819	1.834	0.404
11/10/2013 04:00	-	-	0.377
11/10/2013 05:00	2.285	2.253	0.439
11/10/2013 06:00	2.544	2.549	0.426
11/10/2013 07:00	2.648	2.614	0.479
11/10/2013 08:00	2.677	2.689	0.494
11/10/2013 09:00	2.506	2.513	0.492
11/10/2013 10:00	2.408	2.361	0.547
11/10/2013 11:00	2.104	2.224	0.537
11/10/2013 12:00	1.769	1.722	0.537
11/10/2013 13:00	1.720	1.738	0.527
11/10/2013 14:00	1.829	1.972	0.593
11/10/2013 15:00	1.897	1.881	0.562
11/10/2013 16:00	2.189	2.086	0.481
11/10/2013 17:00	2.511	2.651	0.534
11/10/2013 18:00	2.808	2.829	0.565
11/10/2013 19:00	2.965	2.895	
11/10/2013 20:00	3.078	2.940	
11/10/2013 21:00	3.008	2.970	
11/10/2013 22:00	2.844	2.876	
11/10/2013 23:00	2.567	2.470	
12/10/2013 00:00	2.380	2.373	
12/10/2013 02:00	2.071	2.104	
12/10/2013 03:00	2.177	2.150	
12/10/2013 05:00	2.428	2.433	
12/10/2013 06:00	2.674	2.579	
12/10/2013 07:00	2.891	2.941	
12/10/2013 08:00	3.011	3.135	
12/10/2013 09:00	3.011	3.046	
12/10/2013 10:00	2.979	2.930	
12/10/2013 11:00	2.817	3.123	
12/10/2013 12:00	2.614	2.631	
12/10/2013 14:00	2.396	2.378	
12/10/2013 16:00	2.345	2.373	
12/10/2013 17:00	2.539	2.510	
12/10/2013 18:00	2.780	2.846	
12/10/2013 19:00	2.964	3.062	
12/10/2013 20:00	3.124	3.106	
12/10/2013 21:00	3.277	3.349	
12/10/2013 22:00	3.279	3.266	
12/10/2013 23:00	3.028	2.896	
13/10/2013 00:00	2.800	2.766	

Chapter 4

Results

In this section the results of the main modelling experiments are presented. This includes an atmospheric and oceanic modelled representation of Cyclone Phailin; the results from different resolution atmospheric model runs along with comparisons of the outputs and impact on the ocean domains; and further results from model runs using different simulation start times. These are organised into Sections 4.1, 4.2 and 4.3 respectively and each section answers an objective, as described in Section 1.1.

4.1 Modelling System - Cyclone Phailin Simulation

In this section the modelled simulation of Cyclone Phailin is presented, divided into outputs from the atmospheric and oceanic parts of the WRF, POLCOMS and WAM modelling system. This system is described in detail in Section 3. Firstly, the WRF results are presented, followed by the POLCOMS and WAM outputs.

4.1.1 WRF Results

Cyclone Phailin has been successfully simulated using the WRF model with the set-up described in Section 3.1. Here, the main results are those from the highest resolution simulation which used 1.3 km and 4 km moving nested domains in a larger 12 km resolution parent domain. Figure 3.5 shows the WRF domains, and the nest movement throughout the simulation following the track of Cyclone Phailin. This model simulation is referred to as 'All resolution' as the outputs shown are the combination of the 1.3 km, and 4 km grid size nested domains, with the 12 km grid size parent domain.

The simulation began at 0000 UTC 9 October 2013, and covered the 120 hour period to 0000 UTC 14 October 2013. According to the IMD record, the largest period of cyclogenesis occurs on 10 October 2013 and landfall occurs at 1700 UTC 12 October 2013. These time periods were included within the modelled simulation.

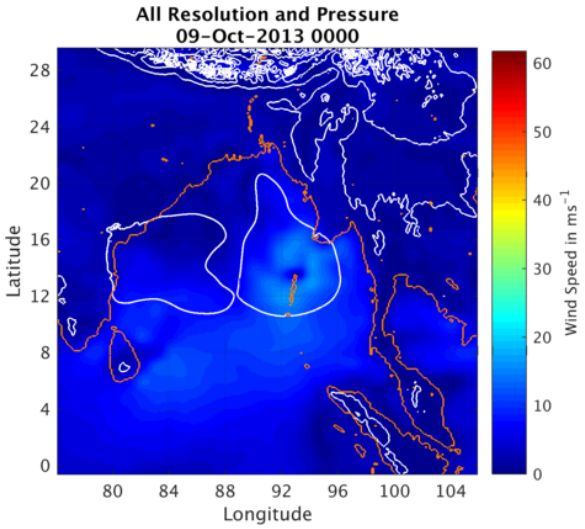
All Resolution and Pressure
09-Oct-2013 0000
Latitude
Longitude
Wind Speed in ms^{-1}

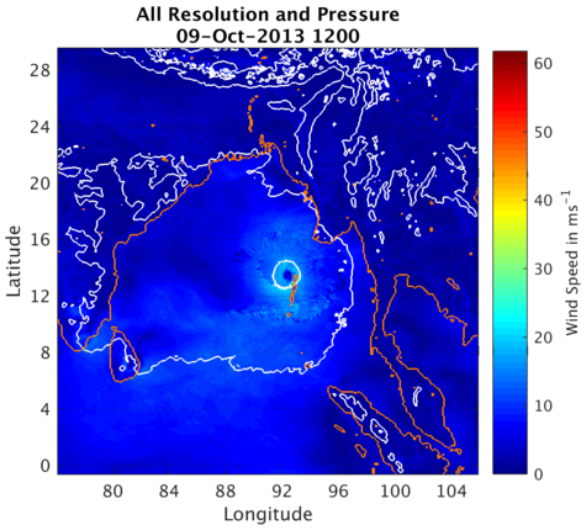
All Resolution and Pressure
09-Oct-2013 1200
Latitude
Longitude
Wind Speed in ms^{-1}

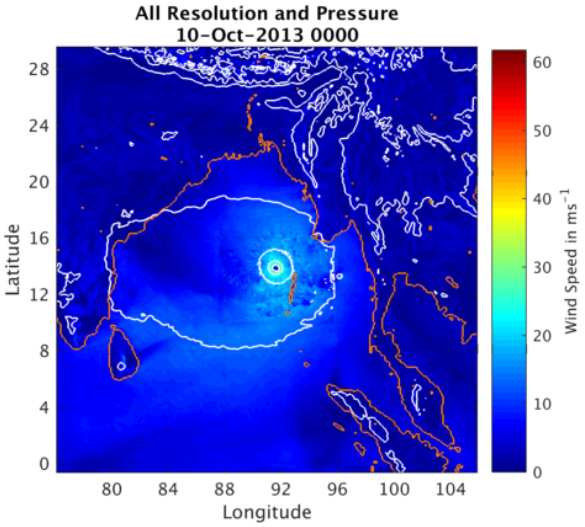
All Resolution and Pressure
10-Oct-2013 0000
Latitude
Longitude
Wind Speed in ms^{-1}

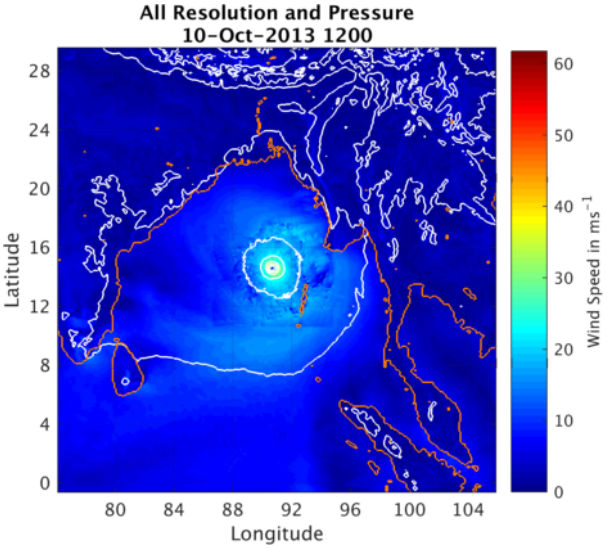
All Resolution and Pressure
10-Oct-2013 1200
Latitude
Longitude
Wind Speed in ms^{-1}

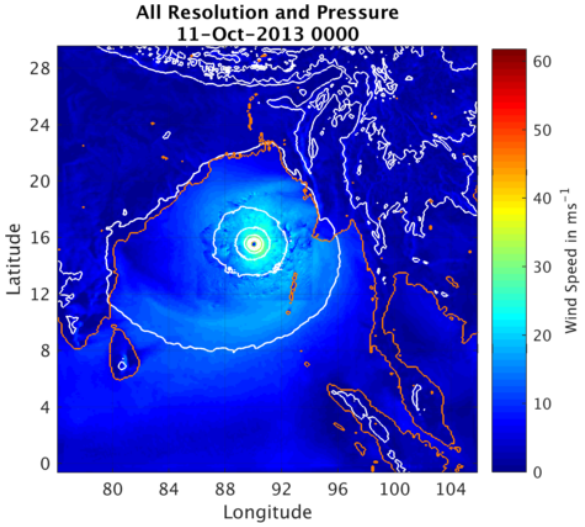
All Resolution and Pressure
11-Oct-2013 0000
Latitude
Longitude
Wind Speed in ms^{-1}

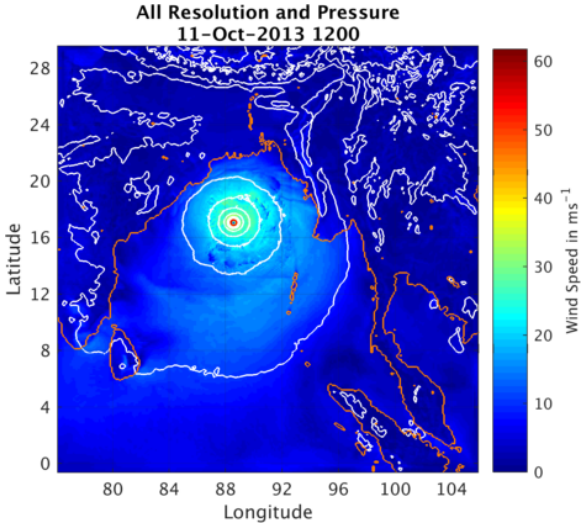
All Resolution and Pressure
11-Oct-2013 1200
Latitude
Longitude
Wind Speed in ms^{-1}

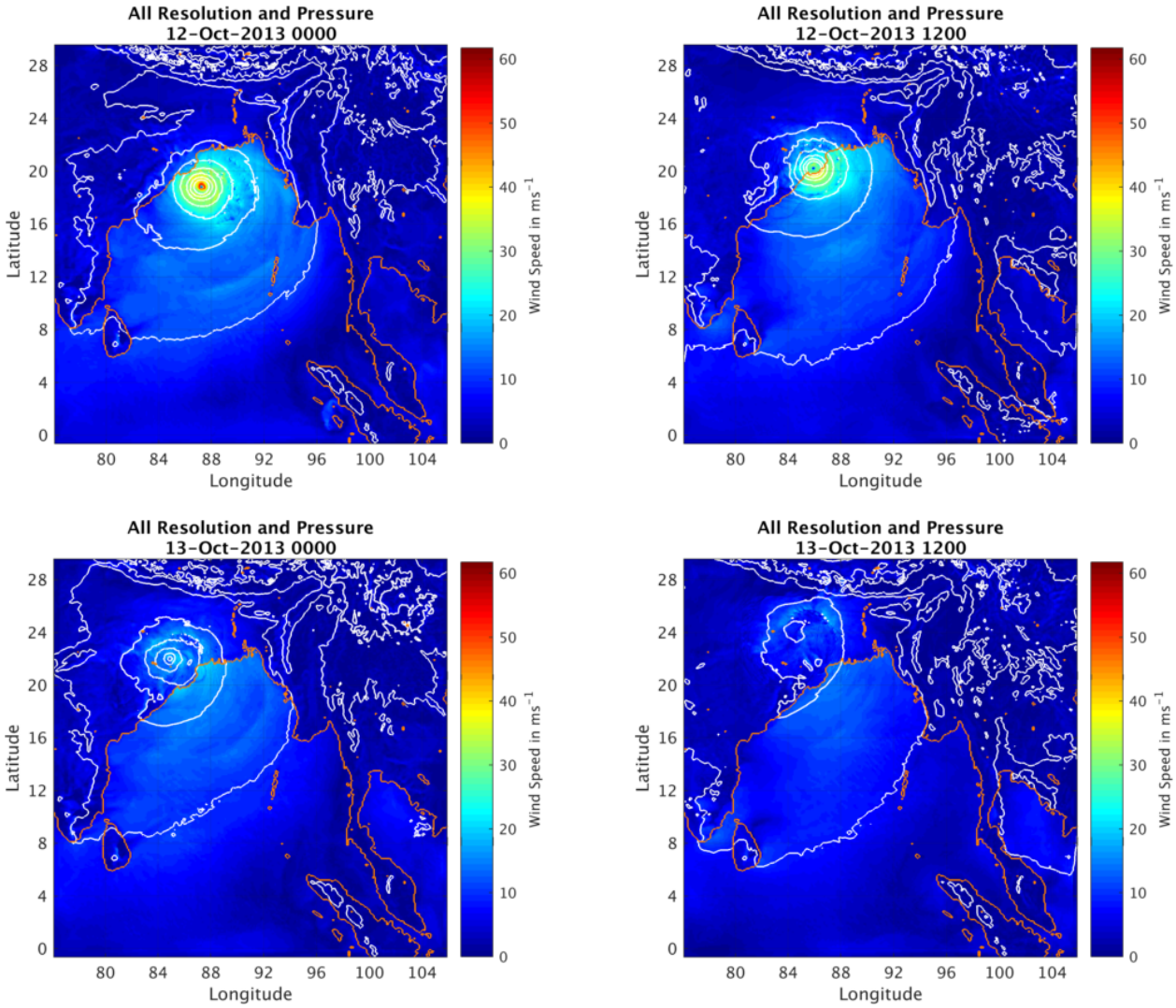

Figure 4.1: Snapshots of the WRF Cyclone Phailin simulation, shown every 12 hours, with colour representing wind speed and isobars presenting the mean sea level pressure.

Figure 4.1 presents model output for 12-hourly snapshots of the Cyclone Phailin simulation beginning with the initial conditions at 0000 UTC 9 October, and finishing at 1200 UTC 13 October after landfall has occurred. The colours represent the wind speed, with red indicating the strongest winds and blue representing the lightest winds. The maps include isobars showing mean sea level pressure at 8 hPa intervals.

Figure 4.1 shows that the WRF model successfully simulates a tropical cyclone, with maximum wind speeds reaching 59 ms^{-1} and minimum pressures of 900 hPa. These values correspond to a TC of category 4 to 5 and a T number of 6.0, known by the IMD as a Very Severe Cyclonic Storm. As described in Section 1.6, according to IMD observations, Phailin reached a maximum wind speed of 59 ms^{-1} which is exactly equal with the wind speeds simulated. The pressure values were not as close a match, with a minimum of 940 hPa observed. This pressure error would equate to a different category on the Saffir-Simpson

scale and a higher T number, and is therefore, significant.

The snapshots shows output from every domain. Nearest to the eye is the 1.3 km resolution domain, the 4 km domain surrounds it and the 12 km domain is near to the boundary. The edge between the domains has not been smoothed, so the changes in resolution can be identified with a keen eye.

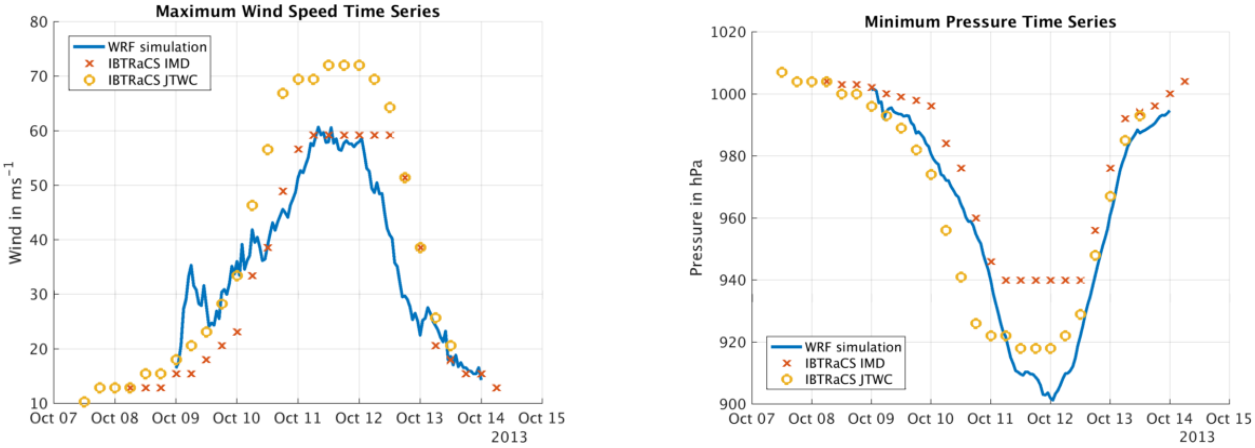

Figure 4.2: Time series plots showing the maximum wind and minimum pressure of the Cyclone Phailin simulation against the IBTrACS data. The yellow circles represent the JTWC observed data, and the orange crosses show the IMD observations.

Figure 4.2 shows the maximum wind and minimum pressure within the domain at each model timestep plotted as a time series. The IBTrACS data is also included in the graphics for comparison, with red x's and yellow circles showing the IMD and JTWC data, respectively.

As seen in Figure 4.1, tropical cyclone wind speed and pressure are simulated. An initial period of intensification occurs in the model on 9 October, which is not seen in reality. This is followed by a decrease in wind speed, coinciding with the modelled cyclone travelling over the Andaman and Nicobar Islands. The decrease in wind speed modelled is likely related to the increased friction over the land, which covers several of the 1.3 km grid boxes.

The rapid intensification seen in reality on 10 October is replicated, with maximum wind speeds increasing from 31 ms^{-1} at 0000 UTC 10 October, to over 51 ms^{-1} by 0000 UTC 11 October. The observations suggest that this intensity was maintained for over 24 hours. In the modelled results, the maximum wind speeds of 57-59 ms^{-1} are maintained for a shorter period, roughly 18 hours.

The minimum pressure time series follows the maximum wind trend very closely, with the pressure decreasing as the wind increases. The intensification shown in the minimum pressure series is more similar to the rate of change of minimum pressure seen in the observation. However, the model intensifies more than the recorded TC by 20-40 hPa.

The rate of change of increase in pressure after landfall matches the observations well. This occurs despite the overall minimum pressure through the simulation being lower than measured.

Overall, it is difficult to assess how well the modelling system hindcasts Cyclone Phailin when looking at the time series plots. The error of modelled maximum wind and minimum pressure are different dependent on which IBTrACS data is used for comparison. The overall trend is represented well using either of the sets of observations, although the magnitude is not exact.

.

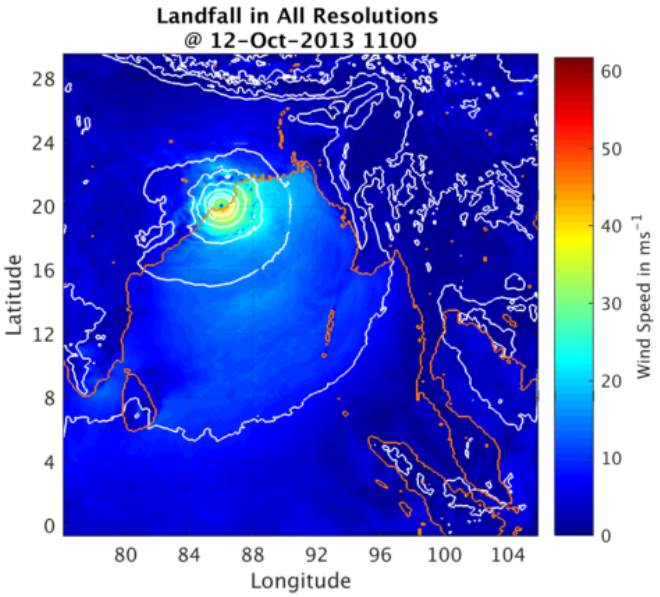

Figure 4.3: WRF model output of the Cyclone Phailin simulation at time of landfall, showing wind speed (colours) and MSLP (lines).

Landfall of TC Phailin occurred at approximately 1700 UTC 12 October at the Andhra Pradesh and Odisha coast. Figure 4.3 shows the model fields at time of landfall. In the simulation, landfall occurs at 0900 UTC 12 October, earlier than the observations. The maximum wind speed at the time of landfall in the model is 46 ms^{-1} at landfall, lower than at the maximum intensity. A reduction in intensity is not observed in reality, with wind speeds remaining between 59 and 62 ms^{-1}.

After landfall occurs, the modelled cyclone dissipates very quickly, with wind speeds reducing and pressure filling rapidly over several time steps. In both the IMD and JTWC observations this also occurs, with maximum wind speeds quickly decreasing from 59 ms^{-1} to less than 21 ms^{-1} in approximately 12 hours. This occurs because the thermal energy and moisture provided by the warm ocean is no longer available to fuel the cyclone as well as the frictional effects of the land.

Figure 4.4 shows the track of the simulated cyclone. This is based on the location of the minimum pressure within the the model domain at each timestep. The figure also shows the observed cyclone locations from IBTRaCS with the orange crosses and yellow circles in the diagram, representing the IMD and JTWC observations, respectively. At first, for the initial 24 hours of model simulation, there is reasonable agreement between the model and the observed vortex locations. After this period, the track of the modelled TC diverges from that of the observational data. The simulated cyclone moves further north, and stays to the east of the IBTRaCS data points for the remainder of the simulation. The modelled TC makes landfall further north-east along the Indian coastline. This figure does not show timings, but as mentioned, landfall occurs earlier in the simulation than in reality.

There may be several reasons why the modelled TC makes landfall at a different location

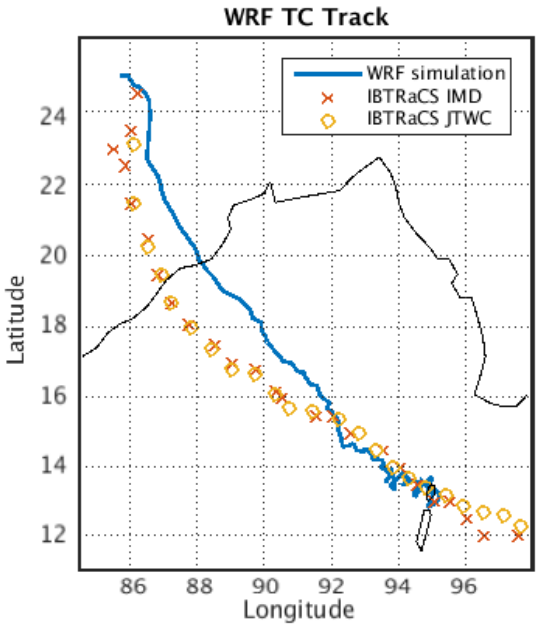

Figure 4.4: TC Phailin simulated track compared with the IBTrACS data points. The yellow circles represent the JTWC observed data, and the orange crosses show the IMD observations.

and different time - 8 hours earlier than reality. As described in Section 1.2, the background 'steering' flow is the local environment flow which impact the TC track. TCs in BoB commonly form in the vicinity of the monsoon trough, and are advected along with it. In our model, the impact of the ITCZ is input via the atmospheric boundary conditions at the edge of the parent domain. It is possible that the GFS boundary data is too low resolution to accurately simulate the ITCZ and the processes involved in advecting TCs along in its synoptic movement. One way to overcome this in the future, may be to improve the accuracy of the boundary conditions, or to increase the size of the parent domain.

4.1.2 POLCOMS-WAM Results

The atmospheric outputs from the Cyclone Phailin WRF simulation described in the previous section were used to force a POLCOMS-WAM model of the Bay of Bengal. The ocean modelling system is described in Section 3.2. The ocean model simulation began at 0000 UTC 9 October, as with the WRF simulation, and ran for 96 hours until 0000 UTC 12 October. This is 24 hours shorter than the WRF model run, consistent with landfall occurring at 0900 UTC 12 October. Shortly after this, the TC moves outside of the ocean domain and is no longer providing meteorological forcing to the ocean model. The results obtained with the higher resolution WRF forcing will be referred to as 'All resolution' as the meteorological input contained output from the 12 km, 4 km and 1.3 km WRF modelled domains.

This section is separated into the two parts - firstly, the output from the POLCOMS simulation, and secondly, the wave output from the WAM model.

4.1.2.1 POLCOMS Output

For storm surge and coastal flooding applications, the oceanic parameter that is of most interest is the sea surface elevation. For the oceanic model this variable was a direct output and is the focus for much of this section.

Figures 4.5 show the sea surface elevation output from POLCOMS for the simulated Cyclone Phailin forcing. As in the previous section, 12-hourly snapshots of the model simulation are shown. The colour bar denotes sea surface elevation in metres, and the track is shown by the grey and black lines.

In frames where the tide is high on the northern coast of BoB, for example at 1200 UTC 9 October, the sea surface elevation is being controlled by the tidal forcing. Sea surface elevation maxima can be seen near to the coast, and higher frequency snapshots would show this high tide maximum travelling along the coastline. As seen in Section 3.3.4, the tidal cycle in this simulation counts for ±0.6 m of the sea surface height.

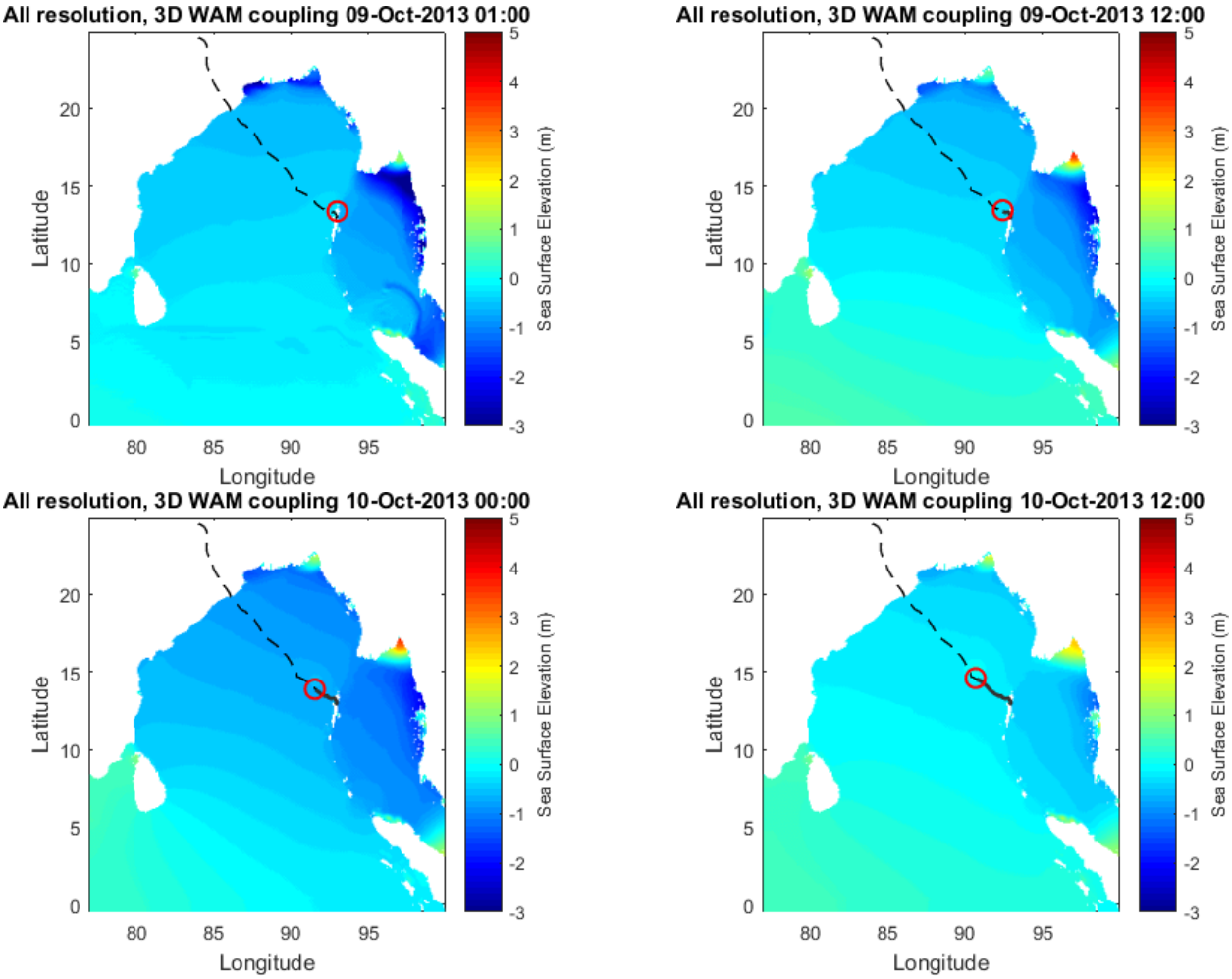

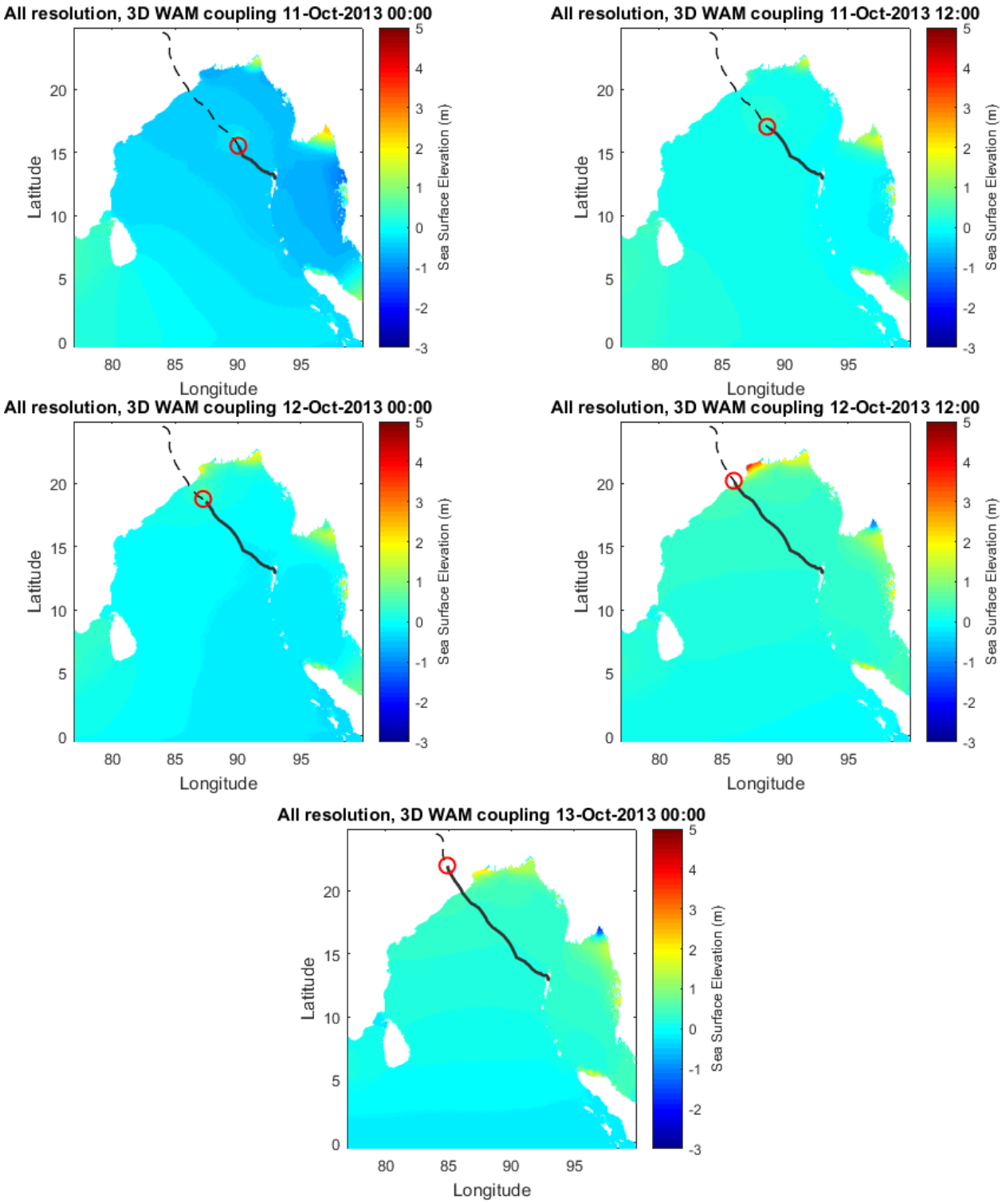

Figure 4.5: Snapshot of the POLCOMS output for Cyclone Phailin, every 12 hours. The colours represent sea surface elevation, the solid line shows the WRF modelled TC track, with the grey dashed line showing the TC‘s future track and the red circle indicating the TC location.

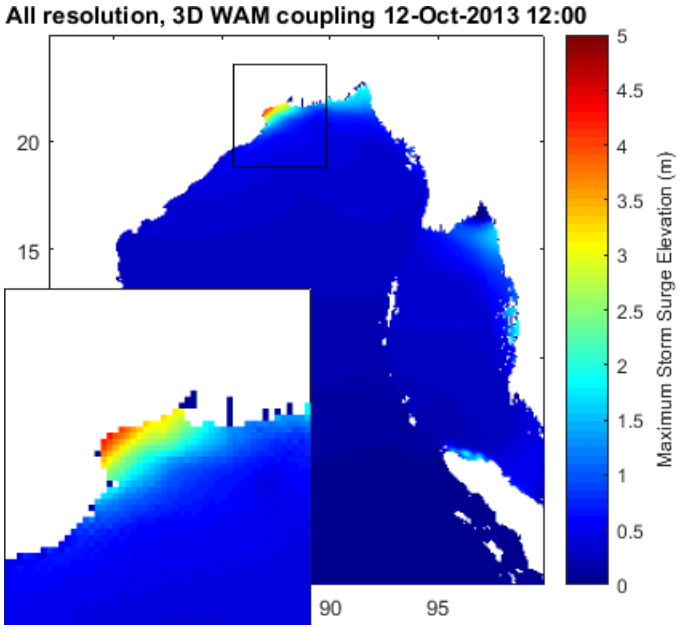

Figure 4.6: Maximum storm surge simulated along the Odisha and West Bengal coastline, with the colour representing the sea surface height.

As the wind becomes stronger and the central pressure decreases with TC intensification, the storm surge signal begins to be significant. The impact of the pressure minimum can be seen by the circle of raised sea surface height, which accounts for roughly 1.0 m of elevation. This is a relatively small contribution, as expected, but can be seen in addition to the tidal forcing.

As the TC moves towards the coastline, the large SSH values near to the coast can be attributed to the wind forcing component. The storm surge is especially clear in the last two frames, with larger sea surface elevations seen along the east Indian coastline.

Figure 4.6 shows the maximum storm surge simulated, the colours signifying the sea surface elevation in metres. A storm surge of 4.2 m was modelled at 1200 UTC 12 October on coast of the India-Bangladesh border.

The location of the storm surge is different to reality, where a storm surge of 3.0 m was reported by the media along the coast of Odisha. Here, the simulated Phailin is further north-east, nearer to the Bangladesh border. In Section 4.1.1, the point of model TC landfall is shown to be further north-west along the coast than observed, therefore it is no real surprise that the simulated storm surge shows the same displacement.

The sea surface elevation of 4.2 m was predicted by the model, which is higher than the 3.0 m surge reported in the Indian Times and on the BBC (Muhr et al., 2013). The media reports are not corroborated by measurements, so may not be accurate. However, the model roughly matched this value with the observational uncertainty, showing that the simulated storm surge was accurate.

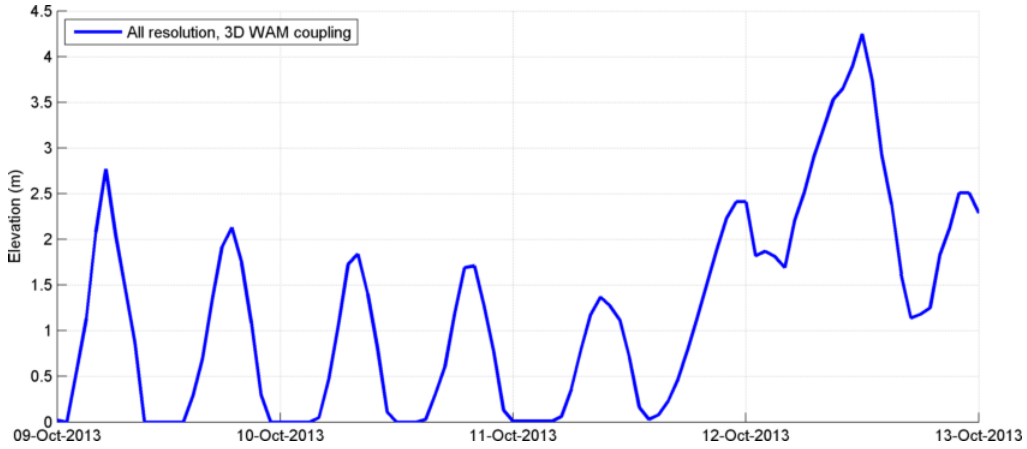

Figure 4.7: Maximum sea surface elevation (metres) in the POLCOMS domain for each time-step of the model simulation.

Figure 4.7 shows the time series of maximum sea surface elevation across the square inset image (see Figure 4.6) for every timestep of the POLCOMS simulation. The maximum value regardless of location in the inset image square is taken in order to highlight the highest storm surge elevation simulated. In this graph, the repeating pattern of the tidal cycles can be seen. At 1200 UTC 12 October, a storm surge of 4.2 m is modelled.

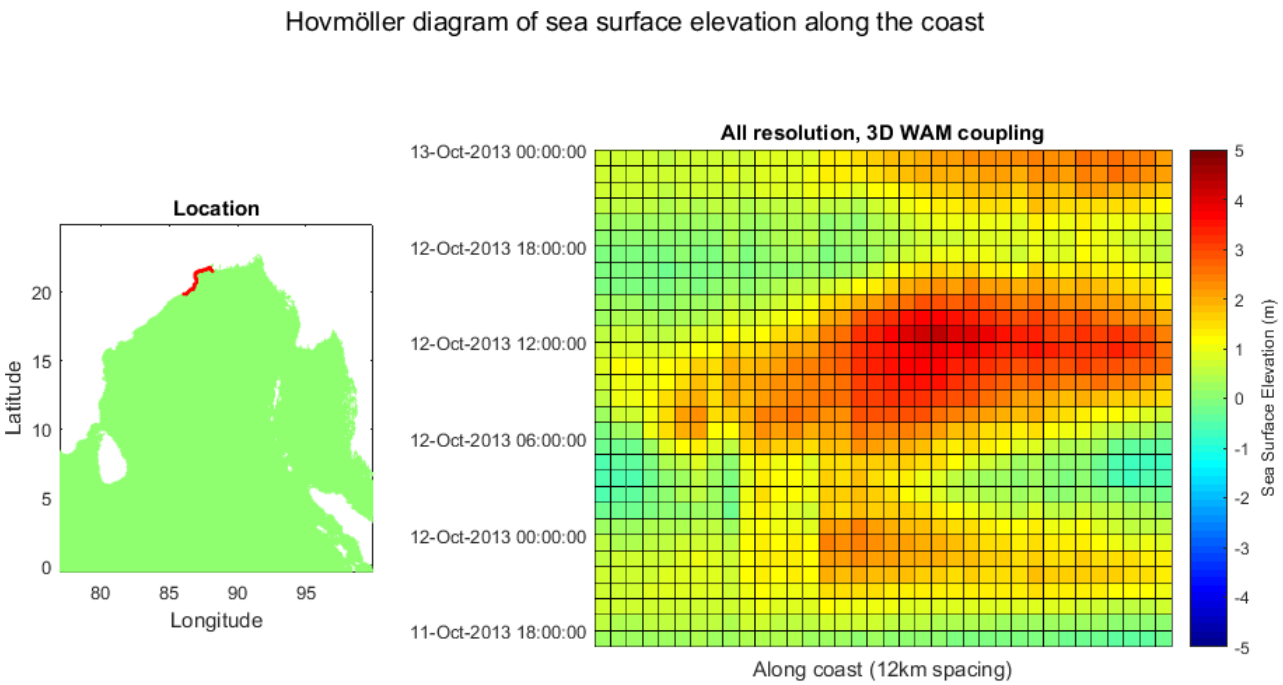

Figure 4.8: Hovmöller plot of sea surface elevation along the coast show in red. The colours on the right plot represent sea surface height.

Figure 4.8 shows a Hovmöller plot of sea surface elevation along the Odisha and West

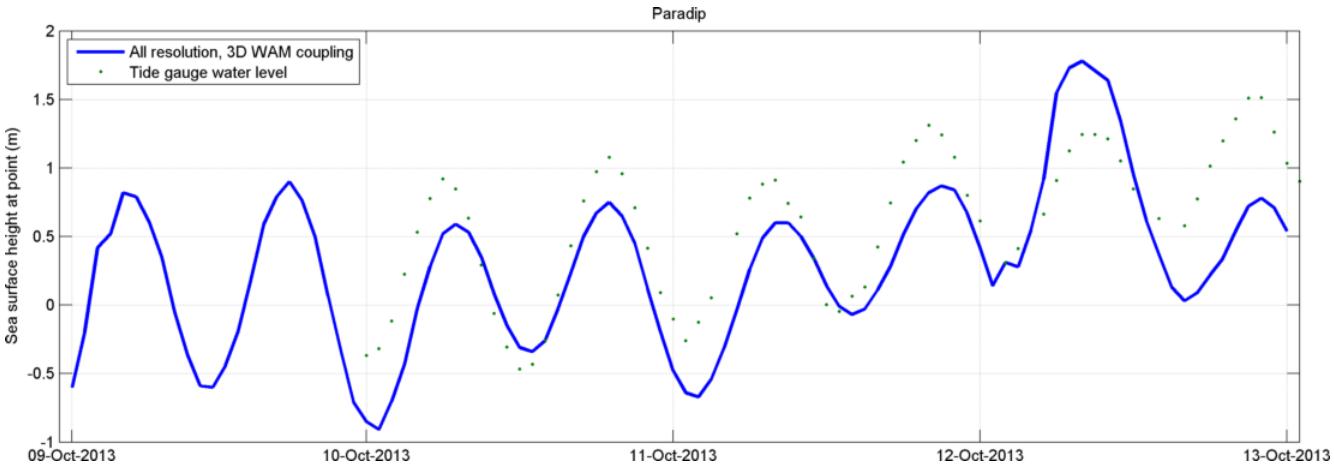

Figure 4.9: The sea surface elevation modelled at Paradip (blue line), compared with the observed tide gauge values (green points).

Bengal coast where the model simulated storm surge occurs. Time increases from the bottom of the plot to the top, with distance along the length of coast, highlighted in the image on the left, on the vertical axis. The plot shows the evolution of sea surface elevation in time and the highest storm surge height can be seen as between 4-5 m. The area of highest increase in sea surface height is elongated slightly from the lower left to upper right of the plot, depicting a movement from west to east.

In Section 1.3, it is stated that storm surges may propagate along the coast as trapped Kelvin waves. In the both hemispheres this occurs cyclonically around ocean basins, and the movement is demonstrated here in the model results.

Figure 4.9 shows the time series of sea surface elevation at Paradip, the location of the tide gauge data described in Section 3.4.2.2. The results of the model are in blue, with the observed values shown as green circles. The surge can be clearly seen in the model time series, the water level rises to 1.75 m. The modelled tidal cycle can also be seen in the plot, which is in phase with the tide gauge data. However, the high tide elevation is roughly 30 cm lower in the model than in the observed water level, and the surge itself is approximately 0.25 m higher in the model than in the record.

The highest water levels in the model output and the observed dataset also occur at different times. The modelled surge occurs at 1200 UTC 12 October, whereas the highest recorded level at Paradip occurs some 12 hours later, at 2100 UTC 12 October.

The model does not verify well against this tide gauge, even before the TC reaches Paradip. This may be due to the differences in TC movement seen in the WRF output, or inconsistencies within the ocean domain boundary data. This is a large source of error and may impact the values of the storm surge modelled. In the future, it is recommended that the tide output is validated against known tide water levels to test the ability of the model to simulate the tide, before adding TC forcing.

4.1.2.2 WAM Output

The significant wave height is probably the most important variable for wave forecasting and modelling and, therefore, is the main wave model output presented in this section. The wave direction is also of interest and is also analysed.

To demonstrate the WAM output for the Cyclone Phailin simulation, the significant wave height and wave directions are shown at regular snapshots throughout the simulation in Figure 4.10. The colours describe the significant wave height, and the arrows show the wave vectors.

The cyclone wind forcing causes waves to be generated across the BoB. From as early as the second frame, large waves can be seen developing. Through the simulation the waves increase both in significant wave height and the area of larger waves. From the start, the wave direction is around the cyclone eye, mirroring the wind forcing direction. The significant wave heights reach some 20 m at peak, and the waves continue to circulate around the cyclone centre throughout the simulation. The impact of the cyclone winds is felt across the whole of the Bay, many kilometres away from the cyclone track.

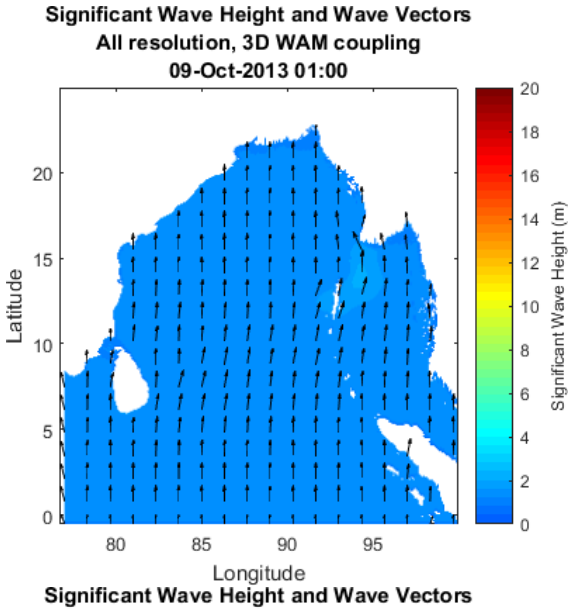
Significant Wave Height and Wave Vectors
All resolution, 3D WAM coupling
09-Oct-2013 01:00
Latitude
Longitude
Significant Wave Height (m)

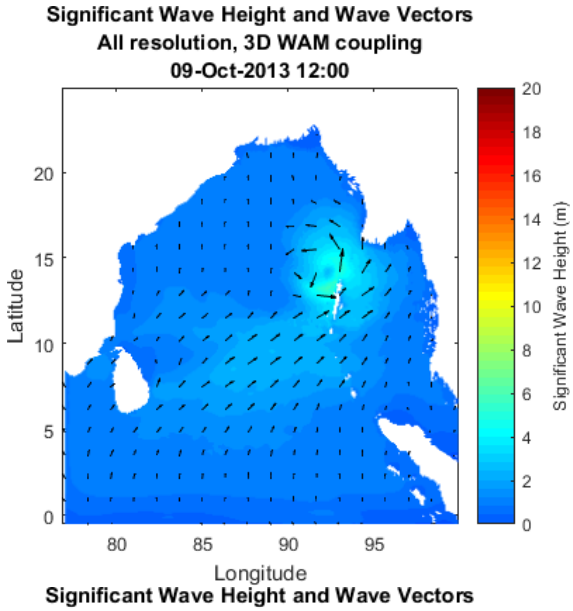
Significant Wave Height and Wave Vectors
All resolution, 3D WAM coupling
09-Oct-2013 12:00
Latitude
Longitude
Significant Wave Height (m)

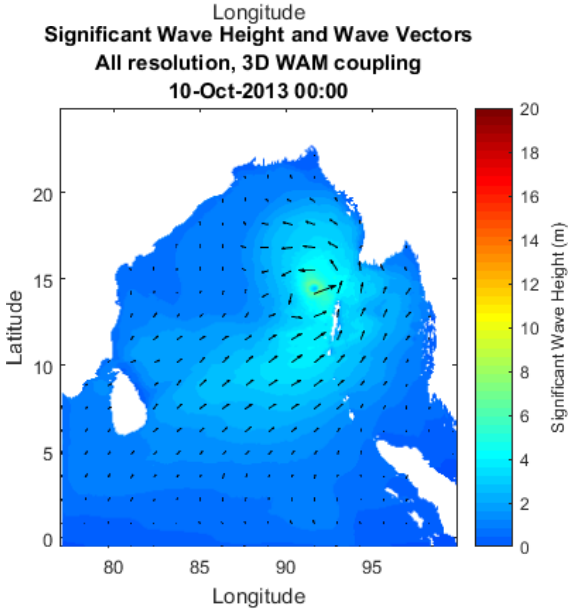
Significant Wave Height and Wave Vectors
All resolution, 3D WAM coupling
10-Oct-2013 00:00
Latitude
Longitude
Significant Wave Height (m)

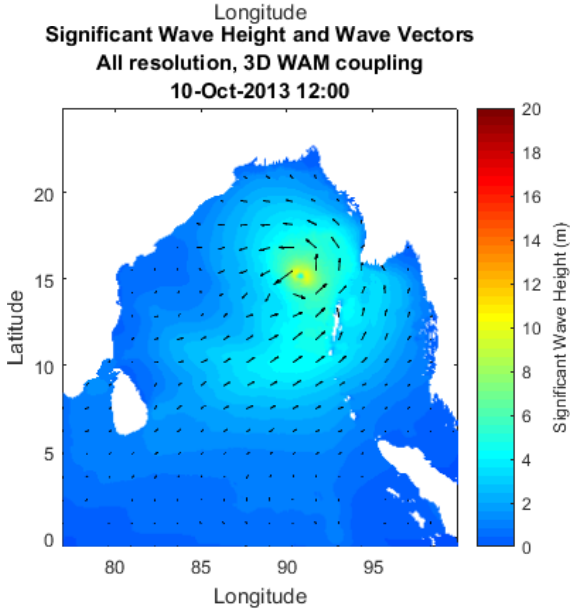
Significant Wave Height and Wave Vectors
All resolution, 3D WAM coupling
10-Oct-2013 12:00
Latitude
Longitude
Significant Wave Height (m)

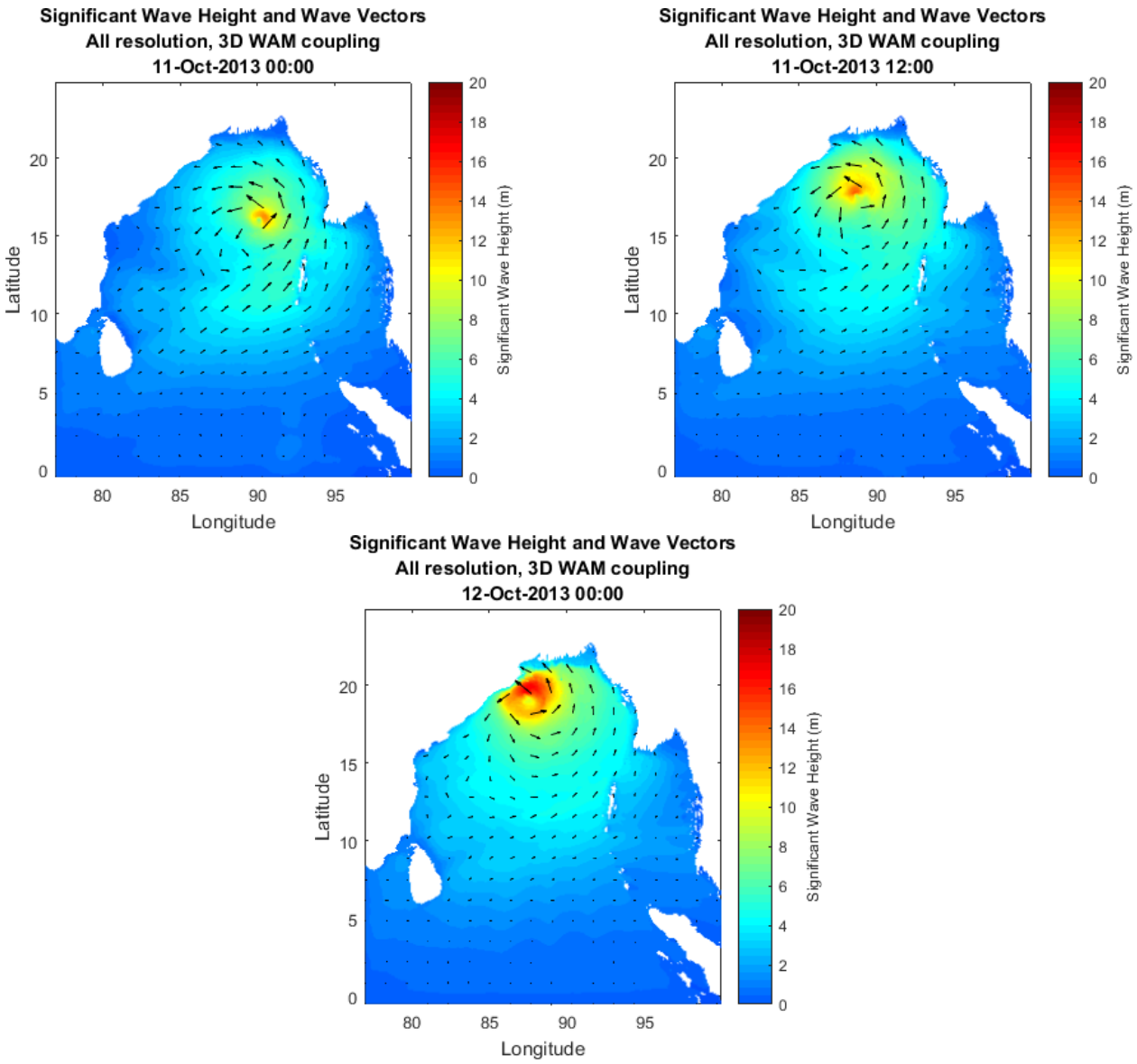

Figure 4.10: Snapshots of the WAM output for Cyclone Phailin, every 12 hours. The colour shows significant wave height and the arrows present the wave direction.

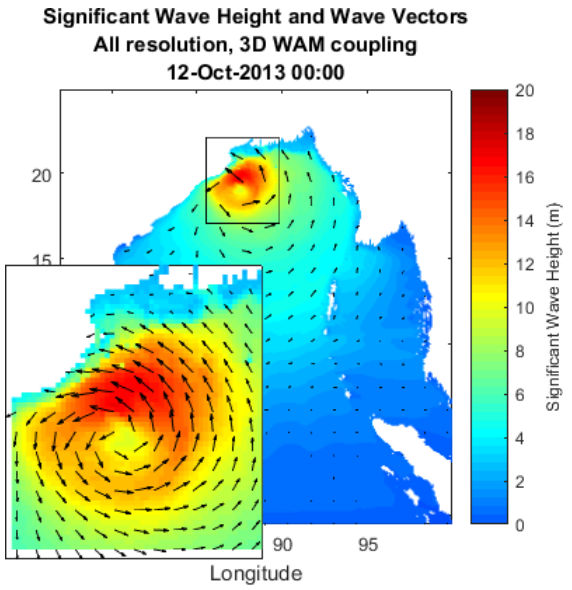

Figure 4.11: Significant wave height and direction at the final model timestep, representing landfall. The colour shows significant wave height and the arrows present the wave direction.

The largest waves occur to the right of the cyclone track. This coincides with the area where the strongest winds are located around a TC. This is due to the additional impact of the TC translation motion, which increases the speed of the wind at the Earth's surface by the amount of the translation speed, and, therefore, the length of time the wind is forcing the sea on the right of the track, and shortens the duration of wind forcing on the left side of the cyclone. The significant wave height increases as the duration of wind forcing increases, so therefore, theory suggests that the largest waves should be on the right side of the TC track. This is known as the effective fetch (Wolf and Woolf, 2006).

Figure 4.11 is a larger version of the final snapshot representing TC landfall, with an enlarged image on the cyclone centre. The maximum significant wave height at landfall is 17.2 m. The large wave vectors show the onshore waves focussing north of Paradip, Odisha on the eastern Indian coast. This is the same location as where the largest storm surge occurs. The storm surge and waves would interact and cause a large storm tide.

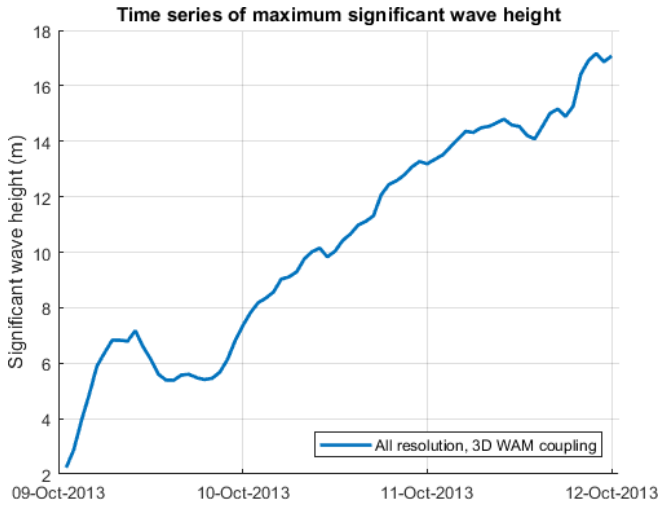

Figure 4.12: Time series of maximum significant wave height across the BoB domain.

The time series of maximum significant wave height is shown in Figure 4.12. This presents

the largest significant wave height simulated across the entire BoB domain at every model timestep. The maximum significant wave height increases at first, but after 12 hours, the significant wave height falls. This corresponds to the initial increase and subsequent decrease in maximum wind speed observed in the WRF simulation described in Section 4.1.1. This is the impact of the modelled cyclone travelling over the Andaman and Nicobar Islands.

After this initial decrease in maximum significant wave height, the waves increase for the remainder of the simulation. The final maximum significant wave height is 17.2 m. The model simulation was too short and did not capture how the waves subsided after the cyclone made landfall.

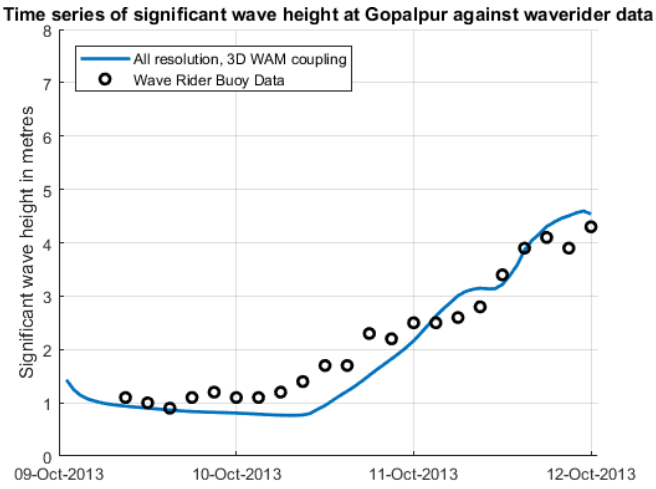

Figure 4.13: Time series of the modelled significant wave height at Gopalpur (blue line) compared with the wave rider buoy observations (black circles) at this location.

Figure 4.13 shows the significant wave height at Gopalpur, comparing the modelled results to the observed time series of the wave rider buoy. The blue represents the modelled output and the circles show the observed wave rider data. The wave rider buoy observational data is described in Section 3.4.2.1. It is worth highlighting that the wave rider buoy lost its mooring during the storm at 0000 UTC 12 October and moved away from the initial location. The data after this time is not included in the comparison.

The time series shows good agreement between the modelled and observed data. The waves begin with roughly 1 m significant wave height, both in the observations and simulation. This significant wave height is maintained through 9 October, and increases during 10 October. The rate of increase of the observations is slower and steadier than that of those modelled. The simulated maximum wave height at Gopalpur is slightly lower, at 4.3 m (prior to losing mooring), and the modelled is 4.6 m.

As described, it appears in the snapshots of Figure 4.10 that the highest wave heights occur to the right of the TC. To investigate this further, Figure 4.14 shows the TC track in orange, and the location of the maximum significant wave height in blue. This image echoes the results inferred from the snapshots, that the highest wave do indeed occur to the right of the cyclone track. This is no surprise, as the theory suggests that this should occur.

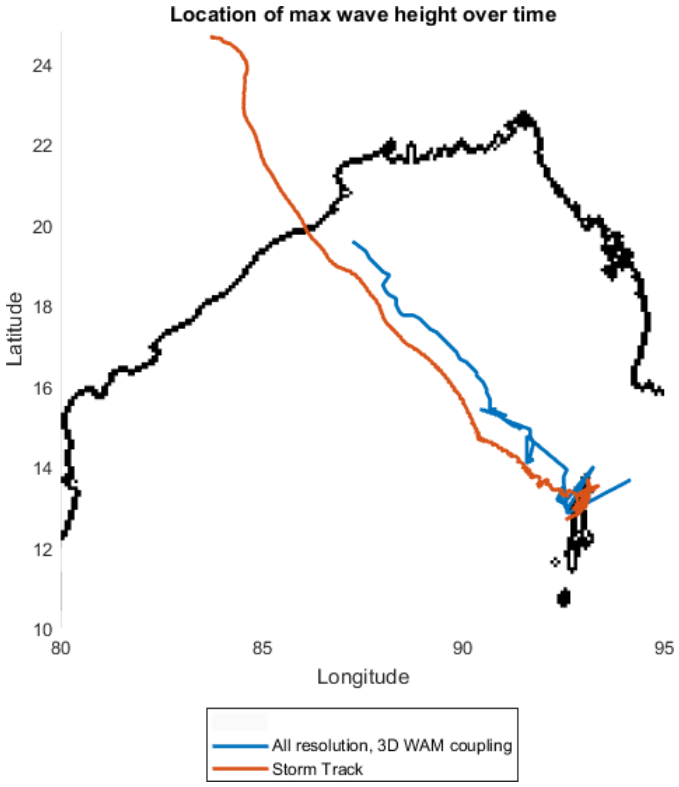

Figure 4.14: Location of the maximum significant wave height during the WAM simulation (blue line), with the WRF modelled TC track (orange line) for comparison.

4.2 Impact of High Resolution

In this section, the impact of high resolution atmospheric modelling is assessed on both the meteorological output as well as indirectly on the ocean components of the modelling system. The different resolution meteorological outputs are compared against each other as well as the observed datasets, to investigate any improvement in accuracy due to higher resolution. For the ocean results, the impact of using different resolution atmospheric forcing is assessed, again by comparing the resulting model outputs.

4.2.1 WRF Results

In the main results in Section 4.1.1 the combined outputs of each of the different resolution domains are presented together. Here, the 12 km, 4 km and 1.3 km resolution domains are presented separately and their results are compared to assess the impact of increasing the modelled horizontal resolution and, as a result, the changes in parametrisation schemes chosen. See Section 3.3 for full details on the set up of each domain.

There are three main model domains: a 12 km grid simulation, and higher resolution runs with smaller grid spacing of 4 km and 1.3 km near to the centre of the tropical cyclone. The nested domains cover progressively smaller areas around the TC centre, so a full comparison of the Bay of Bengal domain is not possible. However, the main TC dynamics occur near to

the eye and this area is covered by all domains and will be examined in full.

Figures 4.15, 4.16 and 4.17 presents 24-hourly snapshots of the model output for each of the domains. These figures introduce the model output, and further plots in the section are used for comparison. The map colour represents the wind speed, with red showing the strongest winds, and the black lines are isobars showing mean sea level pressure, every 8 hPa. The first image at 0000 UTC 9 October shows the initial conditions for each domain. For the 12 km domain the final image pictures the cyclone's rapid dissipation after landfall. For the smaller domains, instead of including this final snapshot, the domain's landfall location is shown in relation to the size of the 12 km domain, to demonstrate the difference in domain size.

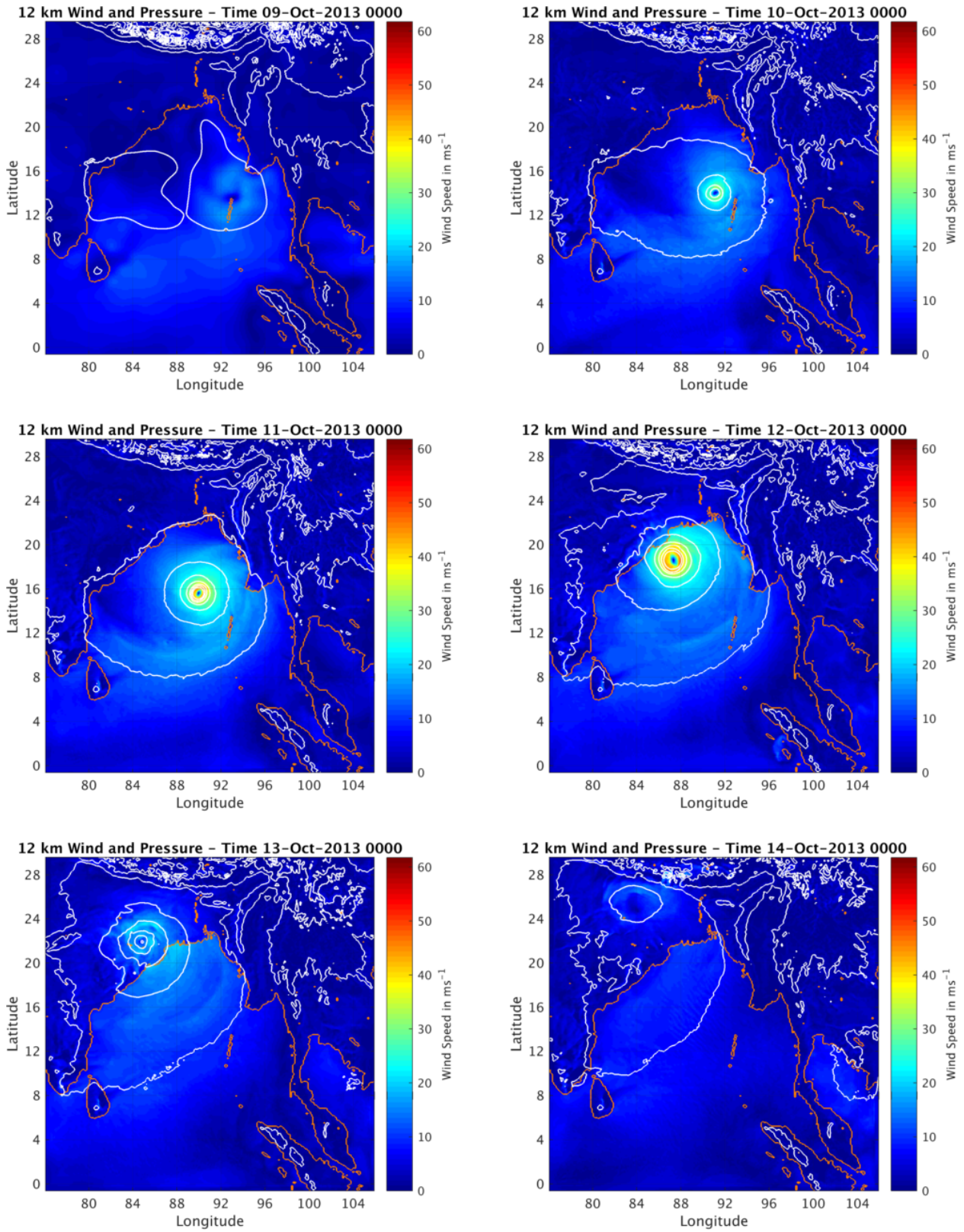

Figure 4.15: Snapshots every 24 hours of the 12 km resolution WRF domain, showing the wind speed (ms^{-1}) in colour, and mean sea level pressure (hPa) as isobars.

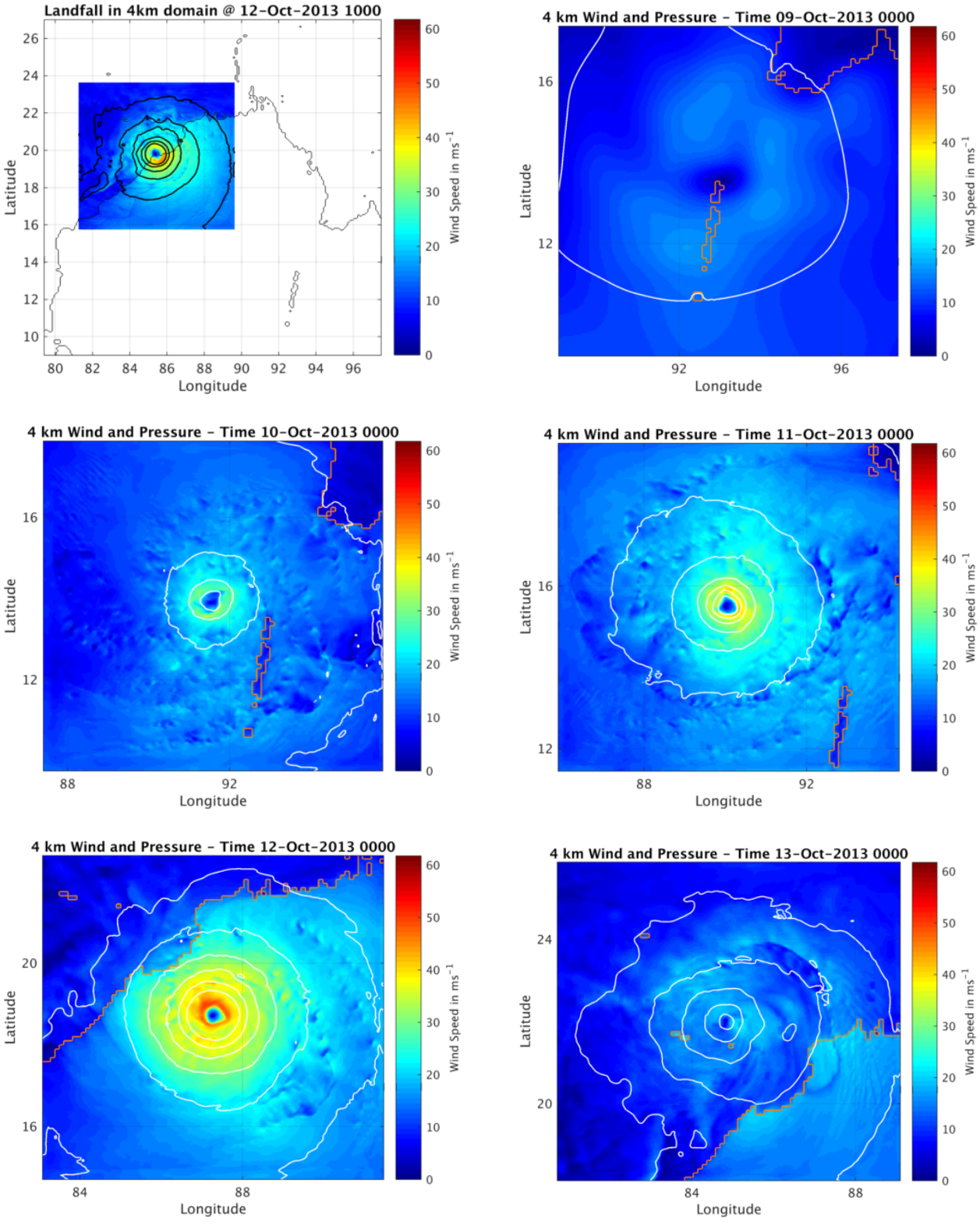

Figure 4.16: Snapshots every 24 hours of the 4 km resolution WRF domain, showing the wind speed (ms^{-1}) in colour, and mean sea level pressure (hPa) as isobars. The first frame demonstrates the 4km domain area.

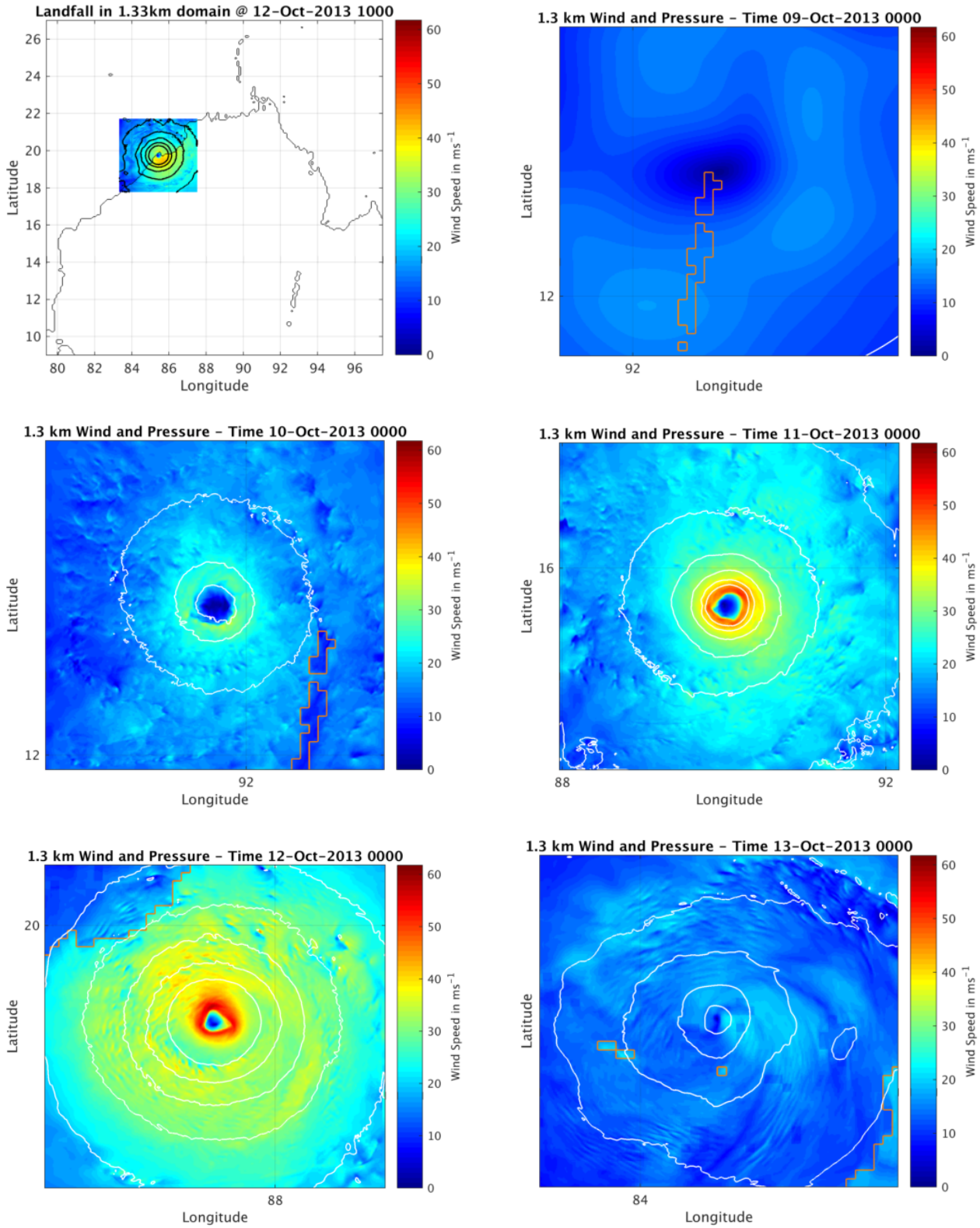

Figure 4.17: Snapshots every 24 hours of the 1.3 km resolution WRF domain, showing the wind speed (ms^{-1}) in colour, and mean sea level pressure (hPa) as isobars. The first frame demonstrates the 1.3 km domain area.

In every domain, tropical cyclogenesis occurs. The TCs simulated have different intensities, both in terms of minimum pressure and maximum wind. From these figures, the simulations appear to be very similar, with cyclone formation, landfall and dissipation occurring at the same time and approximate location in each domain. In the two nested domains at 0000 UTC 12 October, the central band of strong winds around the eye is seen to be non-circular. Theory and numerical analysis of asymmetric TC suggests that a this may be an indication of a decrease in cyclone intensification. The theory behind TC axisymetries and non-circular centres is a complex subject and is discussed in detail in Schubert et al. (1999).

It also seems that the size of the cyclone eye and band of strong winds becomes smaller as the resolution increases. This is described in more detail below.

With each increase in resolution, more detail can be seen in the wind field and in other modelled variables (not shown). With the limited observational data, there is difficulty assessing whether or not this extra detail is more accurate. Therefore, here the differences between the domains are the focus and will be described in more detail in the remainder of this section.

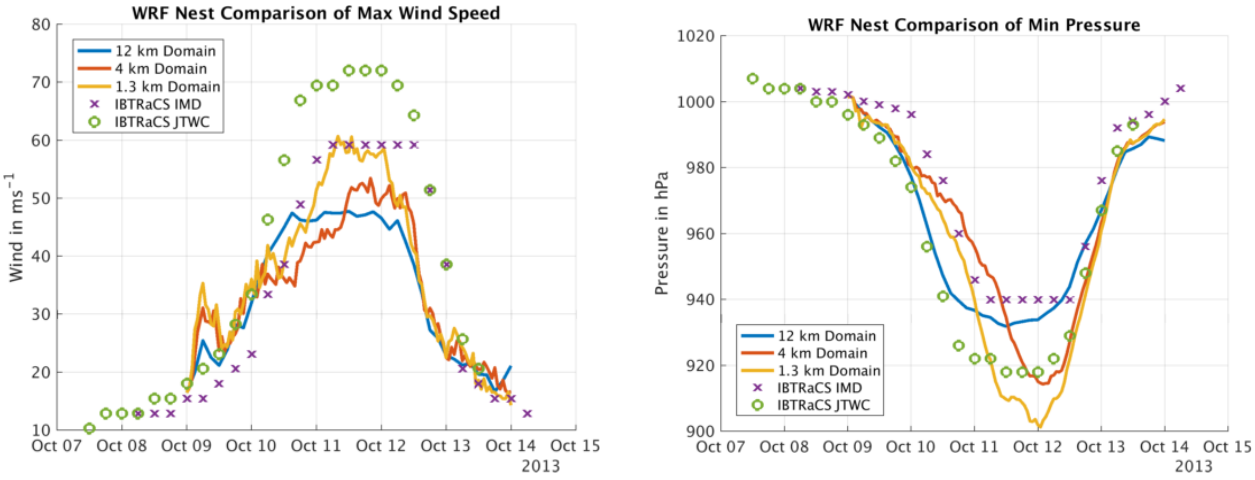

Maximum Wind

Minimum Pressure

Figure 4.18: Output of the different resolution WRF domains compared with the IBTrACS data from both IMD and JTWC. The blue, red and yellow lines represent the 12 km, 4 km and 1.3 km domains, respectively. The purple crosses show the IMD observations and the green circles show the JTWC observation data.

Figure 4.18 shows the maximum wind and minimum pressure time series through the model simulation. Although this is the domain wide minimum pressure and maximum wind for each timestep, it is assumed that in each frame this value is associated with the TC and indicates the intensity of the simulated cyclones. Both the IMD and JTWC observations are included in the plots for comparison, in purple crosses and green circles respectively.

In every resolution domain, a tropical cyclone develops. The TC simulated by each domain differs in intensity, with differences in maximum wind speed of approximately 13 ms^{-1}

and minimum pressure of 30 hPa between the highest and lowest resolution models. The 12 km domain simulates a category 2 TC on the Saffir-Simpson scale with a T number of 5, the 4 km domain develops a category 3 TC, with T number 5.5 and the 1.3 km domain creates a category 4, T number 6. All of the T numbers correspond to a Very Severe Cyclonic Storm according to the IMD categorisation system (see Section 1.2), which is the classification reached by Phailin. The differences between domains are large with respect to the maximum values reached, however the TC classification shows consistency across the different resolutions.

In the maximum wind times series, an initial intensification and dissipation can be seen on 9 October for all domains. The reduction in wind speed coincides with the simulated cyclones travelling over the Andaman and Nicobar Islands, causing a pause in TC intensification. All domains then appear to undergo rapid cyclogenesis. The 12 km parent domain reaches a maximum wind speed of 46 ms^{-1} which is maintained for several model days until landfall. The 4 km and 1.3 km domains reach 54 ms^{-1} and 59 ms^{-1}, respectively, and sustain roughly these values for just over a model day, a shorter period than the parent domain. The 4 km domain intensifies at a slower rate, reaching maximum TC intensity the latest.

In the minimum pressure time series, all the domains show a rapid fall beginning on the 9 October. The rate of this initial decrease in mean sea level pressure is faster than the observed IMD values, although slower than the JTWC data, which shows that the cyclogenesis modelled is within the correct range. The 12 km domain has the sharpest rate of decrease, falling to less than 940 hPa by 1200 UTC 10 October, and the 4 km domain has the slowest rate of decrease, with the pressure steadily falling through the 9, 10 and 11 October. Both the nested domains reach their lowest minimum pressure at 0000 UTC 12 October, later than the parent domain and both the observed datasets. The 1.3 km domain reaches the lowest minimum pressure of the WRF domains, the pressure falling to 900 hPa. This is lower than both the IMD and JTWC observations which reach 940 hPa and 915 hPa, respectively, and coincides with the domain reaching the highest maximum wind speeds. All the domains experience a rapid increase in minimum pressure beginning on 12 October, when the simulated cyclones reaches the coast. All domains have a similar rate of filling, and the time series converge to almost identical values on 13 October.

Both of the nested domain maximum wind speed time series have more high frequency variability than the parent domain. This variability may be the model representation of convective gusts, with wind speeds changing rapidly. It is expected that the higher resolution domains would simulate gusts in more detail, as convection is not parametrised and instead is explicitly resolved. The minimum pressure time series are smooth for all domains. This implies steady changes with little variability. This variable is not impacted by the change in convective parametrisation scheme between the model domains, which is as to be expected.

Figure 4.19 shows the model output at the time of maximum winds for each of the domains. The images show the same physical area, so are more easily comparable than the larger snapshots shown in Figures 4.15, 4.16 and 4.17 above.

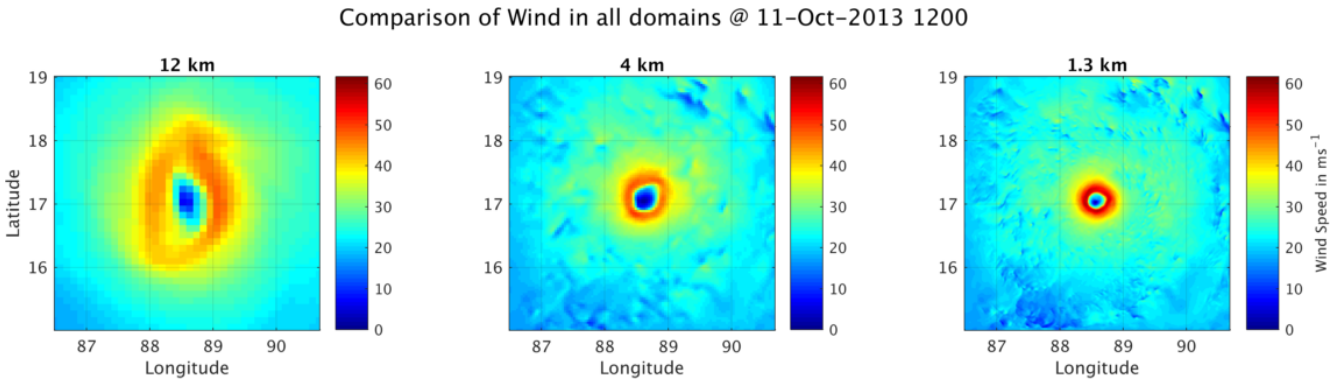

Figure 4.19: Comparison of wind speed across the 12 km, 4 km and 1.3 km resolution WRF domains at the time of maximum wind. The colour shows the wind speed in ms^{-1}.

Here, it is clearly seen that the size of TC centre is very different in each of the domains. The 12 km resolution domain image is pixelated, due to the grid size, and the cyclone eye covers a physical area several times larger than that of both the 4 km and 1.3 km domains. The 4 km and 1.3 km resolution cyclones are much more similar in size, however the eye in the 4 km domain is larger in diameter.

These differing sizes are described by the radius of maximum winds. Figure 4.20 shows the time series of the radius of maximum wind (RMW) for each domain throughout the Phailin simulation. After initial anomalies, the time series show that the RMW of the parent domain is larger than both nested domains throughout the majority of the simulation, before landfall. Similarly, the 1.3 km domain generally has the smallest RMW of the three domains. At the time of maximum intensity, RMW of the highest resolution domain best matches the observed data available, with a value of 10 miles against the observed 10 miles. The parent and 4 km domains have RMW of 24 and 20 miles respectively. This suggests that the higher the resolution, the smaller the RMW for this model simulation. This is likely to have implication for the storm surge simulation, as the increase in water level is closely linked to the area of sea surface impacted by the strong winds.

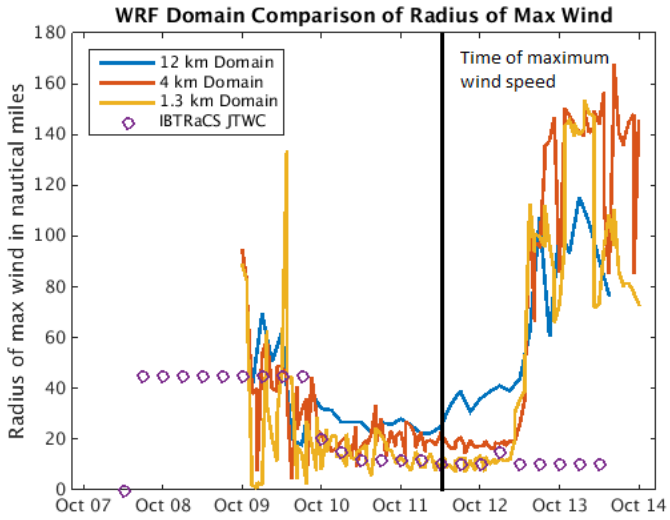

Figure 4.20: Time series of the RMAX in miles for each of the WRF domains, compared with IBTrACS IMD data. The blue, red and yellow lines represent the 12 km, 4 km and 1.3 km domains, respectively. The purple circles show the JTWC observation data.

Figure 4.21 shows the track of the cyclone in each of the domains. The track is created by

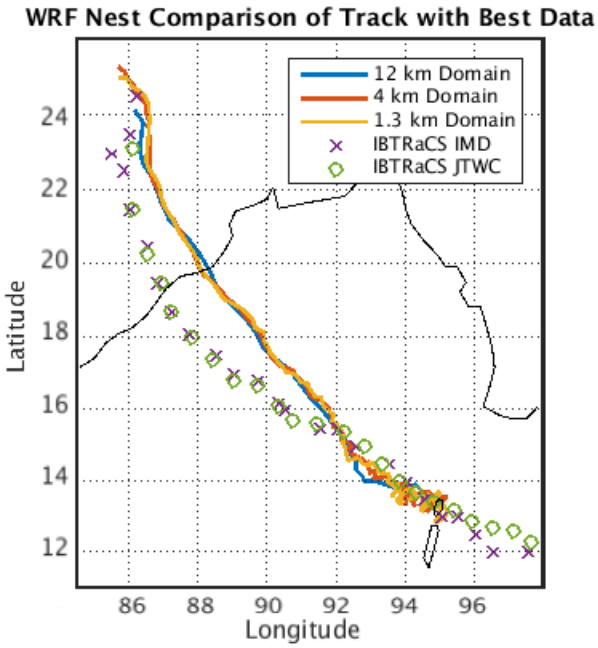

Figure 4.21: Track of the different resolution WRF domains compared with the IBTrACS data from both IMD and JTWC. The blue, red and yellow lines represent the 12 km, 4 km and 1.3 km domains, respectively. The purple crosses show the IMD observations and the green circles show the JTWC observation data.

plotting the location of the minimum pressure for each time step, and shows the movement of the cyclone eye. In the figure, the observed locations are shown with purple crosses and green circles for the IMD and JTWC datasets, respectively.

The tracks for the different domains are very similar. They all begin near to Smith Island of the Andaman and Nicobar Islands. All the cyclones move north-westwards and remain close to the observed locations. The modelled and observed tracks cross at 15°N, 90°E and the simulated cyclones move further northwards. All the domains simulate landfall at approximately 20°N and 85°E, some 30 km away from the recorded landfall location near to Gopalpur.

All the domains appear to have almost identical tracks. This suggests that grid resolution may not play an important role in simulating the synoptic forces which determine a cyclone's translation direction. From Section 2.1.1, it is seen that this result could be expected as the cyclone initialisation and boundary conditions have been seen to impact the track most. Here, each of the smaller domains receive boundary conditions from the larger domain which contains it, so the different resolution domains are not independent of one another.

Figure 4.22 shows the distance between the simulated location of the minimum pressure (cyclone centre) in the WRF domains and the observed IMD location, thus showing the track error time series. The dotted lines represent the average error across the simulation. All the domain errors are very similar, echoing the conclusions stated previously.

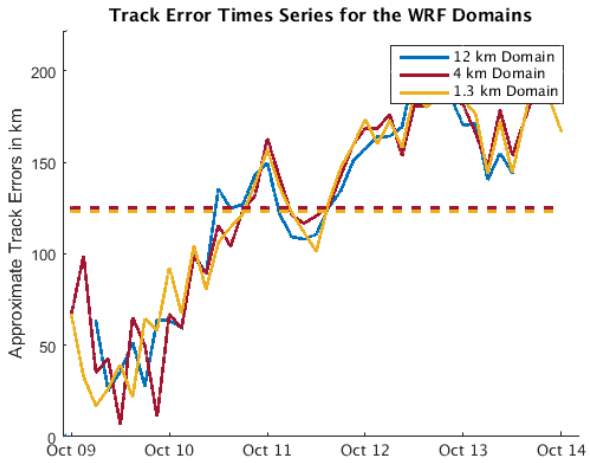

Figure 4.22: Track error time series for the WRF domains compared with the IBTrACS IMD data. The blue, red and yellow lines represent the 12 km, 4 km and 1.3 km domains, respectively.

This figure shows how the track error develops through the simulation. At first, the errors are relatively small remaining less than 1° throughout 9 October. During the 10 and 11 October, the track errors grows as the modelled cyclones move further northwards than the observed locations. Once a distance of approximately 1.5° is reached, the errors remain approximately the same even once landfall has occurred. The average error of the nested domains is incredibly similar.

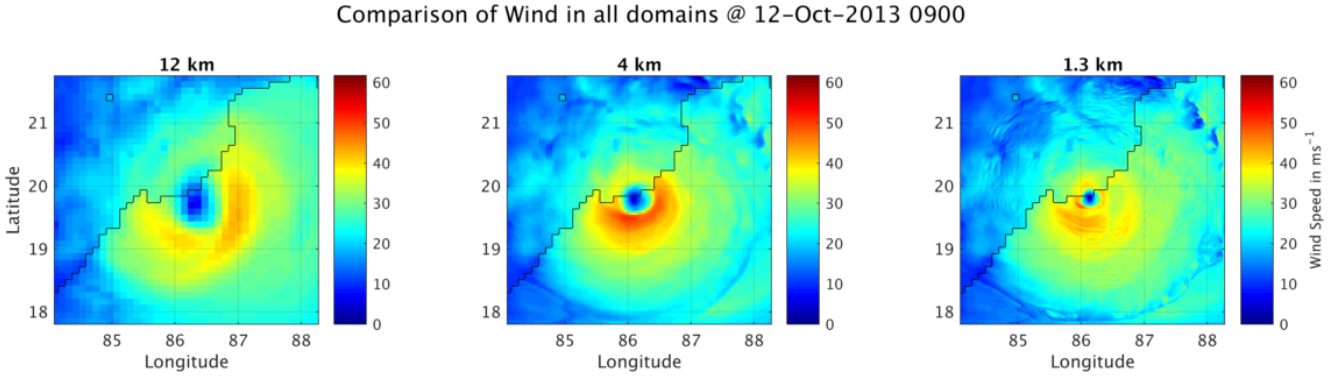

Figure 4.23: Comparison of the different resolution WRF domains at the time of landfall. the colour represents the wind speed in ms^{-1}.

Figure 4.23 compares the three domains at the time of cyclone landfall. For all of the domains, this is on the same time step - 0900 UTC 12 October. It was shown that the cyclone tracks are very similar, and therefore it is no surprise that landfall time is the same for each of the domains.

Similarly, as with Figure 4.19, pixelation can be seen in the image for the parent domain. The simulated cyclones are closer in size at landfall, with comparable RMW values (see Figure 4.20). The winds remain stronger for longest in the 4 km domain. It is unclear why this is occurring, although this does not appear to be in response to higher resolution or the different

parametrisation schemes used, as evidenced by the lack of trend seen into the 1.3km domain.

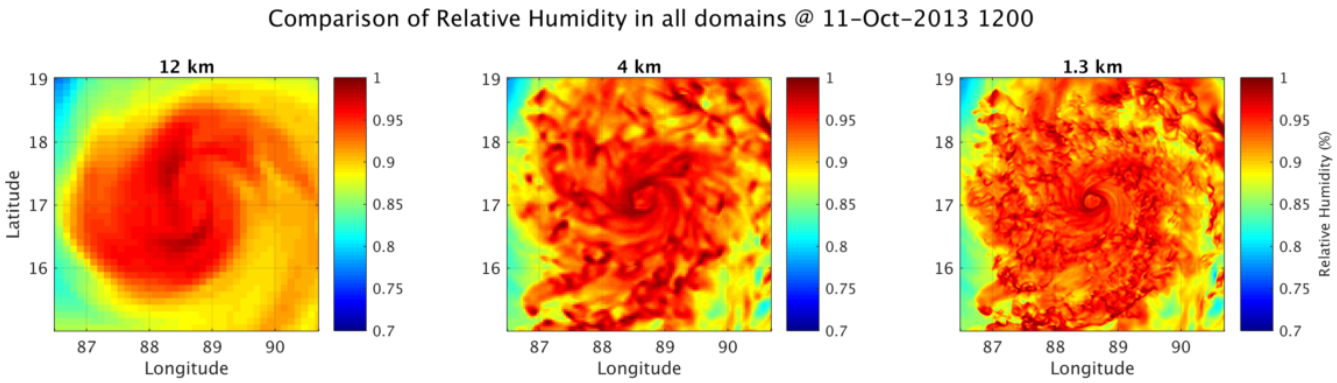

Figure 4.24: Comparison of relative humidity in the WRF domains at 1200 UTC 11 October. The colour represents the relatively humidity.

Figure 4.24 shows the surface relative humidity at the simulated maximum intensity, comparing the three domains. Red indicates high relative humidity, which is used as a proxy for cloud. Blue indicates a lower relative humidity in areas where there is little low cloud.

As resolution increases, more fine detail can be seen. This includes eddy circulations within the relative humidity fields. This is a direct effect of the different convection parametrisation schemes used. The 12 km domain parametrises convection. The nested domains are of a high enough resolution to allow for convection to be explicitly calculated, and therefore, do not include convection parametrisation. The 1.3 km domain shows a very complex cyclone, with numerous 'layers' or cloud bands around the cyclone centre, and many turbulent eddies being resolved. The 4 km domain appears to be a transition regime, where the cyclone complexities appear to be resolved, but without the detail of the finer grid spacing.

4.2.2 POLCOMS-WAM Results

The results shown in Section 4.1.2 are POLCOMS and WAM model output from simulations which were forced using the high resolution WRF results presented in Section 4.1.1.

To assess the impact of higher resolution meteorological forcing, here the POL-WAM simulation results which use meteorological forcing from the WRF 12 km resolution domain alone are presented and compared with the main experiment in the previous section. This will allow the impact of increasing the horizontal resolution of the meteorological forcing on the ocean domain to be assessed.

The WRF results shown in Section 4.2.1 suggest that the high resolution WRF domain gives the most intense tropical cyclone simulation. Therefore, it is expected that the higher resolution meteorological forcing will result in a higher storm surge height, and an increase in significant wave heights.

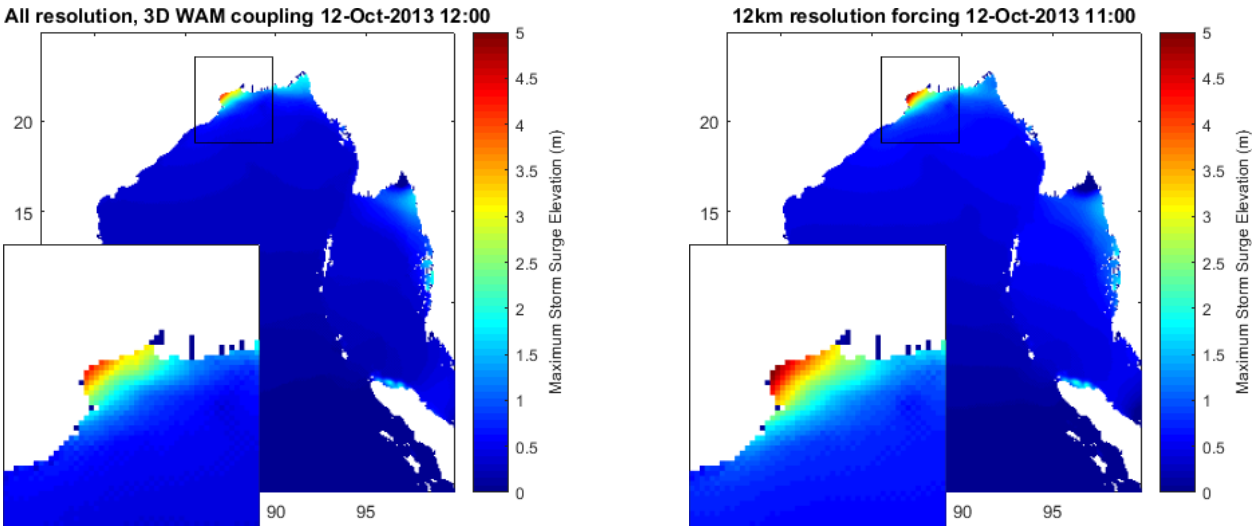

Figure 4.25: Comparison of the maximum storm surge output using different resolution atmospheric forcing, with high resolution forcing on the left. The colour represents the sea surface elevation in metres.

4.2.2.1 POLCOMS Output

In this section, the outputs from POLCOMS using the 12 km WRF forcing will be presented and compared with the main results presented in Section 4.1.2. The results obtained with the higher resolution WRF forcing will be referred to as 'All resolution' as the meteorological input contained output from the 12 km, 4 km and 1.3 km WRF modelled domains. As with POLCOMS model output previously presented, sea surface height will be the main variable assessed.

Figure 4.25 shows the maximum sea surface height simulated for both the 12 km resolution forcing and the All resolution forcing model runs. The colour signifies the sea surface elevation in metres. The inset figures show a larger map of the coastal region, where the sea surface elevation represents the storm surge.

The maps show that the 12 km resolution forcing produces the largest storm surge, with sea surface elevations of 5.0 m along the Indian coast. The All resolution model simulation results in a storm surge of 4.2 m in comparison. This may be caused by the different sizes of the TCs in the different resolution WRF domains. The RMW of the higher resolution simulation is markedly smaller than that simulated in the 12 km domain, see Section 4.1.1 for details. This means that the area of ocean surface experiencing cyclone strength winds may be larger for the larger cyclone, and the strong winds may apply for a longer duration. Both of these factors would results in a larger rise in sea surface elevation.

The model snapshots shown in Figure 4.26 directly compare the sea surface elevation during the different POL-WAM simulations - the All resolution forcing on the left and the 12 km forcing on the right. The colours represent the sea surface height in metres and the cyclone track is shown by the black and grey lines. It is clear from these plots that the raised sea surface elevation associated with the cyclone is larger in diameter for the coarser

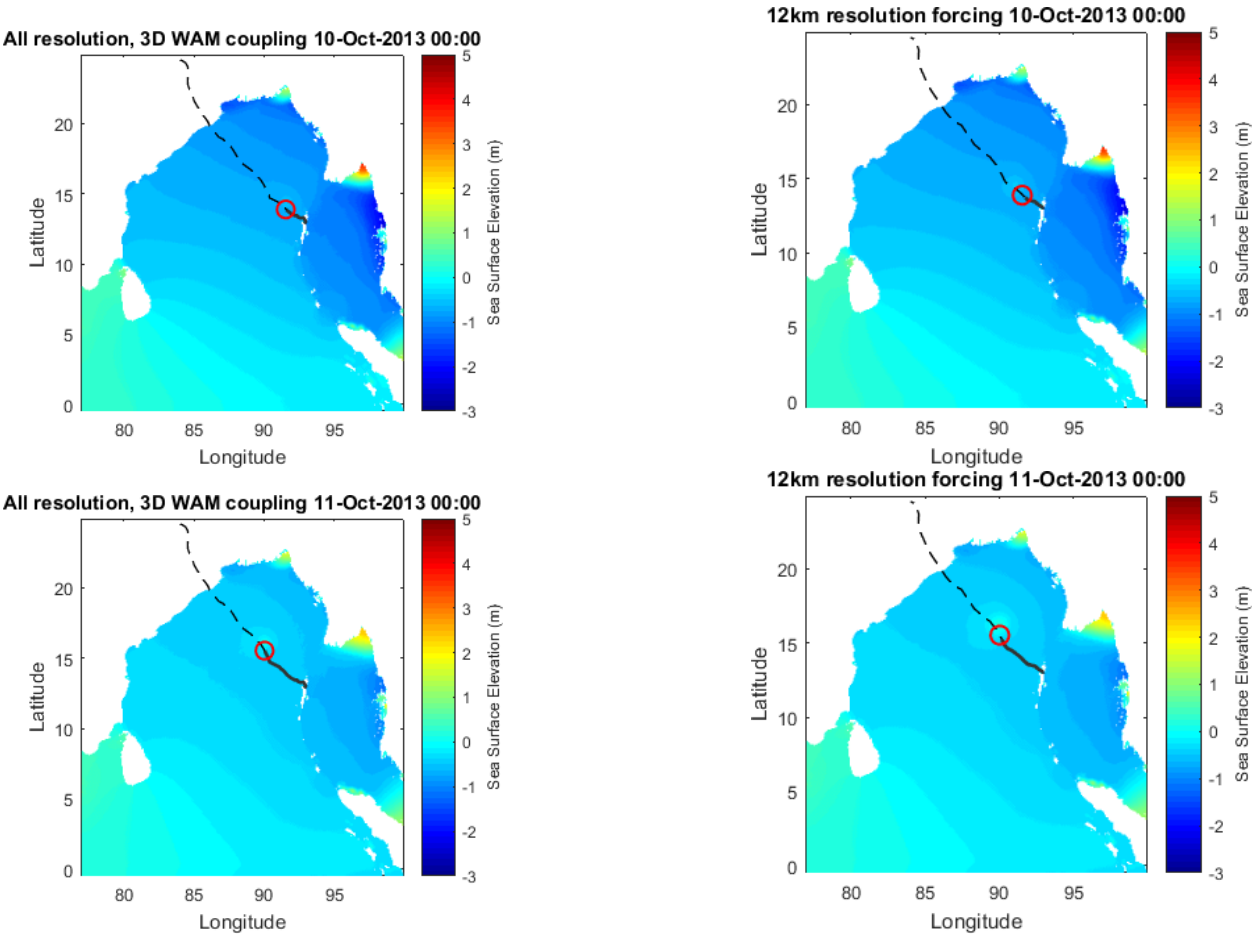

Figure 4.26: Snapshots comparing the POLCOMS sea surface elevation output for the model runs with 12 km resolution on the right and All resolution on the left. The figures include the WRF modelled track in grey and black.

resolution domain and smaller for the high resolution WRF forcing. This echoes the RMW trend seen in the WRF results; with the 12 km resolution domain producing a larger storm than the higher resolution model domains. The impact of the cyclone size in these plots seems fairly small, but the resulting storm surge at the coast is much increased for the lower resolution forcing.

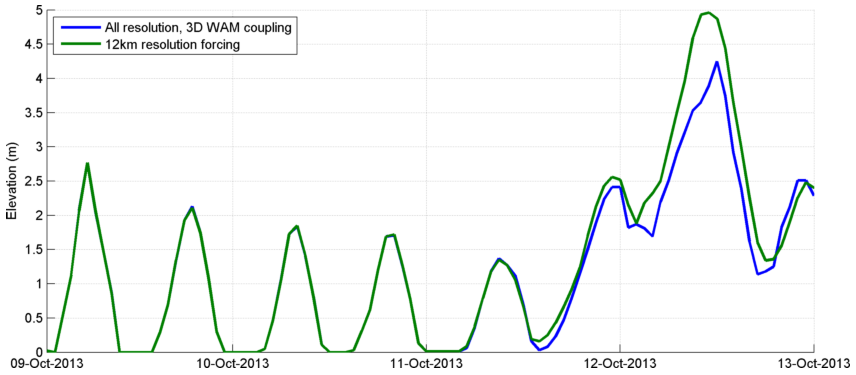

Figure 4.27: Time series of maximum sea surface elevation across the BoB domain for both the 12km resolution (green) and all domain WRF forcing (blue).

Figure 4.27 shows the maximum sea surface elevation near to the coast for the model simulation. This is calculated for the area of the smaller, inset map in Figure 4.25 in order to eliminate increased sea surface elevation due to tides in other parts of the Bay of Bengal. The green line represents the 12km resolution forced simulation, and the blue line is the All resolution simulation.

The figure shows that the impact of using higher resolution atmospheric forcing is to decrease the modelled storm surge height. The coarser resolution WRF boundary conditions resulted in a simulated storm surge of 5.0 m. The All resolution WRF forcing simulated a storm surge of 4.2 m.

This difference is contradictory to what may have been expected, as the higher resolution WRF simulations resulted in more intense cyclones, with higher maximum wind speeds. However, the difference in sea surface elevation may be a result of the different sized cyclones. In the coarser resolution WRF simulation, the cyclone is larger in diameter. This means that the cyclone strength winds are affecting the sea surface over a larger area for a longer period of time. The increased area and duration results in a higher sea surface height.

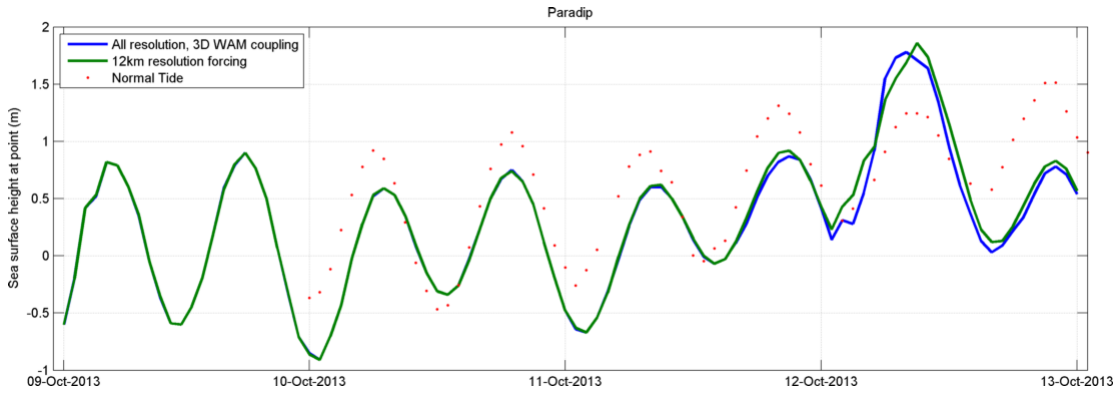

Figure 4.28: Time series of sea surface elevation at Paradip for both model runs with the tide gauge observed data. The 12 km forcing is in green, the all resolution in blue, and the observation is shown by the red dots.

In contrast to the coastal sea surface elevation, Figure 4.28 shows the sea surface height

time series for Paradip. The green line represents the 12 km resolution model output, the blue line shows the All resolution simulation, and the dots are the observed Paradip tide-gauge observations.

As previously described, the observed tide gauge time series is significantly different to the modelled tide. At Paradip there is little difference between the two modelled sea surface elevations. Paradip is located approximately 250 km away from the cyclone track and land-fall location, and therefore the different between the meteorological forcing at this point will be minimal. Therefore, it is not a surprise that the resultant sea surface elevations are not significantly different.

The Hovmöller plot of sea surface height along the Indian coast (shown in red) for the 12 km resolution atmospheric boundary is shown in Figure 4.29. The same pattern as Figure 4.8 is observed, with evidence of a coastally trapped Kelvin wave. The values of sea surface elevation are higher here, echoing the findings shown in Figure 4.25 and Figure 4.27.

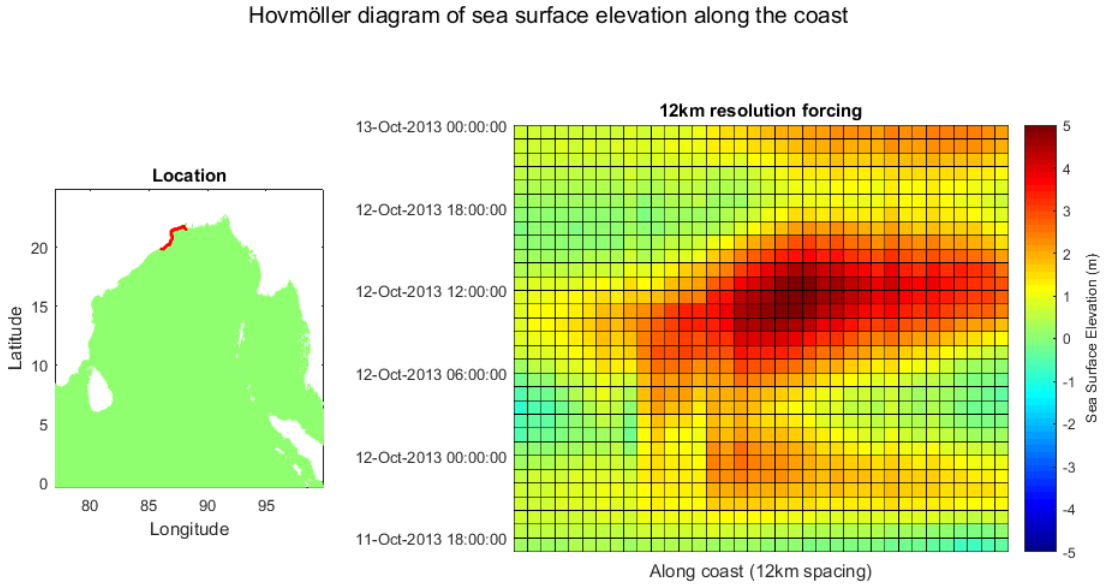

Figure 4.29: Hovmöller plot of sea surface height along the Indian coast, in red, for the 12 km resolution atmospheric forcing. The colours on the right plot represent sea surface height.

4.2.2.2 WAM Output

In this section, the outputs from WAM using the 12 km WRF forcing are presented and compared with the main results presented in Section 4.1.2.2. As with the POLCOMS modelled outputs, the results obtained with the higher resolution WRF forcing will be referred to as 'All resolution'. Here, significant wave height and wave direction are the main variables assessed.

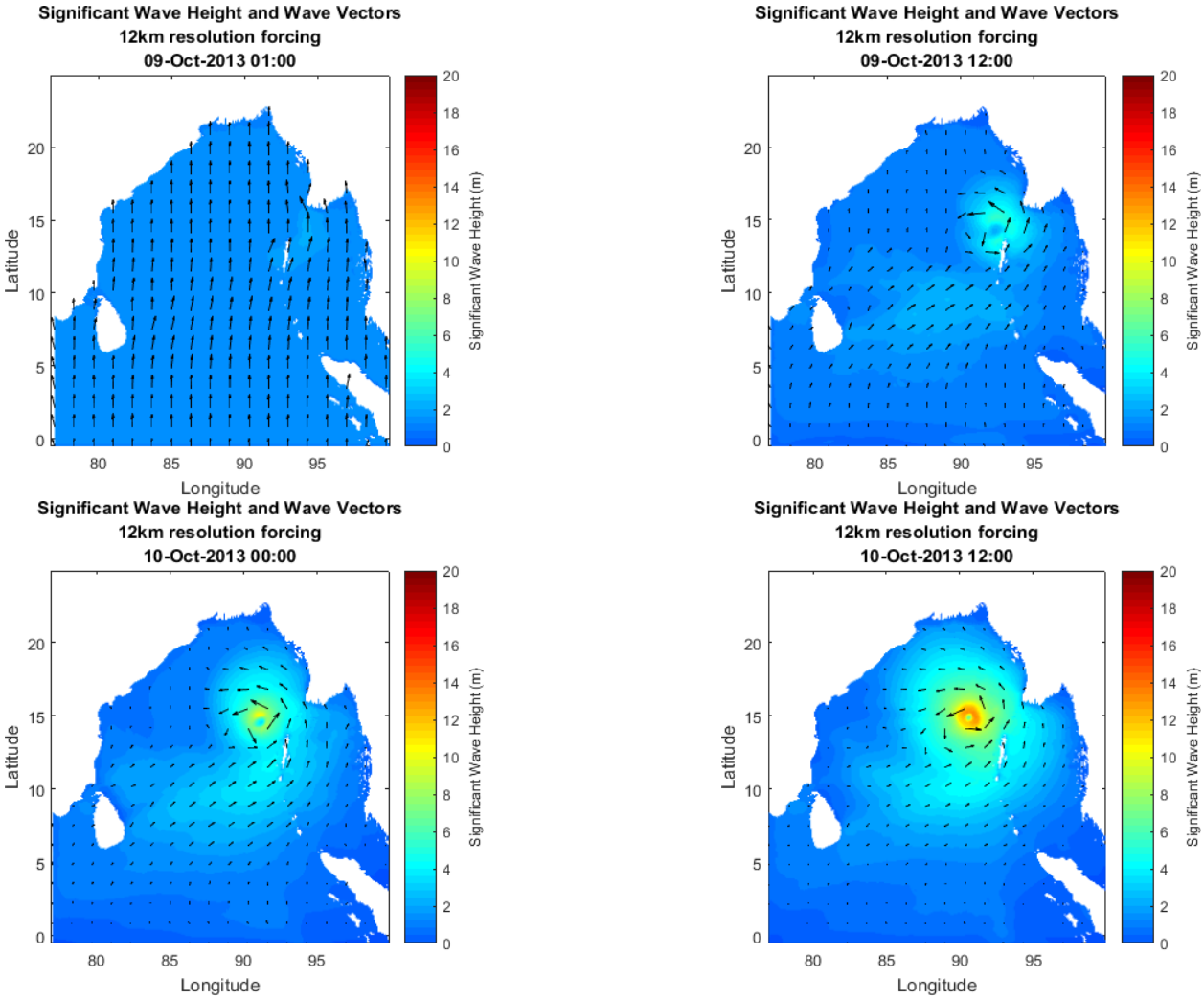

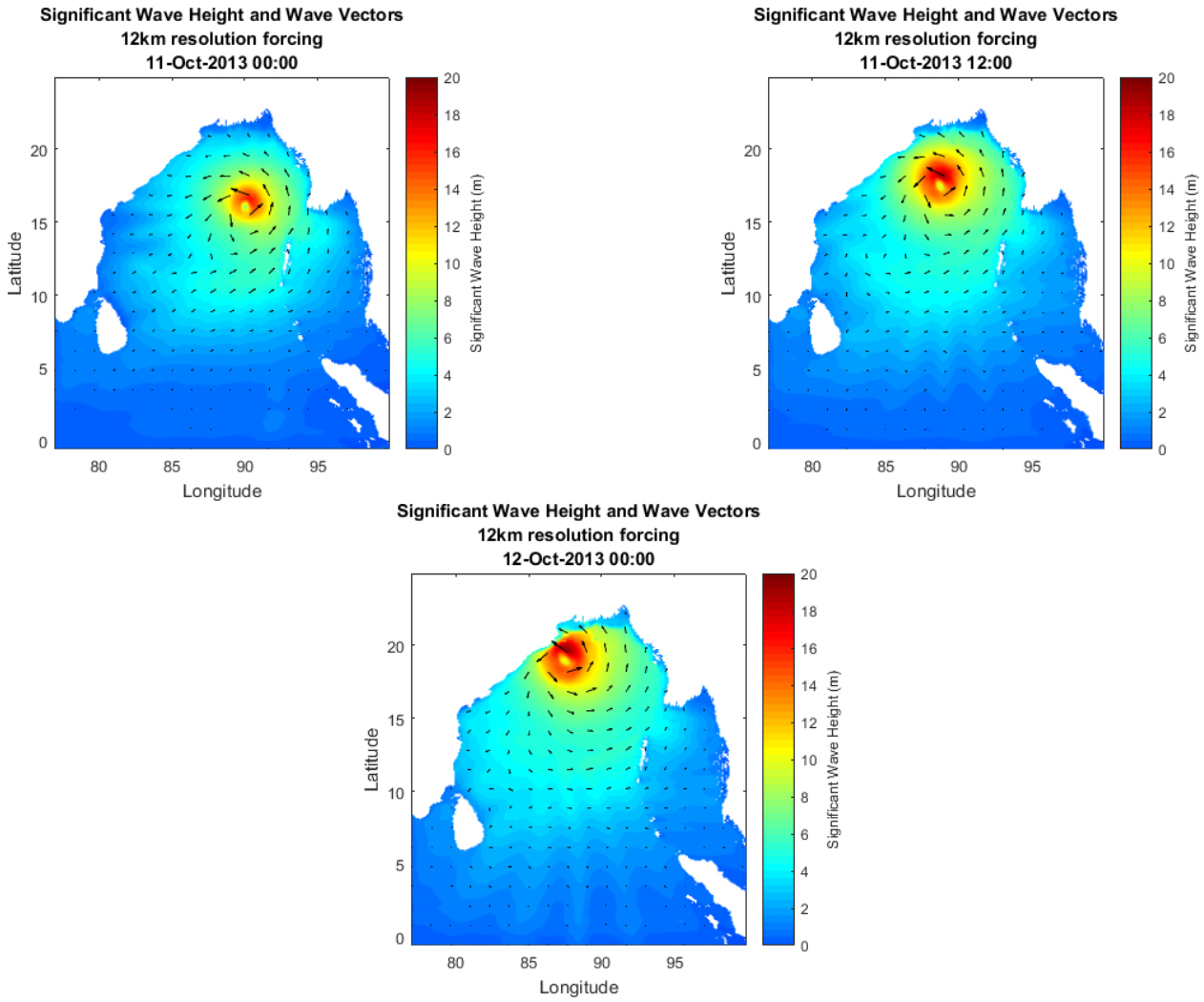

Figure 4.30: Snapshots every 12 hours of the WAM output using the 12 km resolution WRF model forcing. The colour shows significant wave height and the arrows present the wave direction.

The images in Figure 4.30 show the significant wave height predicted by WAM for Cyclone Phailin, using the 12 km resolution WRF model simulation as meteorological forcing. These plots can be compared with those shown in Figure 4.10 to see the impact of increased resolution meteorological forcing on the waves forecast.

The 12 km resolution simulation has many of the same features as the All resolution model run. The coarser cyclone wind forcing is still able to generate large waves across a significant proportion of the BoB, from as early as the third frame. The significant wave height increases through the simulation, as does the area over which waves are generated. The waves circulate cyclonically around the centre of the TC. The largest waves occur to the right of the cyclone track, coinciding with the area of strongest winds.

The maximum significant wave heights for both the 12 km resolution and All resolution forcing WAM model runs are shown in Figure 4.31. The 12 km resolution simulation resulted

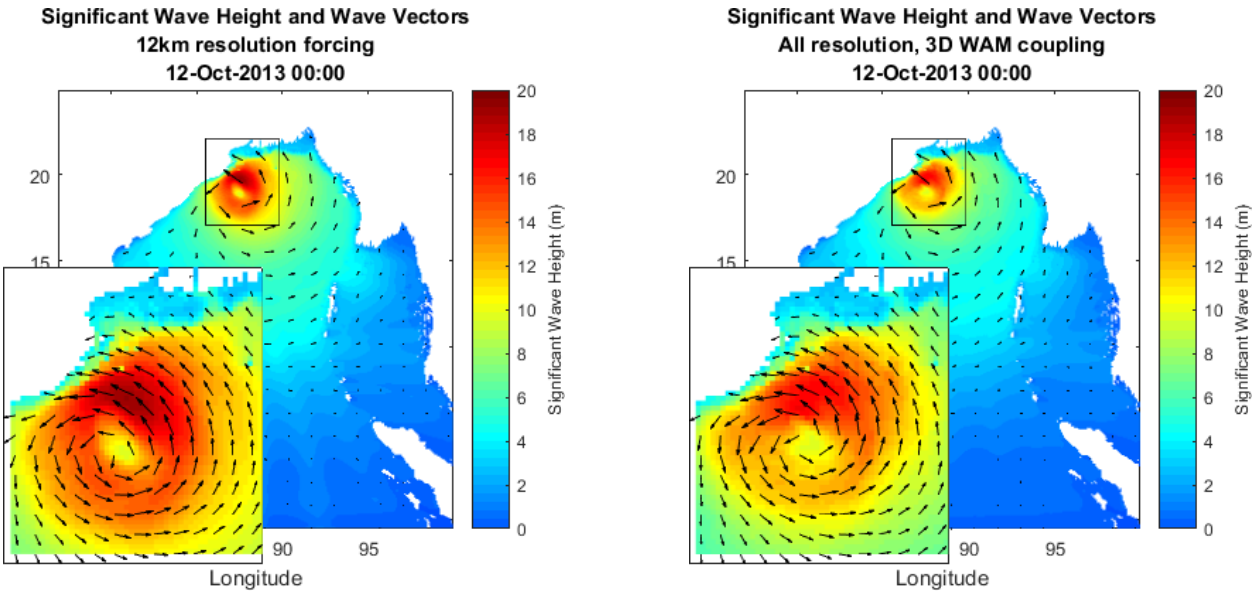

Figure 4.31: Snapshot showing the maximum significant wave height modelled using each of the WRF forcing. The colour shows significant wave height and the arrows present the wave direction.

in larger significant wave heights than the All resolution. This is a similar result to that seen in the POLCOMS output, with larger sea surface elevation occurring with the coarser resolution atmospheric boundary.

Along with larger significant wave heights, the 12 km resolution model run has a larger area with higher waves, as can be seen in Figure 4.32. A larger proportion of the inset frame is red, indicating significant wave heights in excess of 18 m. As with the POLCOMS output, this is likely the impact of the larger cyclone simulated in the 12 km resolution WRF domain.

Figure 4.32 shows the maximum significant wave height across the BoB domain for both the 12 km resolution and All resolution model simulations. The 12 km forcing is shown in orange and the All resolution forcing is in blue. From the snapshots above, we see that the maximum significant wave height is associated with the TC throughout the simulation.

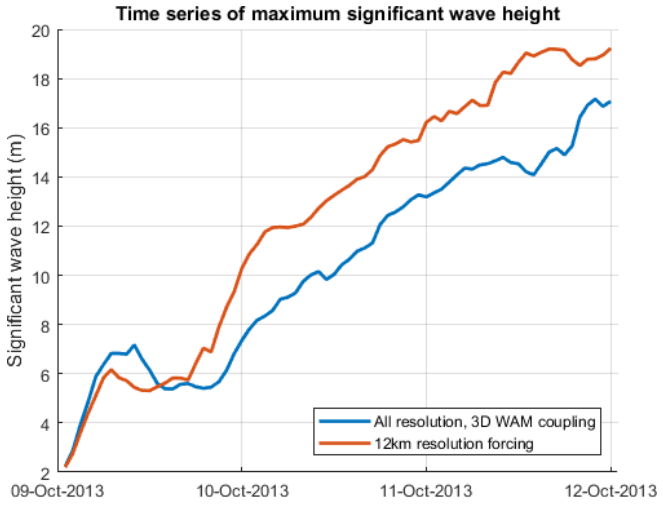

Figure 4.32: Time series showing the maximum significant wave height across the BoB domain for both resolution WRF forcing. The all resolution is shown in red, and the 12 km resolution forcing in blue.

From this graph, it is confirmed that the 12 km resolution meteorological forcing produces the largest significant wave heights. Initially, this is not the case, with the All resolution have

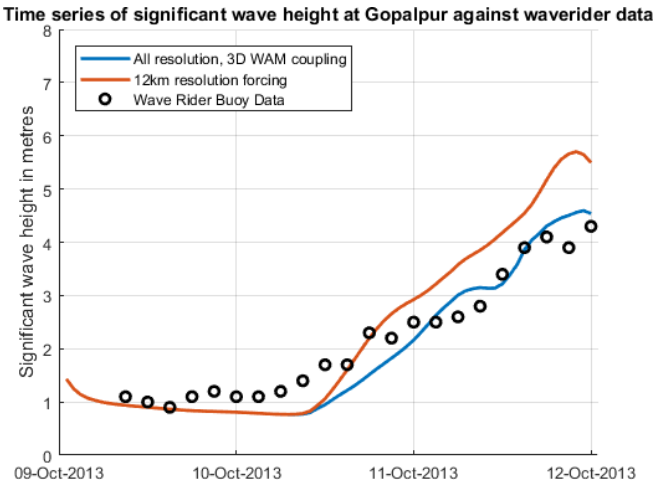

Figure 4.33: Time series of significant wave height at Gopalpur for both the WRF forcing model runs. The all resolution is shown in red, the 12 km resolution forcing in blue and the observations are shown by the black circles.

larger waves for the first 18 hours of model simulation. Both model runs experience a dip in wave growth, associated with the TC's pause in intensification while it travels over the Andaman and Nicobar Islands. After this initial pause, the 12 km resolution model run has a period of intense wave growth, more extreme than that seen in the All resolution run. The final maximum significant wave height is 19.1 m for the 12 km resolution WRF model forcing.

The significant wave height at Gopalpur for both the 12 km and All resolution model runs are shown in Figure 4.33, along with the wave rider buoy observation data. The 12 km resolution model outputs higher waves than those observed at this location, although the trend is very similar. This follows the trends of the 12 km resolution run producing larger waves. Note, that the wave rider buoy loses its mooring at 0000 UTC 12 October, after the end of the time series graph.

Similarly with the main results, in order to assess the location of the largest waves in comparison with the TC location, Figure 4.34 shows the 12 km WRF modelled TC track along with the locations of the highest waves for both of the WAM model runs. The 12 km resolution forcing model is shown in

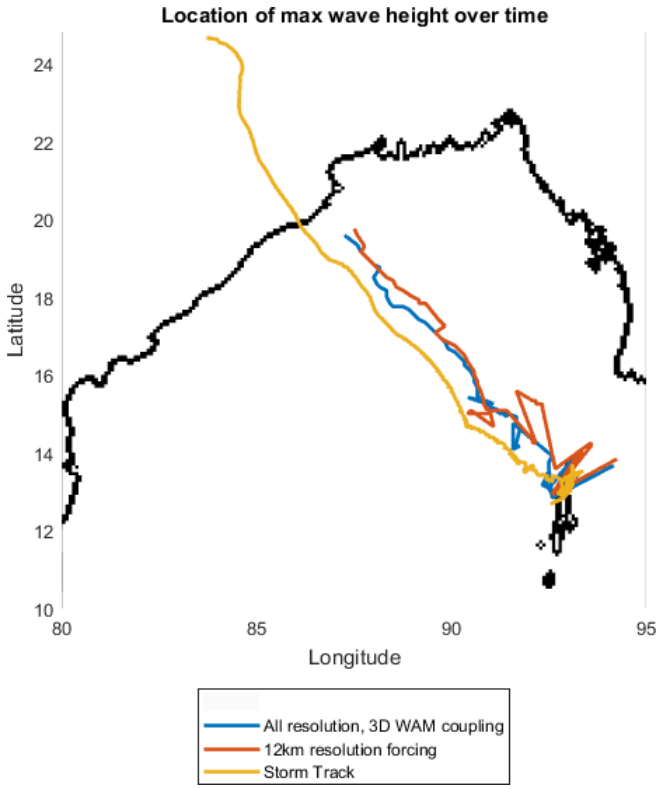

Figure 4.34: The locations of the maximum significant wave height with the modelled TC track for comparison.

orange, the All resolution is shown in blue, and the TC track is in yellow.

For both the simulations the largest significant wave heights are in similar locations. These occur to the right of the TC track. This is to be expected, as this is also the location of the highest wind speeds, and the impact of the translation speed and direction.

4.3 Start Time Sensitivity Tests

Initialisation of tropical cyclone forecasting models is one area where large errors can occur. This is described in Section 2.1.2. In the initial WRF model sensitivity tests described in Section 3.3.3, different initial conditions were trialled including ERA Interim meteorological reanalysis fields and GFS model analysis data. More intense cyclones were produced with the GFS analysis fields, therefore the GFS analyses were chosen to provide initialisation for the main experiments.

The initial conditions, clearly, will be very dependent on the start time used. The start time is chosen to be 0000 UTC 9 October for the main experiments, in order to capture the rapid cyclogenesis which occurred on 10 October in reality.

In Section 4.3.1, different simulation start times are tested using the 30 km WRF model, to assess the impact of different initial fields on the TC simulation. Along with the start time used in the main experiments, 0000 UTC 9 October, another start time is tested using the higher resolution WRF model, 1200 UTC 9 October. The results from this simulation are used to show the impact of start time on the high resolution TC simulated.

Further to this, the impact of the alternative start time WRF simulation on the POL-WAM model system is also investigated in Section 4.3.2.

4.3.1 WRF Results

To more thoroughly demonstrate the importance of initialisation, the WRF model starting time was varied. According to the IMD report, the most rapid intensification occurred on the 10 and 11 October. Therefore, one criterion used is that simulation start time must be before 0000 UTC 10 October to test the model's ability to simulate this cyclogenesis.

Ideally, the start time would be as early as possible in order to assess the skill of WRF to simulate the cyclone accurately from a benign initial synoptic weather pattern to a fully fledged TC, in timescales which are relevant to TC forecasting (i.e. several days). Several different start times are tested with the 30km resolution WRF model used for the earlier sensitivity tests, described in Section 3.3.3. Nine start times are simulated at 6-hourly intervals from 0000 UTC 8 October to 0000 UTC 10 October.

Figure 4.35 shows the time series of maximum wind and minimum pressure for all of these experimental runs, along with the observed IBTrACS data. All of the runs show a

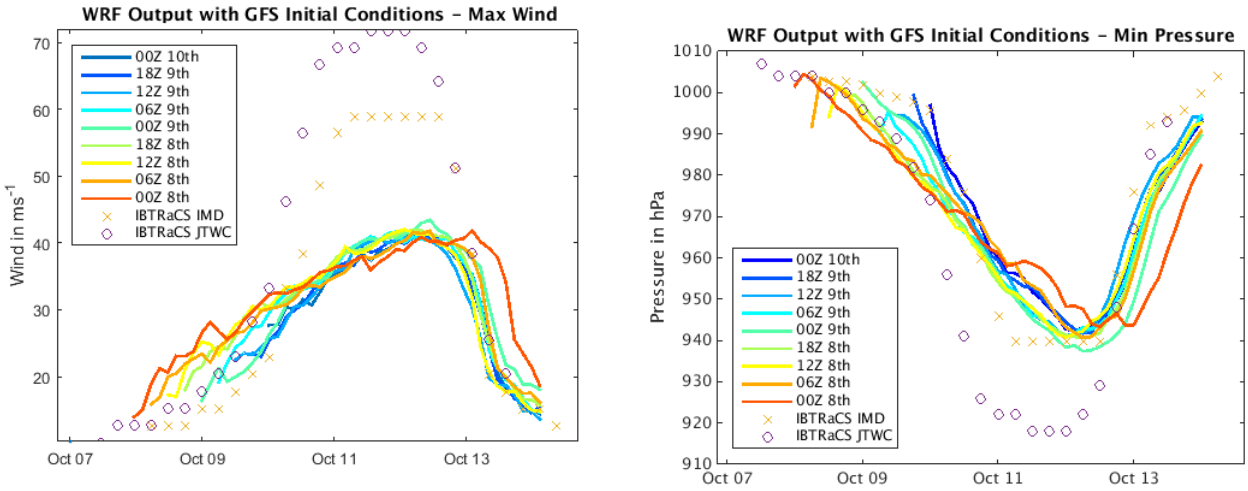

Figure 4.35: Maximum wind (left) and minimum pressure (right) WRF output using GFS Analysis as initial conditions with different simulation start times. The IBTrACS data is also shown for comparison.

cyclone developing, with maximum winds reaching roughly 41 ms^{-1} and minimum pressures of around 940 hPa for all start times. The rate of intensification does differ for each of the runs, with TC intensity peaking at different times. For example, the simulation beginning at 0000 UTC 8 October, intensification is slower, with maximum winds increasing slowly but steadily. The maximum wind speed peaks on the 13 October, and the storm's dissipation occurs later than all other simulations. As expected, a similar pattern occurs in the minimum pressure time series for this start time. For the simulation beginning 0000 UTC 9 October, the intensification happens more rapidly, reaching the highest maximum wind speed of all the simulations. The maximum wind speed peaks on the 12 October, and the storm dissipates during 13 October. Similar features occur for the minimum pressure time series, as expected.

There is no clear reason why this trend is occurring. The earlier start time model runs should have cyclogenesis beginning several time steps after the simulations starts, whereas the later start times begin when cyclogenesis is already occurring. The rate of intensification modelled may be related to this; with the coarse resolution model unable to replicate the details of the initialisation of cyclogenesis in the earlier start time runs.

Figure 4.36 shows the tracks associated with the start time test simulations. The TC tracks show much more variability than the wind and pressure outputs, with landfall location varying by 2° longitude and 1° latitude (roughly 220 km and 110 km respectively). The trend in track with start time is much more clear than for intensity; the later the start time is, the smaller the track error including the point of landfall.

The sensitivity of the TC track to simulation start time may be associated with the magnitude of the initial positioning error. The simulations with later start times have a more accurate starting location closer to the observed locations and this may lead to a smaller track error propagating throughout the rest of the model simulation.

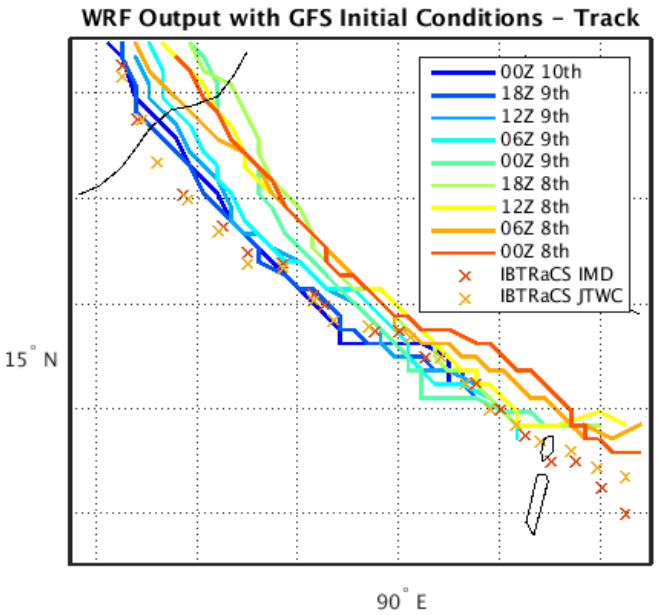

Figure 4.36: Track of WRF simulation using GFS Analysis as initial conditions with different simulation start times.

The difference in track may also be a result of slightly different initial synoptic weather patterns and how WRF develops the situations through the simulation.

The plots above show that a TC develops regardless of the start time chosen. This is an encouraging result, showing that the model is able to simulate cyclogenesis from even a relatively weak depression, move the storm through the model domain, and simulate TC dissipation over land.

The rate of intensification is where the initialisation will be most important. As a 30 km grid is used here, the detail of each TC is lost. For this reason, another start time was tested in the main, high resolution model, to investigate the impact of initialisation on the detailed output.

The remainder of this section will look at a WRF simulation which began at 1200 UTC 9 October, 12 hours later than the start time used in the main experiments. Here, we refer to the additional high resolution WRF run as Start Time 2 (ST2), and the run in the main experiments as Start Time 1 (ST1). Exactly the same WRF model set up is used for ST2, as described in Section 3.3.1 so all differences can be attributed to the different initial conditions. This includes the initial location of the nested domains, so for the ST2 simulation the nests are not centred around the initial TC location. The nests quickly centralise after the first time step.

Figure 4.37 shows the model output at 12-hourly intervals of the ST2 Cyclone Phailin simulation, beginning at 1200 UTC 9 October, and finished at 0000 UTC 13 October after landfall has occurred. As in the previous WRF results sections, the colours represent the

wind speed, and MSLP isobars are included at 8 hPa intervals.

Like the ST1 simulation, the ST2 WRF model simulates a tropical cyclone, with maximum wind speeds reaching roughly 57 ms^{-1} and minimum pressure of 920 hPa. This corresponds with a Very Severe Cyclonic Storm with T number 5.5-6.0, and a category 3 to 4 TC on the Saffir Simpson scale. This is a very similar classification as the ST1 modelled storm, with slightly lighter winds meaning a slightly less intense storm. The ST2 TC simulated correlates reasonably well with the IMD observations, with the maximum wind of 59 ms^{-1} and minimum pressure of 940 hPa recorded.

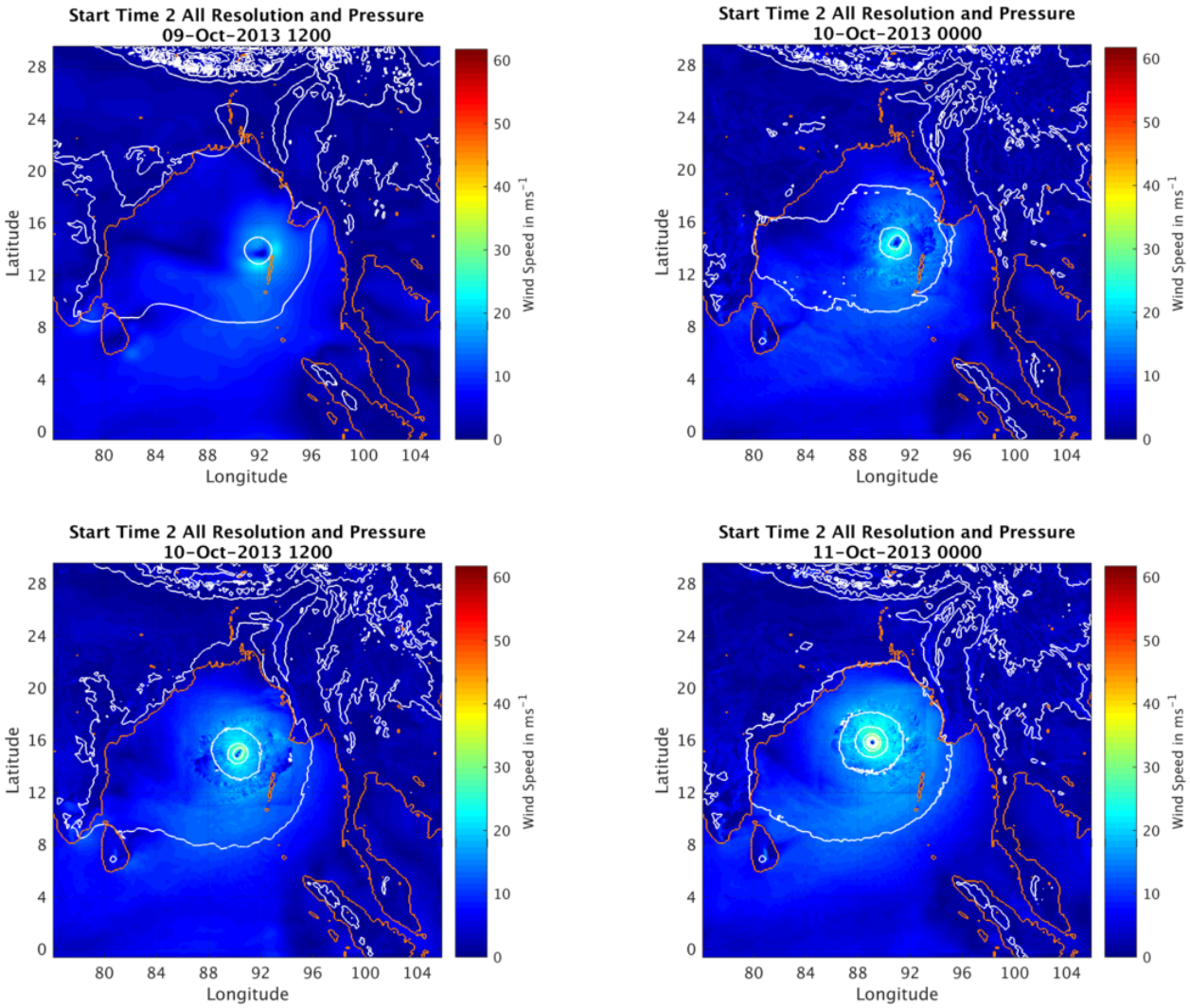

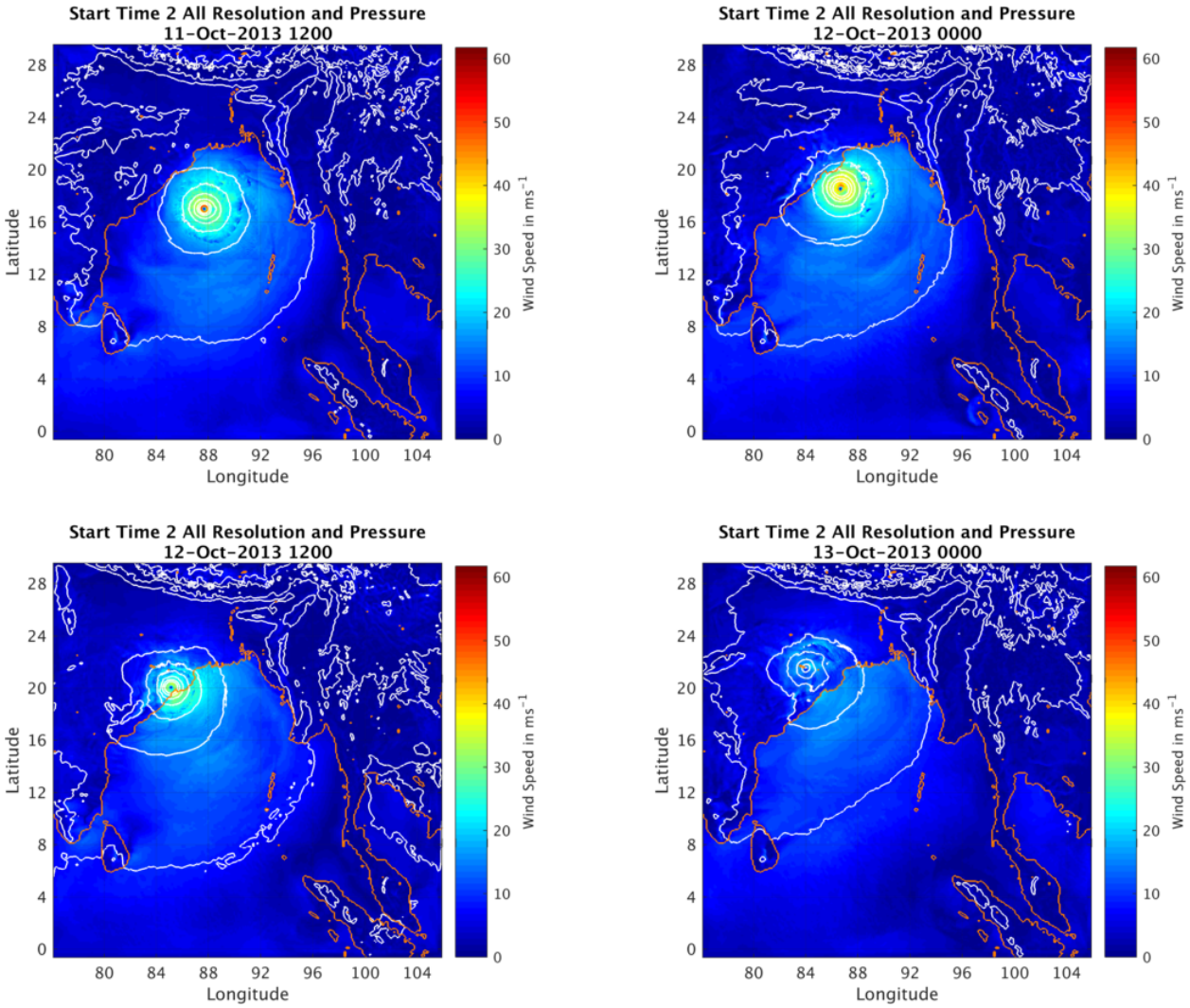

Figure 4.37: Snapshots of the ST2 WRF simulation, every 12 hours. The colours represent wind speed, and isobars show mean sea level pressure.

Figure 4.38 shows the maximum wind and minimum pressure time series of the ST2 model simulation, along with the observed IBTrACS values. The magnitude of maximum wind and minimum pressure show that a TC is simulated.

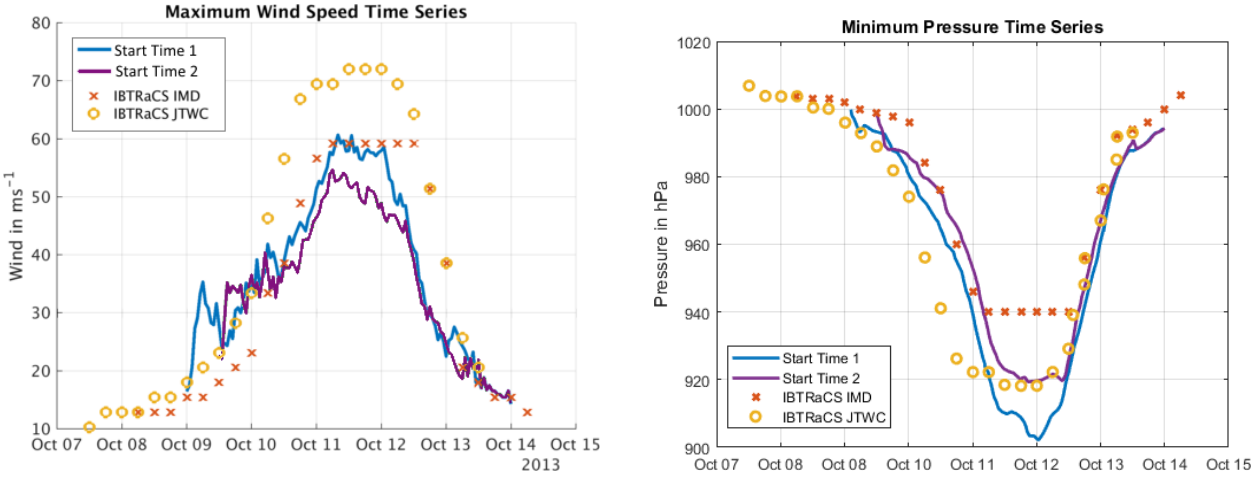

Maximum Wind

Minimum Pressure

Figure 4.38: Output of the Start Time 2 (green) WRF model compared with the State Time 1 outputs (blue) as well as the IBTrACS data from both IMD (red crosses) and JTWC (yellow circles).

The ST2 simulation begins once the cyclone centre has already passed over the Andaman and Nicobar Islands. Therefore, the initial period of dissipation seen in the ST1 simulation, as the cyclone passes over these land masses, does not occur. Instead, a relatively slow rate of intensification is observed for the first 12 hours of simulation. After this pause, rapid intensification on the 10 October occurs with maximum wind speeds increasing from 31 ms^{-1} at 0000 UTC 10 October, to over 51 ms^{-1} by 0600 UTC 11 October. The ST2 cyclone is lower in intensity than the ST1 cyclone, with a maximum wind speed roughly 5 ms^{-1} lower. In ST2 the maximum intensity with wind speeds between 46 ms^{-1} and 54 ms^{-1} is maintained for roughly 12 hours. This is a shorter period at maximum intensity seen both than reality and the ST1 simulation, with over 24 hours and 18 hours respectively.

The minimum pressure time series follows the maximum wind trends very closely, as with the ST1 simulation, with pressure decreasing as the wind speed increases. A minimum pressure of 920 hPa is reached and maintained for roughly 24 hours. This closely correlates with the JTWC observed values of minimum pressure, although the maximum winds have a large error. The minimum pressure values are generally higher than those of the ST1 simulation, echoing the lower maximum wind outputs.

Landfall of the ST2 cyclone occurs at 1000 UTC 12 October. Figure 4.39 shows the model timestep of landfall, which is one hour later than the ST1 simulation. This time is slightly closer to that of the observations - 1700 UTC 12 October.

In this figure, the cyclone looks very similar to the ST1 landfall snapshot, with the wind decreasing to roughly 41 ms^{-1} (compared with 46 ms^{-1} in ST1). The observed cyclone main-

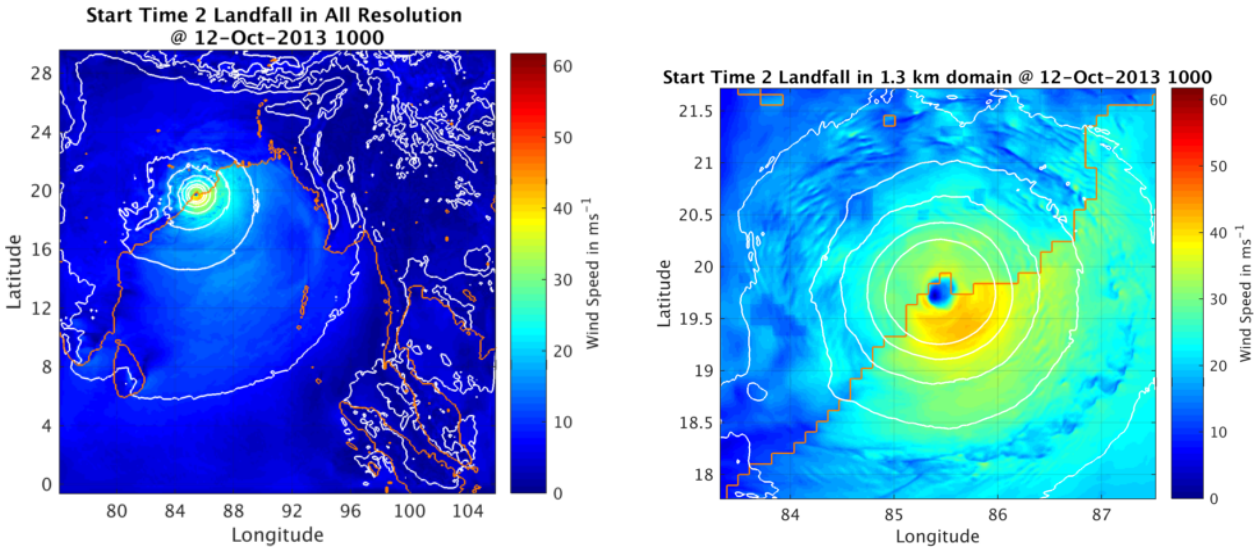

Figure 4.39: Snapshot of the ST2 WRF model run at the time of landfall. The colours represent wind speed in ms^{-1} and the lines show mean sea level pressure in hPa.

tains a maximum speed of 59-62 ms^{-1} until landfall. Frictional processes over the land quickly dissipates the cyclone in the ST2 as well as the ST1 model run.

The modelled landfall location occurs at 85°N and 20°E on the Odisha coast, India. This is further west along the Indian coast, closer to the observed landfall location of Cyclone Phailin, roughly 84.8°N and 19.2°E.

In Figure 4.40 the track of ST2 is shown, along with the IBTrACS data. Comparing this against the ST1 track, the track in ST2 verifies better with the observed data. This is not a surprise. Earlier in this section, it was concluded from the results of the 30 km WRF model runs that the later the start time, the smaller the track error. The same result is found here.

The results in this section demonstrate that the detail of the WRF model simulations is sensitive to the initial conditions and start time chosen. This is expected, and cyclone initialisation is an area of active research. For further work, careful consideration needs to be given when establishing the most appropriate simulation start time, and data assimilation processes may be tested to reduce the uncertainty associated with initialisation.

4.3.2 POLCOMS-WAM Results

In this section the impact of using a cyclone simulation with a different start time as the atmospheric boundary condition on the ocean domain is investigated. To do this, the second high resolution WRF simulation, starting at 1200 UTC 9 October, is utilised as forcing on the POLCOMS-WAM modelling system. The results are compared with those of the main experiment, with start time 0000 UTC 9 October, described in Section 4.1.2. As the POLCOMS-WAM model configuration is exactly the same, any differences can be attributed to the atmospheric forcing, and the impact start-time makes.

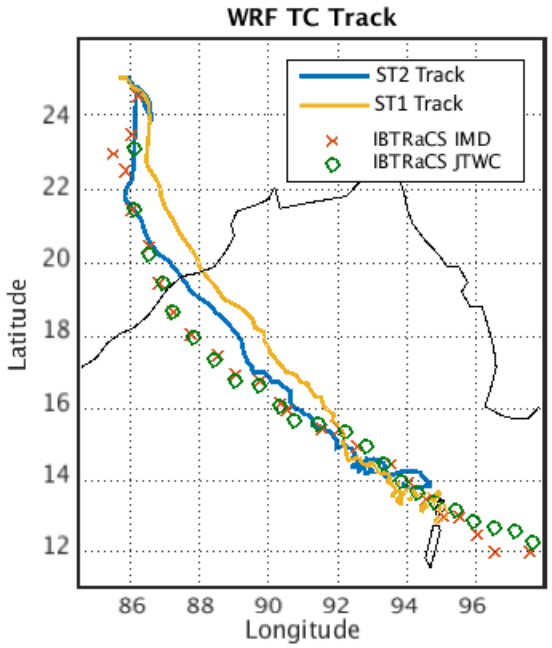

Figure 4.40: Simulated TC track of the ST2 WRF model (blue), along with the ST1 track (yellow) and the IMD (red crosses) and JTWC (yellow circles) observational data.

As with previous section, ST1 refers to the model simulation beginning on 0000 UTC 9 October, and ST2 refers to the alternative start time of 1200 UTC 9 October. The ST2 ocean model run begins at 1200 UTC 9 October and finishes at 0000 UTC 13 October. This is the same model duration as the ST1 simulation. The results are separated into the ocean and wave model outputs.

4.3.2.1 POLCOMS Output

In this section, the POLCOMS output from the two different start time simulations is presented and compared in order to assess the propagation of simulation differences through the atmospheric model to the ocean domain. The sea surface height will be the main variable shown and compared between the two model runs.

Snapshots of sea surface elevation for the ST2 simulation were checked against those of the ST1 simulation, but are not shown as the differences seen were not large or indicative of any particular trend.

Figure 4.41 shows the maximum sea surface height simulated along the coast for the two different start time runs. The colour signifies the sea surface elevation in metres. The storm surge occurs in the same location for both simulations, however, the ST2 atmospheric forcing produces a much smaller storm surge of approximately 3.1 m, in comparison with 4.3 m of the ST1 simulation. This is a reasonably large discrepancy, but is consistent with the lower maximum wind speeds simulated in the ST2 WRF model run as described in Section 4.3.1.

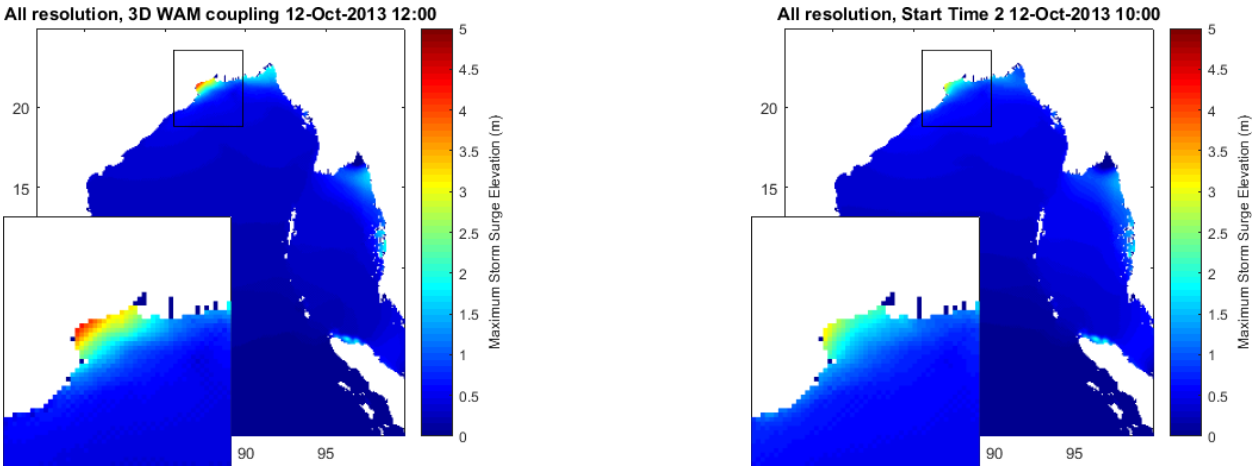

Figure 4.41: Comparison of the maximum storm surge simulated with the ST1 (left) and ST2 (right) WRF forcing. The colour represents sea surface elevation in metres.

From Figure 4.42, it is observed that the time of maximum storm surge is different between the two start time model runs, with ST1 maximum sea surface elevation occurring at 1200 UTC 12 October, where as in the ST2 run the storm surge occurs at 1000 UTC 12 October. The is a discrepancy of 2 hours.

There is also a discrepancy in the cyclone landfall time of the two simulations, described in the previous section: ST1 makes landfalls at 0900 UTC 12 October and ST2 at 1000 UTC 12 October. However, this difference is in the opposite temporal direction with the ST1 simulation making landfall first, but the maximum surge height occurs after that of ST2. It is unclear what process creates this interesting discrepancy. This is most likely associated with the tide-surge interaction of the two POL-WAM model runs. This hypothesis is discussed in more detail below.

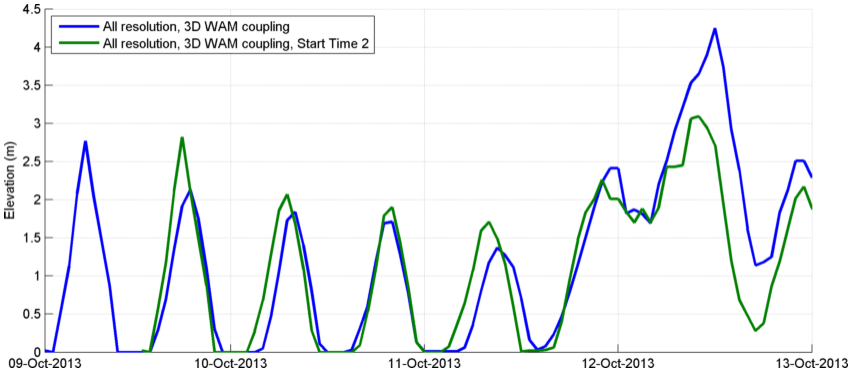

Figure 4.42: Time series showing the maximum sea surface elevation at the storm surge location, comparing the ST1 (blue) and ST2 (green) model forcing.

The track of the ST2 is more consistent with the IBTrACS data than that of the ST1 model run. The ST2 landfall point is also more accurate in comparison to the ST1 location. Therefore, it is expected that the storm surge location may differ between the two simula-

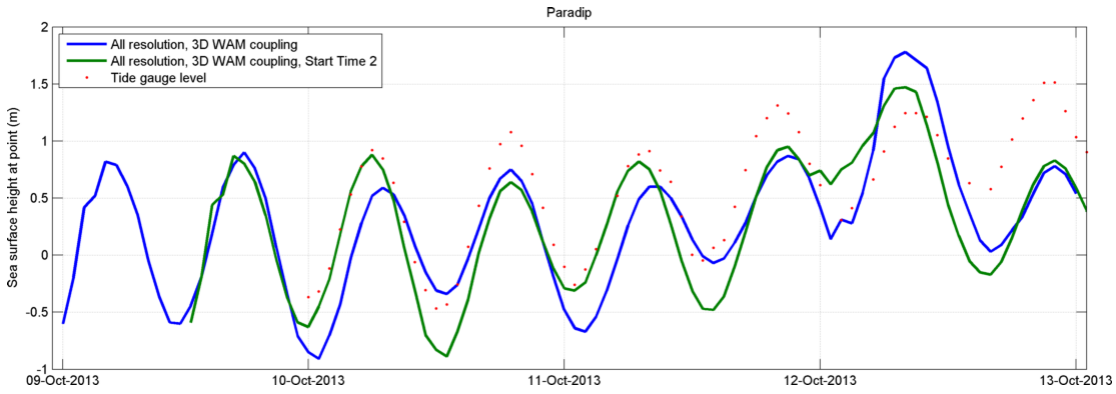

Figure 4.43: Time series of the sea surface height at Paradip for both the ST1 (blue) and ST2 (green) model forcing, with the observed tide gauge data for comparison (red points).

tions. However, this is not the case. Figure 4.41, in the previous section, shows that the storm surge location is very similar for both the POL-WAM model runs. This may also be a result of the tidal forcing used in the ST2 simulation.

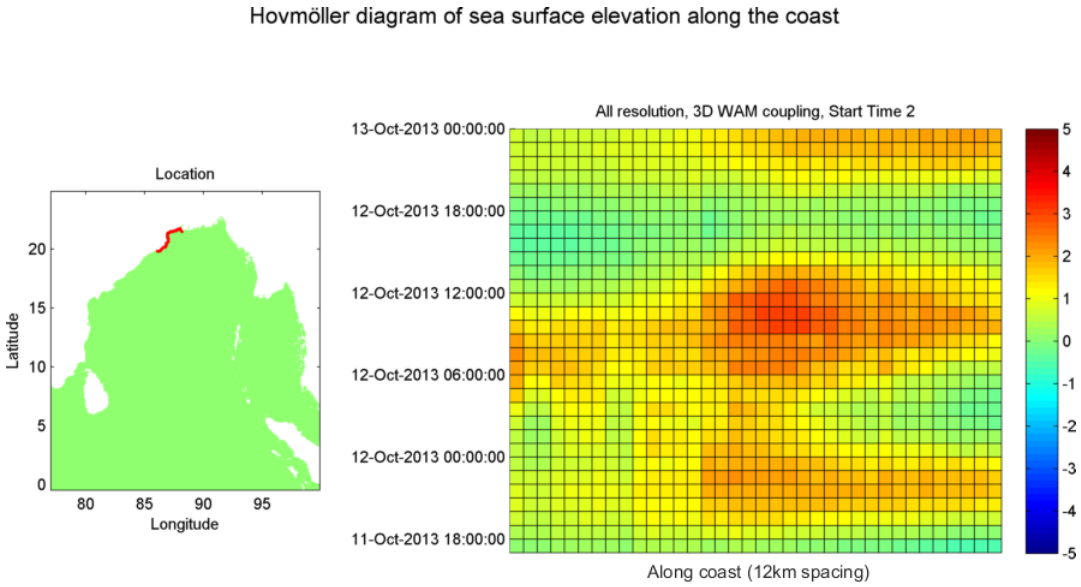

Figure 4.44: The Hovmöller plot showing the sea surface height along the coast, in red. The colours on the right plot represent sea surface height.

The maximum sea surface time series for ST1 and ST2 are shown in Figures 4.42. The series shows that the ST1 simulation produces the larger storm surge of over 4 m. The ST2 maximum storm surge is 1.2 m lower at 3.1 m. Prior to the storm surge signal, the same tidal cycle can be identified, delayed by 12 hours in ST2. This is due to the same tidal boundary being used for both the ST1 and ST2 model simulations. This may be impacting the resultant sea surface elevations at the time of cyclone landfall and if the experiments are repeated in the future, it is advised that a new tidal boundary file be used.

From Figure 4.42, the discrepancy in time of maximum sea surface elevation can be identified. Again, it can be hypothesised that the difference in time of maximum storm surge height may be a consequence of the incorrectly timed tidal boundary used for ST2.

The sea surface elevation time series at Paradip is shown in Figure 4.43. Although the modelled ST1 coastal surge is the highest in magnitude, the ST2 sea surface elevations at Paradip more closely represent the observed tide gauge time series. Even still, the ST2 results do not show good correlation with the tide gauge elevations, both in terms of magnitude and timing of the peak water level. This is likely to be a result of the different landfall location for the ST2 run, which was further away from Paradip.

The results shown in this section are echoed in the Hovmöller plot in Figure 4.44. Comparing this plot to that of Figure 4.8 in Section 4.1.2, it can be seen that the sea surface elevations are lower in magnitude here than in the main ST1 model run. The pattern of how sea surface elevation changes, however, is very similar, showing the propagation of the high sea surface elevations along the coast from west to east.

4.3.2.2 WAM Output

In this section, the outputs of WAM for the ST2 simulation are examined and compared to those of ST1, to assess the propagation of the changes to the meteorological forcing through to the wave model outputs.

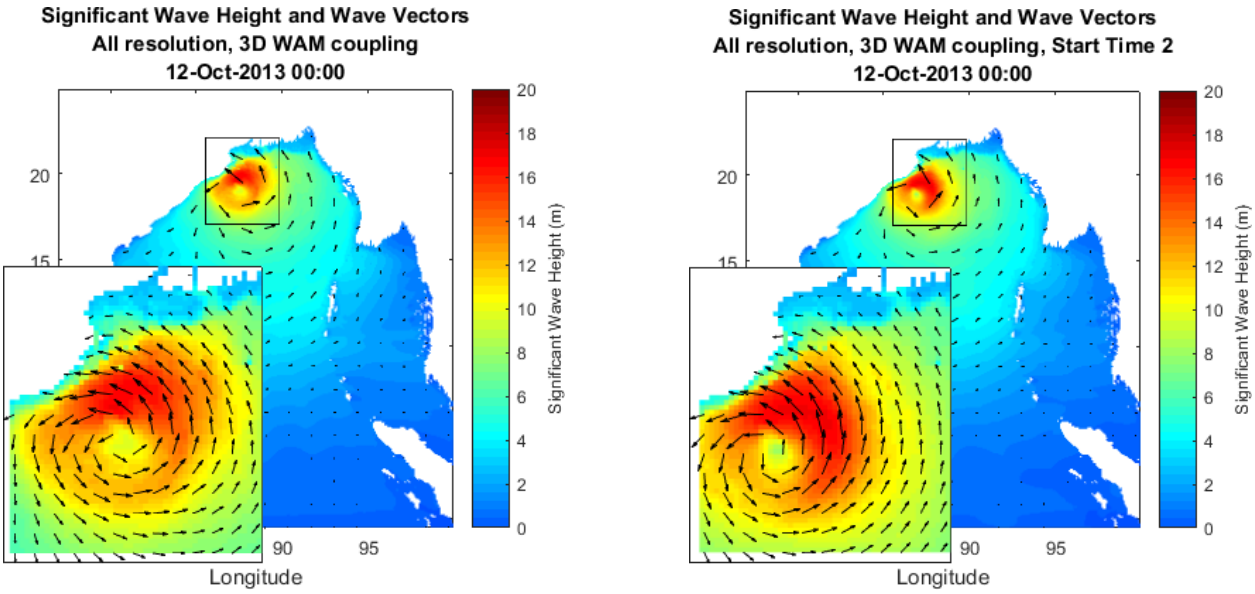

Figure 4.45: Snapshot of timestep with maximum significant wave height from across the BoB domain for both the ST1 (left) and ST2 (right) WRF forcing. The colour represents the significant wave height in metres, and the arrows represent the wave directional vectors.

Snapshots of significant wave height for the ST2 simulation were checked against those of the ST1 simulation, but are not shown as the differences seen were not large or indicative

of any particular trend. The waves develop to the right of the cyclone centre and increase with the wind speed. Once cyclone landfall occurs, the waves rapidly dissipate.

Figure 4.45 compares the significant wave height at landfall for both the ST1 and ST2 simulations. The ST2 simulation shares many characteristics with the ST1 model run; the significant wave heights are of the same magnitude, the wave directions have the same pattern, and the location of the maximum waves is to the north-east of the cyclone centre at landfall.

The ST2 simulation appears to produce the larger significant wave heights, and these larger waves are distributed over a larger area than those of ST1. This is surprising given the results shown in Section 4.3.1, where the maximum wind speed in much lower than that in ST1. This may be due to the duration that the wind forcing is acting on the sea surface in a certain direction or due to a larger fetch, which would both also produce large waves, as well as higher maximum wind speeds.

Figure 4.46 shows the maximum significant wave height of the ST1 and ST2 model simulations. Here, the two simulations are very similar. The initial increase and decrease in wave height of ST1 is not repeated in the ST2 simulation. This is likely due to the fact that the track of ST2 is different and the start time is after the cyclone has passed the Andaman and Nicobar Islands - see Figure 4.40 for the ST2 cyclone track. This supports the hypothesis that the initial decrease in cyclone intensity is associated with translation over the landmasses in ST1.

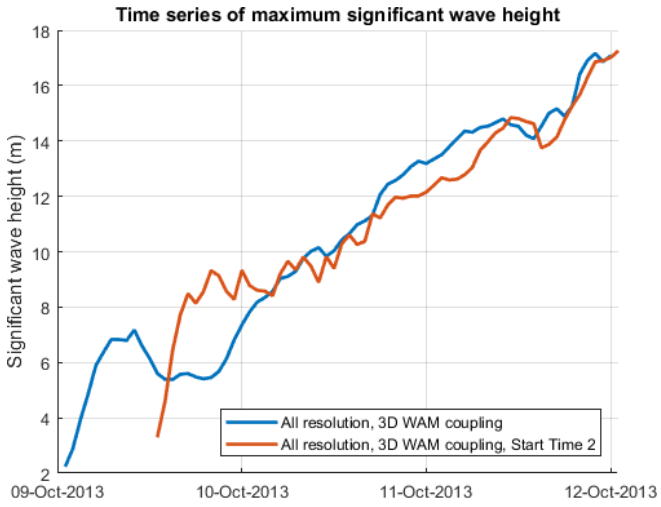

Figure 4.46: Timeseries showing the maximum significant wave height from across the BoB domain for both the ST1 (blue) and ST2 (red) simulations.

Other than this initial difference, there is very little to separate the time series. Both simulations reach a maximum significant wave height of 17 m (ST1 = 17.2 m, ST2=17.5 m). This is unexpected because, as previously mentioned, the maximum wind speed reached in ST1 is much higher than that of ST2. This would suggest the waves generated would also be larger in magnitude. The duration of the wind acting on the sea surface in ST2 must be greater in order to produce similar or larger wave heights.

The time series in Figure 4.47 show the significant wave heights for the Gopalpur location for both the ST1 and ST2 models, and the wave rider buoy data. This plot shows that the ST1 model output better correlates with the observed significant wave height values. The

ST2 wave heights are very similar through 9 and 10 October. The ST2 wave heights are higher during 11 October, peaking at a higher value of 6 m.

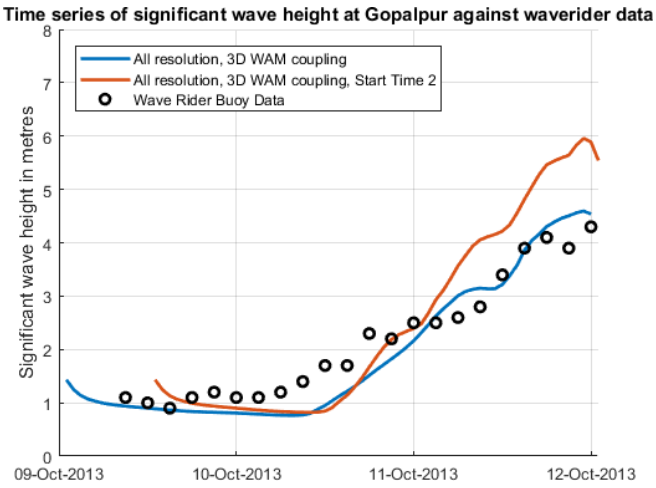

Figure 4.47: Modelling significant wave height at Gopalpur for the ST1 (blue) and ST2 (red) simulations, compared with the observed wave rider buoy data (black circles).

The differences in simulation are largely due to the differences in TC track, where the cyclone centre travels closer to Gopalpur in the ST2 model run. It is expected that larger waves are generated near to the cyclone centre, as shown in Figure 4.45 due to the stronger winds experienced. Although the wind speeds are generally lower across the domain, the wind speed at Gopalpur may be higher or blowing over this location for a longer period in the same direction, therefore, generating larger waves.

Figure 4.48 compares the maximum significant wave height locations for both the ST1 and ST2 model runs. The plots also show the TC track for each of the simulations. For both scenarios, the largest waves occur to the right of the cyclone track. This is to be expected, as the strongest winds theoretically should occur on the right side of the storm. The largest waves in ST2 occur closer to the location of the Gopalpur buoy, confirming that it is no surprise that ST2 generates larger waves at this location.

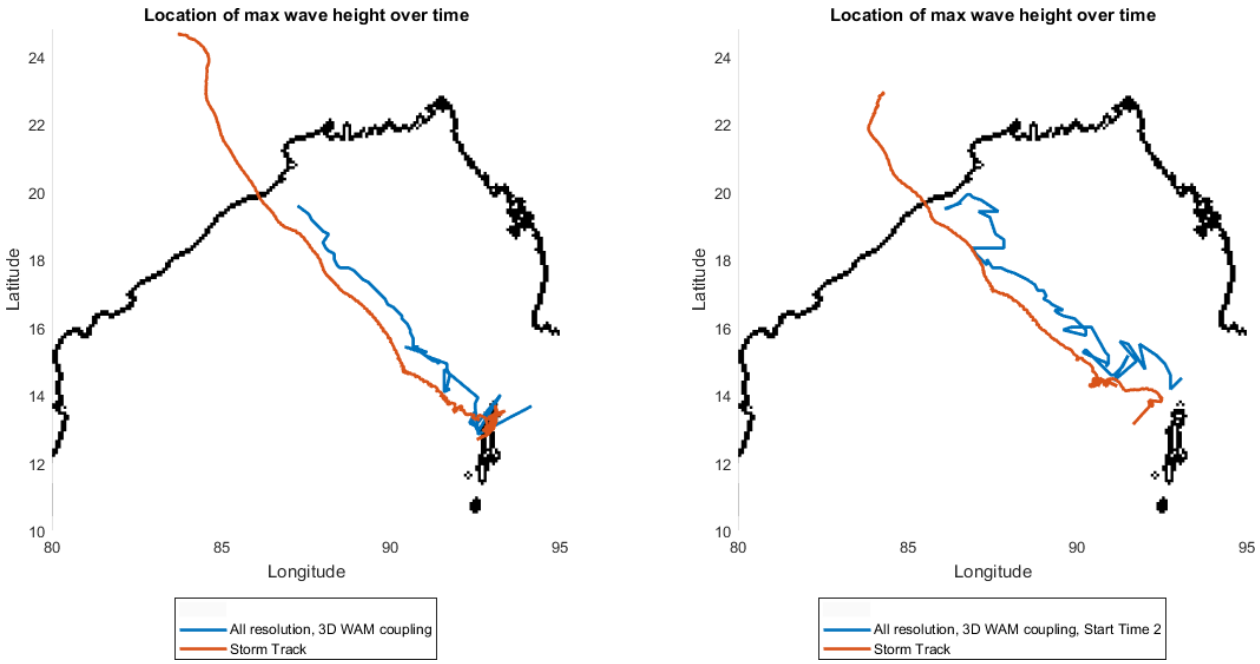

Figure 4.48: Comparison of the location of maximum significant wave height for both the ST1 (left) and ST2 (right) WAM simulations, in blue, with the WRF modelled cyclone track, in red.

Chapter 5

Conclusions

This section takes the results and applies them to the study Objectives described in Section 1.1. A number of conclusions are drawn from the work performed, and we discuss the impact they make on the field of storm surge prediction. Potential further work is also described.

5.1 Objective One - Set up a numerical modelling system for a tropical cyclone in the Bay of Bengal

This manuscript has described the set-up and utilisation of a coupled atmosphere and ocean modelling system. This work has shown how a simulation of Cyclone Phailin can be performed using this coupled modelling system, with various different atmospheric resolutions. Each of the Cyclone Phailin simulations achieves a storm with hurricane strength wind and mean sea level pressure comparable to that of the observed IBTrACS data.

The WRF model domain covers the Bay of Bengal with a grid resolution from 12 km to 1.3 km, near to the cyclone centre, achieved using moving nested gridded domains. AHW model features were used to best simulate the processes which occur at very high wind speeds, including the drag and enthalpy exchange parametrisations. Convection is explicitly resolved near to the centre of the storm in the higher resolution domains, which means the model is only reliant on a parametrisation scheme relationship for convection in the largest domain away from the main area of interest. This set-up was identical to that used in Davis et al. (2008b), where they were able to simulate five landfalling, Atlantic TCs including Hurricane Katrina.

GFS model analysis is utilised as boundary and initial conditions of the Phailin simulations. This data provided a high enough resolution to initiate tropical cyclogenesis in the WRF model. There does not appear to be any adverse impact of the boundary conditions as the domain is large enough to stop this occurring near the TC. The Lakshmi et al. (2017) study also uses the 0.5°x0.5° GFS analysis fields for initial and boundary conditions, however they also gain improvement from access to additional GFS data to provide boundary conditions every 3 hours. Here, the boundary condition frequency is 6-hourly.

The atmosphere model WRF is one-way coupled to the ocean components of the modelling system. The ocean model POLCOMS is two-way coupled to the wave model WAM. Using the WRF Phailin model runs as forcing at the sea surface, a storm surge and very large waves were simulated along the Indian coast. Unlike for Bricheno et al. (2013a), where WRF-POL-WAM simulated extra-tropical storms, storm surges and waves in the Irish Sea, there is very little observational data to confirm whether the magnitude of the ocean hazards is accurately simulated. The little data available shows the sea surface elevation at Paradip may have large errors. The magnitude of the waves at Gopalpur are a closer match to the wave rider buoy data, giving some confidence the results are sensible.

The POLCOMS-WAM model domain covers the ocean parts of the WRF domain for the Bay of Bengal. The model bathymetry is taken from the GEBCO 08 global dataset, which is roughly 1 km resolution, sub-sampled every 12 km, the grid resolution. There are 42 vertical layers in POLCOMS, with a minimum depth of 10 m applied, which prevents numerical instability due to drying areas occurring in the model domain. The 3D two-way coupling of POLCOMS with WAM allows the affect of Stokes' drift, radiation stress and current-wave interaction processes to be represented in the model.

The tidal boundary conditions were calculated using the TPXO 7.2 model which includes the Laplace tidal equations and along track averaged satellite data. 8 harmonic constituents of the tide were input into the model, and were transferred to sea surface height and tidal velocity along the model's open boundary. While this was important to include, further testing is required to ensure the tide is represented correctly. Issues with this boundary may be responsible for the disparities seen with the Paradip tide gauge.

Using the modelling system described, a simulation of Cyclone Phailin was built where the wind speed and pressure are that of a TC of category 4 to 5, and a T number of 6.0. This corresponds to the Very Severe Cyclonic Storm IMD classification, which is what Phailin was observed to achieve in reality. Although comparing the atmospheric outputs against the observed maximum wind and minimum pressure values shows large disparities, the observed data itself has very large uncertainties. It is used as a guide to sensibility check the modelled cyclone, which appears to be realistic of a TC that may occur in the Bay of Bengal.

A storm surge of 4.2 m was generated, which occurred along the Odisha and West Bengal coastline of India. This is similar to the observed value of 3.0 m reported for Cyclone Phailin's storm surge, although this figure is likely to have very large uncertainty. The storm surge travels along the coast as a Kelvin wave, as shown in the Hovmöller plot.

The waves output from the POL-WAM model were very large, with the highest waves occurring to the right of the cyclone track. The wave observations show good correlation with the modelled waves, although as ever, the data is limited in nature. Encouragingly, a similar correlation of modelled and observed significant wave height at Gopalpur was found in Murty et al. (2014a), where an idealised cyclone and ADCIRC coupled with SWAN were used to simulate TC Phailin. For further description of this modelling study, see Section 2.1.3.

TC Phailin occurred in October, the post-monsoon TC season in BoB. This season generally sees more intense TCs than the pre-monsoon period, due to the impact of the barrier layer (Vissa et al., 2013). The barrier layer is the increased stratification which occurs across the bay, due to the large input of freshwater the monsoon brings. This layer is seen to have an impact on the atmosphere-ocean fluxes and may reduce the negative feedback of the cold wake on TC intensity (Vissa et al., 2013). Phailin was potentially impacted by the barrier layer effect, as the storm occurred post-monsoon. Therefore, processes which were not captured in the WRF-POL-WAM modelling system may impact the observational data, and this impact could be a reason for discrepancy seen.

5.2 Objective Two - How sensitive is the modelling system to atmospheric horizontal resolution?

In order to establish an answer to this objective question, the Bay of Bengal modelling system created for Objective One was utilised. The atmospheric model outputs show that as the horizontal resolution increases, the intensity of the simulated cyclone increases and the size of the cyclone (RMW) decreases. This leads to differences in the ocean hazards. For the higher resolution atmospheric forcing, although the cyclone is more intense, the storm surge generated along the coast is smaller in magnitude. Similarly, the waves generated have a lower significant wave height for the higher resolution WRF results.

It is difficult to say which resolution model performed the most accurately, due to the limited available observational data. For the WRF model, the 12 km domain results show good correlation with the minimum pressure observations of IMD IBTrACS, however the 4 km domain outputs better match the JTWC IBTrACS values. The 1.3 km resolution domain outputs show the best correlation with both the IMD and JTWC maximum wind observations.

Davis et al. (2008b) showed that WRF ARW simulation of Atlantic TCs at 12 km and 4 km grid resolutions were generally competitive with operational forecasts for storm position and intensity. They found recurring errors in excessive intensification prior to landfall, and a general inability to capture rapid intensification when observed. Similar errors were found here, with the modelled Phailin reducing in intensity when passing over the Andaman and Nicobar Islands. Davis et al. (2008b) found improved results when coupling WRF to a mixed layer ocean model, which eliminated much of the erroneous intensification prior to landfall, and this would be an interesting experiment to repeat in BoB (see Section 5.5).

For the ocean part, the observed storm surge is 3 m along the Odisha coast. The higher resolution atmospheric forcing produced a storm surge of 4.2 m, and the coarser resolution inputs gave a 5.0 m storm surge height. Both simulations potentially have large errors compared with this observed value, although the higher resolution is a closer match. The

accuracy of the observed value here may be questionable, as storm surge are notoriously difficult to observe using just wrack marks and locations of debris. The sea surface elevations at Paradip are very similar for both the higher and lower resolution models. At Gopalpur, the higher resolution atmospheric forcing produces the best match to the observed wave rider data.

Rather than focus on the accuracy of the model simulations, it is more significant to describe the differences between the various model runs, and investigate why these differences may be occurring.

In the WRF simulations there are higher wind speeds during the increased resolution model run. Increasing the horizontal resolution allows the convection process to be simulated explicitly. Therefore, the uncertainty associated with the cumulus convection parametrisation is removed from the 4 km and 1.3 km domains. This also allows the model to better resolve the inner-core structure of the TC, including the eyewall and rainbands as seen in Figure 4.24 in Section 4.2.1. This change in inner-core representation was also seen in Davis et al. (2008b), where the structure of the convective bands in simulated TC Katrina were significantly improved using grid spacing of 1 km.

The maximum wind speed time series of the 4 km and 1.3 km resolution domains show short term variability, whereas the 12 km domain does not. This noise may be related to the model representation of convective gusts, with wind speeds and directions changing rapidly in the higher resolution models. Again, this is a result of explicitly resolving convection and the gusts associated.

There are still likely to be errors in the highest resolution WRF model runs as even 1.3 km is too coarse to directly compute three-dimensional turbulence. This process needs grid spacing of <100 m resolution to begin to resolve (Bryan, 2011).

The wind speed is directly linked to the pressure gradient, with higher wind speeds corresponding to a tighter pressure gradient. Here, this results in a lower central pressure. Therefore, it is not a surprise that the higher resolution WRF runs which simulate a higher wind speed, also simulate a very low central pressure.

One other noticeable difference in the WRF outputs is the size of the cyclone centre, or the RMAX. With a higher resolution, the central band of strongest winds is much smaller in diameter than in the coarser resolution. This is most obvious when comparing the 12 km resolution domain, with either the 4 km or 1.3 km domains. The 12 km resolution cyclone is much larger, and as well as the cloud bands being wider, the cyclone's eye is also larger in area.

This is likely to be a direct result of the grid sizes ability to resolve the area of strongest winds. In the coarser domain the wind speed is averaged over a larger physical area, and therefore the rainband is several grid cells wide. When the grid cells are larger, then the rainband is wider as a result. A similar result was seen in Davis et al. (2008b) where the

predicted size of the simulated circulation, not just the radius of maximum winds, varied with the grid increment, even in the range of resolutions where the eye is theoretically well resolved. Additionally, they found that the size of the cyclone circulation changed with the drag parametrisation scheme used - something not tested here.

The convection parametrisation is also likely to have an impact in the 12 km model run. Although the parametrisation scheme used includes the effects of detrainment, entrainment, and simple microphysics, it utilises a very simple cloud model and does not resolve convective eddies. The convective processes in the 12 km model are generalised across each grid cell, and therefore are very simplistic in nature and lack the detail available in the higher resolution model simulations.

Unlike several of the physical properties of the cyclone itself and how it develops, the track shows little variation when changing the horizontal resolution. This is not a surprise. Davis et al. (2008a, 2010a) presented similar results, with the cyclone track largely independent of the model resolution used.

It is large scale processes which impact the TC track, including the beta drift and the steering flow, which is usually roughly 10 km above the surface. Winds at this height, which are away from the influence of the boundary layer, adhere to the gradient wind balance. This can be forecast reasonably well with coarse resolution models. Therefore, increasing WRF's resolution will generally not impact the cyclone track significantly, and this is what is found here.

As a result of these atmospheric differences, there are impacts on the storm surge and waves generated in the ocean and wave models. The coarser resolution WRF forcing causes a higher magnitude storm surge along the Odisha coast and larger waves both at Gopalpur and across the ocean domain.

Although the higher resolution WRF domains output higher maximum wind speeds, the 12 km resolution model gives strong winds over a larger area of the ocean. This is the reason that the storm surge and waves generated are significantly larger. A larger area of strong winds will result in a larger area of the ocean surface impacted, as well as the winds acting on the surface for a longer duration - both aspects of which will increase the height of the storm surge and waves. Irish et al. (2008) found that TC size plays an important role in surge generation, particularly for very intense storms making landfall in mildly sloping regions - similar to the 1.3 km domain simulated TC. They found that for a given intensity, storm surge magnitude varies by as much as 30% over a range of storm sizes.

The location of the modelled storm surge along the Odisha and West Bengal coastline is the same for both the high and low resolution simulations. The location of the storm surge is dependent on the track of the TC, and as the tracks show little sensitivity to horizontal resolution, it is expected that the storm surge location will be similar. The Hovmöller plot presented shows the Kelvin wave movement of the storm surge along the coast, again with little difference from the high resolution forced POL-WAM model run results.

The location of the highest significant wave heights for both the high and lower resolution forcing is similar, both to the right of the cyclone track. Again, the location of the highest waves is dependent on the translation of the TC, and as the track shows little difference between the different resolution WRF runs, the highest waves are in the same proximity.

There are limited observations of sea surface height and significant wave height to confirm which of the POL-WAM model runs is more accurate. However, all the available data suggests that the higher resolution values are closer to the truth, and that the 12 km WRF forcing results in an over estimation of both storm surge height observed at the coast and wave height at Gopalpur. This is contradictory to the results of Bricheno et al. (2013b), where for extratropical storms in the Irish Sea, an increased atmospheric domain resulted in an increased wave height of up to 40 cm, which matched the observed values more closely. In this study, the storm surge showed little response to the change in model resolution, although a significant weakness in this study and in others focussed on the BoB is the lack of observed TC, storm surge and wave data.

5.3 Objective Three - Does atmospheric start time make a difference for the modelled Cyclone Phailin simulation?

As with Objective Two, the Bay of Bengal modelling system was used to answer this question. The atmospheric outputs show that the results are reasonably sensitive to the start time chosen. The magnitude of maximum wind and minimum pressure change with just a 12 hour difference in start time. Model runs with start times closer to landfall generally give more accurate track simulations. The differences in the atmospheric outputs lead to changes in the ocean variables. The model run starting 12 hours later than the main experiments results in a smaller storm surge, but generally similar significant wave heights.

The 30 km WRF model, used in the initial experimental stages described in Section 3.3.3, was run for several different start times to establish any overall trends in the atmospheric results. All of the model runs showed a similar intensity cyclone developing, with wind speeds reaching 41 ms^{-1} and mean sea level pressure decreasing to 940 hPa. However, the different start times result in different rates of intensification, with TC intensity peaking at different times. In general, the later the start time, the faster cyclogenesis occurs, and the earlier the maximum intensity is reached.

The simulated track for each of the different start time model runs show more variability than TC intensity, with landfall location varying by 2° longitude and 1° latitude. The later the start time, the smaller the track error is including the point of landfall. This is thought to be related to the magnitude of the initial positioning error. The later start times have a more accurate starting location, which may lead to a smaller track error propagating through the rest of the simulation.

The full WRF-POL-WAM modelling system was used for a Cyclone Phailin simulation with start time 1200 UTC 9 October, 12 hours later than that of the main experiments, and referred to as Start Time 2 (ST2). The WRF outputs are similar, with a category 3 to 4 TC with T number 5.5 to 6.0 simulated. This is also a Very Severe Cyclonic Storm, using the IMD classifications. The cyclone generated in ST2 is slightly less intense with a lower maximum wind speed and a higher minimum pressure. This relates to a larger wind speed error, but a smaller pressure error, when comparing to the IBTrACS data.

The previous finding that the later the model start time the faster cyclogenesis occurs, does not agree well here. The first 24 hours of both simulations are complicated by the impact of the Andaman and Nicobar Islands, which cause intensification to pause in ST2, and causes a slight dissipation in ST1. This means that it is difficult to link the rate of TC intensification to the different start times, other than the cyclogenesis rate is sensitive to small changes in the initial conditions.

The ST2 cyclone track, although similar to the original model runs, verifies better with the observed data. This agrees with the previous hypothesis that the later the start time of the Cyclone Phailin simulation, the smaller the track error. Landfall of the ST2 simulation occurs one hour later than in the main experiments which is closer to the IBTrACS observed value.

The differences between the ST1 and ST2 WRF simulations show that TC models are very sensitive to initial conditions. The different start times have very slightly different initial and boundary conditions. The variations in the initial and boundary conditions propagate through the model simulation to impact the model outputs. Davis et al. (2008b) found that a key shortcoming of their modelling study was the lack of dynamic initialisation, with significant adjustment of the vortex occurring within the first modelled 12 hours. This justifies the attention that TC model initialisation receives in the research community, as clearly the accuracy of initial conditions is significant for an accurate TC model simulation.

As with the Objective Two model runs, the small differences in the WRF simulations for ST1 and ST2 cause changes in the POL-WAM storm surge and wave output. The later start time causes a smaller storm surge to be generated along the Odisha and West Bengal coastline, two hours earlier than the ST1 model run. The waves generated by both model runs are similar in height and there is little difference between them.

The winds in the ST2 WRF simulation are weaker, therefore, it is not a surprise that the storm surge generated is smaller in magnitude. It is strange that landfall of the ST2 TC occurs one hour later than the ST1 simulation, however the maximum storm surge occurs two hours earlier for ST2 than ST1. This may be related to the tidal boundaries used, as the same tide information is used for both model runs, thus effecting and offsetting the modelled sea surface elevation through surge-tide interactions. This unfortunately invalidates most of the sea surface height conclusions that are made.

The ST1 and ST2 model runs share many similar characteristics of the waves generated; the significant wave heights are of the same magnitude, the wave directions are generally the same pattern, and the location of the maximum winds are to the right of the TC track. The ST2 simulation produces very slightly larger significant wave heights, over a larger area than those generated in the ST1 model run. This is unexpected as the winds output from the ST1 WRF simulation are much larger in magnitude. The larger waves in ST2 may be due to the duration that the wind forcing is acting in a certain direction, at a particular point on the ocean surface. This would produce larger waves, than a higher wind speed for a shorter duration.

The significant wave height output at Gopalpur for ST2 are larger than that of ST1. This is due to the differences in TC track, where in the ST2 simulation the cyclone moves closer to the Gopalpur buoy location. Strangely, even though the ST2 track is closer to reality, the significant wave heights seen at Gopalpur are further from the observed values.

The insensitivity of the wave model to the WRF forcing in this experiment is strange, and is fairly counter intuitive. Bricheno et al. (2013b) found that using high resolution WRF forcing simulated higher wind speeds, and higher waves. Here, the wind speeds are higher in the ST1 simulation, but the waves generated are very similar in ST2. This result demonstrates that wave generation is not always as simple as the highest wind gives the highest wave. The duration of wind forcing is also critical for larger wave formation.

5.4 Overall Conclusions

In summary, the main findings from this study include:

- The WRF POLCOMS WAM modelling system set up for this study successfully simulated Cyclone Phailin, with output values of wind, pressure and location reasonably consistent with available observed measurements.
- A storm surge was generated along the Odisha/West Bengal coastline which generally matched the location and storm surge height data available.
- Large waves were simulated near to the modelled TC. Significant wave heights at Gopalpur showed good correlation with the measured wave rider buoy data.
- The WRF simulations were sensitive to horizontal resolution, with maximum wind increasing and minimum pressure decreasing as the resolution increases. The TC track shows little sensitivity to the grid size.
- A larger storm surge is generated using the coarser resolution WRF model output.
- Larger waves are also generated using the 12 km resolution TC simulation.
- The location of the storm surge and area of largest waves remain the same for the different resolution atmospheric forcing.

- The WRF simulation is reasonably sensitive to model start time, as this impacts the initial conditions. Generally, the later the start time, the smaller the track error. There appears to be little correlation between maximum wind and minimum pressure values obtained with the differing initial conditions, other than they are related. The relationship is likely to be more complicated than one which can be described with a linear relationship.

- A larger storm surge is generated with the earlier start time WRF model run. This is likely to be due to the stronger winds simulated.

- The size of the waves generated across the BoB domain seem insensitive to the WRF start time. The waves at discrete locations within the domain change, dependent on their proximity to the cyclone as the track changes, e.g. Gopalpur.

- The results described in this study are similar to those of Davis et al. (2008b), where TC intensity was found to be sensitive to grid resolution, in similar ways including circulation size, maximum intensity, and structure of the eyewall and inner core.

5.5 Future Work

Throughout this project, opportunities for improving have been identified. This section will describe the recommendations of how to improve the modelling system, and increase confidence in the results show. Further potential work is also included, which would enhance the answers of the Objectives central to the study.

The modelling system, although functional, requires enhancements to ensure the results output are as accurate as possible. WRF contains a module for creating bogus vortexes which may be used to produce a more realistic initial circulation for beginning the TC model (as described in Section 3.1.3). It is advised that this be trialled and the results compared to the model runs with GFS analysis as initial conditions. It is expected that vortex bogussing may provide a process for improving TC initialisation, which is found to be critical in the current study.

Other initialisation techniques could be investigated, as described in Section 2.1.2. These include data assimilation as well as the use of ensemble models to lower the initial error (Dupont et al., 2011; Belanger et al., 2012).

The sea surface elevation results presented in this manuscript contain known errors due to the tidal forcing and boundary conditions. In the future, the tidal dynamics should be tested with no other forcing, to establish that the tide is correct for the area with the available information. Once this is established, the atmospheric forcing could be added.

The POLWAM simulation duration does not capture the subsidence of the waves after the TC made landfall. Ideally, the model simulations would be repeated with a longer du-

ration in order to show how quickly the large waves decay.

The other main oceanic dynamical processes and variables could also be added to POLCOMS, including temperature and salinity. It would be of interest to see how the TC forcing impacts the density of the sub-surface ocean layers. In the BoB a barrier layer forms during September, which may act to dampen tropical cyclogenesis (Vissa et al., 2013). Therefore, it would be interesting to include these variables to try to simulate the barrier layer effect, especially for TC Phailin which occurs in October. Instead of using a minimum depth, a parametrisation for wetting and drying of the coastline could be included, to better represent inundation, coastal flooding and the impacts of representing wave set-up.

Once the full 3D ocean model is operational, two-way coupling between WRF and POLWAM would allow the air-sea interactions which take place in TCs to be simulated and studied in detail. This would include incorporation of the negative feedback of the ocean's cold wake on TC intensity. Several authors have found that coupled models provide more accurate TC simulations, as described in Section 2.1.3, and the modelling system created here could test this further, investigating which processes are the most important for storm surge and wave forecasting. With such a model, the important of ocean-wave modelling could be investigated using different levels of ocean-wave interaction and comparing the resultant model simulations.

As well as simulating Cyclone Phailin, it would be important to test the modelling system to hindcast other BoB tropical cyclones. This would allow investigation into the wider Bay of Bengal dynamics, including the interaction with the monsoon trough, the importance of the barrier layer formed during the monsoon, and potential impacts of the El Nino oscillation.

Climate change impacts on the BoB could be investigated using the model to simulate future scenarios with a warmer ocean and atmosphere, and higher sea level. This is critical for the future, as the impact of TC and their ocean hazards are likely to endanger more vulnerable people in the Bay of Bengal.

Bibliography

Ali, A. (1979). Storm surges in the Bay of Bengal and some related problems. *PhD Thesis, University of Reading, England*, page 227.

Ali, M. M., Jagadeesh, P. S. V., and Jain, S. (2007). Effects of eddies on Bay of Bengal cyclone intensity. *EOS*, 88(8):93–104.

Ali, M. M., Swain, D., Kashyap, T., McCreary, J. P., and Nagamani, P. V. (2013). Relationship between cyclone intensities and sea surface temperature in the tropical Indian Ocean. *IEEE Geoscience and Remote Sensing Letters*, 10(4):841–844.

Amrutha, M. M., Kumar, V. S., Anoop, T. R., Nair, T. M. B., Nherakkol, A., and Jeyakumar, C. (2014). Waves off Gopalpur, northern Bay of Bengal during Cyclone Phailin. *Annales Geophysicae*, 32:1073–1083.

Antony, C. and Unnikrishnan, A. S. (2013). Observed characteristics of tide-surge interaction along the east coast of India and the head of Bay of Bengal. *Estuarine, Coastal and Shelf Science*, 131:6–11.

Baisya, H., Wolf, J., and Pattnaik, S. (2014). Coastal impacts of tropical cyclones in Bay of Bengal: Wave modelling. *Master's Thesis, Indian Institute of Technology, Bhubaneswar*.

Barstow, S. F. and Kollstad, T. (1991). Field trials of the directional wave rider. *In Proceedings of the First International Offshore and Polar Engineering Conference, Edinburgh*, pages 55–63.

Batstone, C., Lawless, M., Tawn, J., Horsburgh, K., Blackman, D., McMillan, A., Worth, D., Laeger, S., and Hunt, T. (2013). A UK best-practise approach for extreme sea-level analysis along complex topographic coastlines. *Ocean Engineering*, 71:28–39.

Belanger, J. I., Webster, P. J., Curry, J. A., and Jelinek, M. R. (2012). Extended prediction of North Indian Oean tropical cyclones. *Weather and Forecasting*, 27:757–769.

Beljaars, A. (1994). The parametrisation of surface fluxes in large-scale models under free convection. *Quarterly Journal of the Royal Meterological Society*, 121:225–270.

Bell, M. M., Montgomery, M. T., and Emanuel, K. A. (2012). Air-sea enthalpy and moisture exchange at major hurricane wind speeds observed during CBLAST. *Journal of Atmospheric Sciences*, 69:3197 – 3222.

Bender, M. A. and Ginis, I. (2000). Real-case simulations of hurricane-ocean interaction using a high-resolution coupled model: Effects on hurricane intensity. *Monthly Weather Review*, 128:917–946.

Bender, M. A., Ginis, I., Tuleya, R. E., Thomas, B., and Marchok, T. (2007). The operational GFDL coupled hurricane-ocean prediction system and a summary of its performance. *Monthly Weather Review*, 135:3965–3989.

Black, P. G., D'Asaro, E. A., Drennan, W. M., French, J. R., Niller, P. P., Sanford, T. B., Terrill, E. J., Walsh, E. J., and Zhang, J. A. (2007). Air-sea exchange in hurricanes: Synthesis of observations from the Coupled Boundary Layer Air-Sea Transfer Experiment. *American Meteorological Society*, pages 357–374.

Blumberg, A. F. and Mellor, G. L. (1987). A description of a three-dimensional coastal ocean circulation model. *Three Dimensional Coastal Ocean Models*, Vol. 4:1–16.

Bolanos, R., Osuna, P., Wolf, J., Monbaliu, J., and Sanchex-Arcilla, A. (2011). Development of the POLCOMS-WAM current-wave model. *Ocean Modelling*, 36:102–115.

Booij, N., Ris, R. C., and Holthuijsen, L. H. (1999). A third generation wave model for coastal regions. 1: Model description and validation. *Journal of Geophysical Research*, 104(C4):7649–7666.

Bricheno, L. M., Soret, A., Wolf, J., et al. (2013a). Effect of high-resolution meteorological forcing on nearshore wave and current model performance. *Journal of Atmospheric and Ocean Technology*, 30:1021–1037.

Bricheno, L. M., Soret, A., Wolf, J., Jorba, O., and Baldasano, J. M. (2013b). Effect of high-resolution meteorological forcing on nearshore wave and current model performance. *Journal of Atmospheric and Ocean Technology*, 30:1021–1037.

Brown, J. M. (2010). A case study of combined wave and water levels under storm conditions using WAM and SWAN in a shallow water application. *Ocean Modelling*, 35:215–229.

Brown, J. M., Bolanos, R., and Wolf, J. (2011). Impact assessment of advanced coupling features in a tide-surge-wave model, POLCOMS-WAM, in a shallow water application. *Journal of Marine Systems*, 87:13–24.

Brown, J. M. and Wolf, J. (2009). Coupled wave and surge modelling for the eastern Irish Sea and implications for model wind stress. *Continental Shelf Research*, 29:1329–1342.

Bryan, G. H. (2011). Effects of surface exchange coefficients and turbulence length scales on the intensity and structure of numerically simulated hurricanes. *Monthly Weather Review*, 140:1125–1143.

Bryan, G. H. and Rotunno, R. (2009). The maximum intensity of tropical cyclones in axisymmetric numerical model simulations. *Monthly Weather Review*, 137:1770–1789.

Carlson, T. N. and Boland, F. E. (1978). Analysis of urban-rural canopy using a surface heat flux/temperature model. *Journal of Applied Meteorology*, 17:998–1013.

Charnock, H. (1955). Wind stress on a water surface. *Quarterly Journal of the Royal Meteorological Society*, 81:639–640.

Chen, Y., Rotunno, R., Wang, W., Davis, C., Dudhia, J., and Holland, G. J. (2008). Large eddy simulations of an idealized hurricane. *Ninth WRF Users Workshop, Boulder, CO, NCAR, 9.2*.

Cline, I. (1920). Relation of changes in storm tides on the coast of the Gulf of Mexico to the centre and movement of hurricanes. *Monthly Weather Review*, 48:127–146.

Collins, S. N., James, R. S., Ray, P., Chen, K., Lassman, A., and Brownlee, J. (2013). *Grids in Numerical Weather and Climate Models*. InTech.

Davis, C., Wang, W., Chen, S. S., Chen, Y., Corbosiero, K., DeMaria, M., Dudhia, J., Holland, G., Klemp, J., Michalakes, J., Reeves, H., Rotunno, R., Snyder, C., and Xiao, Q. (2008a). Prediction of landfalling hurricanes with the Advanced Hurricane WRF model. *Monthly Weather Review*, 136:1990–2005.

Davis, C., Wang, W., Chen, S. S., et al. (2008b). Prediction of landfalling hurricanes with the Advanced Hurricane WRF model. *Monthly Weather Review*, 136:1990–2005.

Davis, C., Wang, W., Dudhia, J., and Torn, R. (2010a). Does increased horizontal resolution improve hurricane wind forecasts? *Weather and Forecasting*, 25:1826–1841.

Davis, J. R., Paramygin, V. A., Forrest, D., and Sheng, Y. P. (2010b). Toward the probabilistic simulation of storm surge and innundation in a limited-resource environment. *Monthly Weather Review*, 138:2953 – 2974.

Dee, D. P., Uppala, S. M., Simmons, A. J., Berrisford, P., Poli, P., Kobayashi, S., Andrae, U., Balmaseda, M. A., Balsamo, G., Bauer, P., Bechtold, P., Beljaars, A. C. M., van de Berg, L., Bidlot, J., Bormann, N., Delsol, C., Dragani, R., Fuentes, M., Geer, A. J., Haimberger, L., Healy, A. B., Hersbach, H., Holm, E. V., Isaksen, L., Kallberg, P., Kohler, M., Matricardi, M., McNally, A. P., Monge-Sanz, B. M., Morcrette, J.-J., Park, B.-K., Peubey, C., de Rosnay, P., Tavolato, C., Thepaut, J.-N., and Vitart, F. (2011). The ERA-Interim reanalysis: configuartion and performance of the data assimilation system. *Quarterly Journal of the Royal Meteorological Society*, 137:553–597.

DeMaria, M., Mainelli, M., Shay, L. K., Knaff, J. A., and Kaplan, J. (2005). Further improvements to the Statistical Hurricane Intensity Prediction Scheme (SHIPS). *Weather and Forecasting*, 20:531–543.

Donelan, M. A. (1990). Air-sea interaction. *Ocean Engineering Science*, 9:239–292.

Donelan, M. A., Haus, B. K., Reul, N., Plant, W. J., Stiassnie, M., Graber, H. C., Brown, O. B., and Saltzman, E. S. (2004). On the limiting aerodynamic roughness of the ocean in very strong winds. *Geophysical Research Letters*, 31:L18306.

Drennan, W. M., Taylor, P. K., and Yelland, M. J. (2005). Parametrizing the sea surface roughness. *Journal of Physical Oceanography*, 35(5):835–848.

Dube, S. K., Jain, I., Rao, A. D., et al. (2009a). Storm surge modelling for the Bay of Bengal and Arabian Sea. *Natural Hazards*, 51:3–27.

Dube, S. K., Jain, I., Rao, A. D., and Murty, T. S. (2009b). Storm surge modelling for the Bay of Bengal and Arabian Sea. *Natural Hazards*, 51:3–27.

Dube, S. K., Rao, A. D., Sinha, P. C., Murty, T. S., and Bahulayan, N. (1997). Storm surge in the Bay of Bengal and Arabian Sea: The problem and its prediction. *Mausam*, 48:283–304.

Dudhia, J. (1989). Numerical study of convection observed during the Winter Monsoon Experiment using a mesoscale two-dimensional model. *Journal of Atmospheric Sciences*, 46:3077–3107.

Dupont, T., Plu, M., Caroff, P., and Faure, G. (2011). Verification of ensemble-based uncertainty circles around tropical cyclone track forecasts. *Weather and Forecasting*, 26:664–676.

Dvorak, V. F. (1973). A technique for analysis and forecasting of tropical cyclone intensities from satellite pictures. *NOAA Technical Memorandum NESS-45*, page 14.

Dvorak, V. F. (1975). Tropical cyclone intensity analysis and forecasting from satellite imagery. *Monthly Weather Review*, 103:420–430.

Egbert, G. D., Bennett, A. F., and Foreman, M. G. G. (1994). TOPEX/POSEIDON tides estimated using a global inverse model. *Journal of Geophysical Research*, 99(C12):24821–24852.

Emanuel, K. A. (1986). An air-sea interaction theory for tropical cyclones. Part I: Steady-state maintenance. *Journal of the Atmospheric Sciences*, 43(6):585–604.

Emanuel, K. A. (1999). Thermodynamic control of hurricane intensity. *Nature*, 401.

Emanuel, K. A., DesAutels, C., Holloway, C., and Korty, R. (2004). Environmental control of tropical cyclone intensity. *Journal of the Atmospheric Sciences*, 61:843–858.

Emanuel, K. A., Sundararajan, R., and Williams, J. (2008). Hurricanes and global warming. *Bulletin of the American Meteorological Society*, pages 347–367.

Evans, J. L. (1993). Sensitivity of tropical cyclone intensity to sea surface temperature. *Journal of Climate*, 6:1133–1140.

Fairall, C. W., Bradley, E. F., Hare, J. E., Grachiev, A. A., and Edson, J. E. (2003). Bulk parametrisation of air-sea fluxes: Updates and verification for the COARE algorirm. *Journal of Climate*, 16:571–591.

Fandry, C. B., Leslie, L. M., and Steedman, R. K. (1984). Kelvin-type coastal surges generated by tropical cyclones. *Journal of Physical Oceanography*, 14:582–593.

Flather, R. A. and Williams, J. A. (2000). Climate change effects on storm surges: Methodologies and results. *Climate Scenarios for Water-Related and Coastal Impact. CRU, ECLAT-2 Workshop Report*, (3):66–78.

Flowerdew, J., Horsburgh, K., Wilson, C., and Mylne, K. (2010). Development and evaluation of an ensemble forecasting system for coastal storm surges. *Quarterly Journal of the Royal Meteorological Society*, 136:1444–1456.

Gall, J. S., Ginis, I., Lin, S.-J., Marachok, T. P., and Chen, J.-H. (2011). Experimental tropical cyclone prediction using the GFDL 25-km-resolution global atmospheric model. *Weather and Forecasting*, 26:1008 – 1019.

Garratt, J. (1992). The atmospheric boundary layer. *Cambridge University Press*, page 316 pp.

Gill, A. E. (1982). *Atmosphere-Ocean Dynamics*. International Geophysics Series; 30. Academic Press.

Ginis, I. (2002). Tropical cyclone-ocean interactions. *Atmosphere-Ocean Interactions, Advances in Fluid Mechanics Series*, (33):83–114.

Goni, G. J. and Trinanes, J. A. (2003). Ocean thermal structure monitoring could aid in the intensity forecast of tropical cyclones. *EOS*, 84(51):573–580.

Gopalakrishnan, S. G., Goldenberg, S., Quirino, T., Zhang, X., Jr., F. M., Yeh, K.-S., Atlas, R., and Tallapragada, V. (2012). Toward improving high-resolution numerical hurricane forecasting: Influence of model horizontal grid resolution, initialisation, and physics. *Weather and Forecasting*, 27:647–666.

Gopalan, A. K. S., Krishna, V. V. G., Ali, M. M., and Sharma, R. (2000). Detection of Bay of Bengal eddies from TOPEX and in situ observations. *Journal of Marine Research*, 58:721–734.

Goswami, P. and Mohapatra, G. N. (2014). A comparative evaluation of impact of domain size and parameterization scheme on simulation of tropical cyclones in the Bay of Bengal. *Journal of Geophysical Research: Atmospheres*, 119:10–22.

Gray, W. M. (1979). Hurricanes: Their formation, structure and likely role in the tropical circulation. *Meteorology Over the Tropical Oceans*, pages 155–218.

Green, B. W. and Zhang, F. (2013). Impacts of air-sea flux parameterisations on the intensity and structure of tropical cyclones. *Monthly Weather Review*, 141:2308–2324.

Grell, G. and Devenyi, D. (2002). A generalised approach to parameterising convection combining ensemble and data assimilation techniques. *Geophysical Research Letters*, 29:14.

Holt, J. T. and James, I. D. (2001). An s coordinate density evolving model of the northwest European continental shelf. 1: Model description and density structure. *Journal of Geophysical Research*, 106(C7):14,015–14,034.

Holthuijsen, L. H. (2007). *Waves in Oceanic and Coastal Waters*. Cambridge Unversity Press.

Hong, S.-Y., Dudhia, J., and Chen, S.-H. (2004). A revised approach to ice microphysics process for the bulk parametrisation of clouds and precipitation. *Monthly Weather Review*, 132:103–120.

Hong, S.-Y., Noh, Y., and Dudhia, J. (2006). A new vertical diffusion package with an explicit treatment of entrainment processes. *Monthly Weather Review*, 134:2318–2341.

Horsburgh, K., Williams, J., Flowerdew, J., and Mylne, K. (2008). Aspects of operational model predictive skill during an extreme storm surge event. *Journal of Flood Risk Management*, 4:213–221.

Horsburgh, K. J. and Wilson, C. (2007). Tide-surge interaction and its role in the distribution of surge residuals in the North Sea. *Journal of Geophysical Research*, 112.

IMD Report (2013). Very Severe Cyclonic Storm, PHAILIN over the Bay of Bengal (08-14 october 2013) : A report. *Cyclone Warning Division - India Meteorological Department, New Delhi*.

India Meteorological Department (2009). Best track data of tropical cyclonic distributions over the North Indian Ocean.

Irish, J. L., Resio, D. T., and Ratcliff, J. J. (2008). The influence of storm size on hurricane surge. *Journal of Physical Oceanography*, 38:2003–2013.

Janjic, Z. I. (1994). The step-mountain eta coordinate model: Further developments of the convection, viscous sublayer, and turbulence closure schemes. *Monthly Weather Review*, 122:927–945.

Janssen, P. A. E. M. (1991). Quasi-linear theory of wind generation applied to wave forecasting. *Journal of Physical Oceanography*, 21:1631–1642.

Janssen, P. A. E. M., Saetra, O., Wettre, C., Hersbach, H., and Bidlot, J. (2004). The impact of sea state on the atmosphere and oceans. *Annales Hydrographiques*, 3:3.1–3.23.

Kain, J. S. (2004). The Kain-Fritsch convective parametrization: An update. *Journal of Applied Meteorology*, 43:170–181.

Kalnay, Other, A., and Other, A. (1996). The NCEP/NCAR 40-year reanalysis project. *Bulletin of the American Meteorological Society*, 77:437–470.

Kessler, E. (1969). On the distribution and continuity of water substances in atmospheric circulations. *Atmospheric Research*, 32.

Knapp, K. R., Kruk, M. C., Levinson, D. H., Diamond, H. J., and Neumann, C. J. (2010). The International Best Track Archive for Climate Stewardship (IBTrACS): Unifying tropical cyclone best track data. *Bulletin of the American Meteorological Society*, 91:363–376.

Komen, G. J., Cavaleri, L., Donelan, M., Hasselmann, S., Hasselmann, K., and Janssen, P. A. E. M. (1994). Dynamics and modelling of ocean waves. *Cambridge University Press, Cambridge*, 300:pp.

Kurihara, Y., Bender, M. A., Tuleya, R. E., and Ross, R. J. (1995). Improvements in the GFDL hurricane prediction system. *Monthly Weather Review*, 123:2791–2802.

Lakshmi, D. D., Murty, P. L. N., Bhaskaran, P. K., Sahoo, B., Kumar, T. S., Shenoi, S. S. C., and Srilanth, A. S. (2017). Performance of WRF-ARW winds on computed storm surge using hydrodynamic model for Phailin and Hudhud cyclones. *Ocean Engineering*, 131:135–148.

Lane, A. (1989). The heat balance of the North Sea. *Proudman Oceanography Laboratory Report*.

Large, W. and Pond, S. (1981). Open ocean momentum flux measurements in moderate to strong winds. *Journal of Physical Oceanography*, 11:324–336.

Li, Z., Yu, W., Li, T., Murty, V., and Tangang, F. (2013). Bimodal character of cyclone climatology in the Bay of Bengal modulated by monsoon seasonal cycle. *Journal of Climate*, 26:1033–1046.

Lin, I.-I., Chen, C.-H., Pun, I.-F., Liu, W. T., and Wu, C.-C. (2009a). Warm ocean anomaly, air sea fluxes and the rapid intensification of tropical cyclone Nargis (2008). *Geophysical Research Letters*, 36:L03817.

Lin, I.-I., Goni, G. J., Knaff, J. A., Forbes, C., and Ali, M. M. (2013). Ocean heat content for tropical cyclone intensity forecasting and its impact on storm surge. *Natural Hazards*, 66:1481–1500.

Lin, I.-I., Pun, I.-F., and Wu, C.-C. (2009b). Upper-ocean thermal structure and the Western North Pacific category 5 typhoons. Part II: Dependence on translation speed. *Monthly Weather Review*, 137:3744–3757.

Lin, I.-I., Wu, C.-C., Pun, I.-F., and Ko, D.-S. (2008). Upper-ocean thermal structure and the Western North Pacific category 5 typhoons. Part I: Ocean features and the category 5 typhoons' intensification. *Monthly Weather Review*, 136:3288–3306.

Liu, B., Liu, H., Xie, L., Guan, C., and Zhao, D. (2011). A coupled atmosphere-wave-ocean modeling system: Simulation of the intensity of an idealised tropical cyclone. *Monthly Weather Review*, 139:132–152.

Liu, Q., Surgi, N., Lord, S., Wu, W.-S., Parrish, S., Gopalakrishnan, S., Waldrop, J., and Gamache, J. (2006). Hurricane initialization in HWRF model. *Preprints, 27th Conference on Hurricanes and tropical meteorology, Monterey, CA, American Meteor. Soc.*, 8A:2.

Longuet-Higgins, M. S. and Stewart, R. W. (1964). Radiation stress in water waves; a physical discussion, with applications. *Deep-Sea Research*, 11:529–562.

Lowe, J. A., Howard, T., Pardaens, A., Tinker, J., Holt, J., Wakelin, S., Milne, G., Leake, J., Wolf, J., Horsburgh, K. J., Reeder, T., Jenkins, G., Ridley, J., Dye, S., and Bradley, S. (2009). UK, Climate Projections science report: Marine and coastal projections. *Met Office Hadley Centre, Exeter, UK*.

Luettich, R. A., Westerink, J. J., and Scheffner, N. W. (1992). ADCIRC: An advanced three-dimensional circuation model for shelves, coasts and estuaries. Report 1: Theory and methodology of ADCIRC-2DDI and ADCIRC-3DL. *Dredging Research Program Technical Report DRP-92-6*, 1.

Madsen, O. S. (1994). Spectral wave-current bottom boundary layer flows. *Proc. 21th International Conference of Coastal Engineering, ASCE*, 1:384–398.

Mainelli, M., DeMaria, M., Shay, L. K., and Goni, G. J. (2008). Application of ocean heat content estimation to operational forecasting of recent Atlantic category 5 hurricanes. *Weather and Forecasting*, 23:3–16.

Mastenbroek, C., Burgers, G., and Janssen, P. A. E. M. (1993). The dynamical coupling of a wave model and a storm surge model through the atmospheric boundary layer. *Journal of Physical Oceanography*, 23(8):1856–1866.

McTaggart-Cowan, R., Davies, E., Jr, J. F., Jr., T. G., and Schultz, D. (2015). Revisiting the 26.5c sea surface temperature threshold for tropical cyclone development. *American Meteorological Society*, pages 1929–1943.

Mellor, G. L. (2004). User's guide for a three-dimensional, primitive equation, numerical ocean model. *Program in Atmospheric and Oceanic Sciences, Princeton University*, Revision.

Mlawer, E. J., Taubman, S. J., Brown, P. D., Iacono, M., and Clough, S. (1997). Radiative transfer for inhomogeneous atmospheres: RRTM, a validated correlated k model for the longwave. *Journal of Geophysical Research*, 102:16663–16682.

Monbaliu, J., Padilla-Hernández, R., Hargreaves, J. C., Albiach, J. C. C., Luo, W., Sclavo, M., and Günther, H. (2000). The spectral wave model, WAM, adapted for applications with high spatial resolution. *Coastal Engineering*, 41:41–62.

Moon, I.-J., Kwon, J.-I., Lee, J.-C., Shim, J.-S., Kang, S. K., Oh, I. S., and Kwon, S. J. (2009). Effect of the surface wind stress parametrisation on the storm surge modelling. *Ocean Modelling*, 29:115–127.

Muhr, B., Kobele, D., Bessel, T., Fohringer, J., Lucas, C., and Girard, T. (2013). Super Cyclonic Storm 02B, Phailin. *Center for Disaster Management and Risk Reduction Technology Report*.

Munk, W. H. (1951). Origin and generation of waves. *Proceedings of the First Conference on Coastal Engineering, Long Beach, CA*, pages 1–4.

Murakami, H. (2014). Tropical cyclones in reanalysis data sets. *Geophysical Research Letters*, 41:2133–2141.

Murty, P. L. N., Sandhya, K. G., Bhaskaran, P. K., et al. (2014a). A coupled hydrodynamic modelling system for Phailin cyclone in the Bay of Bengal. *Coastal Engineering*, 93:71–81.

Murty, P. L. N., Sandhya, K. G., Bhaskaran, P. K., Jose, F., Gayathri, R., Nair, T. M. B., Kumar, T. S., and Shenoi, S. S. C. (2014b). A coupled hydrodynamic modelling system for Phailin cyclone in the Bay of Bengal. *Coastal Engineering*, 93:71–81.

Murty, T. S., Flather, R. A., and Henry, R. F. (1986). The storm surge problem in the Bay of Bengal. *Progress in Oceanography*, 16:195–233.

Noh, Y., Cheon, W. G., Hong, S. Y., and Raasch, S. (2003). Improvements on the K-profile model for the planetary boundary layer based on large eddy simulation data. *Boundary Layr Meteorology*, 107:421–427.

Osuna, P. and Wolf, J. (1994). A numerical study on the effect of wave-current interaction processes in the hydrodynamics of the Irish Sea. *Proceedings of the 5th International conference on ocean wave Measurement and Analysis, Madrid, Spain*, 10.

Palmen, E. (1948). On the formation and structure of tropical hurricanes. *Geophysics*, 3:26–38.

Paul, B. K. (2009). Why relatively fewer people died? the case of Bangladesh's Cyclone Sidr. *Natural Hazards*, 50:289–304.

Peng, S. Q., Li, Y., and Xie, L. (2013). Adjusting the wind stress drag coefficient in storm surge forecasting using an adjoint technique. *Journal of Atmospheric and Oceanic Technology*, 30(3):590 – 608.

Peng, S. Q. and Xie, L. (2006). Effect of determining initial conditions by four-dimensional variational data assimilation on storm surge forecasting. *Ocean Modelling*, 14:1–18.

Pollard, R. (1973). Wind driven mixing and deepening of the oceanic boundary layer. *Quarterly Journal of the Royal Meteorological Society*, 99(422):772–773.

Powell, M. D., Vickery, P. J., and Reinhold, T. A. (2003). Reduced drag coefficient for high wind speeds in tropical cyclones. *Nature*, 422:279–283.

Price, J. F. (1981). Upper ocean response to a hurricane. *Journal of Physical Oceanography*, 11:153–175.

Pugh, D. and Woodworth, P. (2014). *Sea-Level Science: Understanding Tide, Surges, Tsunamis and Mean Sea-Level Changes*. Cambridge University Press.

Rappaport, E. N., Franklin, J. L., Avila, L. A., Baig, S. R., II, J. L. B., Blake, E. S., Burr, C. A., Jiing, J.-G., Juckins, C. A., Knabb, R. D., Landsea, C. W., Mainelli, M., Mayfield, M., McAdie, C. J., Pasch, R. J., Sisko, C., Stewart, S. R., and Tribble, A. N. (2009a). Advances and challenges at the National Hurricane Center. *Weather and Forecasting*, 24:395–419.

Rappaport, E. N., Franklin, J. L., Avila, L. A., et al. (2009b). Advances and challenges at the National Hurricane Center. *Weather and Forecasting*, 24:395–419.

Sadhuram, Y., Maneesha, K., and Murty, T. V. R. (2010). Importance of upper ocean heat content in the intensification and translation speed of cyclones over the Bay of Bengal. *Current Science*, 99(9):1191–1194.

Schade, L. R. and Emanuel, K. A. (1999). The ocean's effect on the intensity of tropical cyclones: Results from a simple coupled atmosphere-ocean model. *Journal of the Atmospheric Sciences*, 56:642–651.

Schubert, W., Montgomery, M., Taft, R., Gunn, T., Fulton, S., Kossin, J., and Edwards, J. (1999). Polygonal eyewalls, asymmetric eye contraction, and potential vorticity mixing in hurricanes. *Journal of Atmospheric Sciences*, 56:1197–1223.

Shay, L. K., Goni, G. J., and Black, P. G. (2000). Effects of a warm oceanic feature on hurricane Opal. *Monthly Weather Review*, 128:1366–1383.

Skamarock, W. C., Klemp, J. B., Dudhia, J., Gill, D. O., Barker, D. M., Duda, M. G., Huang, X.-Y., Wang, W., and Powers, J. G. (2008). A description of the Advanced Research WRF Version 3. *NCAR Technical Note*.

Smith, S. D. and Banke, E. G. (1975). Variation in sea surface drag coefficient with wind speed. *Quarterly Journal of the Royal Meteorological Society*, 429(101):665–673.

Souza, A., Dickey, T., and Chang, G. (2001). Modeling water column structure and suspended particulate matter on the Middle Atlantic continental shelf during the passages of Hurricanes Edouard and Hortense. *Journal of Marine Research*, 59:1021–1045.

Tasnim, K. M., Shibayama, T., Esteban, M., Takagi, H., Ohira, K., and Nakamura, R. (2015). Field observation and numerical simulation of past and future storm surges in the Bay of Bengal: Case study of cyclone Nargis. *Natural Hazards*, 75:1619–1647.

Taylor, P. K. and Yelland, M. J. (2001). The dependence of sea surface roughness on the height and steepness of waves. *Journal of Physical Oceanography*, 31:572–590.

Vissa, N. K., Satyanarayana, A. N. V., and Kumar, B. P. (2013). Intensity of tropical cyclones during pre- and post- monsoon seasons in relation to accumulated tropical cyclone heat potential over Bay of Bengal. *Natural Hazards*, 68:351–371.

Weaver, R. (2004). Effect of wave forces on storm surge. *MS Thesis, Dept. of Civil and Coastal Engineering, University of Florida*.

Weisberg, R. H. and Zheng, L. (2006). A simulation of the Hurricane Charley storm surge and its breach of North Captiva Island. *Hydrologic Modelling*, pages 152–165.

Western Pacific Weather (2015). Western Pacific Weather Saffir-Simpson scale.

Whitaker, J. S. and Hamill, T. M. (2002). Ensemble data assimilation without perturbed observations. *Monthly Weather Review*, 130:1913–1924.

Willoughby, H. (1988). The dynamics of the tropical cyclone core. *Austrailian Meteorological Magazine*, 36(3):183–191.

WMO (2011). Guide to storm surge forecasting. *WMO Publication*, WMO-No. 1076.

Wolf, J. (1981). Surge-tide interaction in the North Sea and River Thames. *Floods due to High Winds and Tides*, pages 75–94.

Wolf, J. (2009). Coastal flooding: Impacts of coupled wave-surge-tide models. *Natural Hazards*, 49:241–260.

Wolf, J. and Flather, R. A. (2005). Modelling waves and surges during the 1953 storm. *Philosophical Transactions of the Royal Society A*, 363:1359–1375.

Wolf, J., Wakelin, S. L., and Holt, J. T. (2002). A couple model of waves and currents in the Irish Sea. *Proceedings of the Twelfth International Offshore and Polar Engineering Conference Kitakyushu Japan*, 3:108–114.

Wolf, J. and Woolf, D. (2006). Waves and climate change in the north-east Atlantic. *Geophysical Research Letters*.

World Meteorological Organisation (2016). Tropical cyclone operational plan for the Bay of Bengal and Arabian Sea. *Tropical Cyclone Programme. Report Number TCP-21*.

Xie, L., Liu, B., Liu, H., and Guan, C. (2010). Numerical simulation of tropical cyclone intentisity using an air-sea-wave coupled prediction system. *Advances in Geosciences*, 18:19–43.

Zehr, R. M. (1992). Tropical cyclogenesis in the western North Pacific. *NOAA Technical Report NESDIS 61*, page 181.

Zhang, F. and Sippel, J. A. (2009). Effects of moist convection on hurricane predictability. *Journal of the Atmospheric Sciences*, 66:1944–1961.

Zhu, T. and D.-L.Zhang (2006). Numerical simulation of Hurricane Bonnie (1998). Part II: Sensitivity to varying cloud microphysical processes. *Journal of the Atmospheric Sciences*, 63:109–126.